

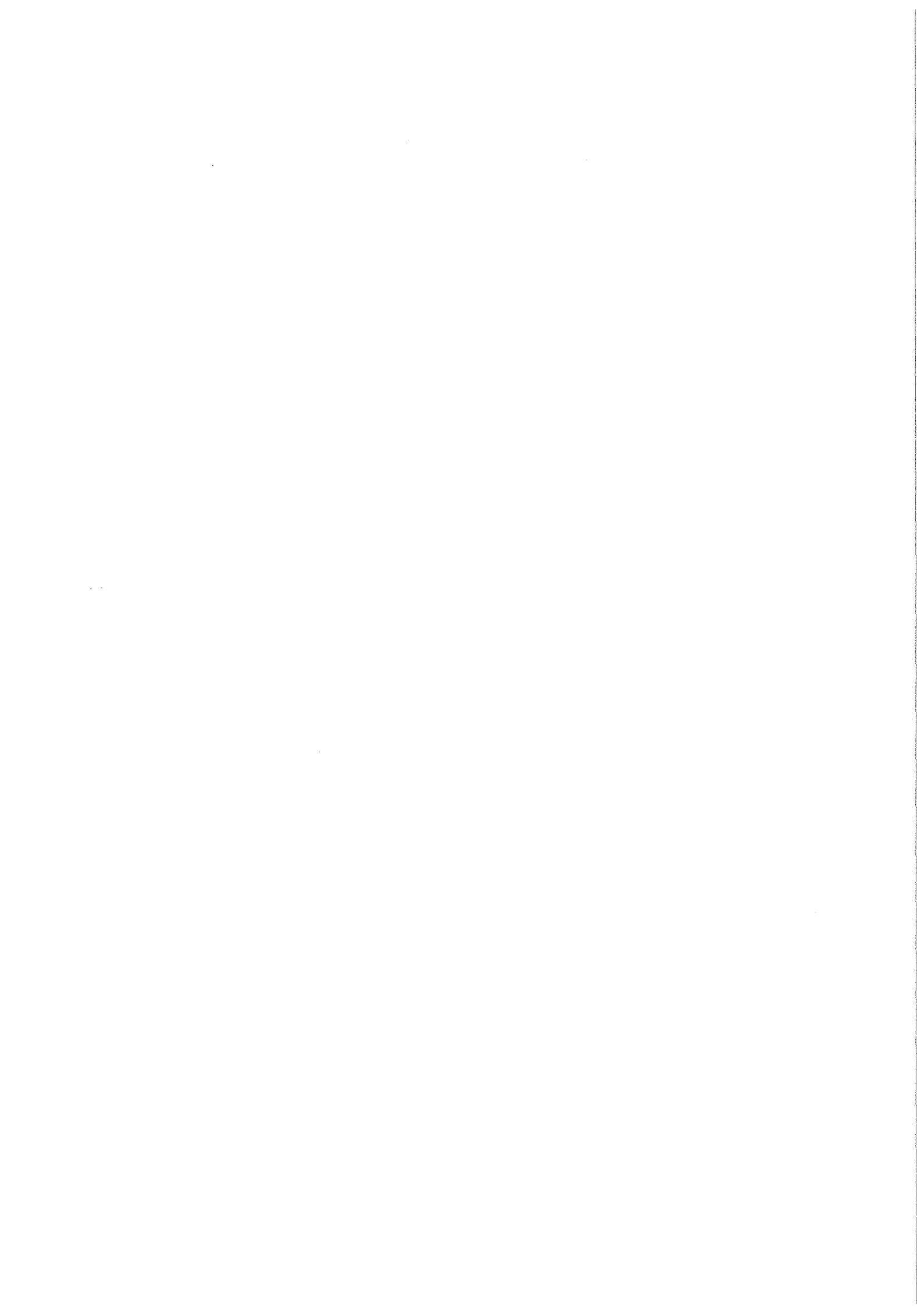
KfK 3427  
November 1982

# Annual Report on Nuclear Physics Activities

July 1, 1981 — June 30, 1982

Editors:  
E. Borie, P. Doll, H. Rebel  
Institut für Kernphysik  
Institut für Angewandte Kernphysik

**Kernforschungszentrum Karlsruhe**



KERNFORSCHUNGSZENTRUM KARLSRUHE

Institut für Kernphysik  
Institut für Angewandte Kernphysik

KfK 3427

ANNUAL REPORT

on

NUCLEAR PHYSICS ACTIVITIES

July 1, 1981 - June 30, 1982

Editors:

E. Borie, P. Doll and H. Rebel

Kernforschungszentrum Karlsruhe GmbH, Karlsruhe

Als Manuskript vervielfältigt  
Für diesen Bericht behalten wir uns alle Rechte vor

Kernforschungszentrum Karlsruhe GmbH  
ISSN 0303-4003

## ABSTRACT

This report surveys the activities in fundamental research from July 1, 1981 to June 30, 1982 at the three institutes of the KfK which are concerned with nuclear physics. The research program comprises laser spectroscopy, nuclear reactions with light ions, neutron physics, neutrino physics and physics at medium and higher energies.

## ZUSAMMENFASSUNG

Der vorliegende Bericht gibt einen Überblick über die Arbeiten an den drei Kernphysikalischen Instituten des Kernforschungszentrums Karlsruhe im Zeitraum vom 1. Juli 1981 bis zum 30. Juni 1982. Das Forschungsprogramm umfaßt die Gebiete Laserspektroskopie, Kernreaktionen mit leichten Ionen, Neutronenphysik, Neutrino-Physik, sowie Mittel- und Hochenergiephysik.

Wir legen hiermit den zweiten gemeinsamen Bericht über die Arbeiten der kernphysikalischen Institute des Kernforschungszentrums Karlsruhe vor.

Um den Gesamtzusammenhang der Arbeiten deutlicher zu machen, haben wir - auch auf Wunsch einiger Leser des ersten Berichtes - etwas ausführlichere Zusammenfassungen der im Berichtszeitraum veröffentlichten Arbeiten mit aufgenommen.

Wir hoffen, damit auch einen größeren Interessentenkreis anzusprechen.

  
(A. Citron)

  
(G. Schatz)

  
(B. Zeitnitz)



Am Institut für Kernphysik I arbeiten drei Arbeitsgruppen auf verschiedenen Gebieten der Kern- und Teilchenphysik:

1. Physik mit schnellen Neutronen:

Am neuerrichteten polarisierten Neutronenstrahl des Karlsruher Zyklotrons (POLKA) werden Streuexperimente an sehr leichten Kernen durchgeführt. Ziele sind die präzise Bestimmung von Streuphasen aus Experimenten mit polarisierten Neutronen an unpolarisierten und später auch an polarisierten Protonen. Außerdem sollen die innere Struktur und Dynamik der Kerne bis zum  $A = 5$  System untersucht werden.

Im Laufe des letzten Jahres konnte die Anlage POLKA bereits in einigen Experimenten erfolgreich genutzt werden.

Das noch im Rahmen der Arbeitsgruppe "Experimentelle Methoden" entwickelte großvolumige polarisierte Target wurde inzwischen erfolgreich getestet und wird voraussichtlich ab Sommer 1983 für Streuexperimente am polarisierten Strahl genutzt werden können.

2. Elementarteilchenphysik:

Diese Gruppe betreibt im Rahmen einer internationalen Kollaboration das Detektorsystem CELLO am  $e^+e^-$  Speicherring PETRA in Hamburg. Der Detektor dient Experimenten zur Untersuchung von  $e^+e^-$  Stößen bei den höchsten zur Zeit erreichbaren Energien. Mit seinem modernen Flüssig-Argon-Kalorimeter ist CELLO besonders geeignet, die elektromagnetische Komponente in diesen Reaktionen zu untersuchen. Damit werden z.B. genaue Studien der Quantenelektrodynamik, detaillierte Untersuchungen von Quark- und Gluon-Jets und die Suche nach neuen Quarks möglich. Der Detektor wurde inzwischen weitgehend überholt und verbessert und befindet sich nach einer mehrmonatigen Pause seit dem Sommer 1982 wieder im Strahl. Er arbeitet in allen seinen Komponenten zufriedenstellend und wird aktiv während der geplanten Energieerhöhungen an der Suche nach einem neuen Quark teilnehmen.

### 3. Experimentelle Methoden:

Im Rahmen dieser Arbeitsgruppe wurde eine kombinierte kryotechnische Anlage zur Erzeugung niedriger Temperaturen ( $< 10$  mK) und starker Magnetfelder (10 Tesla) entwickelt.

Mit dieser Anlage sollen große polarisierte Proben verschiedener Atomkerne, z.B. für Streuexperimente mit Neutronen, erzeugt werden. Inzwischen wurde das Gerät an die Arbeitsgruppe Neutronenphysik übergeben.

Die Gruppe hat sich ferner mit Entwicklungen neuartiger Detektoren für Neutronen beschäftigt.

In der Zwischenzeit wurde durch teilweisen Austausch von Wissenschaftlern und Technikern eine neue Arbeitsgruppe "Neutrinophysik" gebildet. Die Mitglieder der ehemaligen Gruppe "Experimentelle Methoden" sind zum größeren Teil auf dieses neue Arbeitsgebiet übergegangen. Die neue Gruppe beschäftigt sich bereits intensiv mit der Entwicklung eines Detektorsystems für Neutrinos an der Spallationsneutronenquelle SNS des Rutherfordlabors in Chilton England.

Im Institut für Kernphysik II wird Mittelenergiephysik bei CERN und SIN betrieben.

Bei CERN hat sich unsere Gruppe in Fortsetzung einer langen Tradition auf dem Gebiet exotischer Atome auf das Projekt LEAR (Low Energy Antiproton Ring) konzentriert. Dieses Projekt, für dessen Zustandekommen sich Karlsruhe sehr stark eingesetzt hat, verspricht einmalige Arbeitsmöglichkeiten mit langsamen Antiprotonen. Schon für die erste Meßperiode sind zwei Experimentiervorschläge angenommen worden, von denen der eine ganz von Karlsruher Physikern getragen wird, während sie beim anderen in einer Kollaboration maßgeblich mitwirken. Der Karlsruher Vorschlag nutzt die von Herrn Simons vorgeschlagene Idee der Zyklotronfalle aus. Dieses Gerät soll am SIN erprobt und dann zum LEAR gebracht werden. Auch an den technischen Problemen der Erstellung von LEAR, insbesondere am Einsatz der Elektronenkühlung, ist Karlsruhe personell und finanziell beteiligt.

Die Experimente beim SIN befassen sich schwerpunktmäßig mit Fragen der Pionwechselwirkung mit überschaubaren Systemen aus wenigen Nukleonen. Dies gilt für die komplementären Experimente mit Protonen bzw. Pionen im Eingangskanal. Durch Heranziehung der zusätzlichen Informationen, die man unter Ausnutzung von Polarisation erhalten kann, werden theoretische Annahmen, insbesondere über die Existenz von Dibaryonzuständen, überprüft.

Auch das von Karlsruhe entworfene Niederenergiespektrometer wird vorwiegend der Untersuchung sehr einfacher Systeme bei Energien nahe der Pionenschwelle dienen.

Die Arbeiten des Institutes für Angewandte Kernphysik II auf dem Gebiete der kernphysikalischen Grundlagenforschung betreffen im wesentlichen drei Arbeitsgebiete:

1. Am Karlsruher Isochronzyklotron werden Kernreaktionen untersucht, die durch  $\alpha$ -Teilchen und  ${}^6\text{Li}$ -Ionen von 26 MeV/Nukleon induziert werden. Im Vordergrund stehen dabei z.Z. Aufbruchreaktionen des  ${}^6\text{Li}$ -Projektils mit dem Ziel, Informationen über die Impulsverteilung der Nukleonencluster im  ${}^6\text{Li}$  zu erhalten. In einer Teilchen-Teilchen-Koinzidenzmessung der Reaktion  ${}^6\text{Li} + {}^6\text{Li}$  soll versucht werden, die Methoden zur Bestimmung der Impulsverteilung aus den experimentellen Wirkungsquerschnitten zu überprüfen. Für ähnliche Experimente mit schwereren Projektilen ist ein Magnetspektrometer im Aufbau, das Ende 1982 in Betrieb gehen soll.
2. Mit laserspektroskopischen Methoden werden an sehr geringen Mengen ( $\lesssim$  ng) radioaktiver Atome Isotopieverschiebungen optischer Spektrallinien gemessen und daraus Kernradien bestimmt. Die derzeitigen Messungen an Blei-Isotopen umfassen bisher einen Bereich von 14 Masseneinheiten um den Schalenabschluß bei  $N = 126$ . Die Ergebnisse zeigen, daß der Ladungsradius der Kerne oberhalb  $N = 126$  mit wachsender Neutronenzahl wesentlich schneller ansteigt als vor dem Schalenabschluß.

3. Am van-de-Graaff-Beschleuniger des Institutes werden Neutroneneinfangquerschnitte gemessen, die für das Verständnis der Elementsynthese in Sternen von Bedeutung sind. Dabei liegt das Schwergewicht darauf, durch kernphysikalische Messungen Aussagen über die physikalischen Bedingungen zu gewinnen, unter denen der sogenannte s-Prozeß der Elementsynthese abgelaufen ist. Ergänzende kernspektroskopische Arbeiten werden z.T. am ILL in Grenoble und bei der GSI, Darmstadt, durchgeführt.

C O N T E N T S

	page
1. NUCLEAR PHYSICS	
1.1 Nuclear astrophysics	1
1.2 Neutron physics	21
1.3 Nuclear reactions by charged particles	47
1.4 Nuclear theory	75
2. LASERSPECTROSCOPY	79
3. NEUTRINO PHYSICS	85
4. INTERMEDIATE ENERGY PHYSICS	
4.1 Muonic atoms and QED	93
4.2 Hadronic atoms	100
4.3 Pion nucleus interaction	108
4.4 Nucleon-nucleon interaction	118
4.5 Nucleon-antinucleon interaction	
5. HIGH ENERGY PHYSICS	141
6. INSTRUMENTATION	167
7. APPLICATIONS	222
8. LIST OF PUBLICATIONS	233
9. PERSONELL	250

1. NUCLEAR PHYSICS
- 1.1 NUCLEAR ASTROPHYSICS
- 1.1.1 Isotopic Neon Cross Sections for a Study of Neutron Balance and Temperature During s-Process Nucleosynthesis\*

J. Almeida and F. Käppeler  
Kernforschungszentrum Karlsruhe, IAK II

The neutron source of the s-process is believed to be the  $^{22}\text{Ne}(\alpha, n)$  reaction, taking place in the He burning shell of a pulsating red giant. Such a periodic neutron irradiation leads to an exponential distribution of neutron fluences for the seed nuclei, which can be deduced from the observed solar system abundances. Using this empirically determined distribution of neutron fluences and the abundances and the cross sections of the elements present in the He shell, the number of neutrons captured by each nuclear species during the s-process has been calculated. The  $^{22}\text{Ne}$  has as progenitors the C, N and O isotopes involved in the CNO cycle, and is the most abundant nuclear species (apart from  $^4\text{He}$  and  $^{12}\text{C}$ ) in the He shell; it was therefore anticipated that it would be a major neutron absorber. We have thus measured the capture cross sections of the three stable neon isotopes in the energy range 5-400 keV, and we determined the 30 keV Maxwellian averaged cross sections with an accuracy of better than 1 mb; the total cross sections were also measured, between 5 and 800 keV.

As a result it was found that the  $^{22}\text{Ne}(\alpha, n)$  reaction can indeed satisfy the neutron balance condition that as many neutrons should be produced as are absorbed. From this condition we conclude that at least 80 % of the  $^{22}\text{Ne}$  must undergo the  $(\alpha, n)$  reaction, which implies that less than 20 % can undergo the  $(\alpha, \gamma)$  reaction. Therefore, neutron absorption by the light elements from  $^{20}\text{Ne}$  to  $^{56}\text{Fe}$ , is dominated not by  $^{22}\text{Ne}$ , but by  $^{25}\text{Mg}$  which is produced abundantly by the  $^{22}\text{Ne}(\alpha, n)$  reaction. The reaction rate ratio  $^{22}\text{Ne}(\alpha, n)/^{22}\text{Ne}(\alpha, \gamma)$  derived from the neutron balance condition allows an estimate of the s-process temperature  $T_s$  via the energy dependence of these rates. We obtain a lower limit  $T_s > 3.2 \cdot 10^8$  K or  $kT_s > 27$  keV, consistent with the temperature of the He burning shell.

\* The Astrophysical Journal (in press)

1.1.2 Neutron Capture Widths of s-Wave Resonances in  $^{56}\text{Fe}$ ,  $^{58,60}\text{Ni}$  and  $^{27}\text{Al}^*$

K. Wisshak, F. Käppeler, G. Rupp, G. Reffo<sup>+</sup>, and F. Fabbri<sup>+</sup>  
 Kernforschungszentrum Karlsruhe, IAK II

The neutron capture widths of s-wave resonances in  $^{56}\text{Fe}$  (27.7 keV),  $^{58}\text{Ni}$  (15.4 keV),  $^{60}\text{Ni}$  (12.5 keV) and  $^{27}\text{Al}$  (35.3 keV) have been determined, using a set-up completely different from LINAC experiments. A pulsed 3 MV Van de Graaff accelerator and the  $^7\text{Li}(p,n)$  reaction served as a neutron source. The proton energy was adjusted just above the reaction threshold to obtain a kinematically collimated neutron beam. This allowed to position the samples at a flight path as short as  $\sim 90$  mm. Capture events were detected by three Moxon-Rae detectors with graphite, bismuth-graphite and pure bismuth converter, respectively. The measurements were performed relative to a gold standard. The setup allows to discriminate capture of scattered neutrons completely by time of flight and to use very thin samples (0.15 mm) in order to reduce multiple scattering.

The experimental capture yield was analyzed using the FANAC code. As an example Fig. 1 shows the result of fits for resonances in  $^{58}\text{Ni}$  and  $^{60}\text{Ni}$ . The results as obtained with the different detectors were corrected for deviations of the detector efficiency from a linear increase with gamma-ray energy. To this end capture gamma-ray spectra for the respective s-wave resonances were calculated according to the statistical model.

Table I Preliminary results for the capture width of s-wave resonances in  $^{27}\text{Al}$ ,  $^{56}\text{Fe}$  and  $^{58,60}\text{Ni}$  (statistical uncertainties in % are given in brackets).

	Converter Material of Moxon-Rae Detector		
	Graphite	Bismuth- Graphite	Bismuth
$^{58}\text{Ni}$	1.42 (4.2)	1.64 (4.0)	1.60 (3.7)
average	$\Gamma_{\gamma}(15.4 \text{ keV}) = 1.55 (2.3) \text{ eV}$		
$^{60}\text{Ni}$	3.33 (2.6)	3.63 (3.4)	3.48 (2.9)
average	$\Gamma(12.5 + 12.2 + 13.6 \text{ keV}) = 3.45 (1.7) \text{ eV}$		
adopted	$\Gamma_{\gamma}(12.2 + 13.6 \text{ keV}) = 0.56$		
	$\Gamma_{\gamma}(12.5 \text{ keV}) = 2.89 (1.7) \text{ eV}$		
$^{56}\text{Fe}$	1.07 (3.8)	1.14 (4.0)	1.04 (3.8)
average	$\Gamma_{\gamma}(27.7 \text{ keV}) = 1.08 (2.2) \text{ eV}$		
$^{27}\text{Al}$	2.11 (3.0)	2.25 (2.9)	2.00 (2.8)
average	$\Gamma_{\gamma}(35.5 \text{ keV}) = 2.11 (1.7) \text{ eV}$		

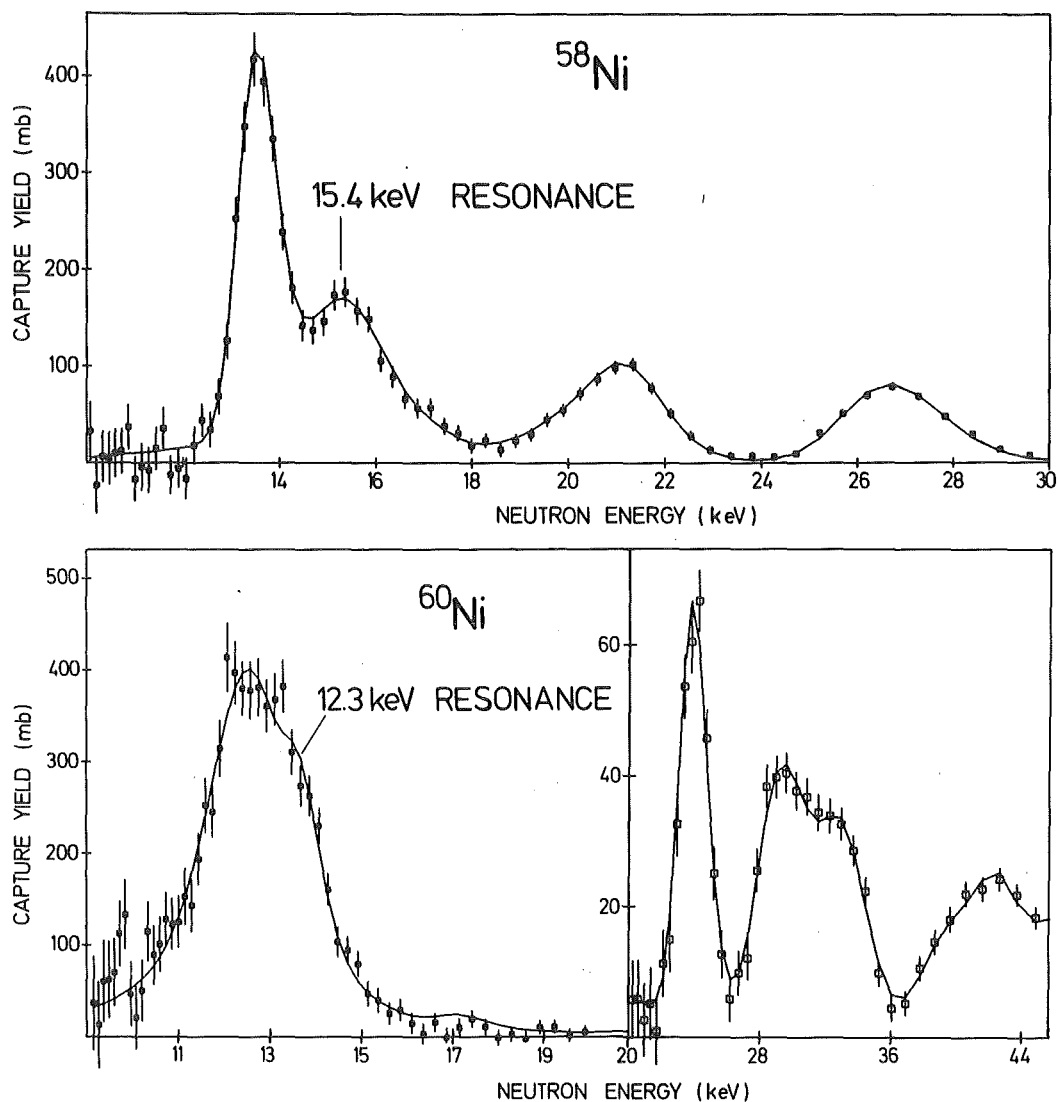


Fig. 1 FANAC fit to the capture yield of  $^{58}\text{Ni}$  and  $^{60}\text{Ni}$

Preliminary results for the capture widths of s-wave resonances are given in Table I. The results obtained with different detectors agree within their remaining systematic uncertainty of  $\sim 5\%$ .

\* Proc. of the NEANDC/NEACRP Specialists Meeting on Fast Neutron Capture Cross Sections, Argonne, April 20-23, 1982 (to be published).

+ Comitato Nazionale Energia Nucleare, Bologna, Italy

### 1.1.3 Neutron Capture Resonances in $^{56}\text{Fe}$ and $^{58}\text{Fe}$ in the Energy Range from 10 to 100 keV\*

F. Käppeler, K. Wisshak, and L.D. Hong

The neutron capture cross sections of  $^{56}\text{Fe}$  and  $^{58}\text{Fe}$  have been measured in the energy range from 10 to 250 keV relative to the gold standard. A pulsed 3 MV Van de Graaff accelerator and the  $^7\text{Li}(p,n)$  reaction

served as a neutron source. Capture gamma rays were detected by two  $C_6D_6$  detectors, which were operated in coincidence and anticoincidence mode. Two-dimensional data acquisition allowed to apply the pulse height weighting technique off-line. The samples were located at a flight path of 60 cm. The total time resolution was 1.2 ns thus allowing for an energy resolution of 2 ns/m. The experimental set-up was optimized with respect to low background and low neutron sensitivity. The additional flight path of 4 cm from the sample to the detector was sufficient to discriminate capture of sample scattered neutrons by the additional time of flight. In this way reliable results were obtained even for the strong s-wave resonances of both isotopes. The experimental capture yield was analyzed with the FANAC code. The energy resolution allowed to extract resonance parameters in the energy range from 10 to 100 keV. The individual systematic uncertainties of the experimental method are discussed in detail. They were found to range between 5 and 10 % while the statistical uncertainty is 3-5 % for most of the resonances. A comparison to the results of other authors exhibits in case of  $^{56}Fe$  systematic differences of 7-11 %. For  $^{58}Fe$  the present results differ up to 50 % from the only other measurement published for this isotope until now.

\* KfK Report 3412 (1982) and submitted for publication to Nucl. Sci. Eng.

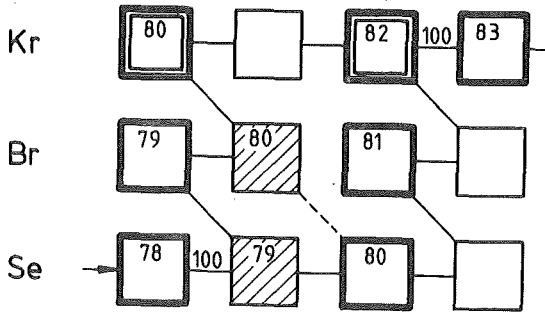
1.1.4 Analysis of the s-Process Branching at  $^{79}Se$  with Improved Cross Sections for the Krypton Isotopes  
G. Walter, F. Käppeler, Z.Y. Bao<sup>+</sup>  
Kernforschungszentrum Karlsruhe, IAK II

The capture cross sections of  $^{80}Kr$  and  $^{82}Kr$  are most important for an analysis of the s-process branching at  $^{79}Se$ . This is illustrated by Fig. 1 which shows the s-process flow through the Se, Br, Kr-region.

The isotopes  $^{80}Kr$  and  $^{82}Kr$  are both of pure s-process origin because they are shielded against the r-process by their Se isobars. While  $^{80}Kr$  is part of that branching which originates from beta decay in  $^{79}Se$ ,  $^{82}Kr$  represents the total s-process flow. This means that the branching ratio at  $^{79}Se$

$$B_{\beta} = \frac{\lambda_{\beta}}{\lambda_{\beta} + \lambda_n} \quad (1)$$

Fig. 1



The s-process flow through the Se, Br, Kr-isotopes.

( $\lambda_\beta$  = beta decay rate,  $\lambda_n$  = neutron capture rate) is to first approximation given by  $B_\beta \approx \sigma N(^{80}\text{Kr}) / \sigma N(^{82}\text{Kr})$ . In the model of Seeger, Fowler and Clayton (1) one obtains

$$B_\beta = \left[ 1 + \frac{\sigma N(^{82}\text{Kr})}{\sigma N(^{80}\text{Kr})} \frac{\zeta(^{79}\text{Br})\zeta(^{80}\text{Kr})}{\zeta(^{79}\text{Se})\zeta(^{80}\text{Se})\zeta(^{81}\text{Br})\zeta(^{82}\text{Kr})} - \frac{\zeta(^{79}\text{Br})\zeta(^{80}\text{Kr})\zeta(^{81}\text{Kr})}{\zeta(^{79}\text{Se})\zeta(^{80}\text{Se})\zeta(^{81}\text{Br})} \right]^{-1} \quad (2)$$

where  $\zeta(A) = \frac{\sigma(A) \tau_0}{1 + \sigma(A) \tau_0}$  is the propagator for the s-process flow;  $\sigma(A)$  is the Maxwell average capture cross section and  $\tau_0$  the mean fluence parameter. Equation (2) is further complicated by the fact that the empirical  $\sigma N$ -curve requires two different neutron fluence distributions characterized by  $\tau_{01} = 0.056 \text{ mb}^{-1}$  and  $\tau_{02} = 0.24 \text{ mb}^{-1}$  (2).

As practically all values  $\zeta(A)$  are close to unity,  $B_\beta$  is mostly determined by the  $\sigma N$  values of  $^{80}\text{Kr}$  and  $^{82}\text{Kr}$ . The isotopic ratio is accurately known and the problem reduces to a measurement of the cross section ratio. After a first series of measurements on the stable Krypton isotopes (3) it was found that an additional run with a  $^{80}\text{Kr}$  sample of higher enrichment was desirable. With this new measurement and with refined theoretical cross sections for all nuclei involved in the branching (4) we have determined the branching ratio

$$B_\beta = 0.55 \pm 0.10.$$

Most of the remaining 20 % uncertainty in  $B_\beta$  is caused by the 30 % uncertainty in the capture cross section of  $^{80}\text{Se}$  (15 - 18 %) and only to a minor extent by the uncertainty of the cross section ratio  $\sigma(^{80}\text{Kr}) / \sigma(^{82}\text{Kr})$  (7 %).

The  $^{79}\text{Se}$ -branching is important because the beta decay rate of  $^{79}\text{Se}$  depends sensitively on the temperature. Fig. 2 illustrates this dramatic change of the  $^{79}\text{Se}$  half life which is due to the increasing population

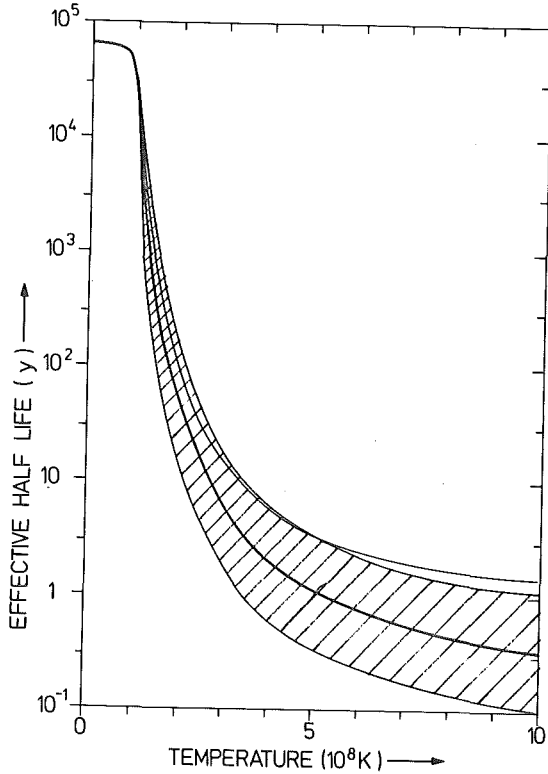


Fig. 2  
The effective half life of  $^{79}\text{Se}$  as a function of temperature.

probability for the first two excited states. These have much smaller log ft-values than the ground state and therefore even a small population of these states accelerates the decay drastically. The solid line was calculated with an estimated value  $(5) \log ft = 5.5 \pm 0.5$  (ground state  $\log ft \leq 10.2$ ) and the hatched area represents the related uncertainty for  $T_{1/2}$ .

With the above determined branching ratio and an estimate for the neutron capture rate  $\lambda_n = v_T \sigma_{79\text{Se}} n_n$  the effective beta decay rate of  $^{79}\text{Se}$  during the s-process can be derived from equation (1). The  $^{79}\text{Se}$  cross section is calculated with an uncertainty of 25-30 % and the neutron density  $n_n$  can be estimated from other branchings with an uncertainty of 50-100 % at present. This leads to  $\lambda_\beta = 0.6 \text{ yr}^{-1}$  or  $T_{1/2}^{\text{eff}} = 1.1 \text{ yr}$ , resulting in an s-process temperature of  $4.9 \cdot 10^8 \text{ K}$  (or  $kT = 25 \text{ keV}$ ). The largest uncertainty is clearly introduced by the log ft-value for the beta decay rate of the excited states in  $^{79}\text{Se}$ , for which we plan a measurement in the near future (see

contribution 1.1.5 to this report).

- (1) P.A. Seeger, W.A. Fowler and D.D. Clayton, Ap. J. Suppl. 11 (1965) 121
- (2) F. Käppeler, H. Beer, K. Wisshak, D.D. Clayton, R.L. Macklin, and R.A. Ward, Ap. J. 257 (1982) 821.
- (3) B. Leugers, KfK-Report 2895 (1979)
- (4) G. Walter, F. Käppeler, Z.Y. Bao, G. Reffo, and F. Fabbri (to be published)
- (5) J.H. Conrad, Ph.D. thesis, University of Heidelberg (1976).

<sup>+</sup>Institute of Atomic Energy, Peking, China

#### 1.1.5 Further Development of the $\beta$ -Spectrometer

G. Walter, G. Rupp, S. Schmitt, F. Käppeler, and H. Beer  
Kernforschungszentrum Karlsruhe, IAK II

When measuring weak  $\beta^-$ -branching ratios in the decay of nuclear isomeric states it is often favourable to suppress low energy conversion lines.

In order to meet this requirement we have developed a system based on the existing  $4\pi$   $\beta$ -spectrometer (1) which allows us to apply a voltage of up to + 100 kV to the  $\beta$ -source. Although we had to abandon the  $4\pi$ -geometry, first tests showed that the effect of scattered electrons can be corrected with the help of a standard  $\beta$ -spectrum.

The high voltage set-up consists of a high-voltage power supply, a low pass filter and a special vacuum feed-through. Special care has been spent to avoid spurious sparks. We were able to demonstrate that the system is stable and does not influence the operation of the Si(Li)-detector for  $e^-$ -counting. As a first experiment with this set-up the investigation of the  $\beta^-$ -branch in the decay of the isomeric state in  $^{79}\text{Se}$  is presently being prepared.

- (1) KfK Report 3280 (1982).

1.1.6 Differential Measurement of the Neutron Capture Cross Section of  $^{86}\text{Kr}$

G. Walter, F. Käppeler, and Z.Y. Bao<sup>+</sup>  
Kernforschungszentrum Karlsruhe, IAK II

At the Karlsruhe 3.75 MV Van de Graaff accelerator we have measured the cross section of the reaction  $^{86}\text{Kr}(n,\gamma)^{87}\text{Kr}$  relative to the standard capture cross section of  $^{197}\text{Au}$  using the time-of-flight-technique. Protons were incident on a water-cooled Li-target on a Ta-backing producing neutrons via  $^7\text{Li}(p,n)^7\text{Be}$ . Our sample consisted of highly enriched (99.5 %  $^{82}\text{Kr}$ ) which was enclosed in a low mass stainless steel sphere of 10 mm radius.

The deexcitation gamma rays of the compound nucleus were detected by two  $\text{C}_6\text{D}_6$ -scintillators, each shielded by 4 mm thick  $^6\text{LiCo}_3$ -layers and viewed by a photomultiplier. The system was operated as a Maier-Leibnitz detector. Coincident events were rejected and separately recorded for correction of multiple weighting of gammas originating from the same cascade.

Monitoring of the neutron flux was performed by a  $^6\text{Li}$ -glass detector at  $90^\circ$  to the neutron beam axis. During 10 weeks of measuring time we collected enough statistics to cover an energy range from 4 to 300 keV.

From the data we calculated the quantity  $\frac{\langle\sigma v\rangle}{v_T}$  needed for s-process analysis. For  $kT = 30$  keV we found it to be  $5.6 \pm 0.7$  (mb). This is in reasonable agreement with the result of  $4.6 \pm 0.7$  (mb) deduced from an activation measurement (1) and with the value of  $4.9 \pm 1.4$  (mb) reported by Fogelberg and Macklin (2).

(1) G. Walter, H. Beer, F. Käppeler, and R.D. Penzhorn (1981) in preparation.

(2) B. Fogelberg and R.L. Macklin (1981) private communication.

<sup>+</sup>Institute of Atomic Energy, Peking, China

1.1.7 Neutron Capture Measurements of  $^{86}\text{Kr}$ ,  $^{85,87}\text{Rb}$ ,  $^{79,81}\text{Br}$  and  $^{86}\text{Sr}$  for the s-Process Branching at  $^{85}\text{Kr}$

G. Walter, H. Beer, F. Käppeler, and R.D. Penzhorn<sup>+</sup>  
Kernforschungszentrum Karlsruhe, IAK II

$^{85}\text{Kr}(T_{1/2} = 10.7 \text{ yr})$  is one of the few branching points where the competition between neutron capture and beta decay is not additionally

complicated by a temperature dependence of the beta decay half life. Therefore, in principle, the isotopic pattern produced for  $^{86,87}\text{Sr}$  and  $^{86}\text{Kr}$ ,  $^{87}\text{Rb}$  offers the possibility to determine the s-process neutron density if their neutron capture cross sections are measured (Fig. 1).

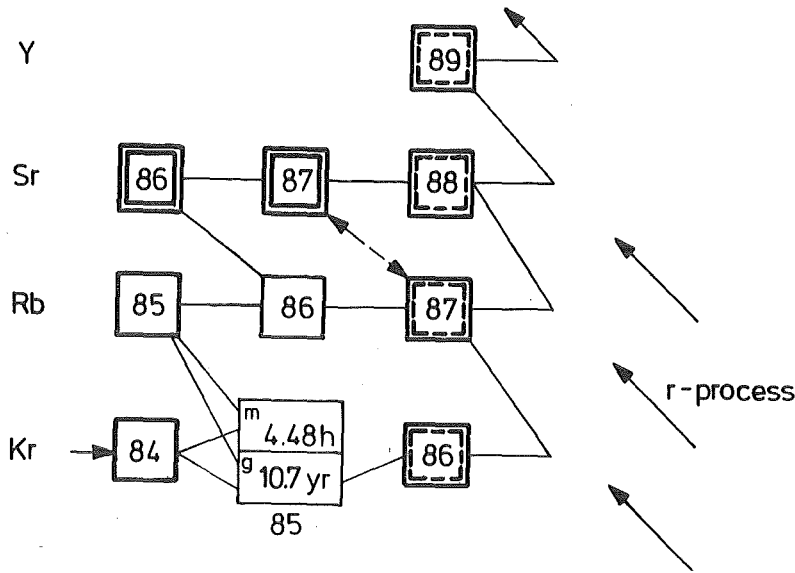


Fig. 1 The s-process path through the Kr-Rb-Sr region.

The present investigations are part of a continued effort to analyze this branching. Previous work was mainly concerned with the measurement of the isomeric population in  $^{85}\text{Kr}^m$  (1). The present measurements were performed by the activation technique (2). For the  $^{85,87}\text{Rb}$  and  $^{79,81}\text{Br}$  cross sections a sample of  $\text{RbBr}$  of natural isotopic composition was used while for  $^{86}\text{Kr}$  a zeolite tablet loaded with isotopically pure  $^{86}\text{Kr}$  gas was used (1). By activation of  $^{86}\text{Sr}$  (83.89 % enrichment) the capture cross section to the 2.8 h isomeric state in  $^{87}\text{Sr}$  was determined. Data reduction and analysis of the  $^{85}\text{Kr}$  branching are in progress. In Table 1 some of the capture results are summarized.

Table I Maxwellian averaged capture cross sections at  $kT = 30 \text{ keV}$ .

Target nucleus	$\frac{\langle\sigma v\rangle}{v_T}$ (mb)
$^{85}\text{Rb}$	$360 \pm 20$
$^{87}\text{Rb}$	$13.9 \pm 1.5$
$^{81}\text{Br}$	$317 \pm 16$
$^{86}\text{Kr}$	$4.6 \pm 0.7$

- (1) H. Beer, R.D. Penzhorn, F. Käppeler, KfK Report 3280 (1982).  
H. Beer, F. Käppeler, Proc. of the Int. Symp. on Neutron Capture  
Gamma-Ray Spect. and Related Subjects, Grenoble, 1981, p. 558
- (2) H. Beer, F. Käppeler, Phys. Rev. C 21, 534 (1980)

+ Kernforschungszentrum Karlsruhe, IRCh

1.1.8 The Neutron Capture Cross Sections and Solar Abundances  
of  $^{160,163}\text{Dy}$ ,  $^{175,176}\text{Lu}$  and  $^{176,177}\text{Hf}$  and the Age of  
Chemical Elements

H. Beer, G. Walter, R.L. Macklin<sup>+</sup>, R.J. Patchett<sup>++</sup>  
Kernforschungszentrum Karlsruhe, IAK II

This investigation is motivated by the recent idea that the isobaric pair  $^{176}\text{Lu}/^{176}\text{Hf}$  in conjunction with a stable s-only isotope like  $^{160}\text{Dy}$  represents one of the best existing cosmic clocks (1). In previous measurements (2), (3), (4) the population probability of an isomeric state in  $^{176}\text{Lu}$  and the question of its thermal equilibration was always considered as the central problem in the application of  $^{176}\text{Lu}$  as a cosmochronometer. However, Beer (1) has shown that complete use of the properties of s-process nucleosynthesis allows the separation of the problems concerned with the isomeric state from the determination of the  $^{176}\text{Lu}$  age.

There is, however, a condition left which already previously represented a challenge for the experimentalists, the requirement of very accurate capture cross sections and solar abundances ( $\leq 1.5\%$ ). For our experiment it was helpful that only ratios of the desired quantities are needed and that the isotopes have relatively high capture cross sections. The measurements are performed in collaboration with the MPI Mainz to account for the solar abundance determinations and the Oak Ridge National Laboratory to obtain a complete and independent second set of the required capture cross sections.

So far the bulk of the capture data has been taken and the analysis is in progress. Fig. 1 shows the capture cross sections of  $^{176}\text{Hf}$  and  $^{176}\text{Lu}$  measured at the Oak Ridge Linear Accelerator (ORELA). In order to meet the requests in accuracy for the  $^{160}\text{Dy}$  capture cross section a measurement on  $^{161}\text{Dy}$  which is the main impurity in the  $^{160}\text{Dy}$  sample must be carried out additionally.

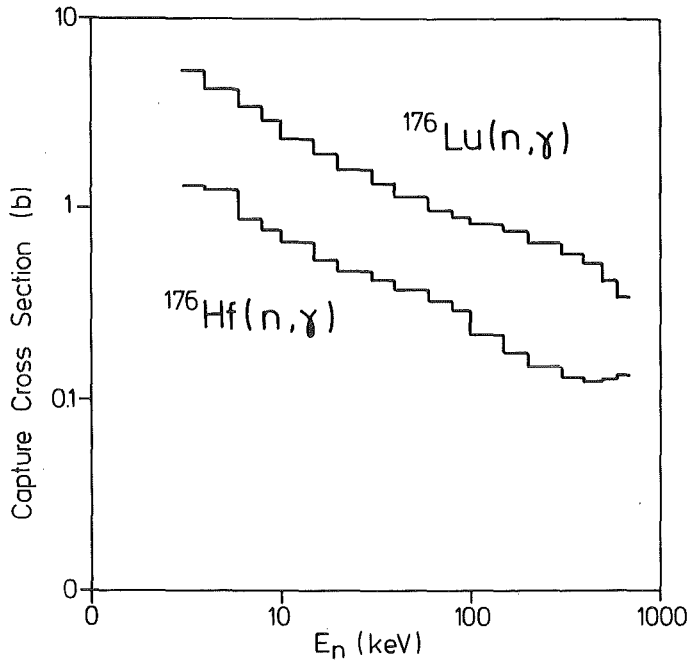


Fig. 1 Effective cross sections for  $^{176}\text{Lu}$ ,  $^{176}\text{Hf}$

- (1) H. Beer, Ap. J. (in press)
- (2) H. Beer, F. Käppeler, R.A. Ward, A. J. Suppl. 46, 295 (1981)
- (4) B.J. Allen, G.C. Lowenthal, J.R. de Laeter, J. Phys. G: Nucl. Phys. 7, 1281 (1981)

<sup>+</sup>Oak Ridge National Laboratory, Oak Ridge, Tenn. 37830, USA

<sup>++</sup>MPI für Chemie, Mainz

1.1.9  $^{176}\text{Lu}$ : Cosmic Clock and Stellar Thermometer \*

H. Beer

Kernforschungszentrum Karlsruhe, IAK II

The s-process nucleosynthesis of the isobaric pair  $^{176}\text{Lu}/^{176}\text{Hf}$ , a long-lived cosmic clock, is examined in conjunction with the s-only isotopes  $^{148,150}\text{Sm}$ ,  $^{160}\text{Dy}$ ,  $^{170}\text{Yb}$ ,  $^{186}\text{Os}$  and  $^{192}\text{Pt}$ . Expressions are derived which allowed us to calculate the s-process age only from measured quantities. A formula is specified which does not contain the population probability P of the 3.68 h isomeric state in  $^{176}\text{Lu}$ . This allowed us to decide if  $^{176}\text{Lu}$  is in addition to a cosmic clock also a stellar thermometer.

\*Astrophysical Journal (in press)

1.1.10 The  $^{180}\text{Lu}$  Beta Decay to the  $^{180}\text{Hf}$   $8^-$  Isomeric State and the r-Process Formation of  $^{180}\text{Ta}^m$ \*

G. Walter, H. Beer, W. Kurcewicz<sup>+</sup>, R. Kirchner<sup>++</sup>, E. Roeckl,<sup>++</sup> and D. Schardt<sup>++</sup>

Kernforschungszentrum Karlsruhe, IAK II

The fractional decay of  $^{180}\text{Lu}$  ( $T_{1/2} = 5.7$  min) to the  $8^-$  isomeric state  $^{180}\text{Hf}^m$  ( $T_{1/2} = 5.5$  h) is investigated, applying multi-nucleon transfer reactions between a 11.7 MeV/u  $^{136}\text{Xe}$  beam and a tantalum/tungsten target, on-line mass separation and gamma-ray spectroscopy. The branching ratio of  $^{180}\text{Lu}$   $\beta$ -decays to the  $8^-$   $^{180}\text{Hf}^m$  state is estimated to be 5.7 %, which leads to the interpretation of a dominant formation of  $^{180}\text{Ta}^m$  by r-process nucleosynthesis.

\* KfK Report 3417 (1982)

<sup>+</sup> Institute of Experimental Physics, University of Warsaw, Warsaw, Poland

<sup>++</sup> Gesellschaft für Schwerionenforschung mbH, Darmstadt

1.1.11  $^{178,179,180}\text{Hf}$  and  $^{180}\text{Ta}(n,\gamma)$  Cross Sections and Their Contribution to Stellar Nucleosynthesis\*

H. Beer and R.L. Macklin<sup>+</sup>

Kernforschungszentrum Karlsruhe, IAK II

The neutron capture cross sections of  $^{178,179,180}\text{Hf}$  were measured in the energy range 2.6 keV to 2 MeV. The average capture cross sections were calculated and fitted in terms of strength functions. Resonance parameters for the observed resonances below 10 keV were determined by a shape analysis. Maxwellian averaged capture cross sections were computed for thermal energies  $kT$  between 5 and 100 keV. The cross sections for  $kT = 30$  keV were used to determine the population probability of the  $8^-$  isomeric level in  $^{180}\text{Hf}$  by neutron capture as  $(1.24 \pm 0.06)$  % and the r-process abundance of  $^{180}\text{Hf}$  as 0.0290 ( $\text{Si} \approx 10^6$ ). These quantities served to analyze s- and r-process nucleosynthesis of  $^{180}\text{Ta}$ .

\* Physical Review C (in press)

<sup>+</sup> Oak Ridge National Laboratory

1.1.12 Search for a  $\beta^-$  Branch in the Decay of  $^{180}\text{Hf}^m$

F. Käppeler, H. Beer, S. Kerr<sup>+</sup>, K. Schreckenbach<sup>+</sup>, and H. Börner<sup>+</sup>  
 Kernforschungszentrum Karlsruhe, IAK II

The idea that the rarest isotope in nature,  $^{180}\text{Ta}^m$ , could have been produced in the astrophysical s- or r-process via a small  $\beta^-$ -branch in the decay of the isomeric state  $^{180}\text{Hf}^m$  (1) had initiated a measurement at the ILL high flux reactor. Irradiation of a hafnium sample enriched to 73.7 % in  $^{179}\text{Hf}$  was expected to produce enough  $^{180}\text{Ta}^m$  that capture gamma rays of this isotope became detectable with the curved crystal spectrometers GAMS (2). This estimate was based on the large  $^{180}\text{Ta}^m$  capture cross section of 3000 barn that was quoted by Larsen and Lanier (3). Then,  $^{180}\text{Ta}^m$  would reach its equilibrium abundance after about 10 days of exposure in the reactor. Two measurements were performed, each over a period of two weeks. Our interest was concentrated on the energy intervals  $165.0 < E_\gamma < 167.5$  keV and  $221.0 < E_\gamma < 223.5$  keV which contain gamma-ray lines from  $^{180}\text{Ta}^m(n,\gamma)$  and from  $^{179}\text{Hf}(n,\gamma)$  for normalization. These intervals were

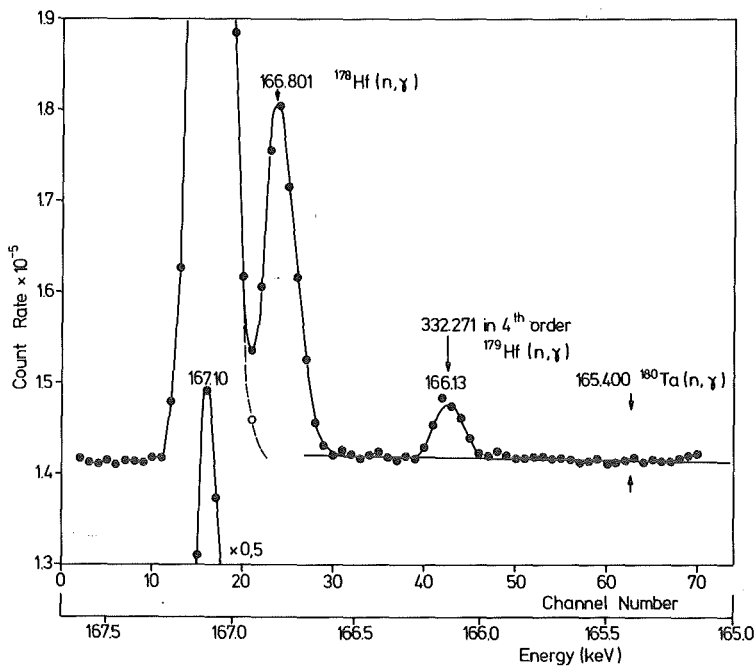


Fig. 1 Gamma-ray spectrum after 11.5 days of burn-up. Peaks correspond to the 167.10 keV reference line from  $^{179}\text{Hf}(n,\gamma)$  and to the 166.801 keV line from  $^{178}\text{Hf}(n,\gamma)$ . No significant peak was found for the 165.400 keV transition in the  $^{180}\text{Ta}^m(n,\gamma)$  reaction. The point size reflects the statistical uncertainty.

continuously scanned and Fig. 1 presents a sum spectrum which was accumulated during the second week of the first measurement. Obviously, there is no indication for neutron capture in  $^{180}\text{Ta}^m$ . Also, the second measurement with improved statistics yielded the same, negative result. This allowed to establish an upper limit for the branching factor  $f_{\beta^-}$  which was somewhat smaller than the lower limit estimated in Ref. (1) from log ft-systematics.

After data analysis had been carried through so far, a new and more accurate value for the capture cross section of  $^{180}\text{Ta}^m$  became available (4). This new value of 150-200 barns was 15-20 times smaller than the one from which the experimental sensitivity was first calculated. This means that our experimental upper limit corresponds now to the estimated upper limit (1), and therefore no meaningful conclusions can be drawn from this measurement on the possible production of  $^{180}\text{Ta}^m$  in neutron capture nucleosynthesis.

- (1) H. Beer and R.A. Ward, *Nature* 291 (198 ) 308.
- (2) H.R. Koch, H.G. Börner, J.A. Pinston, W.F. Davidson, J. Fandon, R. Rousille, and O.W.B. Schult, *Nucl. Instr. Meth.* 175 (1980) 401
- (3) L.T. Larsen and R.G. Lanier, private communication
- (4) P. v. Brentano, private communication

<sup>+</sup>Institut Max von Laue - Paul Langevin, Grenoble, France

#### 1.1.13 The Solar Mercury Abundance

G. Walter and H. Beer

Kernforschungszentrum Karlsruhe, IAK II

For the determination of elemental solar abundances C1 type carbonaceous meteorites represent the primary source of information. This is true for the bulk of the elements. Exceptions are the highly volatile noble gases but also mercury which shows an enormous variability in meteoritic samples (1). In this situation it appears justified to refer to the concepts of nucleosynthesis to obtain a reliable abundance by interpolating between neighbouring nuclei.

For the decomposition of the isotopic mercury abundances into s- and r-process contributions the neutron capture cross sections are required. In the present investigation the reactions  $^{196}\text{Hg}(n,\gamma)$ ,  $^{197}\text{Hg}^{o,m}$ ,  $^{198}\text{Hg}(n,\gamma)$

$^{199}\text{Hg}^m$  and  $^{202}\text{Hg}(n,\gamma)^{203}\text{Hg}$  have been studied by the activation method at 25 keV neutron energy. The capture cross section of  $^{202}\text{Hg}$  in conjunction with the  $\sigma N_s (A=202)$  value reported by Käppeler et al. (2) was used to estimate the solar mercury abundance. The r-process contribution of  $^{202}\text{Hg}$  was approximated by the abundance of r-only  $^{204}\text{Hg}$ . The analysis yielded  $N_{\odot}(\text{Hg}) = 0.25/10^6 \text{ Si}$ . This result is in excellent agreement with the estimated value  $0.259/10^6 \text{ Si}$  of a recent compilation by Anders and Ebihara (3).

- (1) B. Mason, Data of Geochemistry Chapter B Cosmochemistry, Part 1 Meteorites 1979, Geol. Survey Prof. Paper 440-B-1, U.S. Govt. Print Off.
- (2) F. Käppeler, H. Beer, K. Wisshak, D.D. Clayton, R.L. Macklin, R.A. Ward, Ap. J. 257, 821 (1982).
- (3) E. Anders, M. Ebihara, Geochim. Acta (to be published).

#### 1.1.14 Population Probabilities of Excited States in Radioactive Nuclei for s-Process Studies\*

G. Walter and H. Beer

Kernforschungszentrum Karlsruhe, IAK II

The population probabilities of excited states for a series of important unstable nuclei on the s-process path have been calculated as a function of temperature. The data are presented in graphic and tabulated form.

\*KfK Report 3327 (1982)

#### 1.1.15 Self-Absorption of Neutron Capture Gamma Rays in Gold Samples

G. Walter, K. Wisshak, D. Erbe, and F. Käppeler

Kernforschungszentrum Karlsruhe, IAK II

In neutron capture cross section measurements often gold is used as a cross section standard. This is especially the case for measurements in the keV range if a Van de Graaff accelerator and the  $^7\text{Li}(p,n)$  reaction is used for neutron production, where normalization at thermal energies or by the saturated resonance method cannot be applied like in Linac experiments. Gold is favoured as a standard since this cross section is known with an accuracy of  $\sim 2\%$  and samples are monotopic and easily available.

A disadvantage in relative measurements with gold standards is the strong absorption of gamma rays in the sample material due to its density and high Z-value. In particular, this holds for measurements with artificially collimated neutrons. Normally, in this set-up the sample is placed perpendicular to the neutron beam and the detectors are located at 90° with respect to the beam axis. This means that the detectors are directed towards the edge of the samples where absorption is most severe. Accurate results can therefore be obtained only, if they are corrected properly for this effect.

For this reason, the gamma-ray self-absorption in gold has been determined experimentally. The set-up which has been widely used in the last years for the determination of neutron capture in noble gases (1), (2), (3) and in iron isotopes (4) has been described in detail in Ref. 2. The neutron beam was collimated by a shielding of  $^6\text{LiCO}_3$ ,  $^{10}\text{B}$  and paraffin to

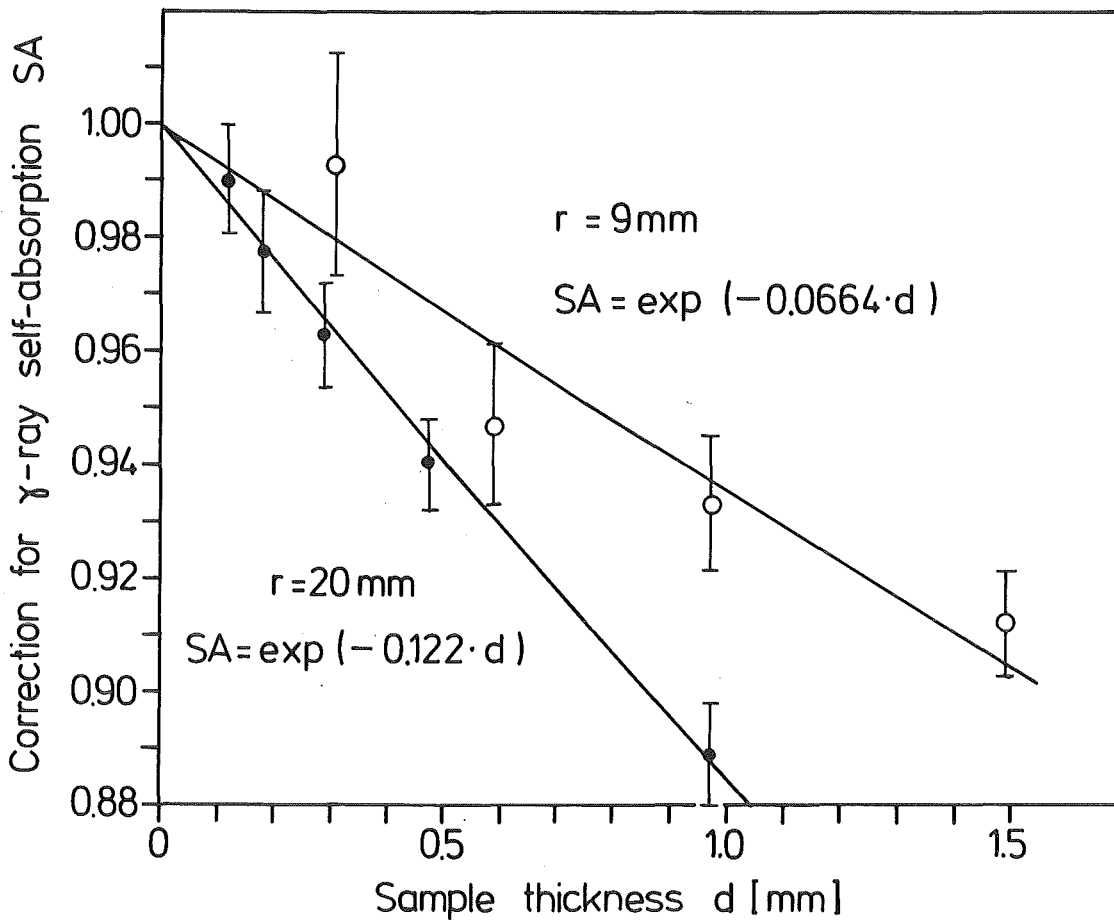


Fig. 1 Correction factor SA for gamma-ray self absorption in gold samples of 20 mm and 9 mm radius.

a diameter slightly larger than the sample diameter. The samples are located perpendicular to the neutron beam at a flight path of  $\sim 60$  cm. They are viewed by two  $C_6D_6$  detectors at  $90^\circ$  with respect to the neutron beam axis. The gold samples with different thickness are fixed in a low mass sample changer and are cyclically brought into the measuring position. A  ${}^6Li$  glass detector at  $90^\circ$  to the beam direction and at a distance of 45 cm from the neutron target served as a neutron monitor. The count rate of this detector was used to normalize the spectra of the individual samples to the same neutron flux.

Spectra were taken from samples with 18 and 40 mm diameter, as they were actually used in the krypton, neon and  ${}^{56,58}Fe$  measurements, respectively (1), (2), (3), (4). The result is shown in Fig.1. The correction factors SA defined as

$$SA = C(d) / C(o)$$

where  $C(d)$  and  $C(o)$  are the gamma-ray count rates per gram sample material for a sample of thickness  $d$  and for an infinitely thin sample. Therefore, in an actual measurement using a gold standard the measured gold spectrum has to be divided by SA to correct for gamma-ray self absorption.

- (1) F. Hensley, KfK Report 2918 (1980)
- (2) B. Leugers, KfK Report 2895 (1979)
- (3) J. Almeida, KfK Report 3347 (1982)
- (4) F. Käppeler, K. Wisshak, and L.D. Hong, contribution to this report.

1.1.16 Proposal for a Bismuth-Germanate  $4\pi$  Detector for  
Precise Measurements of Neutron Capture Cross Sections  
F. Käppeler, K. Wisshak, and G. Schatz  
Kernforschungszentrum Karlsruhe, IAK II

Existing techniques for measurements of neutron capture cross sections in the keV energy range have been developed over the past two decades and have now reached the limits of their capabilities. This means that their accuracy of  $\sim 5-10\%$  is very difficult to improve, although more precise measurements are urgently requested. Especially, in the field of nuclear astrophysics, there are many problems associated with s-process

nucleosynthesis, where uncertainties of  $\lesssim 1\%$  are needed. The most important examples are the analysis of the  $^{176}\text{Lu}$  cosmochronometer (1), the  $\sigma N$  systematics (2) isotopic anomalies (3) as well as the investigation of various s-process branchings which yield information on the physical conditions of the s-process (temperature, neutron density).

These demands can be satisfied only with a new technique. We propose therefore a  $4\pi$  bismuth germanate (BGO) detector for neutron capture cross section measurements

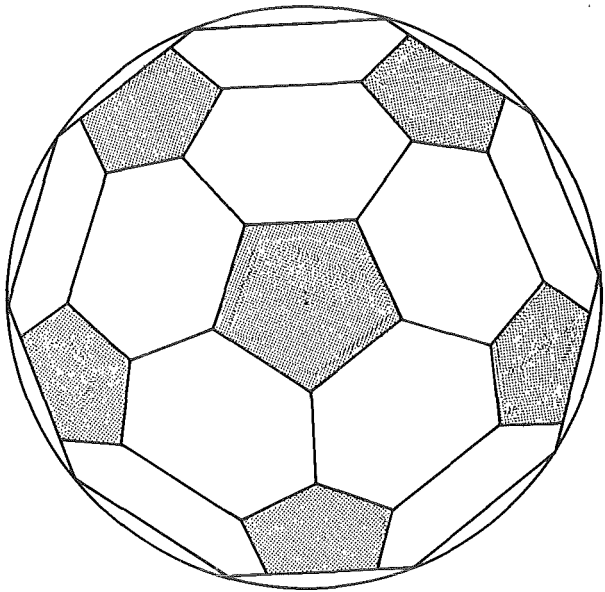


Fig. 1

The configuration of the proposed  $4\pi$  bismuth-germanate detector for neutron capture cross section measurements. The detector consists of 12 pentagons and 20 hexagons.

Such a system would be similar to NaI-arrays as they were developed in nuclear physics (4). But as our requirements are different and less stringent than e.g. in spectroscopy (total energy of capture gamma-ray cascades 5-10 MeV, multiplicity  $< 7$ ) the proposed detector is much less complex. Fig. 1 shows the configuration, a sphere composed of 12 pentagons and 20 hexagons.

This detector would have the following advantages

- (i) *high efficiency*: With a thickness of 12 cm BGO the efficiency is better than 96 % for any gamma-ray energy in the cascade. The high efficiency allows to use small samples so that uncertainties due to sample effects (neutron multiple scattering and self shielding, gamma-ray self absorption) are small.
- (ii) *good energy resolution*: This is the major advantage of the BGO detector because it allows for superior background discrimination. Fig. 2 shows

a pulse height spectrum as it is expected for a capture gamma-ray cascade of 6 MeV total energy. It can be seen, that 97 % of all cascades are detected above a threshold of 3 MeV and can thus be distinguished from low energy background. With less conservative assumptions one might expect an even better peak/total ratio (5).

The unique background discrimination of the BGO detector results in very clean spectra with signal/background ratios which are expected to be ~30 times better than with existing detectors. This means that the measuring

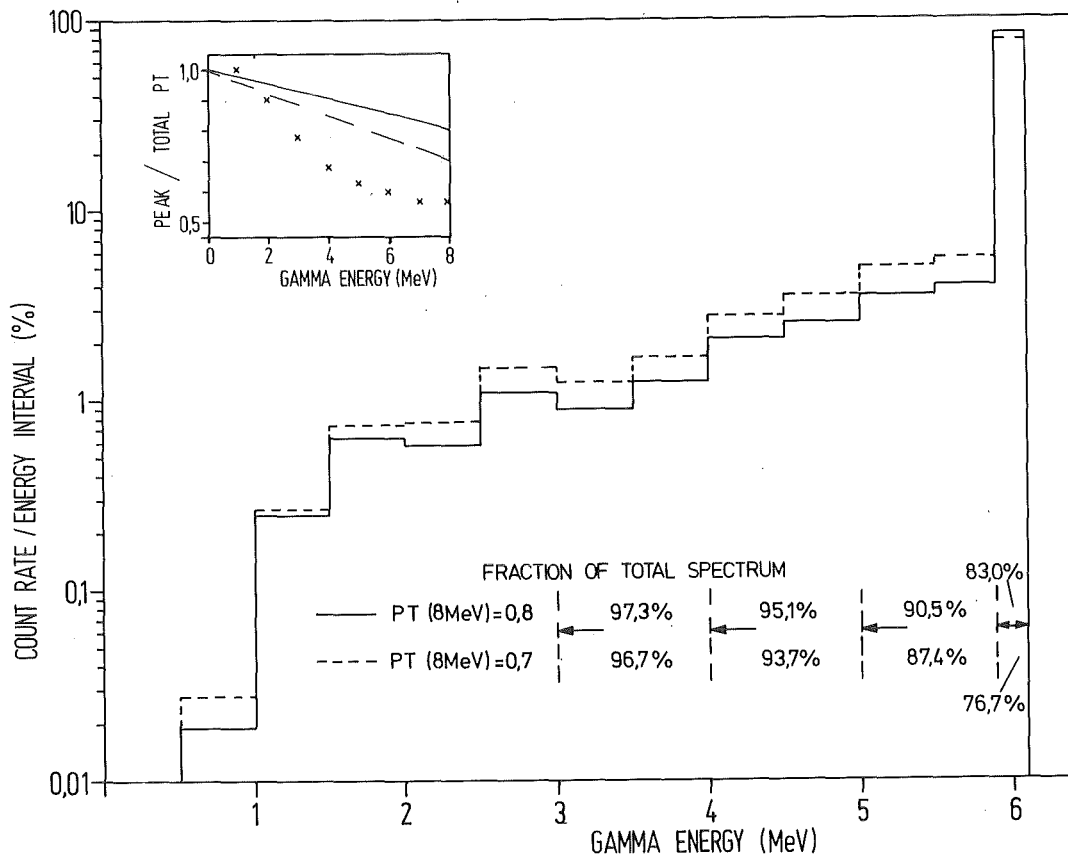


Fig. 2 Calculated pulse height spectrum for a capture gamma-ray cascade of 6 MeV total energy and an average multiplicity of 3. The insert shows the assumed peak/total ratio as a function of gamma-ray energy. The crosses in the insert represent experimental values for a 15 cm thick NaI-detector.

times will be reduced by more than a factor 10 and this in turn allows for a more detailed investigation of systematic uncertainties.

- (1) H. Beer, F. Käppeler, K. Wisshak, and R.A. Ward, Ap. J. Suppl. 46 (1981) 295
- (2) F. Käppeler, H. Beer, K. Wisshak, D.D. Clayton, R.L. Macklin, and R.A. Ward, Ap. J. 257 (1982) 821
- (3) G.J. Mathews and W.A. Fowler, Preprint OAP-625, Calif. Inst. of Technology (1981)
- (4) D. Habs, F.S. Stephens, R.M. Diamond, Report LBL-8945 (1979).
- (5) H.A. Helms, Harshaw Holland (1982)

## 1.2 NEUTRON PHYSICS

### 1.2.1 PROPERTIES OF THE POLARIZED FAST NEUTRON BEAM AT THE KARLSRUHE CYCLOTRON

P.Doll, B.Haesner, J.Hansmeyer, J.Hiebert<sup>+</sup>, H.O.Klages,  
H.Krupp, J.Oexner, P.Plischke, G.Schmalz, P.Schwarz,  
J.Wilczynski

Kernforschungszentrum Karlsruhe, IK I

V.Bechtold, L.Friedrich, P.Ziegler

Kernforschungszentrum Karlsruhe, IAK II

In October 1981 the polarized neutron facility POLKA at the Karlsruhe cyclotron went into operation.

Fig.1 shows a total view of the neutron production and the scattering facility. The polarized deuteron beam from the Karlsruhe Lambshift source (1) is bunched to a frequency of 11 MHz before accelerating the ions to 52 MeV. The polarization of the external beam is monitored on-line during the neutron scattering experiments by measuring the left-right asymmetry of the deuterons elastically scattered by carbon at laboratory angles of  $\pm 47^\circ$ . More details are given in contribution 1.5.

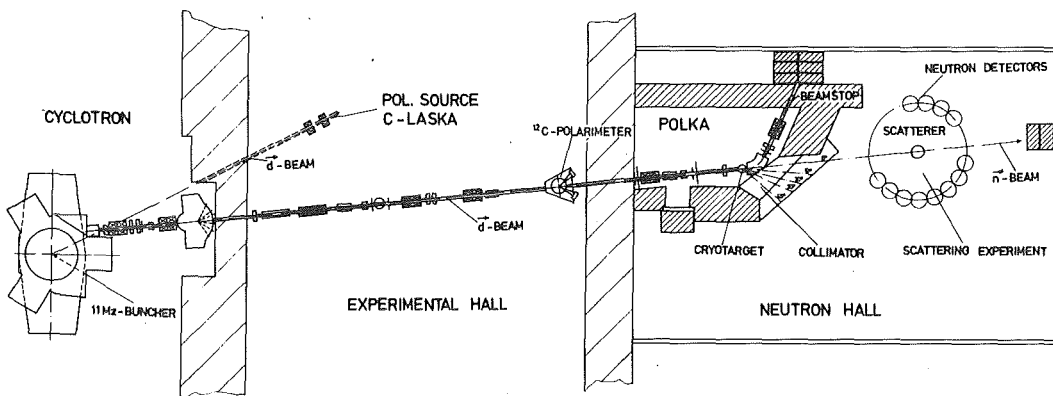


Fig.1: Schematic view of the Karlsruhe polarized neutron facility POLKA

<sup>+</sup>Texas A&M University, College Station, Texas U.S.A.

The deuteron beam interacts with a liquid deuterium sample inside a well-shielded target area to produce fast neutrons. The cryogenic target is described in section 1.5 of this report. The target thickness was chosen to be equivalent to an energy loss of 4 MeV for the 52 MeV deuterons. The ion beam is brought to a shielded beam dump by means of a  $60^\circ$  bending magnet. The neutrons produced in the target are collimated to a solid angle of  $\sim 10^{-4}$  sr by heavy metal shielding. At a distance of 6 m from the neutron source the beam is used for scattering experiments.

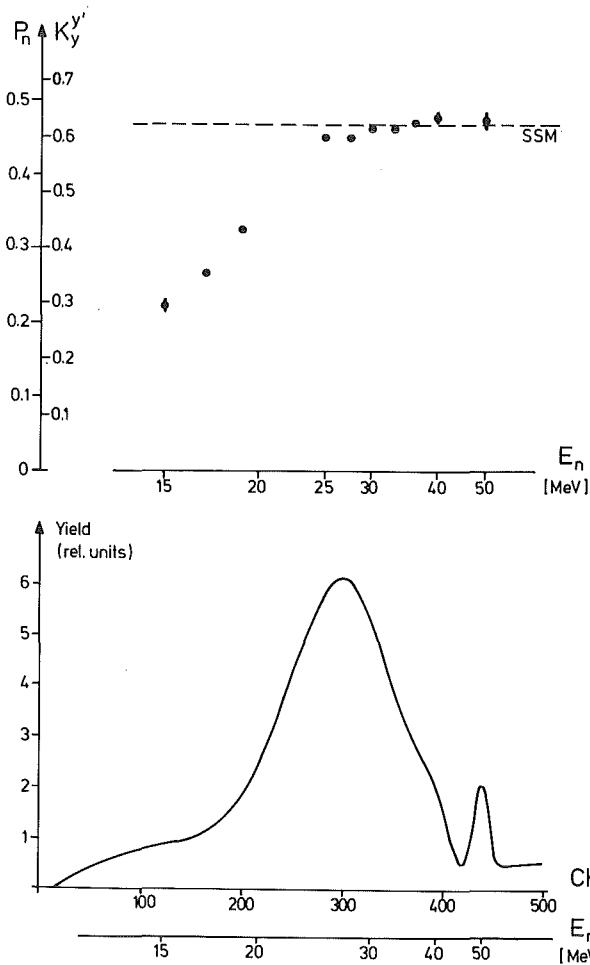


Fig.2: Distribution of flux and polarization in the "white" polarized neutron beam at POLKA. Note the nonlinear energy scale.

Fig.2 shows the distribution of neutron flux and polarization in the beam as a function of energy. This data stem from the first experiments carried out with POLKA, which are reported in contributions 1.2.2 and 1.2.4, respectively. The dashed line in fig.2 labeled SSM is the prediction of the simple stripping model (2) for a deuteron polarization of 50% and a deuteron D-state probability of 4%. The relation used for the spin trans-

fer coefficient is given by:  $K_y^{y'} = \frac{2}{3} p_n/p_d$ .

The high degree of polarization in the break-up part of the spectrum makes this "white" neutron beam a powerful tool for the study of the spin dependence of nuclear forces.

- (1) H.Brückmann et al., Z.f.Physik 224 (1969), 468
- (2) J.E.Simmons et al., Phys.Rev.Lett. 27 (1971), 113

#### 1.2.2 ANALYZING POWER OF THE NEUTRON-PROTON SCATTERING IN THE ENERGY RANGE FROM 17 TO 50 MeV

J.Hansmeyer, P.Doll, B.Haesner, J.Hiebert<sup>+</sup>, H.O.Klages, P.Plischke, P.Schwarz, J.Wilczynski

Kernforschungszentrum Karlsruhe, IK I

To improve the nucleon-nucleon phase shifts in the energy range below 50 MeV it is necessary to provide more accurate data for spin dependent observables in the two nucleon systems (1). In the first experiment carried out at the Karlsruhe polarized neutron facility POLKA we measured angular distributions of the n-p analyzing power. The "white" energy spectrum of the polarized beam allows the simultaneous measurement at all neutron energies from 17 to 50 MeV.

<sup>+</sup>Texas A&M University, College Station, Texas, U.S.A.

The neutrons were scattered after a flight path of 6 m by a liquid scintillator sample (NE 213). 14 detectors at 7 angles covering the range from  $16^\circ$  to  $71^\circ$  (lab.) were used for the scattered neutrons. Multiparameter data acquisition was performed to allow off-line reduction of the 6-dimensional data. The procedures used to analyse the raw data and to correct for multiple scattering and finite geometry effects are described briefly in contribution 1.5 to this report. Fig.1 shows a two-dimensional representation of the data for the scattering of 30 MeV neutrons by  $\Theta_{lab} = 52^\circ$ . These spectra allow the clean separation of n-p elastic scattering events from background contributions mainly due to the carbon content of the scattering sample.

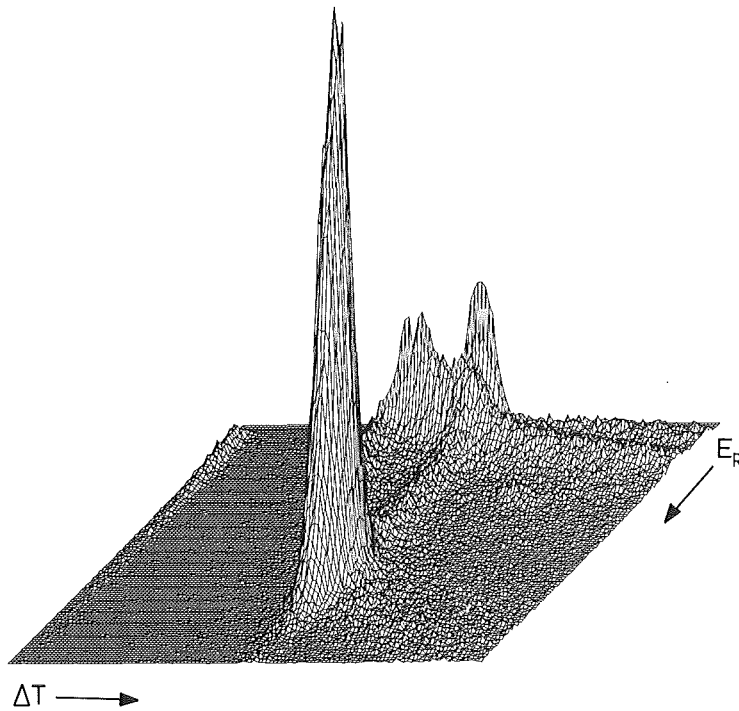


Fig.1: Neutron time-of-flight versus recoil particle pulse height for 30 MeV neutrons scattered by  $52^\circ$  on NE 213

Analyzing power distributions were deduced for ten energy bins with their centers at 17, 19, 22, 25, 27.5, 30, 33, 36, 40 and 50 MeV, respectively. At the lowest energies the results cannot match the very accurate data of Tornow et al. (2) due to the insufficient flux and the low polarization in the beam. The existing data base was considerably improved, however, for all higher energies up to 50 MeV. The data will be included in a new phase shift analysis. Fig.2 shows our results at 25 MeV together with the distribution calculated from a preliminary phase shift analysis and a prediction of an energy dependent analysis (3).

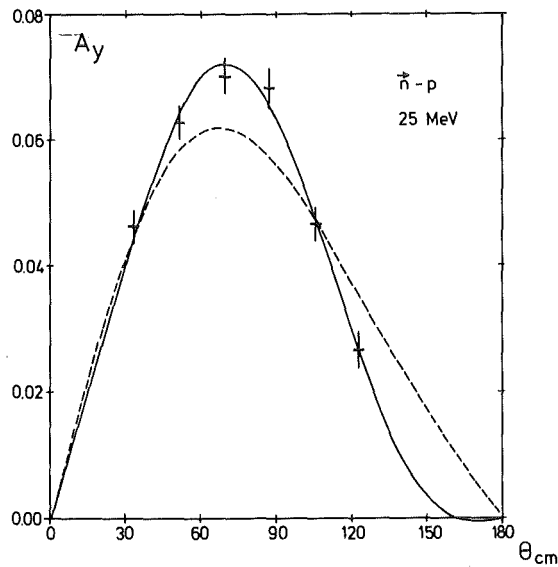


Fig.2: Analyzing power of n-p scattering at 25 MeV. Solid line: preliminary phase shift analysis Karlsruhe 82, dashed line: energy dependent phase shifts by Arndt + Verwest (3)

- (1) R.Garret et al., Phys.Rev. C21 (1980) 1149
- (2) W.Tornow et al., Nucl.Phys. A340 (1980), 34
- (3) R.A.Arndt, private communication

### 1.2.3 SELECTION OF EXPERIMENTS TO IMPROVE NUCLEON-NUCLEON PHASE SHIFTS BELOW 100 MeV

J. Wilczynski, H.O. Klages

Kernforschungszentrum Karlsruhe, IK 1

In the past, different phase shift analyses (1,2) have shown that there are still problems left in analyzing nucleon-nucleon scattering data below 100 MeV. Erroneous neutron-proton data cause two isospin-singlet parameters to be undetermined especially at energies below 50 MeV.

Inclusion or exclusion of different neutron-proton differential cross section data sets at 50 MeV (3) results in a variation of the  $^1P_1$  phase shift from  $-7.5^\circ$  to  $0.3^\circ$ , which is far away both from the predictions of OPEC models ( $^1P_1 \sim -9^\circ$ ) and from interpolated values from adjacent energies.

The other problem parameter  $\epsilon_1$ , which mixes the  $^3S_1$  and  $^3D_1$  states, is undetermined in the range from  $-10^\circ$  to  $+3^\circ$  because a broad minimum of  $\chi^2$  versus  $\epsilon_1$  is covering this range. Therefore, in early phase shift analyses  $\epsilon_1$  was taken from theory which predicts a value of  $2-3^\circ$ . Taking this choice, however, affects again the  $^1P_1$ -problem because  $\epsilon_1$  and  $^1P_1$  are strongly correlated by the existing data base. This problem causes the need for new precise neutron-proton data at energies up to 50 MeV.

To decide which experiment should be conducted to solve the problem, the sensitivity of various np-observables on  $\epsilon_1$  and  $^1P_1$  was investigated.

The values of  $^1P_1$  and  $\epsilon_1$  were taken from predictions of the Paris potential (4) and varied by three standard deviations. The effect of this variation of  $^1P_1$  and  $\epsilon_1$  was calculated independently. It turned out that a very precise measurement of the anisotropy of the differential cross section would help to pin down the  $^1P_1$  phase shift. Even the very accurate data for the n-p analyzing power that came out of the recent Karlsruhe experiment (see 1.2.2) have little impact on  $\epsilon_1$  and  $^1P_1$  but help

to determine in particular the  $^3D$  phase shifts.

Fig.1 shows that a measurement of the shape of the differential cross section of the angular distribution at backward angles would bring a strong improvement for the  $^1P_1$  phase shift at 50 MeV.

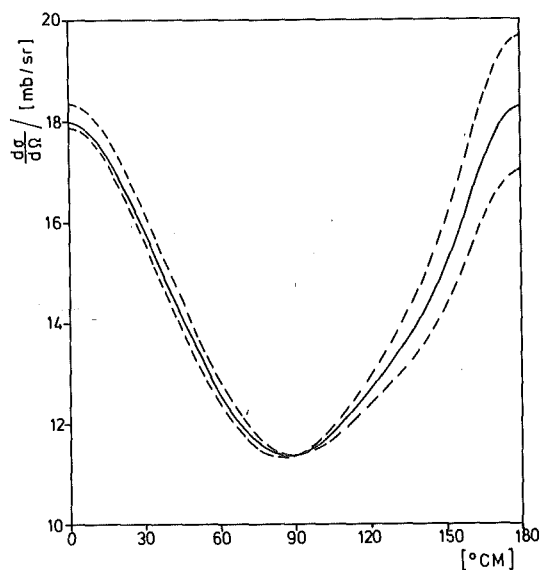


Fig.1: Differential cross section of the elastic n-p scattering at 50 MeV. Solid line: prediction of the phase shift parameters of ref.4, dashed line:  $^1P_1$  phase shift varied by  $\pm 2 \cdot \sigma_{\text{exp}}$  ( $\sigma_{\text{exp}}$  from ref.5).

A measurement of the spin correlation parameter  $A_{yy}$  at  $90^\circ$  is extremely sensitive to determine  $\epsilon_1$  but has no influence on  $^1P_1$ , whereas at more forward angles both parameters would play a role. This behaviour is shown in fig.2 for the 50 MeV case. The situation at lower energies is quite similar.

The even more sensitive experiment to measure  $A_{zz}$  cannot be conducted at Karlsruhe due to the high polarized neutron flux required in connection with the use of thin polarized proton targets and proton detection.

Therefore the proposed experiment for the polarized neutron facility POLKA is the measurement of  $A_{yy}$  for the energy range from 20 MeV to 50 MeV.

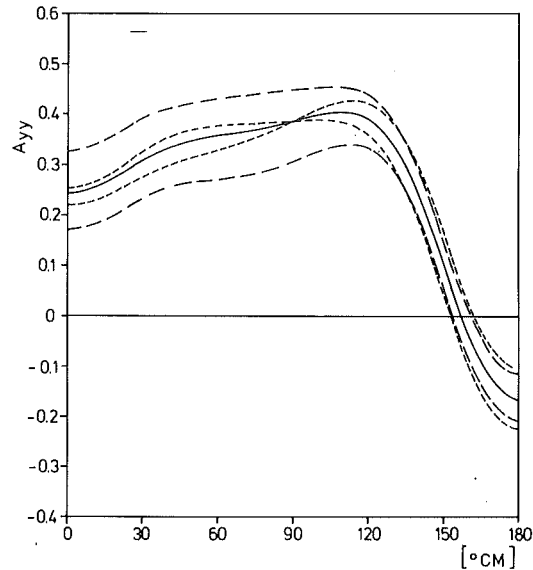


Fig.2: Spin correlation parameter  $A_{yy}$  of the elastic n-p scattering at 50 MeV. Solid line: prediction of the phase shift parameters of ref.4, dashed line:  $\epsilon_1$  parameter varied by  $\pm 2 \cdot \sigma_{\text{exp}}$ , short-dashed line:  $^1P_1$  phase shift varied by  $\pm 2 \cdot \sigma_{\text{exp}}$  ( $\sigma_{\text{exp}}$  from ref.5).

- (1) M.H.McGregor et al., Phys.Rev. 173, (1966), 1772
- (2) R.Arndt et al., Phys.Rev. D8, (1973), 1397
- (3) F.P.Brady, Lecture Notes in Physics 82, (1978), 137
- (4) M.Lacombe et al., Phys.Rev. C21, (1980), 861
- (5) R.Arndt, private communication, 1982

### 1.2.4 ANALYZING POWER OF $n-\alpha$ -SCATTERING IN THE ENERGY RANGE FROM 15 TO 50 MeV

H.Krupp, P.Doll, B.Haesner, J.Hansmeyer, J.Hiebert<sup>+</sup>,  
H.O.Klages, P.Plischke, P.Schwarz, J.Wilczynski

Kernforschungszentrum Karlsruhe, IK I

The experimental situation for the  $n-{}^4\text{He}$  system has been reviewed (1) recently. Up to a neutron energy of 20 MeV many reliable data exist, because neutron scattering on  ${}^4\text{He}$  is widely used to analyze the polarization of fast neutron beams in this energy range. For higher energies only few and less accurate results (2,3) are published. The quality of data (4,5) for the  $p-\alpha$  scattering is much better in this energy range. Several attempts (6,7) have been made to calculate the Coulomb corrections to the phase shifts for  $p-\alpha$  scattering to predict  $n-\alpha$  observables.

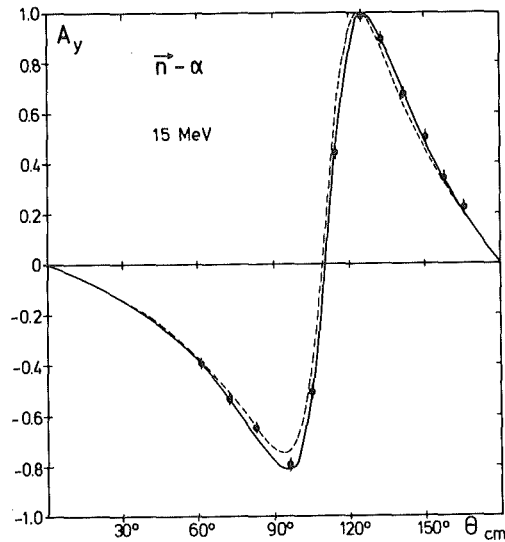


Fig.1:  $n-\alpha$  analyzing power at 15 MeV, solid curve: preliminary phase shift analysis Karlsruhe, dashed curve: phase shift prediction of ref.8; data points: this work.

<sup>+</sup>Texas A&M University, College Station, Texas, USA

It was the aim of the present work to determine the analyzing power for the  $n-\alpha$  scattering in the energy range from 15 MeV to 50 MeV simultaneously. The polarized neutron beam of POLKA (see 1.2.1) was used in connection with a liquid  $^4\text{He}$  scintillating sample and 14 detectors for the scattered neutrons.

Multiparameter off-line data analysis was performed in 10 energy bins. Corrections for multiple scattering and finite geometry have been applied. The calibration to the hitherto unknown polarization of the neutron beam was done using the predictions of a previous phase shift analysis (8) at lower energies and from a  $p-\alpha$  calculation (7) above 25 MeV. In both cases the scale is normalized in the region of the backward maximum, where the dependence on the various assumptions turned out to be smallest. The first results of these analyses are presented in contribution 1.2.1 to this report as the polarization of the Karlsruhe neutron beam.

The angular distributions for the  $n-\alpha$  analyzing power agree with the previous data at the lower energies as is shown in fig.1.

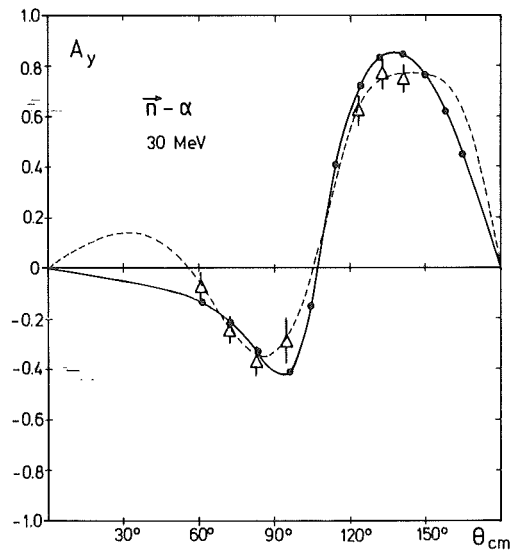


Fig.2: Comparison of the new Karlsruhe data ( $\blacklozenge$ ) and phase shift predictions (solid curve) with the results of ref.2 at 30 MeV

At higher energies the accuracy has been improved considerably, e.g. by a factor of more than five at 30 MeV. Figure 2 shows the measured distribution at this energy together with the data of Broste et al. (2). In both figures the solid line gives the result of our preliminary phase shift analysis which is described in the following contribution. The dashed lines are the predictions of previous phase shift analyses.

- (1) F.Ajzenberg-Selove, Nucl.Phys. A 320, (1979), 1
- (2) W.B.Broste et al., Phys.Rev. C5 (1972), 761
- (3) R.York, Thesis, Texas A&M Univ. 1979
- (4) A.D.Bacher et al., Phys.Rev. C5 (1972), 1147
- (5) K.Imai et al., Nucl.Phys. A 325 (1979), 397
- (6) J.Fröhlich et al., Nucl.Phys. A 384 (1982), 97
- (7) H.Zankel, priv. communication and UNIGRAZ-UTP 03/82
- (8) B.Hoop, H.H.Barschall, Nucl.Phys. 83 (1966), 65

We thank H.Wirth from MPI Heidelberg for help in evaporating the DPS wave length shifter in the helium scintillation container.

#### 1.2.5 A PRELIMINARY PHASE SHIFT ANALYSIS FOR $n$ - $\alpha$ SCATTERING

H.Krupp, H.O.Klages, J.Wilczynski

Kernforschungszentrum Karlsruhe, IK I

In neutron polarization studies  $^4\text{He}$  is widely used as polarization analyzer. Accurate knowledge of  $n$ - $\alpha$  phase shifts is crucial in such experiments. Below 20 MeV  $n$ - $^4\text{He}$  scattering is rather well represented by experimental data and phase shifts. At 25.7, 27.3 and 30.3 MeV Broste et al.(1) made single energy phase shift analyses. Up to 30 MeV a set of phase shifts based on  $p$ - $\alpha$  measurements was given by Hoop and Barschall (2). A new attempt to predict  $n$ - $\alpha$  phase shifts from  $p$ - $\alpha$  data was made by Fröhlich et al. (3).

Our new analyzing power data (see 1.2.4) are the basis for a preliminary phase shift analysis at ten energies from 15 to 50 MeV. The data of ref.1 with large statistical uncertainties were discarded in the first step. Total cross section data were taken from unpublished results from the Karlsruhe group, differential cross section data from Hoop and Barschall (2) and Drogg (4) at 17 MeV. The analyzing power measurement of York et al. (5) at 50 MeV was included in the analysis.

In order to overcome the lack of differential cross section data above 30 MeV, predicted values from Zankel (6) were used to obtain a reliable shape of the angular distribution. The improvement of the representation of all experimental data by the new phase shifts compared to the Broste analysis is shown in fig.1. The  $\chi^2$  value is lower by a factor of 25 for our curve. The predicted analyzing power from the p- $\alpha$  calculation doesn't match the results at 27.5 MeV. The 50 MeV predictions are closer to experiment as can be seen in figure 2. Differences are found mainly in the forward angle region.

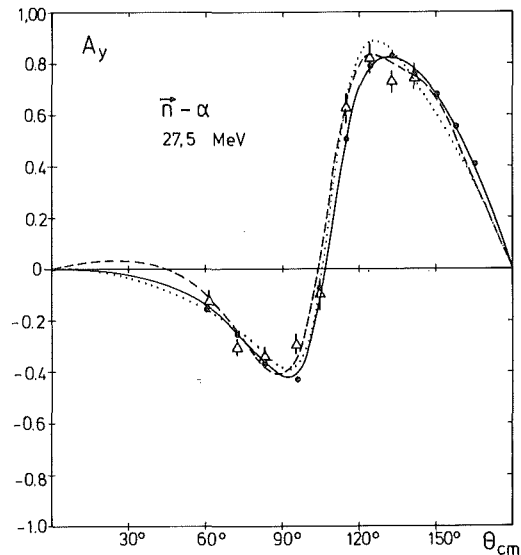


Fig.1: n- $\alpha$  analyzing power at 27.5 MeV. Our results (dots, solid line) are shown together with the values from ref.1 (triangles, dashed line) and a prediction (ref.6) calculated from p- $\alpha$  phase shifts.

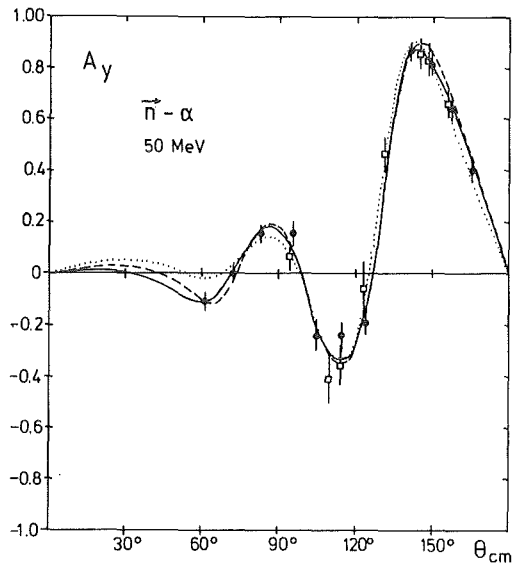


Fig.2:  $n-\alpha$  analyzing power at 50 MeV. Our results (dots, solid line) are shown together with the values from ref.5 (squares, dashed line) and a prediction (ref.6) calculated from  $p-\alpha$  phase shifts.

Fig.3 shows the real part of the phase shifts for  $l = 0, 1, 2$  as a function of energy. At the higher energies complex phase shifts up to  $l = 4$  have been taken into account. The analysis will be continued taking into account all reliable data for the  $n-\alpha$  system.

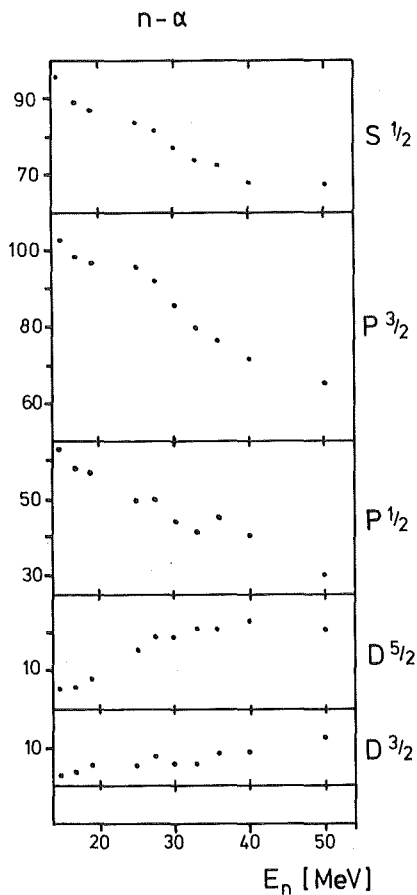


Fig.3: Real part of the  $l = 0, 1, 2$  phase shifts for the  $n-\alpha$  system.

- (1) W.B.Broste et al., Phys.Rev. C 5, 761 (1972)
- (2) B.Hoop and H.H.Barschall, Nucl.Phys. 83 (1966) 65
- (3) J.Fröhlich et al., Nucl.Phys. A 384 (1982) 97
- (4) M.Drosg, Los Alamos Report LA-7269 (1978)
- (5) R.York, Thesis, Texas A&M Univ.(1979)
- (6) H.Zankel, priv. communication

#### 1.2.6 SCATTERING OF A "WHITE" NEUTRON BEAM FROM Ti AND TiH<sub>2</sub> SAMPLES

A.Bischoff, R.Aures, P.Doll, E.Finckh<sup>+</sup>, W.Heeringa,  
H.O.Klages, H.Skacel

Kernforschungszentrum Karlsruhe, IK I

For 1983 a spin correlation experiment with polarized neutrons on polarized protons is planned, using in a combined effort the neutron beams from POLKA and a polarized proton target. The polarized protons are embedded in a Ti lattice and, therefore extensive knowledge on differential cross sections of elastic and inelastic scattering on Ti is mandatory. However, not only scattering on titanium over the full energy range of the "white" neutron beam had to be studied experimentally, but also the performance of beam POLKA and an additional post-collimator for the small TiH<sub>2</sub> targets ( $\phi = 20$  mm) had to be investigated.

While the flight-path from the neutron source to the TiH<sub>2</sub> target was kept at a distance of  $D1 = 5.1$  m, the flight path to the side detectors D2 has been varied to find a reasonable separation in time-of-flight between scattering events from Ti and H. Based on optical model predictions, for which optical model parameters (1) have been extrapolated to neutron energies up to 50 MeV, the scattering angle was varied between 30° to 40° to find a minimum in the n+Ti angular distribution. To achieve a careful comparison for runs with a TiH<sub>2</sub> target and a pure Ti

<sup>+</sup>Physikalisches Institut der Universität Erlangen-Nürnberg

target the primary neutron flux was monitored by a thin (3 mm) plastic scintillator. Independently, one neutron detector was kept at a fixed forward angle ( $30^\circ$ ). Fig. 1 shows time-of-flight spectra taken on a  $\text{TiH}_2$  sample (a) and on a Ti sample (b) separately. Figure 1 (c) is obtained after subtracting (b) from (a) and represents the scattering distribution from the protons in the  $\text{TiH}_2$  target. Neutron time-of-flight and incident neutron energy is indicated on the bottom scales. The spectra demonstrate the possibility of using the "white" neutron beam for measuring the energy dependence of left - right asymmetry due to the spin-spin interaction in the  $\vec{n} + \vec{p}$  system. However, the preliminary investigation confirms the need for a careful layout of the neutron collimators and for reliable neutron flux monitors.

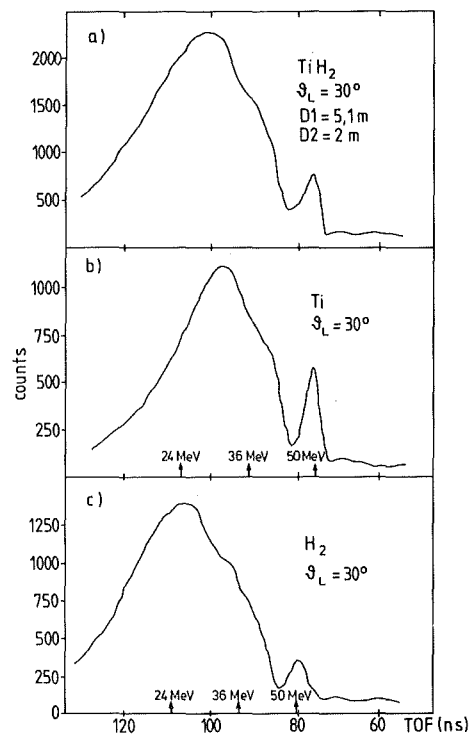


Fig.1: Time-of-flight spectra of neutrons scattered by a  $\text{TiH}_2$  sample (a) and a Ti-sample (b); the difference of the spectra is due to scattering on hydrogen (c).

### 1.2.7 DIFFERENTIAL CROSS SECTION OF THE ELASTIC n-d-SCATTERING IN THE ENERGY RANGE 2.5 MeV - 30 MeV

P.Schwarz, P.Doll, B.Haesner, L.Husson, J.Kecskemeti<sup>+</sup>,  
H.O.Klages, G.Schmalz, J.Wilczynski

Kernforschungszentrum Karlsruhe, IK I

The results of the elastic n-d scattering measurement (1) at the collimated "white" neutron beam of the Karlsruhe cyclotron are presented. The experimental set-up and method, data acquisition and data reduction were described in the preceding annual report of the institute (2). The final results of the measurement are displayed in fig.1.

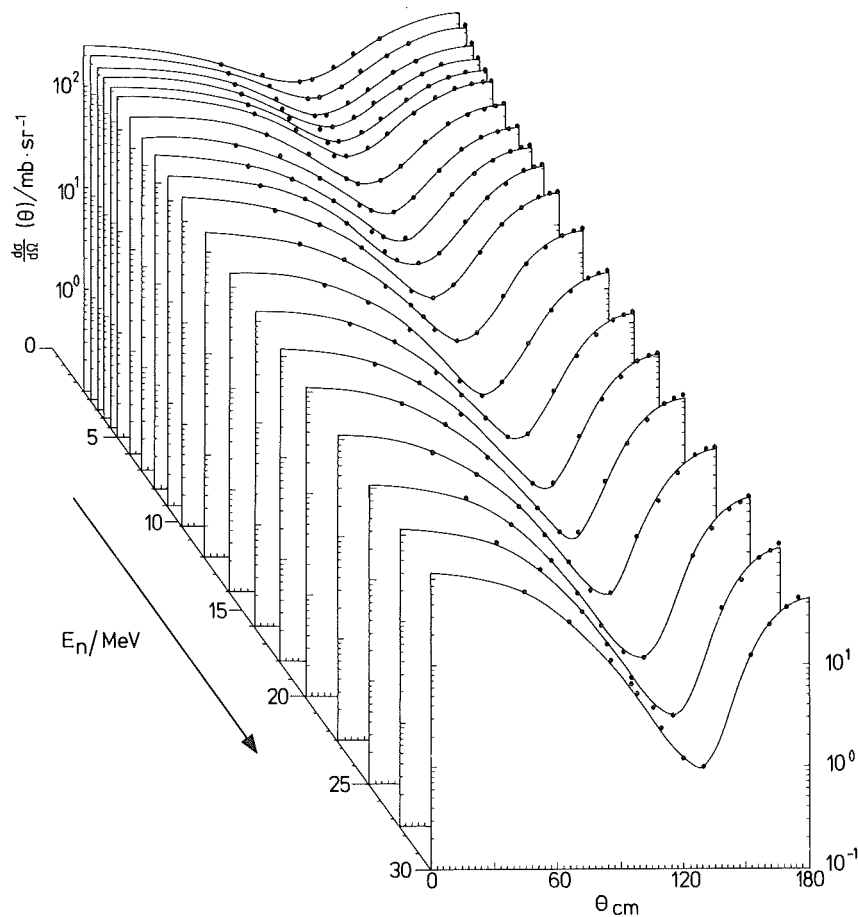


Fig.1: Differential cross section for the elastic n-d scattering

<sup>+</sup> Central Research Institute for Nuclear Physics, Budapest

The angular distributions of the elastic n-d scattering are plotted against the energy of the incident neutrons. The data points are fitted by Legendre polynomials, which are represented by the solid lines.

All twenty angular distributions were measured simultaneously using the "white" neutron beam. This method provides a consistent set of cross sections for the energy range 2.5 to 30 MeV. The shape of the angular distributions varies smoothly with energy. The absence of resonant structure is in agreement with the present knowledge of the three-nucleon system.

To demonstrate the high precision of the data presented here the differential cross sections at 7, 14 and 22.5 MeV are displayed together with older data (3,4,5,6,7) in fig.2.

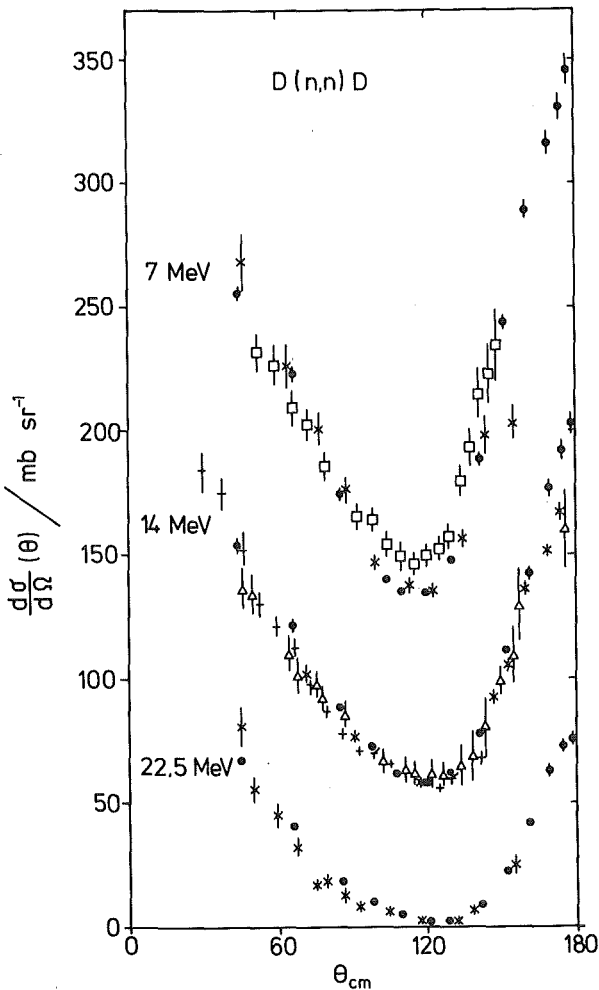


Fig.2: Comparison between the results of this work ( ) older data from refs.3, 5 (x), ref.4 ( ), ref.6 (Δ) and ref.7 (+). To get numerical values at 7 MeV: subtract 100 mb/sr; at 14 MeV: subtract 50 mb/sr.

The uncertainties of our results are smaller by factors of 2 to 10. The main advantage of this work is the determination of the cross sections for scattering angles greater than  $130^\circ$ . Until now only few data points existed for the backward region. The only accurate measurements (8) for scattering angles up to  $170^\circ$  provided results about 15% above the predictions of exact 3-body calculations by Faddeev methods. These experimental values are now verified by our results. Thus we conclude, that the new accurate data should be used for comparison with new Faddeev results to get better information on the two-body input of these calculations.

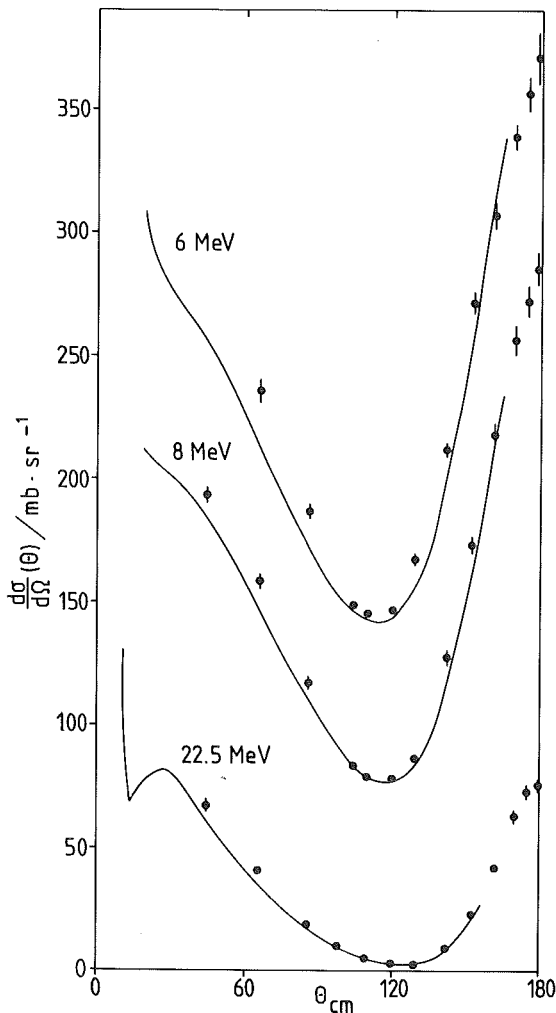


Fig.3: Angular distributions of elastic p-d data (solid lines, refs. 9,10) and the present n-d results. To get numerical values at 6 MeV: subtract 100 mb/sr; at 8 MeV: subtract 50 mb/sr.

In fig.3 our results are compared with differential cross sections of the elastic n-d scattering (9,10) at 6, 8 and 22.5 MeV, which are represented by the solid lines. The accuracy of our n-d data is in the same order of magnitude as the precision

of the p-d data. Therefore, one has the possibility to study Coulomb effects by comparing the corresponding angular distributions. Until now this was impossible because of the large uncertainties of the older n-d measurements (see fig.2).

(1) KfK Report 3396 (1982)

(2) KfK Report 3280 (1982)

(3) J.D.Seagrave et al., Ann.of Phys. 74 (1972) 250

(4) B.E.Bonner et al., Nucl.Phys. A 128 (1969) 183

(5) J.D.Seagrave et al., Phys.Rev. 97 (1954) 757

(6) J.C.Allred et al., Phys.Rev. 91 (1953) 90

(7) K.Gul et al., Proceedings of the International Conference on Nuclear Cross Sections for Technology, University of Tennessee, Knoxville, USA (1979)

(8) L.Antén, Ph.D.Thesis, University of Uppsala (1977)

(9) D.C.Kocher et al., Nucl.Phys. A 132 (1969) 455

(10) S.N.Bunker et al., Nucl.Phys. A 113 (1968) 461

#### 1.2.8 DIFFERENTIAL CROSS SECTIONS FOR THE ELASTIC SCATTERING OF NEUTRONS FROM $^3\text{He}$

B.Haesner, P.Doll, L.Husson, J.Kecskemeti<sup>+</sup>, H.O.Klages,  
G.Schmalz, P.Schwarz, J.Wilczynski

Kernforschungszentrum Karlsruhe, IK I

<sup>+</sup>Central Research Institute of Physics, Budapest

In connection with the investigation of the  $A = 4$  system with neutron and  $^3\text{He}$  in the entrance channel, differential cross sections for the elastic  $n\text{-}^3\text{He}$ -scattering were measured. It was the aim of this experiment to determine complete angular distributions of the  $n\text{-}^3\text{He}$ -scattering with high precision in a large energy range from 5 to 30 MeV (1).

The experiment was conducted using the pulsed "white" neutron beam at the Karlsruhe neutron time-of-flight facility which was described in the preceding annual report (2). Angular distributions of the elastic  $n\text{-}^3\text{He}$ -scattering were evaluated for 15 energy bins covering an angular range from  $33^\circ$  to  $179^\circ$  c.m.. Figure 1 gives an overview on all new data. The solid curves are fits to the data with Legendre polynomial. This representation gives an impression of the high accuracy of the data in this complete set of differential cross sections.

For the first time, high quality data are available also for the backward angles which is important when the data are included in a phase shift analysis.

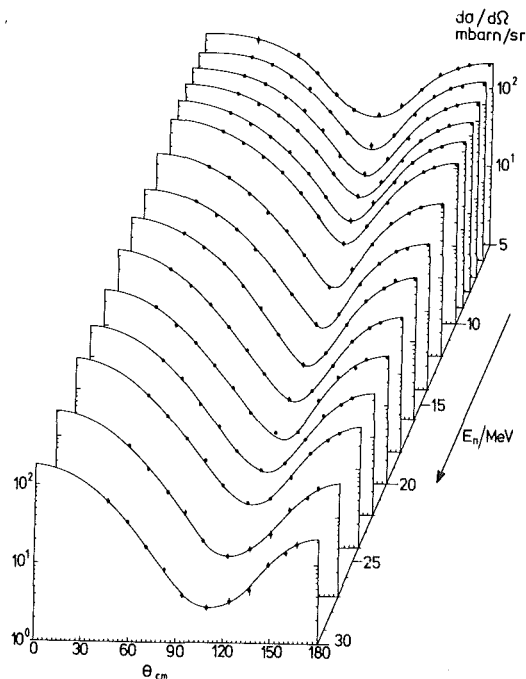


Fig.1: Differential cross sections for the elastic  $n\text{-}^3\text{He}$  scattering

Comparisons at some energies, with the results of ref.3 which have set the quality standard until now, shows good agreement. The accuracy of the data was improved considerably by our results. Figure 2 shows the differential cross section at 12 MeV. The data of ref.3 are plotted together with our results and a prediction of a preliminary phase shift analysis. This analysis included also the data of ref.4 for the analyzing power at 12 MeV as well as the total cross sections for the elastic scattering and for the inelastic channels from ref.1.

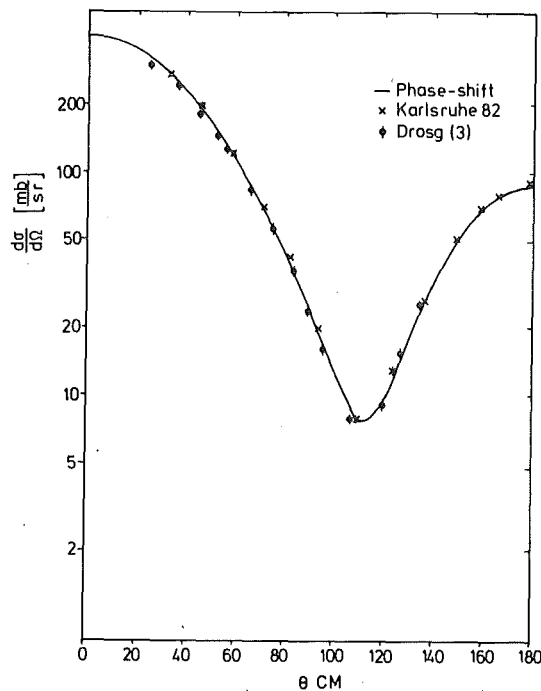


Fig.2: Experimental data and phase shift predictions at 12 MeV  
Karlsruhe 1982, ref.3

The data of this work will be used for a complete phase shift analysis for the  $n$ - $^3\text{He}$  system in the energy range up to 30 MeV.

(1) KfK-Report 3395 (1982)

(2) KfK-Report 3280 (1982)

(3) M.Drogg et al., Phys.Rev. 10 (1974) 179

(4) P.W.Lisowski et al., Nucl.Phys. A 259 (1976) 61

1.2.9 CROSS SECTIONS FOR THE REACTIONS  $n+{}^3\text{He} \rightarrow p+t$  AND  
 $n+{}^3\text{He} \rightarrow d+d$  UP TO 30 MeV

B.Haesner, J.Kecskemeti<sup>+</sup>, H.O.Klages, P.Schwarz

Kernforschungszentrum Karlsruhe, IK I

Absolute cross sections for the two-body reaction channels were measured using a collimated "white" neutron beam incident on a liquid  ${}^3\text{He}$  scintillating detector. The experiment has been described in detail in ref.1. The most important feature is that the liquid  ${}^3\text{He}$  sample serves (both) as target and as detector for the charged reaction products.

The incident neutron energy is measured by time-of-flight methods. The data were evaluated at 30 energies for an interval width of  $\pm 5\%$  in energy. Figure 1 shows the pulse height spectra measured with the  ${}^3\text{He}$  scintillator for two energy bins. The peak in the spectra due to events in the p+t-channel is isolated for all energies. Above 12 MeV the d+d-events can be separated from the elastic scattering distribution.

The peak contents do not represent the full reaction cross section because of non-negligible wall effects. With increasing energy this effect grows considerably based on the long range of the charged reaction products in the liquid. Due to an error in the necessary corrections, the first evaluation of cross sections (2) turned out to be unreliable at higher energies.

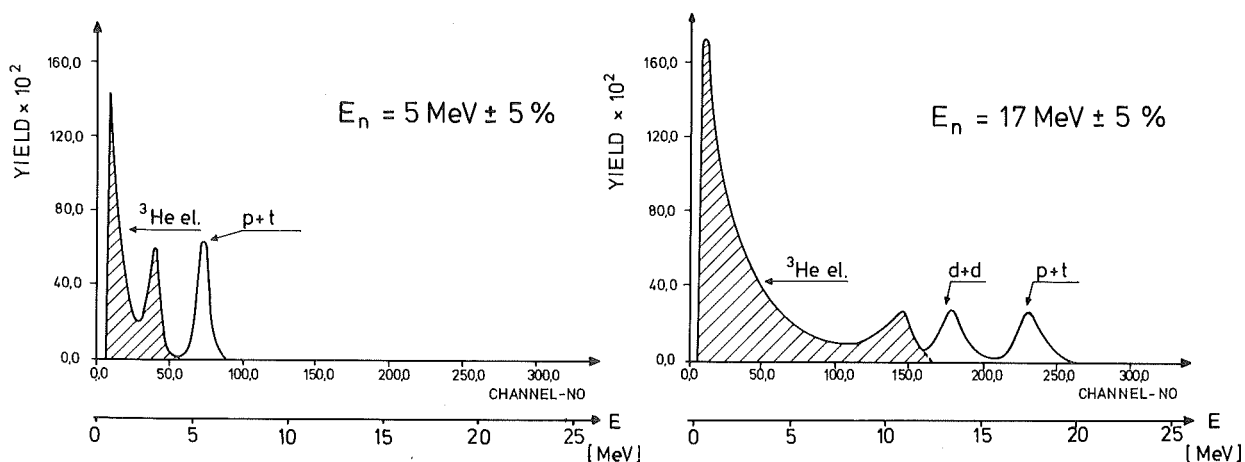


Fig.1: Pulse height spectra of the liquid  ${}^3\text{He}$  scintillation detector for two energies

<sup>+</sup>Central Research Institute for Nuclear Physics, Budapest

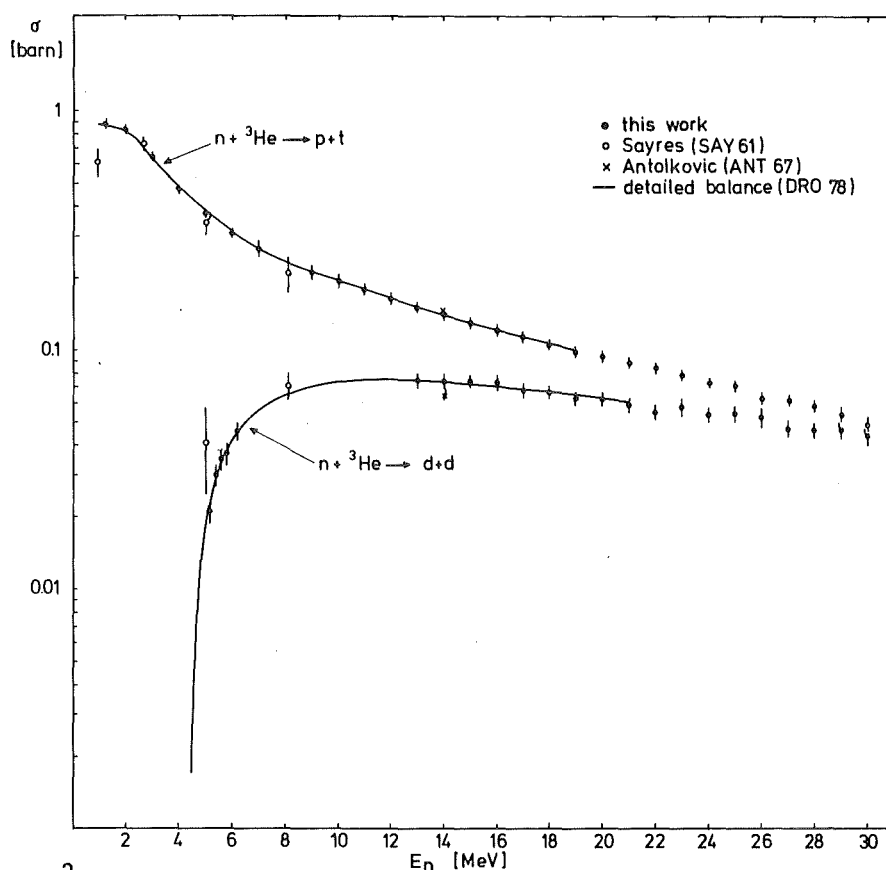


Fig.2:  $n + {}^3\text{He}$  reaction cross sections compared to older data and to the results of a detailed balance calculation.

The results of a careful reanalysis are shown in figure 2.

The errors are dominated by the uncertainties of the corrections. No deviation from a prediction based on detailed balance calculations (3) can be seen. The comparison to older data (4,5) shows the large improvement of the data base by the new results.

Especially the knowledge of the  $p+t$  - reaction channel cross section makes the liquid  ${}^3\text{He}$  scintillation detector an absolute flux monitor for neutron energies up to 30 MeV.

- (1) KfK-Report 3395 (1982)
- (2) KfK-Report 3280 (1982)
- (3) M.Drosg, Los Alamos Report LA-7269 (1978)
- (4) A.R.Sayres et al., Phys.Rev. 122 (1961), 1853
- (5) B.Antolkovic et al., Phys.Rev. 159 (1967), 777

We thank H.Wirth from MPI Heidelberg for help in evaporating the DPS wave length shifter in the helium scintillation container.

1.2.10 THE NEUTRON CAPTURE CROSS SECTION OF  $^{243}\text{Am}$  IN THE ENERGY RANGE FROM 5 TO 250 keV\*

K.Wisshak, F.Käppeler and G.Rupp

Kernforschungszentrum Karlsruhe, IAK II

The neutron capture cross section of  $^{243}\text{Am}$  was measured in the energy range from 10 to 250 keV using  $^{197}\text{Au}$  as a standard. Kinematically collimated neutrons were produced via the  $^7\text{Li}(p,n)$  and the  $\text{T}(p,n)$  reaction with the Karlsruhe 3-MV pulsed Van de Graaff accelerator. Capture events were detected by two Moxon-Rae detectors with graphite and bismuth-graphite converters. Fission events were observed by a NE 213 liquid scintillator with pulse shape discriminator. A  $^{243}\text{Am}$  sample of  $\sim 1$  g was positioned at flight paths as short as  $\sim 5$  cm from the neutron target in order to obtain a signal-to-background ratio of the order of one.

The detectors are shielded with lead against the strong gamma-radiation from the sample material. In order to study the individual systematic uncertainties in detail, several runs have been performed using different lead absorbers (0.5 - 2 cm) and different flight paths (5.0 - 7.2 cm).

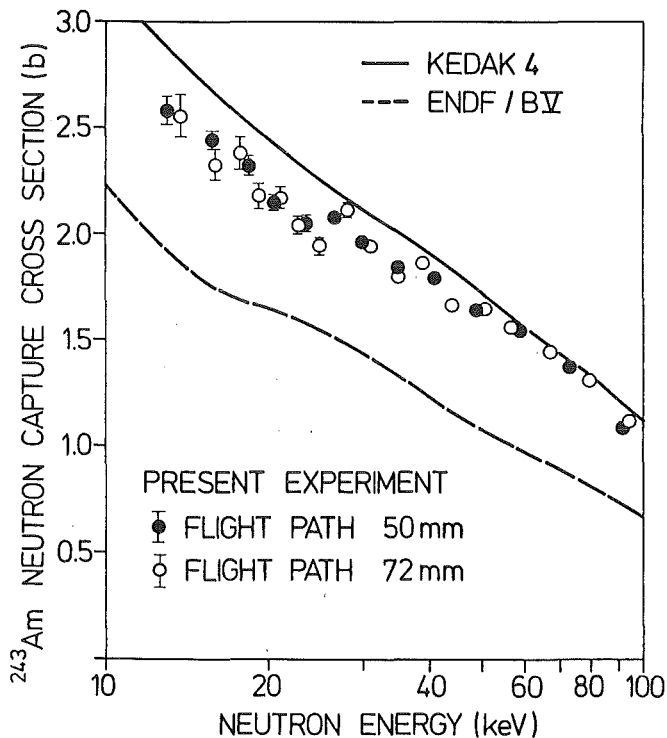


Fig.1: Preliminary results for the neutron capture cross section of  $^{243}\text{Am}$  compared to predictions from model calculations

The data were corrected for deviations of the efficiency of the individual detectors from their ideal shape ( $\epsilon_{\gamma} = kE_{\gamma}$ ) using capture gamma ray spectra calculated by means of the statistical model. No systematic differences are observed in the results obtained with different detectors, flight paths or lead shieldings. Preliminary results for the capture cross section of  $^{243}\text{Am}$  in the energy range from 10 to 100 keV are given in fig.1.

\*Proc. of the Int.Conf. on Nuclear Data for Science and Technology  
Antwerp 6-10 Sept.1982, to be published

1.2.11 CALCULATED GAMMA-RAY SPECTRA FOR keV NEUTRON CAPTURE  
IN  $^{240}\text{Pu}$ ,  $^{242}\text{Pu}$  AND  $^{238}\text{U}$ \*

G.Reffo<sup>+</sup>, F.Fabbri<sup>+</sup>, K.Wisshak and F.Käppeler

Kernforschungszentrum Karlsruhe, IAK II

Capture gamma-ray spectra of  $^{240}\text{Pu}$ ,  $^{242}\text{Pu}$  and  $^{238}\text{U}$  were calculated in the framework of the spherical optical model and the statistical model. A consistent set of input parameters was determined from available experimental information or from model guided systematics. The complete gamma-ray cascades were calculated considering all possible transitions up to multiplicity 7. All experimental information on level schemes and gamma-ray transition probabilities of the compound nuclei was explicitly included as input.

The capture gamma-ray spectra were used to correct experimental data for the capture cross sections of  $^{240}\text{Pu}$  and  $^{242}\text{Pu}$  from a relative measurement using a Moxon-Rae detector with graphite converter and  $^{197}\text{Au}$  as well as  $^{238}\text{U}$  as standards. This correction is required to take into account that the detector efficiency is not exactly proportional to the gamma-ray energy. The resulting correction factors proved to be negligible for measurements relative to  $^{238}\text{U}$  whereas they are ~ 3% if gold is used as a standard.

\* accepted for publication in Nucl.Sci.Eng.

<sup>+</sup>E.N.E.A., Centro di Calcolo, Bologna, Italy

1.2.13 Review of the  $^{240}\text{Pu}$  and  $^{242}\text{Pu}$  unresolved resonance  
Region \*

K. Wisshak, F. Käppeler and F.H. Fröhner <sup>+</sup>  
Kernforschungszentrum Karlsruhe, IAK II

Recent measurements and evaluations of neutron cross section for  $^{240}\text{Pu}$  and  $^{242}\text{Pu}$  in the unresolved resonance region are reviewed. The most conspicuous data gaps could be closed during the last few years but a number of discrepancies between different sets of experimental data and between data and nuclear reaction theory remain problematic.

<sup>+</sup> Kernforschungszentrum Karlsruhe, INR

\* Invited Talk on the IAEA Consultants Meeting, Vienna  
28. September 1981 INCD (NDS) - 129/GJ

International Atomic Energy Agency, Vienna, 1982

### 1.3 NUCLEAR REACTIONS BY CHARGED PARTICLES

#### 1.3.1 Spectroscopy of $^{25}\text{Na}$ and $^{25}\text{Mg}$

P. Grabmayr<sup>+</sup>, T. Kihm<sup>+</sup>, G. Mairle<sup>+</sup>, G. Seegert<sup>+</sup>, K. Schindler<sup>+</sup>,  
G.J. Wagner<sup>+</sup>, V. Bechtold, and L. Friedrich

Kernforschungszentrum Karlsruhe, IAK II

Vector-polarized deuterons of 52 MeV from the Karlsruhe cyclotron were used to extend the systematic investigation (1) of the  $1p_{1/2}$  and  $1p_{3/2}$  hole states in sd-shell nuclei. In earlier measurements (2) of the  $^{26}\text{Mg}(d, ^3\text{He})$  reaction the states of  $^{25}\text{Na}$  at 4.00 MeV and 5.19 MeV were identified as  $1p$

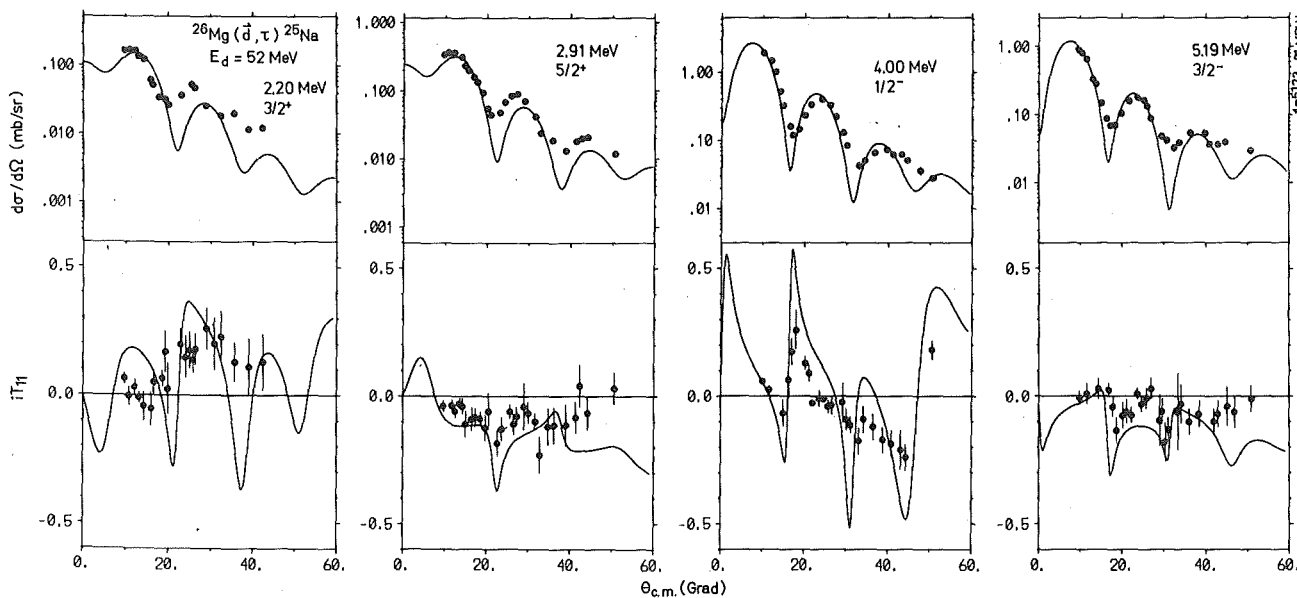


Fig. 1 Cross section and analyzing power of the  $^{26}\text{Mg}(d, ^3\text{He})$  reaction in comparison with DWBA

hole states. This experiment was repeated with polarized deuterons. Fig. 1 shows the angular distributions of cross sections and analyzing powers of states excited with  $J = \ell \pm 1/2$  ( $\ell = 1, 2$ ). The spins of states at 4.00 and 5.19 MeV in  $^{25}\text{Na}$  are now determined as  $1/2^-$  and  $3/2^-$ , respectively. Comparing energy and strength of states in a simultaneous measurement of the  $(d, ^3\text{He})$  and  $(d, t)$  reaction on  $^{26}\text{Mg}$  the  $T = 3/2$  analogs in  $^{25}\text{Mg}$  are identified. The spin assignments are taken from the respective parent states in  $^{25}\text{Na}$ .

- (1) G. Mairle, G.J. Wagner, K.T. Knöpfle, Liu Ken Pao, and H. Riedesel, Nucl. Phys. A363 (1981) 413.
- (2) E. Krämer, G. Mairle, and G. Kaschl, Nucl. Phys. A165 (1971) 353.

<sup>+</sup>Max-Planck-Institut für Kernphysik, Heidelberg

### 1.3.2 The 1d Spin Orbit Splitting in <sup>58</sup>Ni

P. Grabmayr<sup>+</sup>, T. Kihm<sup>+</sup>, G. Mairle<sup>+</sup>, G. Seegert<sup>+</sup>, K. Schindler<sup>+</sup>,  
G.J. Wagner<sup>+</sup>, V. Bechtold, and L. Friedrich

According to theory the spin orbit splitting should be reduced by spin-nonsaturated nucleons. Indeed, a slight decrease of the 1d spin orbit splitting was observed going from <sup>40</sup>Ca to <sup>48</sup>Ca (1). The reduction was overestimated in heavier nuclei as, e.g., in <sup>90</sup>Zr and in <sup>144</sup>Sm (2). Having a large ratio of spin-nonsaturated to spin-saturated nucleons <sup>58</sup>Ni is well suited to check this problem. Fig. 1 shows an energy spectrum of the <sup>58</sup>Ni(d, <sup>3</sup>He) reaction measured in the first maximum of an  $\ell = 2$  angular distribution at 52 MeV. The broad structure between 7 and 14 MeV exhibits mostly 1d strength which exhausts almost the full shell model value for the  $d_{5/2}$  shell. The broken line describes the DWBA cross section for a hypothetical quasihole state at  $E_x = 10$  MeV with FWHM of 7 MeV exhausting the full  $d_{5/2}$  strength. With a centroid of the  $1d_{3/2}$  strength at  $E_x = 4.5 \pm 1$  MeV a preliminary value of  $5.5 \pm 2$  MeV was deduced for the 1d spin orbit splitting. A more accurate result is expected to come from recent measurements of this reaction with vectorpolarized deuterons.

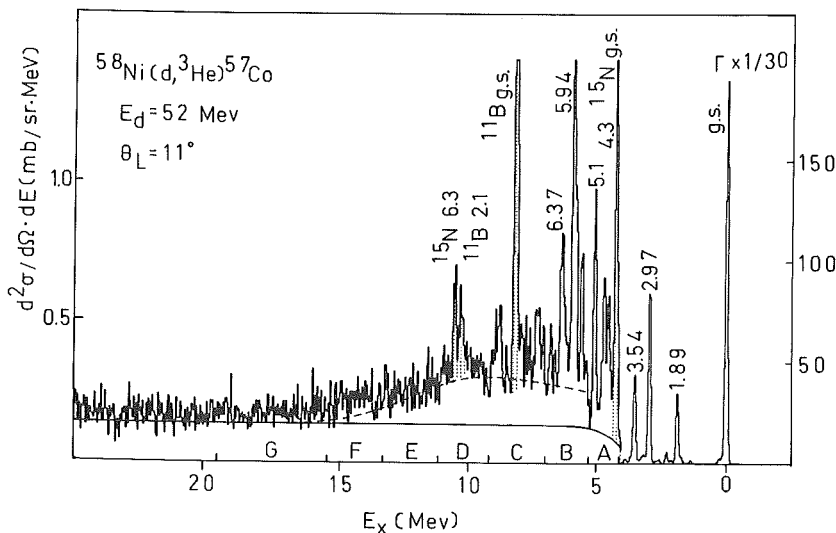


Fig. 1. <sup>3</sup>He spectrum of the <sup>58</sup>Ni(d, <sup>3</sup>He) reaction at 11°. The full line shows the assumed background. The broken line indicates the Breit-Wigner strength distribution of a quasihole state at 10 MeV.

- (1) P. Doll, G.J. Wagner, K.T. Knöpfle, and G. Mairle, Nucl. Phys. A263 (1976) 210.
- (2) A. Stuirbrink, G.J. Wagner, K.T. Knöpfle, Liu Ken Pao, G. Mairle, H. Riedesel, K. Schindler, V. Bechtold, and L. Friedrich, Z. Phys. A297 (1980) 30.

<sup>+</sup>Max-Planck-Institut für Kernphysik, Heidelberg

### 1.3.3 Deeply Bound Proton Hole States in Heavy Nuclei

P. Grabmayr<sup>+</sup>, T. Kihm<sup>+</sup>, G. Mairle<sup>+</sup>, G. Seegert<sup>+</sup>, K. Schindler<sup>+</sup>, G.J. Wagner<sup>+</sup>, V. Bechtold, and L. Friedrich

The first spin determination of deeply bound proton hole states in  $^{89}\text{Y}$  ( $1f_{7/2}$ ) and  $^{143}\text{Pm}$  ( $1g_{9/2}$ ) (1) by means of the ( $\vec{d}, ^3\text{He}$ ) reaction prompted search for such states in  $^{91}\text{Y}$  and  $^{91}\text{Nb}$ . Typical examples of angular distribution and analyzing powers are shown in Fig. 1. For the first time the spin of the  $1f_{7/2}$  proton hole state and, therefore, the  $\ell = 3$  spin orbit splitting could be determined uniquely (2). Due to a reduced experimental

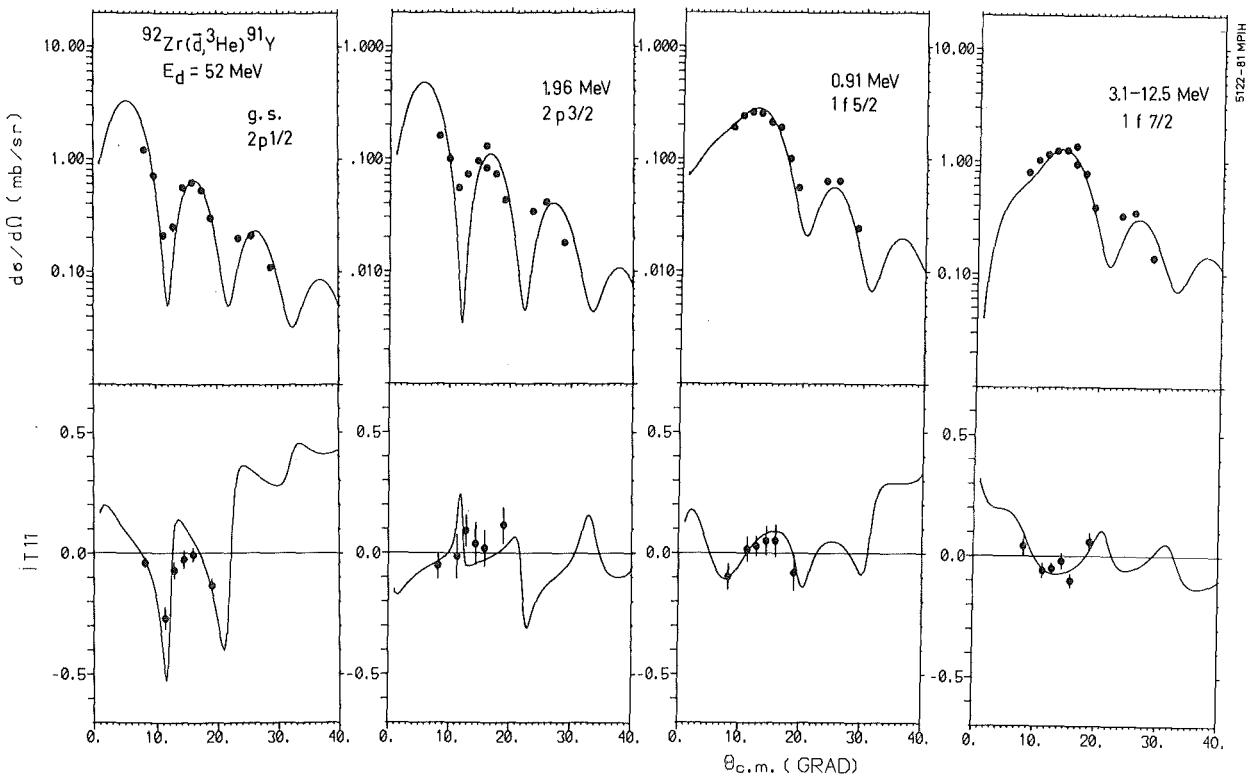


Fig. 1 Angular distribution of cross section and analyzing powers of the  $^{92}\text{Zr}(\vec{d}, ^3\text{He})^{91}\text{Y}$  reaction in comparison with DWBA.

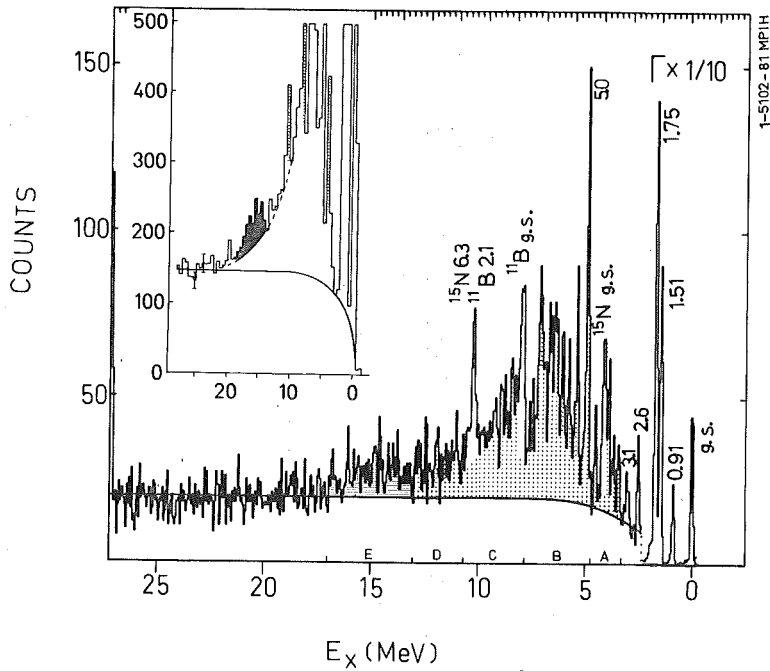


Fig. 2  $^3\text{He}$  energy spectrum of  $^{90}\text{Zr}(\vec{d}, ^3\text{He})$  reaction. The dotted areas give  $f_{7/2}$  strength. The  $s_{1/2}$  strength is seen more clearly when 16 channels are added (insert).

background a remeasurement of the  $^{90}\text{Zr}(\vec{d}, ^3\text{He})$  reaction showed a second gross structure at 15.3 MeV besides the known  $1f_{7/2}$  pickup from the  $2s_{1/2}$  shell. This is in agreement with theory (3,4) which predicts smaller binding energy for  $2s$  protons in  $^{90}\text{Zr}$  than for the  $1d_{3/2}$  shell.

- (1) A. Stuirbrink, G.J. Wagner, K.T. Knöpfle, Liu Ken Pao, G. Mairle, H. Riedesel, V. Bechtold, and L. Friedrich, Z. Phys. A297 (1980)307.
- (2) G. Seegert, Diplomarbeit, 1982, Heidelberg.
- (3) F. Malaguti, A. Uguzzoni, E. Verondini, and P.E. Hodgson, Il Nuovo Cim. 53A, N.1 (1979) 1.
- (4) M. Beiner, H. Flocard, Nguyen van Giai, and P. Quentin, Nucl. Phys. A238 (1975) 29.

#### 1.3.4 Spin Determination of States with Stretched Configurations in $^{16}\text{N}$ and $^{32}\text{P}$ via the $(\vec{d}, \alpha)$ Reaction at 52 MeV\*

G. Mairle<sup>+</sup>, G.J. Wagner<sup>+</sup>, P. Grabmayr<sup>+</sup>, K.T. Knöpfle<sup>+</sup>, Liu Ken Pao<sup>+</sup>, H. Riedesel<sup>+</sup>, K. Schindler<sup>+</sup>, V. Bechtold, L. Friedrich, and P. Ziegler  
Kernforschungszentrum Karlsruhe, IAK II

The reactions  $^{12}\text{C}(\vec{d}, \alpha)^{10}\text{B}$ ,  $^{18}\text{O}(\vec{d}, \alpha)^{16}\text{N}$  and  $^{34}\text{S}(\vec{d}, \alpha)^{32}\text{P}$  have been investigated at  $E_d = 52$  MeV. Vector analyzing powers as large as  $|iT_{11}| = 0.85$  are observed. They exhibit patterns characteristic for final spins  $I = |L-1|$ ,  $L$  or  $L+1$  and provide spin determinations at least for states of unique  $L$ -transfer. Local, zero-range DWBA calculations assuming deuteron-cluster pick-up reproduce qualitatively the observed effects. The method has

been tested for states of known spin and then has been applied to determine spins of states with stretched coupling in  $^{16}\text{N}$ :  $J^\pi = 3^+(3.96 \text{ MeV})$ ,  $4^-(6.17 \text{ MeV})$  and in  $^{32}\text{P}$ :  $J^\pi = 5^+(4.75 \text{ MeV})$ . There is strong evidence for further  $5^+$  states in  $^{32}\text{P}$  at 6.43, 7.96, 8.09 and 8.54 MeV.

\*Nucl. Phys. A382 (1982) 173

<sup>†</sup>Max Planck-Institut für Kernphysik, Heidelberg

### 1.3.5 Comparison Between Radial Sensitivity of Different Strongly Interaction Probes\*

E. Friedman<sup>†</sup>, H.J. Gils, and H. Rebel  
Kernforschungszentrum Karlsruhe, IAK II

A comparison is presented between the radial sensitivity of different strongly interacting probes to neutron density distributions in nuclei. The experiments considered are elastic scattering of 104 MeV alpha particles, of 1 GeV protons, of 130 MeV pions and also shifts and widths of pionic atom levels. The Fourier-Bessel method is used, thus avoiding any prior assumption on the neutron densities. To enable statistically meaningful comparisons between the different experiments, "pseudo data" are used, which are based on the real data.

The results show rather similar radial regions of sensitivity, with the alpha particles probing better the extreme surface and the protons probing better the interior. Pion scattering appears to be inferior to the other two scattering experiments because of the gradient terms in the potential. Surprisingly there are some indications that  $\pi^+$  could be better than  $\pi^-$  in determining neutron densities. Pionic atoms are sensitive mainly to the surface region. A critical discussion of error analyses is presented.

\*Phys. Rev. C25 (1982) 1551

<sup>†</sup>The Racah Institute of Physics, The Hebrew University of Jerusalem

1.3.6 Elastic Alpha Particle Scattering from  $^{43}\text{Ca}$  and  $^{51}\text{V}$  and the Problem of Odd-Even-Staggering of Nuclear Matter Radii

H.J. Gils, H. Rebel, J. Buschmann, S. Zagromski, and E. Friedman<sup>+</sup>  
Kernforschungszentrum Karlsruhe, IAK II

Studies of variations of nuclear radii along isotopic and isotonic chains are an important source of information on nuclear properties and provide stringent tests of nuclear structure theories. A most interesting example is the behaviour of the nuclear charge radii of the calcium isotopes. Superimposed on the quasi parabolic variation of the mean-square charge radii is a remarkable "odd-even-staggering". (1)

Studies of the corresponding neutron or total nuclear matter densities of the even isotopes support that the behaviour of the nuclear charge radii

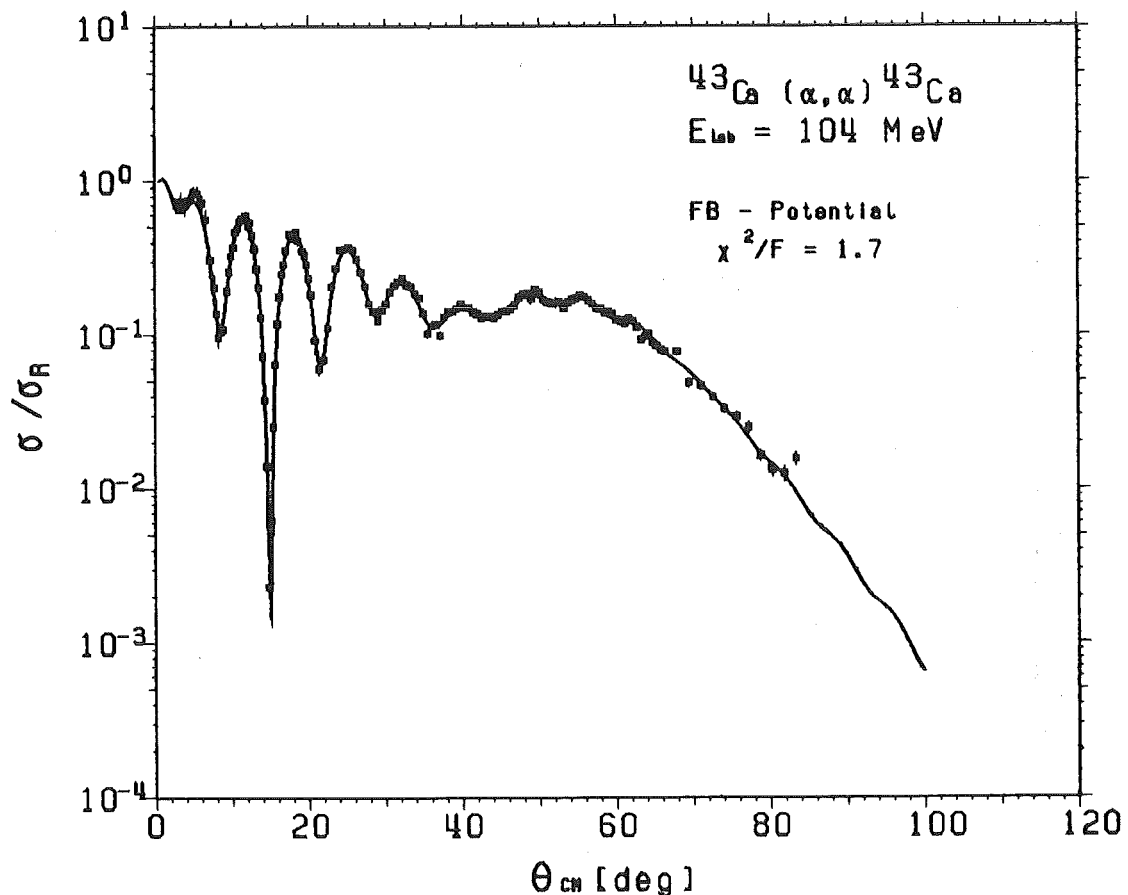


Fig. 1 Differential cross section (divided by the Rutherford cross section) of elastic alpha particle scattering from  $^{43}\text{Ca}$ . The solid curve is the result of a Fourier-Bessel optical potential fit.

is mainly due to a polarization of the proton distribution by the added neutrons (2,3). Information on the neutron densities of the odd nuclei is - so far - not available. Here we report on the first attempt to investigate the nuclear matter distributions and radii of the two odd nuclei  $^{43}\text{Ca}$  and  $^{51}\text{V}$  each occupied by three neutrons or protons, respectively, in the  $1f_{7/2}$  shell. The neighbouring isotopes  $^{42}\text{Ca}$ ,  $^{44}\text{Ca}$  and isotones  $^{50}\text{Ti}$ ,  $^{52}\text{Cr}$  have previously been investigated (3,4) by the same method briefly described below.

The elastic scattering of 104 MeV alpha particles from  $^{43}\text{Ca}$  and  $^{51}\text{V}$  was measured at the Karlsruhe Isochronous Cyclotron with high angular accuracy (partly in steps of  $0.25^\circ$ ) over a wide angular range in order to get unique information about the interaction potential (optical potential) which

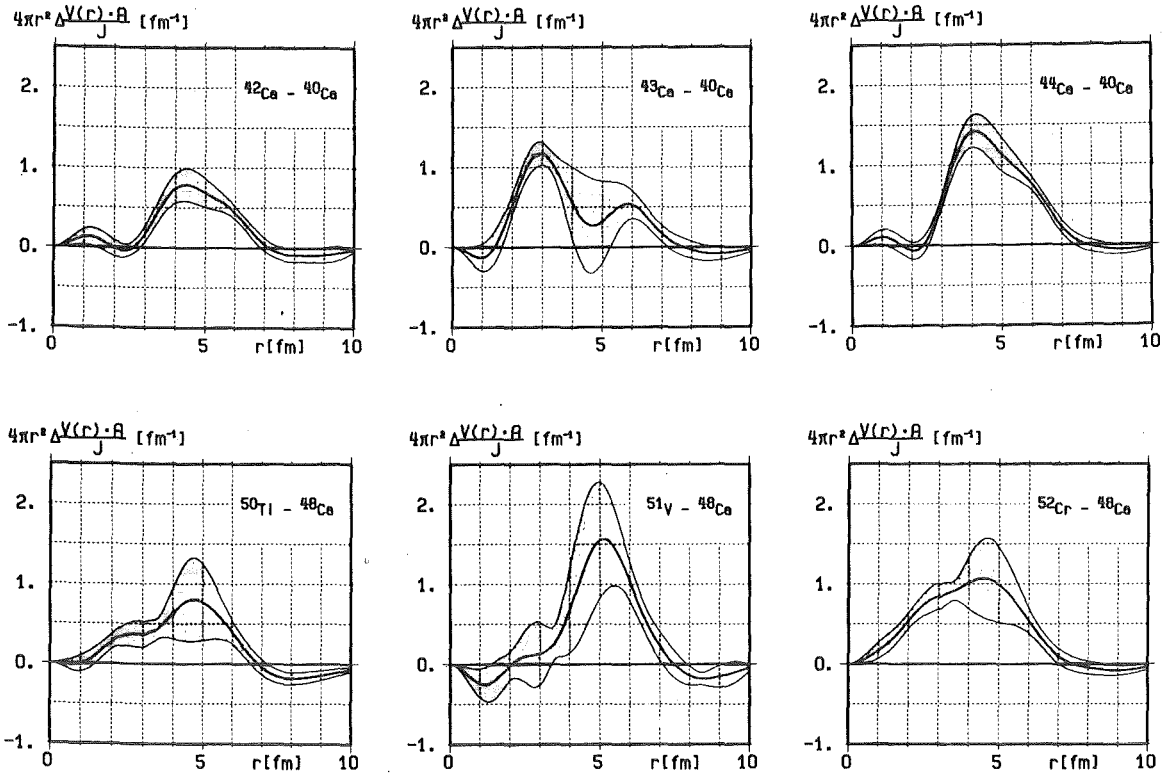


Fig. 2 Differences of the real optical potentials of the isotope chain  $^{42,43,44}\text{Ca}$  as compared to  $^{40}\text{Ca}$  and of the isotone chain  $^{50}\text{Ti}$ ,  $^{51}\text{V}$ ,  $^{52}\text{Cr}$  as compared to  $^{48}\text{Ca}$ . The shaded areas indicate the error bands, obtained from the Fourier-Bessel fit procedure.

is a precondition for microscopic interpretations in terms of the nuclear density (3). A first analysis neglecting all possible effects due to target spin, quadrupole moment etc. aims at a "model independent" determination of the shape and integral quantities of the real optical potential by use of the Fourier-Bessel method (5). Figure 1 shows the differential cross section for  $^{43}\text{Ca}$  which is well reproduced by the optical model fit (solid line). The differences of the resulting real potentials as compared to the potentials of the corresponding closed shell isotope  $^{40}\text{Ca}$  and isotone  $^{48}\text{Ca}$  are displayed in Figure 2 together with the respective differences of the neighbouring even isotopes and isotones. In order to emphasize the shell structure the differences are multiplied by  $4\pi r^2$ .

The differences between the potentials of the even Ca isotopes and  $^{40}\text{Ca}$  show a rather smooth behaviour with the potential strength which is assumed to represent the added neutrons. This trend is also observed for the difference  $^{48}\text{Ca} - ^{40}\text{Ca}$  not shown here. The even isotone chain shows up a similar continuous behaviour of the potential differences. However, the peaks are much smaller than in case of the isotones and extend to very small radii ( $r = 1$  fm) whereas in the outermost radial regions ( $r \gtrsim 7$  fm) the differences are negative. The differences between the odd nuclei  $^{43}\text{Ca}$ ,  $^{51}\text{V}$  and their respective closed shell reference nuclei are peaked in radial regions different from the even nuclei differences. For  $^{43}\text{Ca}$  the peak position is at about  $r = 3$  fm whereas for  $^{51}\text{V}$  the peak is positioned at  $r \approx 5.5$  fm. This observation is reflected by the rms radii of the real potentials. The potential rms radius of  $^{43}\text{Ca}$  is smaller than those of the neighbouring even isotopes  $^{42,44}\text{Ca}$  whereas the radius of  $^{51}\text{V}$  is larger than those of  $^{50}\text{Ti}$ ,  $^{52}\text{Cr}$  and even larger than that of  $^{48}\text{Ca}$ .

These interesting features have to be confirmed by more refined investigations considering the effects due to target spin and ground state quadrupole moment, and also including more microscopic approaches like folding model calculations.

- (1) A. Andl, K. Bekk, S. Göring, A. Hanser, G. Nowicki, H. Rebel, G. Schatz, and R.C. Thompson, Phys. Rev. C (submitted).
- (2) G. Igo et al., Phys. Lett. 81B (1979) 151  
L. Ray, Phys. Rev. C19 (1979) 1855
- (3) H.J. Gils, E. Friedman, H. Rebel, and Z. Majka  
Phys. Rev. C21 (1980) 1245.

- (4) R. Pesl, H.J. Gils, H. Rebel, E. Friedman, J. Buschmann, and S. Zagromski (in preparation).
- (5) E. Friedman and C.J. Batty, Phys. Rev. C17 (1978) 34.

<sup>+</sup>The Racah Institute of Physics, The Hebrew University of Jerusalem

1.3.7 104 MeV Alpha Particle Scattering from  $^{90,92}\text{Zr}^*$

V. Corcalciuc<sup>+</sup>, H.J. Gils, H. Rebel, J. Buschmann, R. Pesl, R. Dumitrescu<sup>+</sup>, S. Zagromski, and K. Feißt  
Kernforschungszentrum Karlsruhe, IAK II

One of the more general results of recent elastic alpha-particle scattering investigations shows that the overall radial shape of the real part of the alpha-particle scattering optical is significantly better represented by a squared Saxon-Woods-form rather than by the standard Saxon-Woods parametrization. The question, however, whether the phenomenological squared Saxon-Woods form has to be extended also to the shape of (permanently or dynamically) deformed optical potentials is not sufficiently investigated. The collective model provides the radial form factors for the nuclear excitation induced by scattering as derivatives of the radial shape of the diagonal optical potential. All procedures for extracting isoscalar transition rates from inelastic alpha-particle scattering basically rely on the particular parametrization of the transition potentials. In view of the interest in comparing consistently the strengths of electromagnetic ( $p, p'$ ) ( $\pi, \pi'$ ) and ( $\alpha, \alpha'$ ) excitations which involve proton and neutron transition matrix elements in a different way, it seems worthwhile to study to which extent different alternative models influence the theoretical descriptions of the experimental results and how they affect the extracted values of the transition rates.

We report on experimental studies of 104 MeV alpha-particle scattering from low-lying levels of  $^{90,92}\text{Zr}$ . Differential cross sections are analyzed in terms of coupled channels on the basis of a flexible anharmonic vibrator model and using different parametrizations of the radial shape of the extended optical potential. The results favour the squared Saxon-Woods type for the real part. Additionally to a radial momentum analysis of the real potentials a semimicroscopic folding model has been applied for extracting isoscalar quadrupole and hexadecapole transition rates.

\*Z. Phys. A 305, (1982) 351

<sup>+</sup>Institute for Physics and Nuclear Engineering, Bucharest, Romania

1.3.8 Isoscalar Octupole Transition Rates in  $^{50}\text{Ti}$ ,  $^{52}\text{Cr}$  and  $^{208}\text{Pb}$  from Model-Independent Analyses of 104 MeV Alpha-Particle Scattering\*

V. Corcalciuc<sup>+</sup>, H. Rebel, R. Pesl, and H.J. Gils  
Kernforschungszentrum Karlsruhe, IAK II

The question of relative amount of neutron and proton strength in nuclear transitions is currently of considerable interest. Up to now only  $0^+ - 2_1^+$  transitions, mostly in single-closed shell nuclei, have been seriously considered with this aspect, referring often to a vibrational model picture and discussing in terms of different nuclear deformations. The primary quantities, however, are the transition matrix elements which can be extracted in a less model dependent way. In this spirit, we applied a recently proposed method (1) for analyzing inelastic alpha-particle scattering and present reliable values of isoscalar octupole transition rates in  $^{50}\text{Ti}$ ,  $^{52}\text{Cr}$  and  $^{208}\text{Pb}$ . The experimental basis is given by experimental differential cross sections measured at  $E_\alpha = 104 \text{ MeV}$ . The method of analysis provides in an intermediate step the quasi-model independent shapes of the transition potentials which display the shape of the transition densities. As an example Fig. 1 shows the coupling potential and its uncertainty for the  $0^+ - 3_1^-$  transition in  $^{208}\text{Pb}$  (compared with the best-fit vibrational model derivative form). In order to preserve general requirements for the transition densities the extreme inner part has been parametrized by a polynomial with zero value at  $r=0$ . This constraint of the analysis obscures somewhat the fact that the region with  $r \lesssim 2 \text{ fm}$  is completely black for the probing alpha-particles. However, the details and deviations from the derivative form appear to be significant for  $r \geq 2 \text{ fm}$ . In  $^{208}\text{Pb}$  the shape of the coupling potential  $v_3$  resembles conspicuously the charge transition density as found by theoretical and inelastic electron scattering studies.

Table 1 compiles results which are derived on the basis of an implicit folding model of the real coupling potentials. The transition rates are given by the enhancement factors  $G_3 = B(\text{IS}; 0^+ - 3_1^-) / B_{\text{sp}}$  and compared to corresponding electromagnetic and theoretical results.

In the case of  $^{52}\text{Cr}$  and  $^{208}\text{Pb}$  electromagnetic ( $0^+ - 3_1^-$ ) transition rates are known and the comparison seems to reveal a significant difference in  $^{52}\text{Cr}$ . While for the  $0^+ - 2_1^+$  transition the proton transition strength

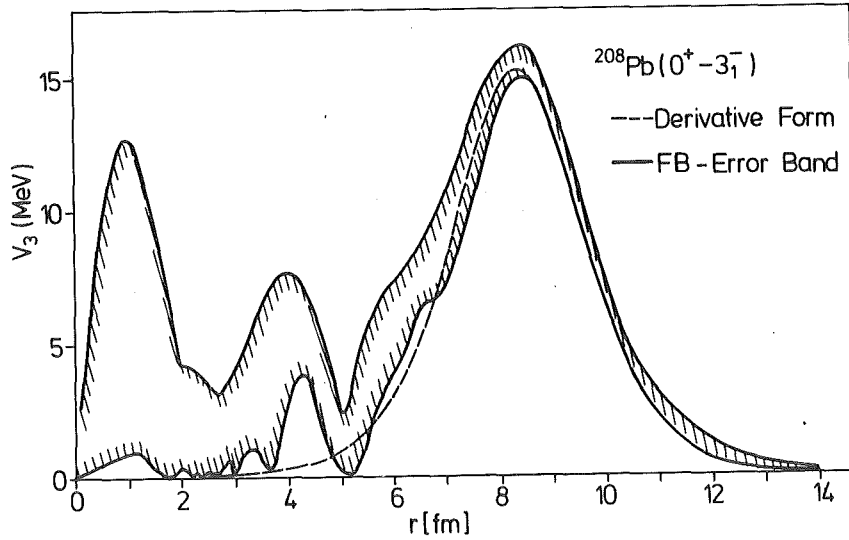


Fig. 1 Coupling potentials for the  $0^+ - 3_1^-$  transition in  $^{208}\text{Pb}$  induced by 104 MeV alpha-particle scattering

Table 1 Isoscalar (IS)  $0^+ - 3_1^-$  transition rates compared to electromagnetic (EL) and theoretical results

	$^{50}\text{Ti}$	$^{52}\text{Cr}$	$^{208}\text{Pb}$
$G_3(\text{IS})$	$12.1 \pm 0.5$	$11.1 \pm 0.3$	$43.0 \pm 1.3$
$G_3(\text{EL})$	-	$6.1 \pm 0.3$	38.4
$G_3(\text{Th})$	9.6	9.7	52.

appears to be stronger than the neutron transition strength (1,2), the pure isoscalar octupole transition rate is larger indicating some cancellation in the electromagnetic transition with isovector contribution.

- (1) H. Rebel, R. Pesl, H.J. Gils, and E. Friedman, Nucl. Phys. A368 (1981) 61
- (2) C. Lunke, J.P. Egger, F. Goetz, P. Gretillat, E. Schwarz. C. Perrin, B.M. Freedom, and R.E. Mischkew, J. Phys. G: Nucl. Phys. 7 (1981) 895

<sup>+</sup> Central Institute of Physics, Bucharest, Romania

1.3.9 Neutron Decay of the Giant Quadrupole Resonance  
Region in  $^{208}\text{Pb}$ \*

H. Steuer<sup>+</sup>, W. Eyrich<sup>+</sup>, A. Hofmann<sup>+</sup>, H. Ortner<sup>+</sup>, R. Stamminger<sup>+</sup>,  
D. Steuer<sup>+</sup>, and H. Rebel

Kernforschungszentrum Karlsruhe, IAK II

The n decay of the giant resonance region between 8.5 and 12.5 MeV in  $^{208}\text{Pb}$  has been studied in an  $(\alpha, \alpha'n)$  coincidence experiment at  $E_x = 104$  MeV. The energy resolution was sufficient to observe the decay into the different states of  $^{207}\text{Pb}$  separately. The strong population of the  $13/2^+$  state shows that large contributions of the total strength excited in the giant quadrupole resonance region have multipolarities  $\geq 4$ . The  $\alpha$  spectra coincident with the decay neutrons show fine structures in the giant quadrupole resonance region of  $^{208}\text{Pb}$ .

\*Phys. Rev. Lett. 47 (1981) 1702

<sup>+</sup>Physikalisches Institut d. Univ. Erlangen-Nürnberg

1.3.10 Search for E0 Strength in the Giant Resonance Region  
of  $^{12}\text{C}$ \*

W. Eyrich<sup>+</sup>, H. Hassold<sup>+</sup>, A. Hofmann<sup>+</sup>, B. Mühldorfer<sup>+</sup>, U. Scheib<sup>+</sup>,  
and H. Rebel

Kernforschungszentrum Karlsruhe, IAK II

The giant resonance region of  $^{12}\text{C}$  has been investigated by small angle scattering of 104 MeV alpha particles. No evidence was found for concentrated monopole strength. Monopole strength around  $E_x = 9.15$  MeV ( $\Gamma = 1.8$  MeV, 2.1 % energy-weighted sum rule) recently observed in a  $^3\text{He}$  scattering experiment could not be confirmed.

\*Phys. Rev. C24 (1981) 2720

<sup>+</sup>Physikalisches Institut d. Univ. Erlangen-Nürnberg

### 1.3.10 Excitation and Decay of Isoscalar Electric Giant Resonances in Heavy Nuclei

W. Eyrich<sup>+</sup>, K. Fuchs<sup>+</sup>, A. Hofmann<sup>+</sup>, H. Rebel, U. Scheib<sup>+</sup>,  
and H. Steuer<sup>+</sup>

Kernforschungszentrum Karlsruhe, IAK II

In the preceding annual report we showed results of the first direct observation of the neutron decay of the giant quadrupole resonance (GQR) region ( $8.5 \text{ MeV} \lesssim E_x \lesssim 12.5 \text{ MeV}$ ) in  $^{208}\text{Pb}$  into the individual states of  $^{207}\text{Pb}$ . In the meantime the analyses of this experiment have been completed and extended to the region of the giant monopole resonance (GMR) in  $^{208}\text{Pb}$ .

For the region of the GQR the strengths for decaying into the individual states in  $^{207}\text{Pb}$  could be deduced separately. Due to their relative small energy the decay neutrons can carry away only small angular momenta. Thus, the spins of the states in the residual nucleus  $^{207}\text{Pb}$  act as a "filter" for the multipolarity of the decaying strength. The extracted resonating E2-strength in  $^{208}\text{Pb}$  of about 50 % EWSR corresponding roughly to the strength for decaying into the low spin states ( $1/2^-$  and  $3/2^-$ ) in  $^{207}\text{Pb}$  (Fig. 1 middle part) shows significant fine structure in good agreement with the results of a recent ( $e, e'$ ) experiment (1). The strong population of the  $13/2^+$  state at 1.63 MeV in  $^{207}\text{Pb}$  (Fig. 1 upper part) provides clear evidence for the existence of considerable strength of higher multiplicities ( $L \geq 4$ ) in the region of the GQR in  $^{208}\text{Pb}$ . Also this strength shows significant fine structure, which, however, is nearly anticorrelated to the strength for decaying into the low spin states of  $^{207}\text{Pb}$ , as can be seen from the lower part of Fig. 1. Summing up the total strength one gets a smooth distribution corresponding to the resonating strength usually seen in the singles alpha-spectra and which - misinterpreted as E2-strength - obviously overestimates the percentage of the E2 EWSR. The branching ratios of the decay of the E2-strength into the different low spin states which can be extracted in a model independent way from our experiment agree fairly well with statistical model calculations demonstrating a dominant statistical decay of the GQR in  $^{208}\text{Pb}$ .

In order to get further information about the decay properties of the GR's in  $^{208}\text{Pb}$  the excitation energy was extended to the region of the GMR

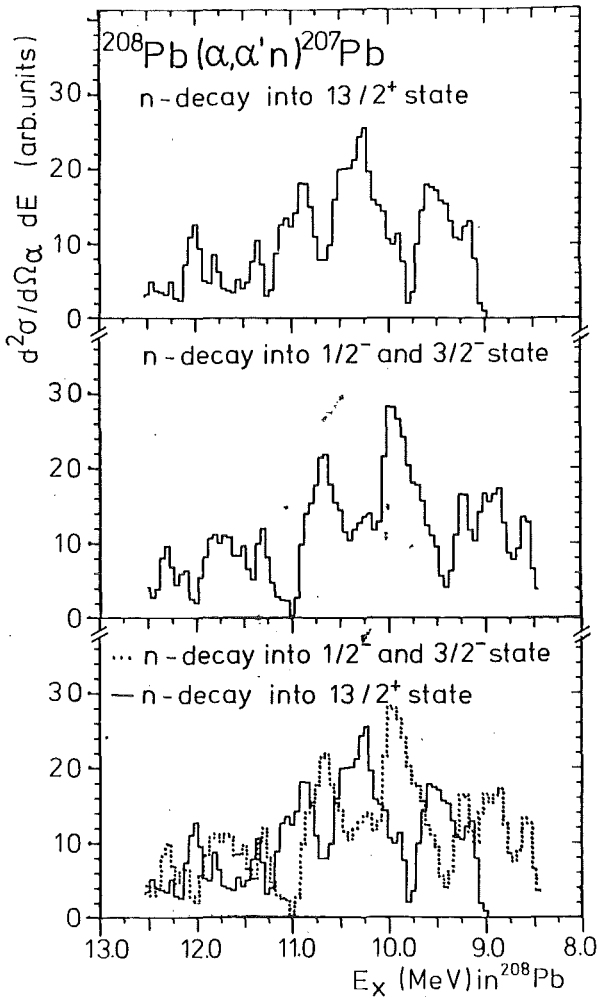


Fig. 1 Distribution of the resonating strengths in  $^{208}\text{Pb}$  decaying into the  $13/2^+$  state in  $^{207}\text{Pb}$  (upper part), into the  $1/2^-$  and  $3/2^-$  states (middle part), and a comparison of both (lower part).

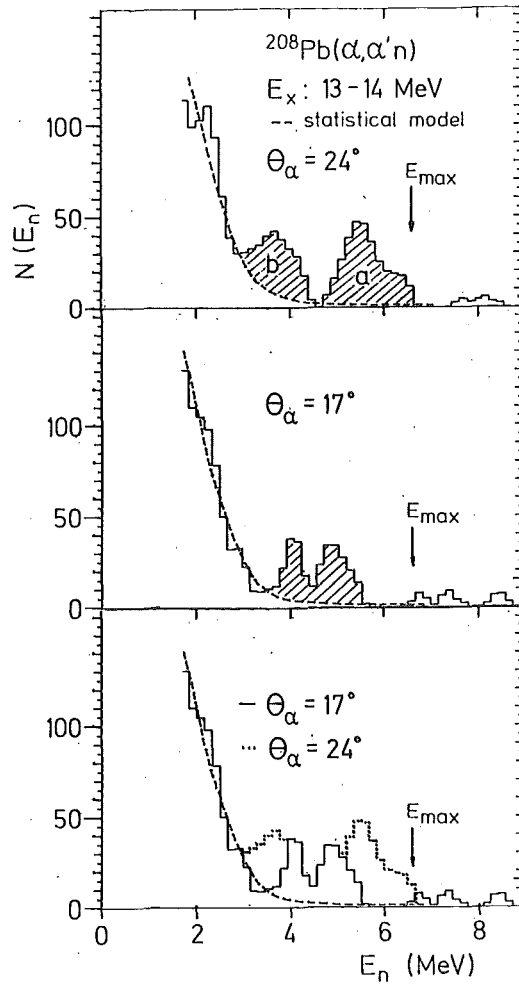


Fig. 2 Spectra of the decay neutrons from the GMR region in  $^{208}\text{Pb}$  for a maximum (upper part) and a minimum (middle part) of the alpha-angular distribution and a comparison of both (lower part).

around  $E_x = 13.5$  MeV. As known from an earlier  $(\alpha, \alpha'\gamma)$ -coincidence experiment (2) in this region similar strengths of multipolarities different from E0 appear (E2 and higher). For this energy region the decay into the different residual states in  $^{207}\text{Pb}$  could no longer be resolved. However, due to the larger possible energy range which can be covered in the residual nucleus important information about the decay mode can be already extracted from the shape of the n-spectra. This is demonstrated in Fig. 2. Here the spectra of the decay neutrons for  $13 \leq E_x \leq 14$  MeV in  $^{208}\text{Pb}$  are shown for a maximum (upper part) and a minimum (middle part) of the alpha-

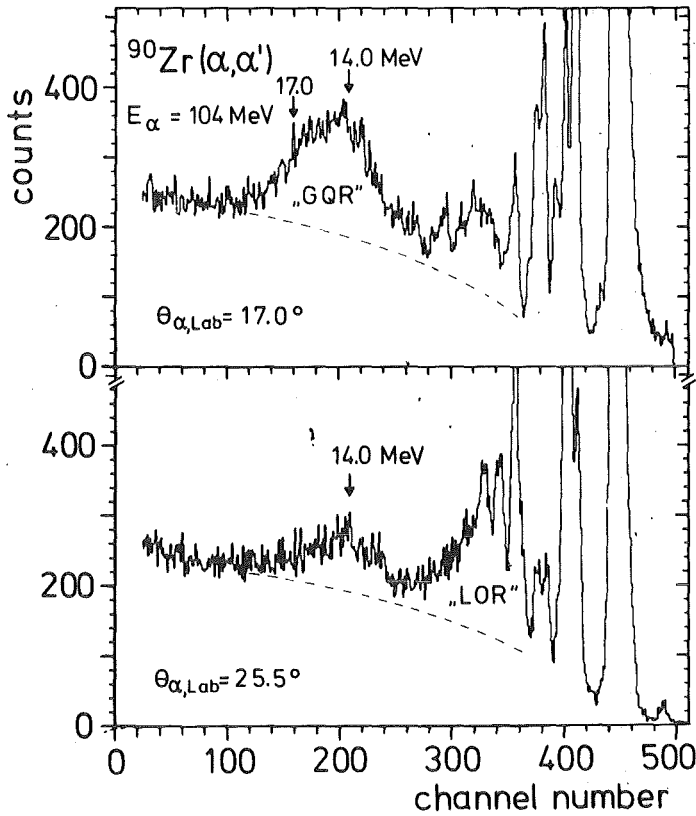


Fig. 3  
 $^{90}\text{Zr}(\alpha, \alpha')$ -spectra at  $E_\alpha = 104$  MeV for a maximum (upper part) and a minimum (lower part) of the E2-angular distribution.

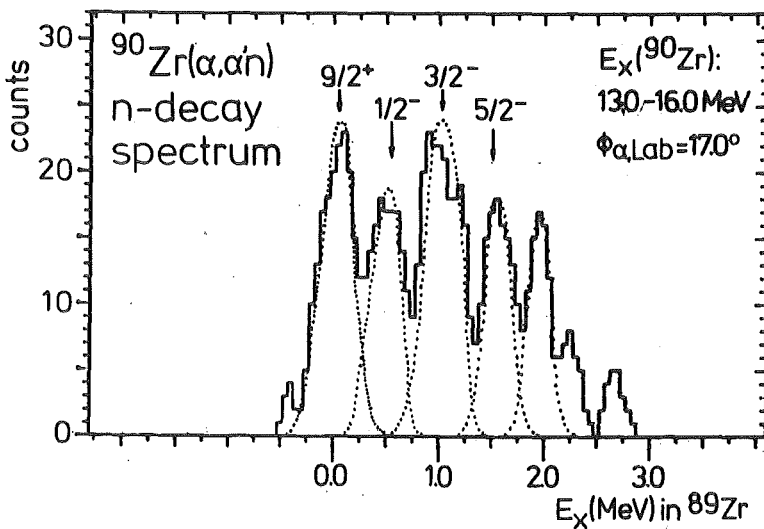


Fig. 4  
Spectra of the n-decay of the GQR-region in  $^{90}\text{Zr}$  into the individual states of  $^{89}\text{Zr}$ .

angular distribution of the resonating strength. The spectra show significant deviations from the shape of a pure statistical decay (evaporation spectrum) at their high energy tail. From the excess of fast neutrons (a) which is much stronger for the maximum of the angular distribution of the GR's than for the minimum (lower part of Fig. 2) a direct decay component of about 15 % of the resonating strength can be extracted. Obviously, Fig. 2 shows a second enhancement (b) in comparison to an evaporation spectrum. This excess gives strong evidence for the decay of the resonating strength into 1 phonon - 1 hole states in  $^{207}\text{Pb}$  which reflects the coupling of the 1p1h doorway states of the GR's to the low lying collective 1 phonon states in  $^{208}\text{Pb}$ , especially the  $3^-$  state at 2.61 MeV. This decay mode is of fundamental interest for the understanding of the structure and dynamics of the GR's (3).

The  $\alpha$ 'n coincidence experiments to study excitation and decay of GR's have recently been extended to  $^{90}\text{Zr}$  in order to investigate a nucleus between  $^{208}\text{Pb}$  and the light nuclei ( $A \leq 60$ ) which had been studied in coincidence experiments by observation of the charged particle decay. In Fig. 3 ( $\alpha, \alpha'$ )-singles spectra are shown for a maximum (upper part) and a minimum (lower part) of the GQR angular distribution. The decay situation for  $^{90}\text{Zr}$  is as favourable as for  $^{208}\text{Pb}$ . The n-decay of the GQR into the individual low lying states of  $^{89}\text{Zr}$  can again be resolved in the  $\alpha$ -n-coincidence experiment. This is demonstrated in Fig. 4 for a maximum of the alpha-angular distribution of the GQR for one position of a n-detector. Similar as in  $^{207}\text{Pb}$  the spins of the low lying states in  $^{89}\text{Zr}$  form a "spin filter" for the decaying strength. The strong population of the  $9/2^+$  ground state, which is apparent from Fig. 4, clearly indicates the existence of strength of higher multipolarities ( $L \geq 4$ ) also in the GQR-region of  $^{90}\text{Zr}$ . To get a more quantitative result measurements at additional positions of the n-detectors are needed. The decay spectra of the strength in the GMR region of  $^{90}\text{Zr}$  show again an excess of fast neutrons similar as in Fig. 2, from which a direct decay component of the resonating strength of about 15 % can be roughly estimated. This value seems to be characteristic for heavy nuclei.

- (1) G. Kühner et al., Phys. Lett. 104B(1981) 189
- (2) W. Eyrich et al., Phys. Rev. Lett. 43 (1979) 1369
- (3) R.A. Broglia et al., Phys. Lett. 101B(1981) 135

<sup>+</sup>Physikalisches Institut d. Univ. Erlangen-Nürnberg

1.3.11 High-Lying Collective Excitations in Light Nuclei Studied by Small Angle Scattering of 104 MeV Alpha-Particles

B. Mühlhörfer<sup>+</sup>, W. Eyrich<sup>+</sup>, H. Hassold<sup>+</sup>, A. Hofmann<sup>+</sup>, H. Rebel, and U. Scheib<sup>+</sup>

Kernforschungszentrum Karlsruhe, IAK II

The small angle scattering of alpha-particles is a sensitive method for the determination of high-lying strength of different multipolarities in nuclei (1,2). It proved to be a powerful tool for the identification of monopole and isoscalar dipole strength due to the characteristic angular distributions of small angle alpha-scattering. In practice, however, the experimental background, which is usually considerably larger than the interesting strength proves to be a limit for this method.

In the preceding annual report we showed a new method to eliminate this background by getting a second independent information about the excitation energy from the time-of-flight of the scattered alpha-particles. This method was used for improved measurements on the nuclei  $^{12}\text{C}$ ,  $^{16}\text{O}$ ,  $^{24}\text{Mg}$ ,  $^{28}\text{Si}$ ,  $^{40}\text{Ca}$  and  $^{58}\text{Ni}$  to search especially for isoscalar monopole and isoscalar dipole strength. In no case concentrated high-lying monopole strength was found. This result is in contradiction to several other experiments but in agreement with very recent measurements of small angle alpha-scattering of the Texas A&M group (3). Thus the question of the existence of the giant monopole resonance in light nuclei is still open.

The extracted isoscalar dipole strength is in agreement with earlier measurements of our group (2,4) with the exception of the strengths around 13.3 MeV and 16.3 MeV in  $^{40}\text{Ca}$ , for which the improved measurements give only weak evidence for dipole contributions. In  $^{58}\text{Ni}$  the strength between 9.2 and 11.2 MeV excitation energy shown in the spectrum at  $\theta_{\alpha,\text{lab}} = 4^\circ$  in Fig. 1 could be decomposed into three components. Whereas in the component around 11.0 MeV there is no indication for E1-strength, the angular distributions of the strengths around 9.66 MeV and 10.34 MeV (see Fig. 2) can be described in the framework of DWBA only if  $L = 1$  excitation is assumed.

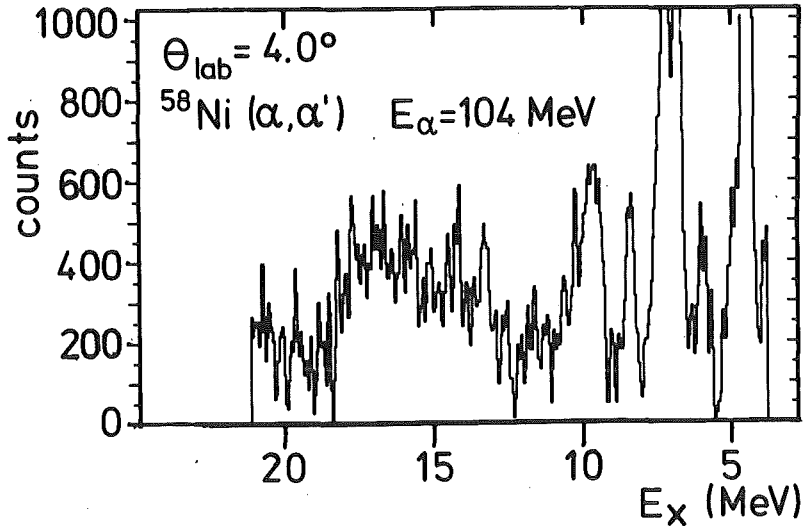


Fig. 1  $^{58}\text{Ni}(\alpha, \alpha')$ -spectrum, taken at  $\theta_{\alpha, \text{lab}} = 4^\circ$

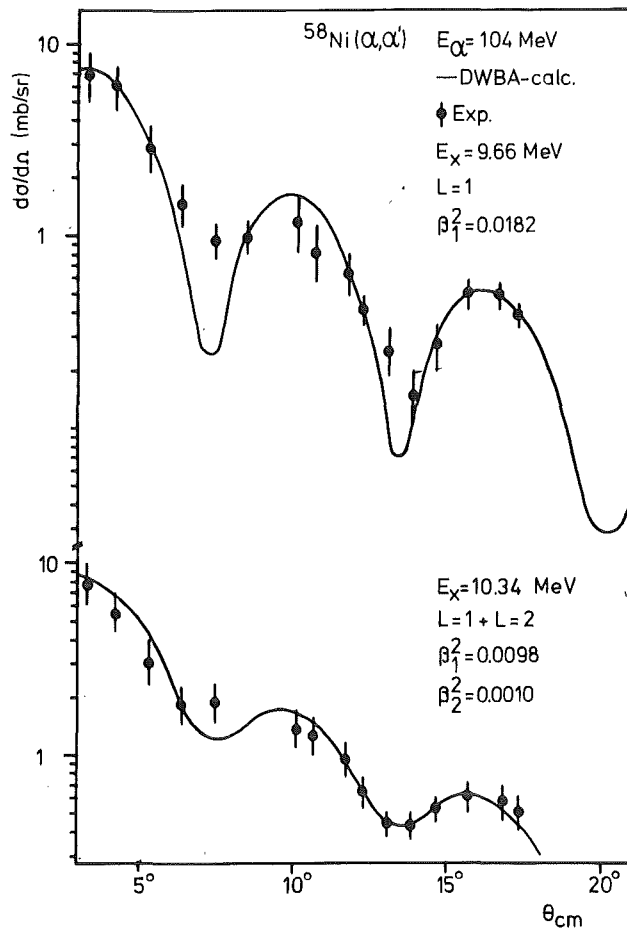


Fig. 2  $^{58}\text{Ni}(\alpha, \alpha')$  angular distributions of the strengths around  $E_x = 9.66 \text{ MeV}$  and  $E_x = 10.34 \text{ MeV}$

The strengths of the giant quadrupole resonance in  $^{28}\text{Si}$ ,  $^{40}\text{Ca}$ , and  $^{58}\text{Ni}$  which were found to be about 30 %, 30 %, and 60 % EWSR, respectively, agree fairly well with the results of earlier experiments of various groups.

- (1) D.H. Youngblood et al., Phys. Rev. Lett. 39 (1977) 1188
- (2) H. Rost et al., Phys. Lett. 88B (1979) 51
- (3) D.H. Youngblood et al., Phys. Rev. C23 (1981) 1997
- (4) H. Rost et al., KfK Report 3068 (1980) p. 43.

<sup>+</sup>Physikalisches Institut d. Univ. Erlangen-Nürnberg

1.3.12 Investigation of Fusion Cross Sections in the  $\alpha + ^{40}\text{Ca}$ -System

M. Albinska<sup>+</sup>, H. Klewe-Nebenius<sup>++</sup>, R. Planeta<sup>+</sup>, J. Buschmann, K. Grotowski<sup>+</sup>, and H. Rebel

In the framework of investigations of the various mechanisms contributing to the  $^6\text{Li} + ^{40}\text{Ca}$  reaction (1) the channel of incomplete fusion of an alpha-fragment of the  $^6\text{Li}$ -projectile with the target nucleus turned out to play an important role (2). An investigation of the product mass-distribution for the  $^6\text{Li} + ^{40}\text{Ca}$  reaction suggested the incomplete fusion cross section to be at least of the same order of magnitude or even larger than the complete fusion of  $^6\text{Li} + ^{40}\text{Ca}$ .

In order to study this  $\alpha + ^{40}\text{Ca}$  channel separately, we have measured the product mass-distribution for alpha-induced reactions of  $^{40}\text{Ca}$  using three different alpha-beam energies (60, 80, 104 MeV), aiming at an easier identification of the products on the basis of the excitation functions. The cross sections for the individual reaction products were determined via the intensities of their characteristic prompt gamma rays.

The alpha-beam of the Karlsruhe Isochronous Cyclotron was focussed onto a 42.9 mg/cm<sup>2</sup> thick target of natural Ca (96.9 %  $^{40}\text{Ca}$ ). The beam current of typically 10 pA was measured by means of a well shielded Faraday cup ca. 6 m away from a small (10 x 10 x 20 cm) target chamber within the external beam line. The spectra of prompt gamma rays were measured with a 84 cc Ge(Li)-detector (resolution 1.9 keV, efficiency 15 % for the 1332 keV gamma rays of  $^{60}\text{Co}$ ). The well shielded detector was placed at 90° with respect to the beam direction in order to avoid

Doppler shift effects for the gamma lines. The spectra taken at 3 beam energies were analyzed using the computer code SAMPO providing energy and intensity for each gamma ray. Each spectrum contained an average of 260 gamma rays, from which about 88 % were identified as to belonging to nuclei with masses  $9 \leq A \leq 43$ . Cases of ambiguous or multiple assignments of gamma rays were taken into account by means of a respective cross section error. Thus, the errors quoted in Table 1 mainly reflect the uncertainties in the identification of specific product nuclei.

Table I Experimental and calculated cross sections for different processes contributing to the  $\alpha + {}^{40}\text{Ca}$ -reaction

Channel (mb)	$E_{\text{projectile}}$ (MeV)		
	59.1	79.5	104
$\sigma_{\text{comp.fusion}}^{\text{exp}}$	1373 $\begin{smallmatrix} +331 \\ -235 \end{smallmatrix}$	1235 $\begin{smallmatrix} +209 \\ -161 \end{smallmatrix}$	1201 $\begin{smallmatrix} +177 \\ -156 \end{smallmatrix}$
$\sigma_{\text{direct}}^{\text{exp}}$	145 $\begin{smallmatrix} +207 \\ -104 \end{smallmatrix}$ (A=43-43)	168 $\begin{smallmatrix} +124 \\ -62 \end{smallmatrix}$ (A=41-43)	248 $\begin{smallmatrix} +55 \\ -30 \end{smallmatrix}$ (A=41-43) =
$\sigma_{\text{total}}^{\text{exp}}$	1566 $\begin{smallmatrix} +391 \\ -257 \end{smallmatrix}$	1389 $\begin{smallmatrix} +243 \\ -173 \end{smallmatrix}$	1447 $\begin{smallmatrix} +186 \\ -159 \end{smallmatrix}$
$\sigma_{\text{reaction}}^{\text{opt.mod.}}$	1484	1473	1451
$\sigma_{\text{fusion}}^{\text{statistic.}}$	1105	1150	1183

We assume that for alpha-incident reactions the main contribution to the total reaction cross section is due to complete fusion of target and projectile with subsequent nucleon evaporation, leading to products with masses between 27/31 and 40/41 (depending on the projectile energy). In addition a (small) contribution from direct processes is expected in the mass region  $A = 41-43$ .

The total reaction cross section was obtained by summing up the individual production cross sections from  $A = 28$  to  $A = 43$ . The low mass part (beyond the evaporation region)  $A = 28-29$  can probably be explained by background reactions ( $\alpha + {}^{12}\text{C}$ ,  $\alpha + {}^{16}\text{O}$ ,  $n + {}^{27}\text{Al}$ ). Cross sections for the direct and the complete fusion channels as well as the total reaction cross section were obtained by summing up the contributions of the individual

products in the mass regions mentioned above. A comparison of the total reaction cross sections with those obtained by an optical model calculation showed, however, a strong discrepancy, which may be probably due to a normalization error when calculating the individual production cross sections. Since now suitable background gamma ray could be found in the spectra, we have decided - for the time being - to normalize the experimental total reaction cross sections to the value obtained by the optical model calculation. We find for all three projectile energies a normalization factor of 2.3. As a further test we compared experimental fusion cross sections to values predicted by the model of Glas and Mosel (3) using values for the model parameters taken from the calculated optical potential.

Table 1 compiles all experimental and calculated cross section values mentioned above.

- (1) B. Neumann, H. Rebel, H.J. Gils, R. Planeta, J. Buschmann, H. Klewe-Nebenius, S. Zagromski, R. Shyam, and H. Machner Nucl. Phys. A382, 296 (1982).
- (2) B. Neumann, J. Buschmann, H. Klewe-Nebenius, H. Rebel, and H.J. Gils, Nucl. Phys. A329, 259 (1979).
- (3) D. Glas and U. Mosel, Nucl. Phys. A237 (1975) 268

<sup>+</sup> Jagellonian University and Technological University, Institute of Physics, Cracow, Poland

<sup>++</sup> Kernforschungszentrum Karlsruhe, IRCh

1.3.13 Elastic Scattering of 156 MeV <sup>6</sup>Li Ions from <sup>6</sup>Li  
S. Micek, H.J. Gils, H. Rebel, J. Buschmann, and S. Zagromski  
Kernforschungszentrum Karlsruhe, IAK II

The investigation of elastic scattering of <sup>6</sup>Li projectiles is of considerable interest as there is a change in the character of elastic scattering observed in the transition from light to heavy ions. At higher bombarding energies and light target nuclei nuclear rainbow scattering is observed, a feature, which has been found to lead to an increased sensitivity to the shape of the real potential in case of alpha-particle scattering. Previous studies (1) of elastic scattering of 156 MeV <sup>6</sup>Li ions analyzing the experimental differential cross sections on the basis

of the optical model have indeed established a remarkable sensitivity of the data to the shape of the real part of the potential, in particular for light target nuclei. When applying a semi-microscopic approach based on a usual double-folding model, the strength of the real part of the optical potential is overpredicted by the M3Y effective interaction (in contrast to its success for heavy ion scattering). Following the suggestion that this difficulty might originate from the cluster structure of both the projectile and the target, a double-folding cluster model generated from  $d-\alpha$  and  $\alpha-\alpha$  interactions and internal cluster wave functions has been worked out (2). A rather good description of elastic scattering from  $^{12}\text{C}$  has been obtained. This success leads us to study additionally a highly clusterized system such as ( $^6\text{Li}-^6\text{Li}$ ). The present status of the

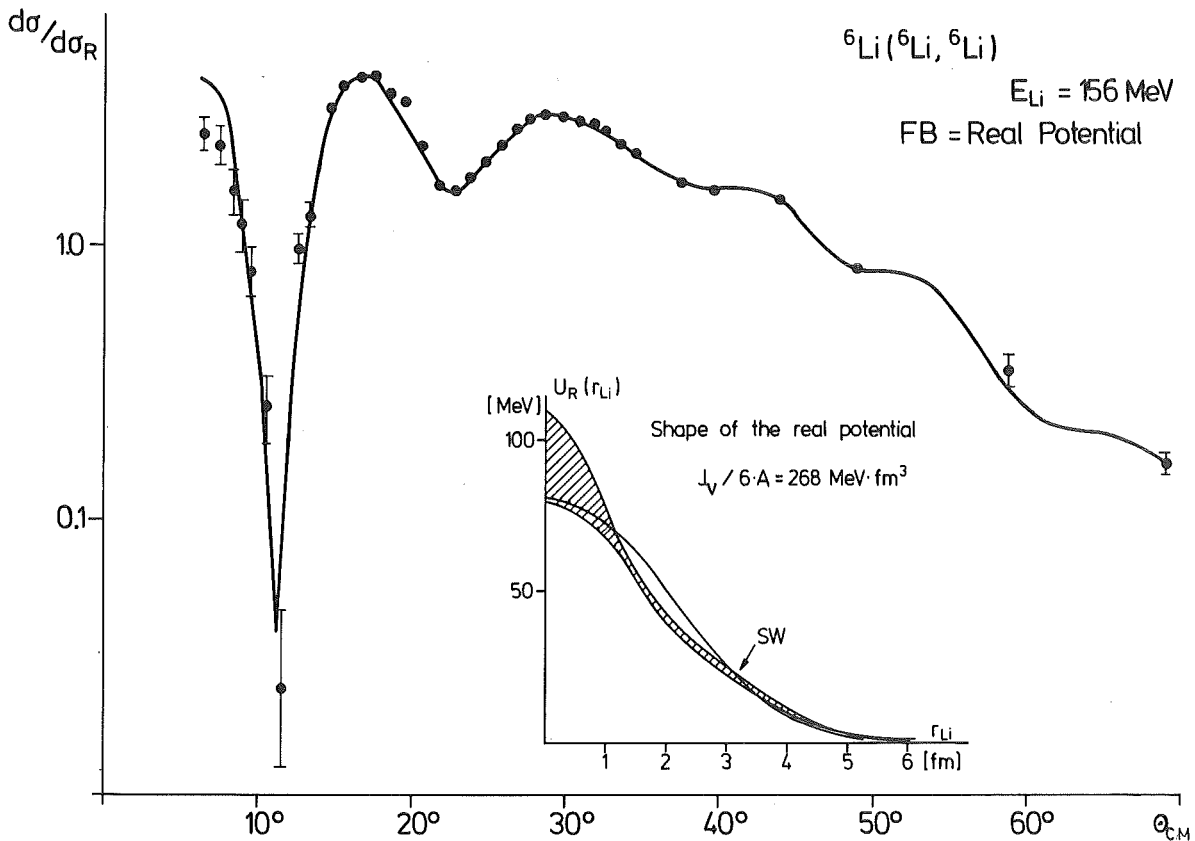


Fig. 1 Experimental and theoretical results for elastic scattering of 156 MeV  $^6\text{Li}$  from  $^6\text{Li}$ .

experimental results for the elastic scattering is given in Fig. 1 together with some results of the phenomenological optical model analysis, using the quasi-model-independent Fourier-Bessel method. The resulting shape of the FB potential (inset of Fig. 1) reproduces the available data considerably better than the more conventional Saxon-Woods (SW) and Saxon-Woods squared forms. Microscopic studies on the basis of usual double folding and cluster folding models are in preparation and should clarify the question whether there are cluster effects contributing to the detailed shape of the interaction potential.

- (1) J. Cook, H.J. Gils, H. Rebel, Z. Majka, and H. Klewe-Nebenius, Nucl. Phys. A388 (1982) 173.
- (2) Z. Majka, H.J. Gils, and H. Rebel, Phys. Rev. C25 (1982) 2996.

#### 1.3.14 Cluster Folding Model for $^{12}\text{C}(^6\text{Li}, ^6\text{Li})$ Scattering at 156 MeV\*

Z. Majka<sup>†</sup>, H.J. Gils, and H. Rebel  
Kernforschungszentrum Karlsruhe, IAK II

A double-folding cluster model generated from d- $\alpha$  and  $\alpha$ - $\alpha$  interactions and internal cluster wave functions of the projectile and the target nuclei is proposed to describe the differential cross sections for  $^6\text{Li}$  elastic scattering from  $^{12}\text{C}$  at 156 MeV. Results of these calculations are compared with standard double-folding models and the phenomenological optical model predictions and provide a significantly improved description of the experimental data.

\*Phys. Rev. C25 (1982) 2996

<sup>†</sup>Institute of Physics, Jagellonian University, Cracow, Poland

#### 1.3.15 Single Nucleon Transfer Reactions in Collisions of 156 MeV $^6\text{Li}$ with $^6\text{Li}$

S. Micek, H.J. Gils, H. Klewe-Nebenius<sup>†</sup>, and H. Rebel  
Kernforschungszentrum Karlsruhe, IAK II

In course of our investigations of the reaction mechanisms of 156 MeV  $^6\text{Li}$  ions colliding with  $^6\text{Li}$ , we observed single nucleon transfer reactions leading to unbound ground and excited states of  $^5\text{Li}$  and  $^5\text{He}$  (Fig. 1).

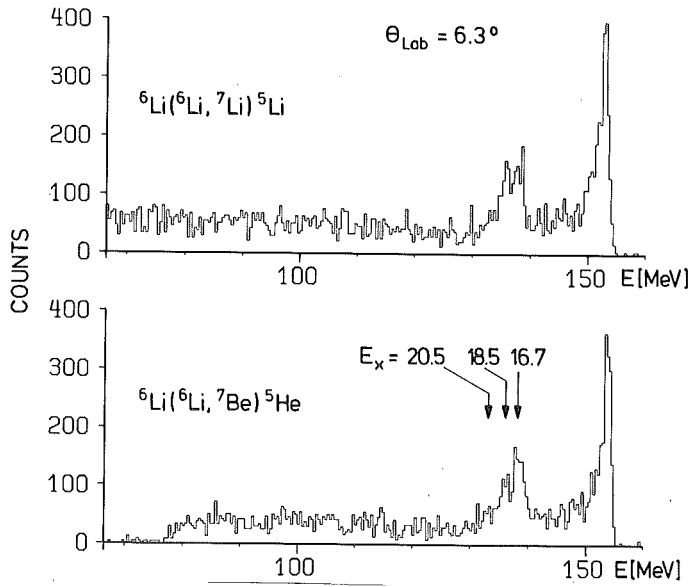


Fig. 1  
Energy spectra of out-  
going  ${}^7\text{Li}$  and  ${}^7\text{Be}$  partic-  
les from  ${}^6\text{Li}+{}^6\text{Li}$  colli-  
sions at 156 MeV.

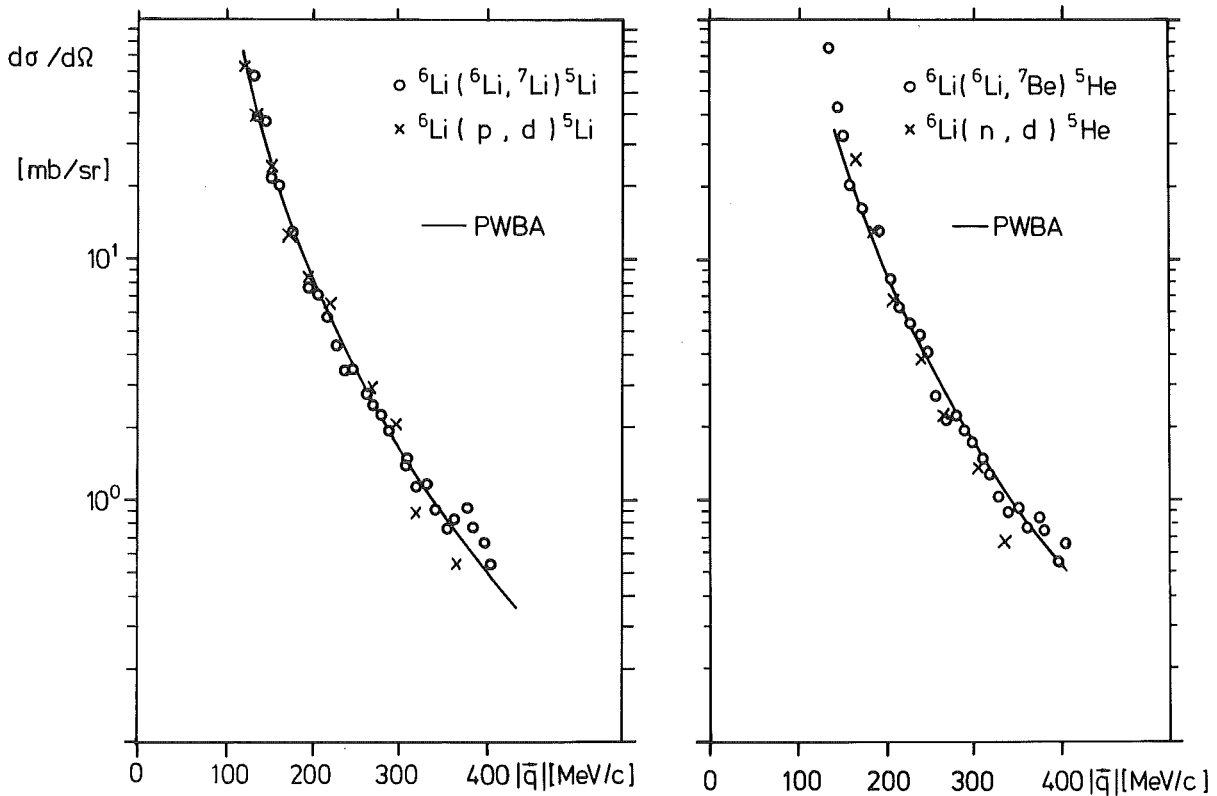


Fig. 2 Cross sections of neutron and proton transfer reactions  
from  ${}^6\text{Li}$

Interesting features are revealed when comparing the differential cross sections of the  ${}^6\text{Li}({}^6\text{Li}, {}^7\text{Li}){}^5\text{Li}$  and  ${}^6\text{Li}({}^6\text{Li}, {}^7\text{Be}){}^5\text{He}$  reactions at the same momentum transfer with corresponding neutron and proton transfer in  ${}^6\text{Li}(p, d){}^5\text{Li}$  (1) and  ${}^6\text{Li}(n, d){}^5\text{He}$  (2) reactions, respectively. As displayed in Fig. 2 there appears a conspicuous similarity in shape, and in addition, relatively small differences in the absolute magnitude of the cross sections are found ( $d\sigma(p+{}^6\text{Li})$  is multiplied by a factor of 1.58 in Fig. 2,  $d\sigma(n+{}^6\text{Li})$  by 1.12). These features indicate the minor importance of distortion and of finite range effects and suggest a simple PWBA description with cross sections dominantly given by the momentum distribution of the transfer nucleon bound in  ${}^6\text{Li}$ . Moreover, in all four types of reactions the loosely bound transferred nucleons seem to play similar roles of quasi-free constituents. Results of a simple PWBA calculations agree indeed quite well with the experimental data (Fig. 2).

- (1) T.Y. Li and S.K. Mark, Nucl. Phys. A123(1969) 147
- (2) F.P. Brady, N.S.P. King, B.E. Bonner, M.W. McNaughton, J.C. Wang and W. True, Phys. Rev. 16C (1977) 31

<sup>+</sup>Kernforschungszentrum Karlsruhe, IRCh

### 1.3.16 Inclusive Break-Up Reactions of ${}^6\text{Li}$ at an Incident Energy of 26 MeV/Nucleon\*

B. Neumann<sup>+</sup>, H. Rebel, H.J. Gils, R. Planeta, J. Buschmann, H. Klewe-Nebenius<sup>+</sup>, S. Zagromski, R. Shyam<sup>++</sup>, and H. Machner<sup>+++</sup>  
Kernforschungszentrum Karlsruhe, IAK II

Inclusive charged particle spectra were measured from nuclear reactions induced by 156 MeV  ${}^6\text{Li}$  on  ${}^{40}\text{Ca}$ . At forward angles the spectra exhibit broad break-up distributions centered around the energy corresponding to the beam velocity. The double differential cross sections together with previous results for a  ${}^{208}\text{Pb}$  target were analyzed in the framework of the DWBA approach to projectile break-up taking into account elastic and inelastic reactions of the break-up fragments. The high energy tails of the background due to preequilibrium emission of complex charged particles were estimated on the basis of the coalescence model. The combination of both theoretical approaches leads to rather good descriptions of the break-up contributions seen in inclusive charged particle spectra.

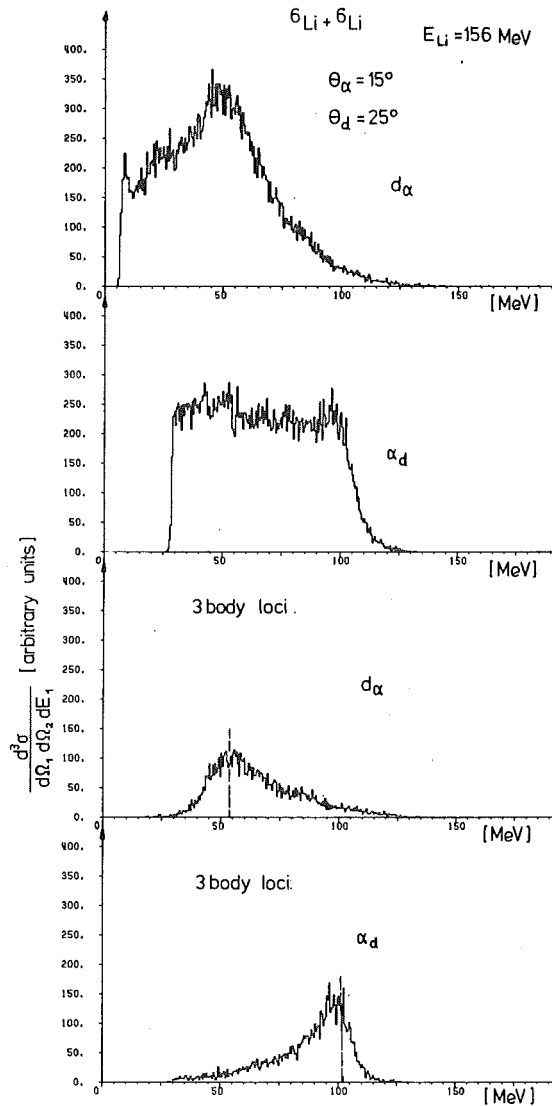


Fig. 1 Single target spectator pole processes (kinematic conditions and cross sections) seen by ( ${}^6\text{Li}, d$ ) and ( ${}^6\text{Li}, \alpha$ ) coincidences when bombarding  ${}^6\text{Li}$  by 156 MeV  ${}^6\text{Li}$  ions.

have been detected in plane by two  $\Delta E$ -E detector telescopes. Five-parameter events (two  $\Delta E$  signals, two E signals and the timing signal) were stored on magnetic type and analyzed off-line. Fig. 1 shows as examples energy spectra of deuterons correlated with alpha-particle emission and of alpha particles correlated with deuterons. In the lower part of the figure only events located on the kinematical loci of  ${}^6\text{Li} + {}^6\text{Li} \rightarrow \alpha + d + {}^6\text{Li}$  reactions are projected out (due to restricted energy resolution in one of the counters elastic break-up and break-up with excitation of the first excited target state are not resolved). The result demonstrates the importance of direct elastic and inelastic  ${}^6\text{Li}$ -break-up processes with flying spectators, but indicates also the considerable contributions of more complicated processes (e.g., four-body reactions) with correlated emission of two particles.

\*Nuclear Physics A382 (1982) 296

+ Kernforschungszentrum Karlsruhe, IRCh

++ Daresbury Laboratory, Daresbury, England

+++ Kernforschungsanlage Jülich, IK

1.3.17 Particle-Particle Coincidence Studies of Break-Up Processes in the  ${}^6\text{Li}+{}^6\text{Li}$  Reaction

S. Micek, J. Buschmann, H.J. Gils, H. Klewe-Nebenius<sup>+</sup>,

H. Rebel, and S. Zagromski

Kernforschungszentrum Karlsruhe, IAK II

Whenever the energy of a complex projectile is considerably larger than the binding energy of its constituents, fragmentation or break-up processes do play an important role in the projectile-target interaction. A typical feature of continuous spectra of outgoing light particles is that in such reactions at least one break-up partner emerges from the interaction zone with about the incoming beam velocity, and except for elastic scattering, it leaves the interaction region as a spectator.

In the case of  ${}^6\text{Li}$  projectiles the high probability of the weakly bound  ${}^6\text{Li}$  and the well-developed cluster structure lead at forward angles to rather strong break-up contributions in the inclusive charge particle spectra signalled by distinct bell-shaped continua centered around the energy corresponding to the beam-velocity (1).

The break-up process is called "elastic or "inelastic" depending on whether the second particle elastically or inelastically interacts with the target nucleus. There is a large variety of inelastic reaction paths competing quasifree processes. Most often, in the inelastic reaction a secondary compound nucleus is formed, e.g., decaying in a preequilibrium stage.

In order to ascertain the extent to which various mechanism play a role in  ${}^6\text{Li}$  induced reactions and to isolate the quasi-free reaction path more in details particle-particle coincidences have been measured in collisions of 156 MeV  ${}^6\text{Li}$  on  ${}^6\text{Li}$ . The system ( ${}^6\text{Li}+{}^6\text{Li}$ ) was chosen as it may provide a realistic chance to understand the details and the relative importance of all competing reaction channels more completely. The correlated particles

In addition to the projectile break-up processes with flying spectator fragments the reaction proceeding via single target spectator pole processes has been observed by ( ${}^6\text{Li},\alpha$ ) and ( ${}^6\text{Li},d$ ) coincidence measurements. There is also some interest (2) in double spectator probe processes for the particular projectile-target combination. In such a reaction one cluster of each nucleus keeps its initial momentum. Up to now we have not identified this particular reaction channel conclusively.

- (1) B. Neumann, H. Rebel, H.J. Gils, R. Planeta, J. Buschmann, H. Klewe-Nebenius, S. Zagromski, R. Shyam, and H. Machner, Nucl. Phys. A382 (1982) 296.
- (2) R.E. Warner, G.C. Ball, W.G. Davies and J.S. Forster, Nucl. Phys. A365 (1981) 142.

<sup>+</sup>Kernforschungszentrum Karlsruhe, IRCh

## 1.4 NUCLEAR THEORY

### 1.4.1 On Calculating Matrix Elements of Slater-Determinant Wave Functions in the Cluster Model\*

R. Beck

Kernforschungszentrum Karlsruhe, IAK II

This report is concerned with the calculation of matrix elements of Slater-determinant wave functions. These matrix elements are the basic input to any calculation with the Generator Coordinate Method (GCM). The main emphasis lies upon the projection of angular momentum and parity. The projection method is an analytical one making extensive use of Racah algebra and leads to closed expressions of these matrix elements in terms of 3-j, 6-j and 9-j symbols. It is shown that matrix elements of the kinetic energy operator may be obtained in a simple way from those of the normalization. The spurious contribution of the kinetic energy operator to the center-of-mass energy is eliminated by projecting the linear momentum of the states.

\* KfK-Report 3261 (1981)

### 1.4.2 On Calculating Matrix Elements of Slater Determinant Wave Functions in the Cluster Model II. Clusters with Intrinsic Orbital Angular Momentum\*

R. Beck and F. Dickmann

Kernforschungszentrum Karlsruhe, IAK II

A method for projecting angular momentum in two-cluster systems with intrinsic orbital angular momentum is presented. The method is an analytical one making use of Racah algebra and exploiting tensor properties of two-cluster shell model wave functions. As an application, reduced matrix elements of spin-isospin independent scalar operators and of the electric charge multipole operator are calculated in the case where one of the clusters in the two-cluster wave function may carry an intrinsic orbital angular momentum.

\*KfK-Report 3402 (1982)

1.4.3 Application of the Algebraic Programming System Reduce 2 to Calculations in the Cluster Model of Light Nuclei\*

R. Beck, F. Dickmann, and J. Oehlschläger  
Kernforschungszentrum Karlsruhe, IAK II

Matrix elements of a two-body interaction with a Gaussian radial shape, the kinetic energy and the charge multipole operator are calculated using two-cluster many-body wave functions. The wave functions are antisymmetrized products of 1s and 1p harmonic oscillator single particle functions centered at the origin of their respective oscillator wells. All single particle functions have the same oscillator length. The dependence of the matrix elements on both the vectors connecting the positions of the oscillator wells and the oscillator length, the strength and range, parameters of the two-body interaction and - in the case of the charge operator - the transferred momentum is obtained analytically. The calculation is based on the Reduce 2 programming system making extensive use of its capability of symbolic differentiation, symbolic evaluation of determinants and pattern matching.

\*KfK-Report 3404 (1982)

1.4.4 On the Valence Contribution to the Radiative Width of s-Wave Resonances in Fe and Ni Isotopes

A. Mengoni, G. Reffo<sup>+</sup>, and F. Fabbri<sup>+</sup>  
Kernforschungszentrum Karlsruhe, IAK II

The necessity for a valence contribution to the radiative width of the neutron resonances in some structural materials like iron and nickel was claimed by various authors (1,2). In recent, more precise experiments (3,4) some of the systematic errors were avoided providing a new data basis for a reinvestigation of the valence model. This was done for the s-wave resonances in  $^{58,58}\text{Fe}$  and  $^{58,60}\text{Ni}$ .

We express the total gamma amplitude for a transition from a resonant state  $\lambda$  to a final state  $\mu$  as a sum of a compound plus a valence contribution

$$(\Gamma_{\lambda\gamma\mu}^{1/2})_{\text{T}} = (\bar{\Gamma}_{\gamma\mu}^{1/2})_{\text{CN}} + (\Gamma_{\lambda\gamma\mu}^{1/2})_{\text{VAL}}$$

The bar in the expression for the compound part means that the statistical model gives only an average value of the gamma width over a wide energy range containing many resonances.

The total radiative width will be:

$$\Gamma_{\lambda\gamma}^T = \bar{\Gamma}_{\gamma}^{CN} + \Gamma_{\lambda\gamma}^{VAL} + 2(\bar{\Gamma}_{\gamma}^{1/2})^{CN} (\Gamma_{\lambda\gamma}^{1/2})^{VAL}$$

where the interference term is included.

We calculated the compound nucleus part using the Brink-Axel model and the valence part using the optical model approach.

Experimental and calculated radiative widths for some resonances in  $^{60}\text{Ni}$  are shown in Fig. 1.

From the analysis of the results, we conclude that the fluctuations of the gamma widths for the various resonances might (and even should if the correlations between neutron and radiative widths are small as it is shown by the recent measurements) be explained terms of the statistical fluctuations of the compound component. A  $\chi^2$  distribution with an effective number of degrees of freedom

$$\nu_{\text{eff}} = \frac{\sum_{\mu} (\bar{\Gamma}_{\gamma\mu}^{CN})^2}{\sum_{\mu} (\bar{\Gamma}_{\gamma\mu}^{CN})^2}$$

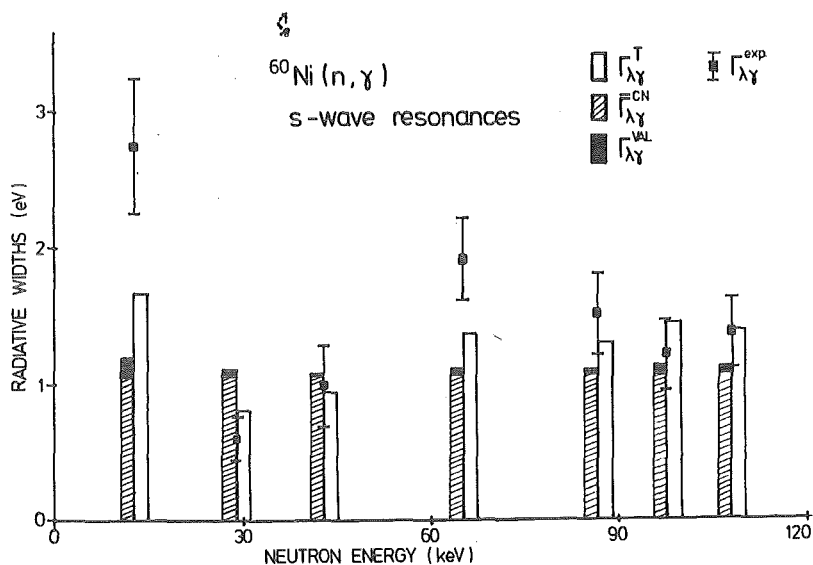


Fig. 1

Calculated and experimental (Ref. 5) radiative widths for several resonances in  $^{60}\text{Ni}$ .

and  $\bar{\Gamma}_{\gamma}^{\text{CN}}$  as mean value is able to reproduce the entire sample of experimental values. In addition, we calculated  $\xi_{\lambda} = (1 - \Gamma_{\lambda\gamma}^{\text{exp}}/\Gamma_{\lambda\gamma}^{\text{calc}})$  for the total ensemble of investigated resonances but also in this case the inclusion of a valence component seems not to be essential.

- (1) B.J. Allen, R.L. Macklin, J. of Physics G6 (1980) 381.
- (2) B.J. Allen, A.R. de L. Musgrove, Advances in Nuclear Physics (New York: Plenum Press), Vol. 10 (1978) 129.
- (3) F. Käppeler, K. Wisshak, L.D. Hong, private communication
- (4) H. Beer, R.R. Spencer, F. Käppeler, Z. Physik A294 (1978) 173
- (5) F. Fröhner, Proc. Conf. Neutron Data of Structural Materials, for Fast Reactors, Geel (1978) 138.

<sup>+</sup>Comitato Nazionale Energia Nucleare, Bologna, Italy

## 2. LASERSPECTROSCOPY

### 2.1 Isotope Shifts and Hyperfine Structure of the $4s^2 \ ^1S_0 - 4s4p \ ^1P_1$ Transition in Calcium Isotopes by Laserspectroscopy\*

A. Andl, K. Bekk, S. Göring, A. Hanser, G. Nowicki<sup>+</sup>, H. Rebel,  
G. Schatz, and R.C. Thompson

Kernforschungszentrum Karlsruhe, IAK II

Isotope shifts and hyperfine structure splittings of the CaI resonance line ( $4s^2 \ ^1S_0 - 4s4p \ ^1P_1$ ,  $\lambda = 422.7$  nm) have been measured for all calcium isotopes between  $^{40}\text{Ca}$  and  $^{48}\text{Ca}$ , including the short-lived isotope  $^{47}\text{Ca}$  ( $T_{1/2} = 4.54$  d). Resonance fluorescence was observed in a well-collimated atomic beam of calcium excited by a narrow band tunable CW dye laser. Combining the results with muonic X-ray data for the stable isotopes accurate values for the changes of mean square charge radii of the Ca nuclei are obtained, in addition to information on electromagnetic moments for the measured hyperfine structure constants. The influence of ground state correlations (represented by quadrupole and octupole mean square deformations) on the observed peculiar variation of the Ca charge radii is discussed as well as the relation to the droplet model and to a mixed  $(f_{7/2})^n$  model.

\*Phys. Rev. C (in press)

<sup>+</sup>Present address: Messerschmitt-Bölkow-Blohm GmbH, 8898 Schrobenhausen

### 2.2 High Resolution Measurements of Isotope Shifts in Lead

R.C. Thompson, M. Anselment, K. Bekk, B.A. Brown<sup>+</sup>, S. Göring,  
A. Hanser, G. Meisel, H. Rebel, and G. Schatz

Kernforschungszentrum Karlsruhe, IAK II

Isotope shifts in lead are of particular interest because they give information on the behaviour of nuclear radii in the region of the doubly magic nucleus  $^{208}\text{Pb}$ . We have made measurements on 14 lead isotopes (including one isomeric state) using the observation of resonance fluorescence from a well-collimated atomic beam. Light at the resonance wave length (283.3 nm) was generated by frequency-doubling the output of a ring dye-laser in a temperature-tuned ADA crystal; typically, the power obtained at the interaction region was 200  $\mu\text{W}$ . The fluorescence was monitored at 405.8 nm to avoid problems with scattered laser light. A second dye laser also running in the green provided an optical reference frequency;

this was stabilized to a 2 GHz cavity which in turn was stabilized to a frequency-stabilized He-Ne laser. The difference frequency of the two dye lasers was generated on a fast photodiode and analyzed by an r.f. frequency analyzer. This difference frequency was then stabilized to a preset value which was slowly scanned in order to obtain a spectrum.

An accuracy of order 4 MHz with samples containing 1 ng of the isotope of interest and an experimental line width of the order 40 MHz are routinely obtained. The samples were all produced with the aid of an electromagnetic mass-separator in order to purify the isotope under study. Figure 1 shows a typical spectrum obtained from a sample which contained 700 pg of  $^{202m}\text{Pb}$  (half life 3.6 h). The peak corresponding to  $^{202}\text{Pb}$  can also be seen, along with some of the stable isotopes which were included in the sample for calibration purposes. With the apparatus refined so that the typical background count is about 10 Hz. We have been able to measure samples down to 50 pg ( $^{209}\text{Pb}$ ,  $^{212}\text{Pb}$ ).

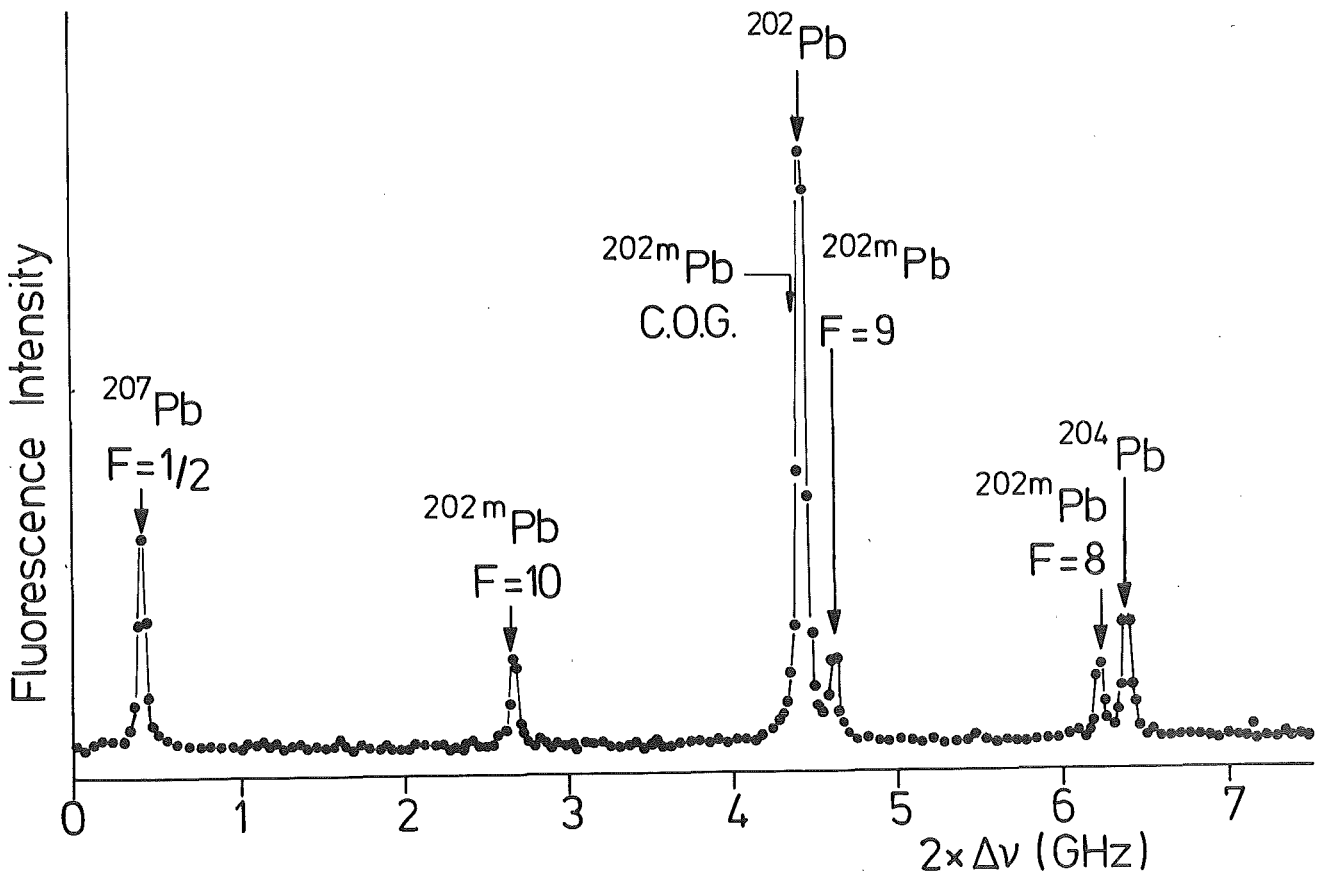


Fig. 1 Laser spectroscopy of the  $^{202m}\text{Pb}$ - $^{202}\text{Pb}$  isomeric shift

In order to extract changes in nuclear mean square charge radii, it is necessary to use some independent measurements of  $\delta\langle r^2 \rangle$  for the stable isotopes as a calibration. To do this, we have taken the results of Fricke et al. (1) which were obtained by a combined analysis of muonic X-ray and electronic scattering data. The so-called King plot procedure then enables one to derive values of  $\delta\langle r^2 \rangle$  for the unstable isotopes and also improved values for the stable ones. The results of this are displayed in Fig. 2. The error bars represent systematic errors arising from the calibration procedure. The errors arising from experimental uncertainty in the optical data are all less than  $\pm 0.003 \text{ fm}^2$ .

The variation of the ms radii shows following features

- a. with decreasing neutron number the radii vary more slowly than predicted by the liquid drop model (the  $A^{1/3}$  law with an overall radius parameter  $r_0 = 1.2 \text{ fm}$ ).

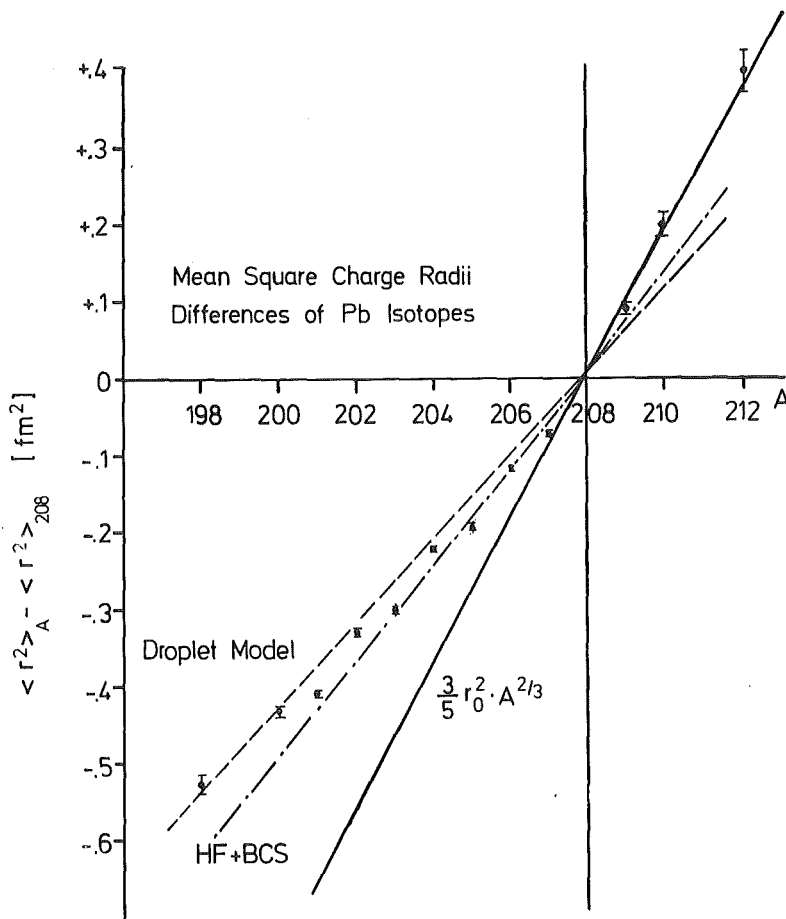


Fig. 2 Variation of the ms charge radii in Pb isotopes. The experimental results are compared with predictions from the droplet model and microscopic structure calculations.

- b. the overall trend is superimposed by an odd even staggering, which is well known in all mass regions, but never consistently and quantitatively explained.
- c. the remarkable jump after closing the neutron shell is correlated with the decreasing binding energy.

The refinement of the liquid drop model, the *droplet model* predicts the general trend of the radii fairly well. Simultaneously, the droplet model requires a *neutron skin* in  $^{208}\text{Pb}$ , a nonvanishing difference of the rms radii of the neutron and proton distributions. The required value of  $\Delta r_{\text{ms}} \approx 0.2$  fm is consistent with results from high energy proton and  $\alpha$ -particle scattering.

We have also calculated the isotope shift in the even-A Pb isotopes in a microscopic approach based on Hartree-Fock calculations using the Skyrme VI force with a constraint. The  $^{207}\text{Pb}$  single-hole energies are used and a BCS calculation of the ground states of  $^{198-206}\text{Pb}$  is performed. This gives a set of occupation probabilities for the valence hole orbits. Then the density of the given Pb isotope is defined in terms of these occupation numbers. The Hartree-Fock calculations implicitly include, in all orders, the monopole effects that are treated in perturbation theory of Speth (2), and no "effective" neutron radii are needed. The BCS occupation numbers are an approximation to the exact occupations which result from the shell-model diagonalizations. The results are also shown in Fig. 2. Generally, they underestimate the shifts consistently. This feature may indicate the necessity of including effects due to ground-state quadrupole (and higher order) fluctuations (deformation effects).

- (1) G. Fricke, H. Miska and D. Rychel, private communication
- (2) J. Speth, L. Zanich and P. Ring, Nucl. Phys. A232 (1974) 1

<sup>+</sup>Michigan State University, East Lansing, Mich. 48824, USA

## 2.2 Improved Calibration of Optical Isotope Shifts in BaI by Muonic X-Ray Data

H. Rebel and K. Bekk

Kernforschungszentrum Karlsruhe, IAK II

Shera et al. (1) published new data of X-ray measurements in muonic atoms of stable Ba isotopes  $^{134-138}\text{Ba}$ . The extracted ms charge radii enable

a check of the semi-theoretical values of the electronic factor  $F_i$  and of the specific mass shift as used in Ref. 2 ( $F_i = -3929$  MHz/fm<sup>2</sup> and  $S_i = 0 \pm N_i$  with the normal mass shift factor  $N_i = 31.45$  MHz) and provide an improved calibration of the optical isotope shifts in terms of nuclear radii. The consistency of both sets of data is confirmed by a King plot with the results of the stable isotopes, resulting in an electronic factor

$$F_i = -(3085.88 \pm 302.56) \text{ MHz/fm}^2$$

and practically vanishing total mass shift

$$M_i = N_i + S_i = 7 \pm 13 \text{ MHz}$$

implying a specific mass shift contribution of

$$S_i = -24 \pm 13 \text{ MHz.}$$

Table I Mean square charge radius differences extracted from measured optical isotope shifts

a. Calibration by measured muonic X-ray shifts (1)

b. Previous calibration by semitheoretical values of  $F_i$  and  $S_i$  (2)

A	$\Delta v$ MHz	$\delta \langle r^2 \rangle^a$ fm <sup>2</sup>	$\delta \langle r^2 \rangle^b$ fm <sup>2</sup>
137	215.00	-0.071 (7)	-0.059 (4)
136	128.90	-0.041 (6)	-0.041 (8)
135g	260.90	-0.088 (11)	-0.079 (12)
135m	161.70	-0.056 (8)	-0.053 (12)
134	143.00	-0.051 (10)	-0.053 (16)
133g	249.90	-0.087 (14)	-0.084 (20)
133m	202.10	-0.071 (13)	-0.072 (20)
132	167.90	-0.062 (14)	-0.067 (24)
131	249.20	-0.089 (18)	-0.093 (29)
130	207.30	-0.077 (19)	-0.086 (33)
129g	312.30	-0.112 (23)	-0.117 (38)
129m	362.70	-0.128 (24)	-0.130 (38)
128	271.10	-0.100 (30)	-0.111 (42)
126	355.80	-0.130 (30)	-0.142 (51)
124	447.00	-0.163 (36)	-0.175 (60)
139	-473.00	0.154	
140	-1075.00	0.351 (39)	
141	-1505.30	0.491 (49)	
142	-2019.00	0.659 (65)	
143	-2493.00	0.813 (98)	
144	-3027.00	0.987 (98)	
146	-3893.00	1.270 (125)	

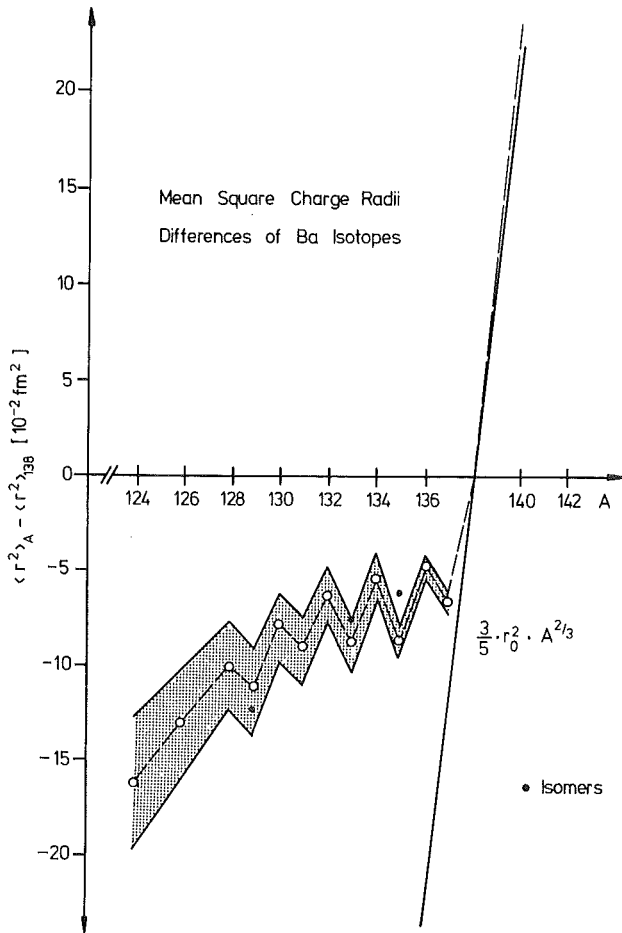


Fig. 1  
Differences of ms charge radii of Ba nuclei as extracted from optical isotope shifts and calibrated by muonic X-ray data.

Table 1 presents the variation of nuclear charge radii based on the experimental results given in ref. 2 ( $A > 138$ ) and ref. 3 ( $A < 138$ ). For convenience the previously given  $\delta \langle r^2 \rangle$  values are added in the table. The quoted errors include the errors from calibration (actually the dominating part). As displayed in Fig. 1 the new muonic X-ray data reduce the systematic uncertainties considerably.

- (1) E.B. Shera, H.D. Wohlfahrt, M.V. Hoehn, and Y. Tanaka, Phys. Lett. 11B (1982) 124
- (2) H. Rebel, K. Bekk, G. Nowicki, G. Schatz, Nukleonika 25 (1980) 145
- (3) R. Neugart, F. Buchinger, W. Klempt, A.C. Müller, E.W. Otten, C. Ekström, and J. Heinemeier, Hyperfine Int. 9 (1981) 151.

### 3. NEUTRINO PHYSICS

G.Giorginis, R.Gumbsheimer, L.Husson, H.Hucker,  
 S.Kiontke, R.Maschuw, P.Plischke, E.Remane, F.K.Schmidt,  
 R.Schulz, G.Spohrer, J.Wochele, B.Zeitnitz

Kernforschungszentrum Karlsruhe, IK 1 and University of  
 Karlsruhe

#### 3.1 Neutrino Physics at the Spallation Neutron Source SNS of the Rutherford Appleton Laboratories in Chilton, England

The SNS is based on an 800 MeV rapid cycling proton syn-  
 chrotron with an averaged current of 200  $\mu$ A protons. The machine  
 will produce pairs of 100 nsec long pulses with a gap of 230 nsec  
 in between. The repetition rate is 50 Hz. Besides for neutrons  
 the spallation target is also a source for neutrinos,  $\nu_\mu$ ,  $\bar{\nu}_\mu$  and  
 $\nu_e$  from the decay of the produced pions  $\pi^+$ . Monoenergetic  $\nu_\mu$ 's  
 with  $E_{\nu_\mu} = 27.79$  MeV and  $\bar{\nu}_\mu$ 's and  $\nu_e$ 's with a maximum energy of  
 $E_{\max} = 52.83$  MeV are produced with an average intensity of the  
 order of  $10^{14}$   $\nu$ /sec for each kind. The time structure for the  
 different types of neutrinos is shown in fig.1.

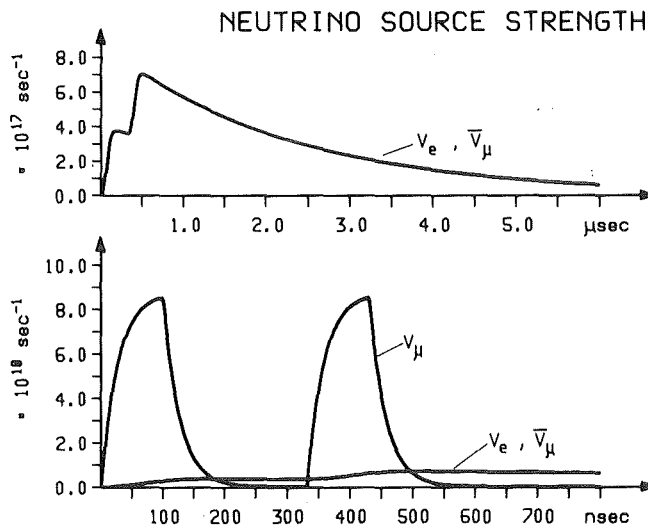


Fig.1: Time dependence of the neutrino source strengths at the  
 SNS spallation neutron source ( $t_p = 100$  nsec;  $\Delta t_p = 330$  nsec;  
 $I_p = 200 \mu\text{A}$ ;  $f = 50$  Hz)

This neutrino source gave rise to the proposal of a facility for neutrino physics at the SNS (ref.1). The main interest will be concentrated on

1. neutrino oscillation experiments
2. neutrino electron elastic scattering
3. neutrino hadron interaction experiments.

Thorough investigations on the background (2) - accelerator associated as well as from cosmic rays - led to the requirement of a separated neutrino cave 22 m below the SNS target to perform such experiments with a suitable detector system (fig.2). A multi-purpose detector is proposed consisting of a 50 ton segmented organic scintillator detector and another 50 ton "wide gap" liquid argon detector. For this system experimental sensitivities were investigated in detail for neutrino oscillation experiments and purely leptonic weak interaction processes i.e. neutrino electron scattering.

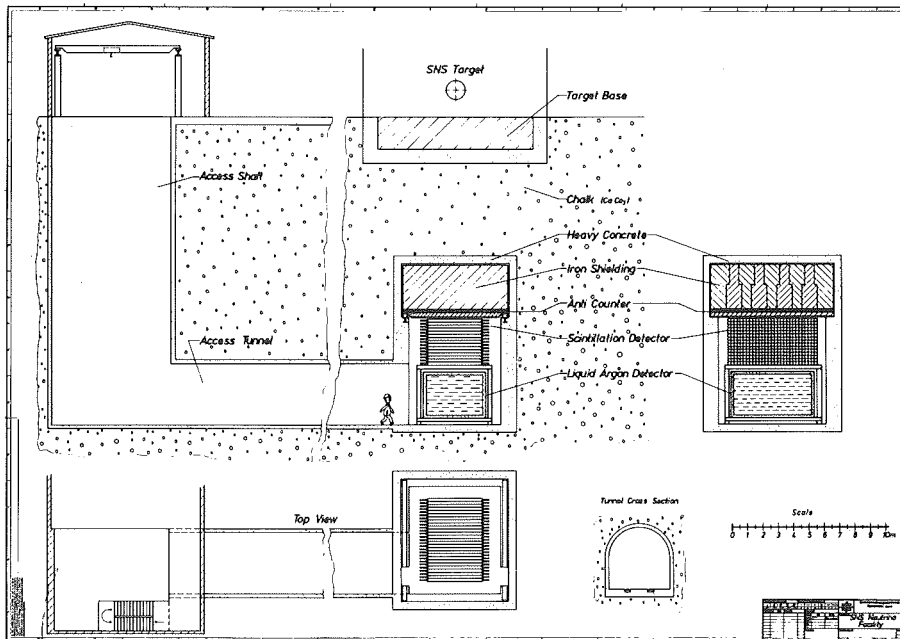


Fig.2: Proposed neutrino facility at the Rutherford SNS

For the neutrino electron scattering a measurement of the expected energy spectra of the recoil electrons (see 3.2) allows to deduce another value of the Weinberg angle from pure leptonic interaction at an energy of about 35 MeV where up to now this value has not been determined. The expected result for a 50 ton

liquid argon detector is shown in fig.3 as an ellipse in the  $g_V/g_A$  plane having assumed  $\sin^2 \theta_w = 0.23$ , together with the results from high energy and reactor neutrino experiments. In addition measurement of the  $\nu_e$ -e scattering allows to observe interference between neutral current and charged current weak interaction. The difference in the counting rates for no interference being present compared to the assumed interference from the standard Weinberg Salam model, is an 80% effect.

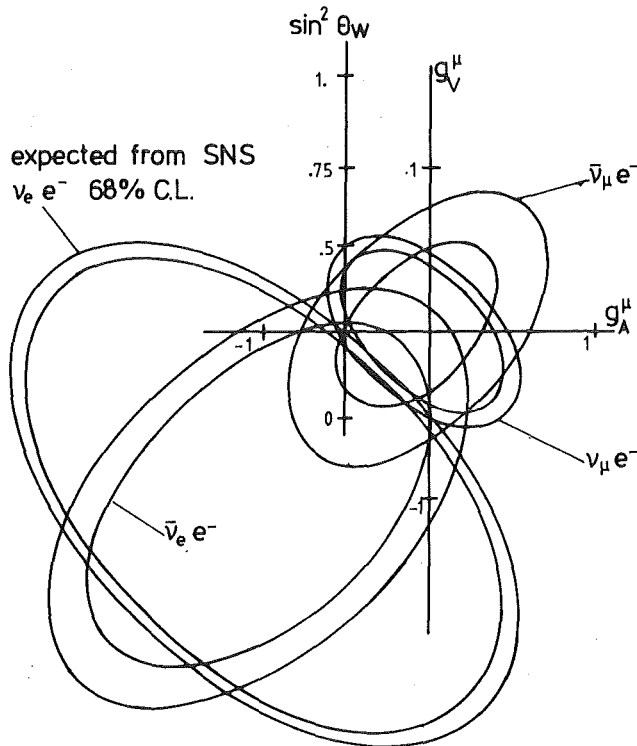


Fig.3: Expected 68% confidence ellipses in the  $g_V^\mu/g_A^\mu$  plane for the proposed  $\nu_e$ - $e^-$  total cross section measurement at SNS, together with results from other  $\nu$ -e scattering experiments

The presence of different kinds of neutrinos and the associated time structure allows to observe neutrino oscillations  $\nu_\mu \leftrightarrow \nu_e$  and  $\bar{\nu}_\mu \leftrightarrow \bar{\nu}_e$  simultaneously making use of the inverse  $\beta$ -decay processes  $\nu_e + {}^{12}\text{C} \rightarrow e^- + {}^{12}\text{N} \rightarrow e^- + e^+ + {}^{12}\text{C}$  and  $\bar{\nu}_e + {}^1\text{H} \rightarrow e^+ + n$ .

The oscillation  $\nu_\mu \leftrightarrow \nu_e$  can be observed independent from the actual  $\nu$ -flux defining an asymmetry for the observation of

$\nu_e$ 's during beam on and beam off time making use of the time structure of the  $\nu_\mu$ 's (see fig.1). This asymmetry for a 50 ton organic scintillation detector is plotted versus the square of the neutrino mass difference  $\delta m^2$  for the assumption of different mixing angles thus representing the experimental sensitivity to oscillations  $\nu_\mu \leftrightarrow \nu_e$ .

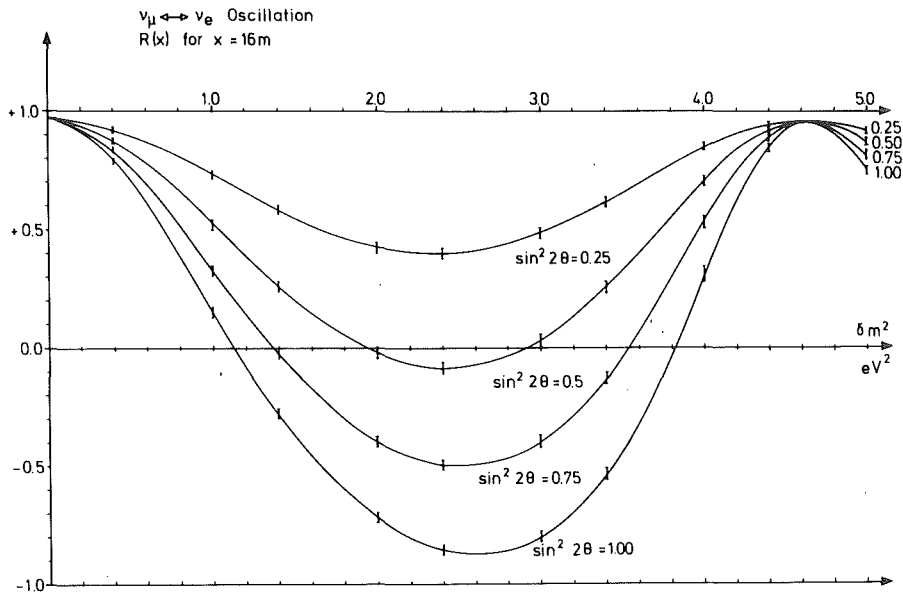


Fig.4: Asymmetry of  $\nu_e$ -counting rates during and after beam on time

References

- (1) R.Maschuw, B.Zeitnitz  
Neutrino Physics at the Pulsed Spallation Source SNS  
KfK 3362 (1982)
- (2) Calculations where carried out in collaboration with  
T.A.Gabriel, R.A.Lillie and R.L.Children, ORNL

### 3.2 Neutrino induced Reactions in a Liquid Argon Detector

For the neutrino experiment at the Rutherford Spallation Neutron Source (SNS) a 50 ton Liquid Argon Detector (LAD) has been proposed to measure elastic  $\nu_e - e^-$ ,  $\nu_\mu - e^-$  and  $\bar{\nu}_\mu - e^-$  scattering<sup>1)</sup>. The "inverse beta decay":  $\nu_e + {}^{40}\text{Ar} \rightarrow e^- + {}^{40}\text{K}^+$ , though of great interest for itself, causes a serious background for the elastic scattering process. The LAD which is essentially an ionization chamber provides an energy resolution  $< 10\%$  and a granularity of 5 - 10 mm. Simultaneously measuring energy and angle of the electron should allow to separate the  $\nu - e^-$  processes from other reactions. We therefore investigated the angular distribution of the recoil electrons from  $\nu_e - e^-$  scattering as well as from the inverse beta decay.

The elastic scattering cross section was calculated from the Weinberg Salam model. Calculations for the inverse beta decay were carried out by S.Furui<sup>2)</sup> in collaboration with our group. Three reaction modes were taken into account: Fermi transition to the 4.38 MeV isobaric analogue state (30% of total cross section), Gamow-Teller transitions (53%), and first forbidden processes (17%). Energy dependent absolute cross sections were obtained from a statistical model. Angular distributions resulted from microscopic calculations.

Due to relativistic kinematics, electrons from  $\nu - e^-$  scattering are strongly forward peaked. Fig.1 shows the angular distribution of recoil electrons with energies  $> 10$  MeV which are restricted to angles less than  $16^\circ$ , evaluated for the  $\nu_e$  spectrum from SNS. With a mean neutrino flight path of 20 m, a total amount of 150  $\nu_e - e^-$  events with  $E_e > 10$  MeV would be obtained during one year of full beam intensity. The dashed curve in fig.1 corresponds to the inverse beta decay. As one cannot distinguish between forward and backward directions, the counting rates for angles  $\theta$  and  $\pi - \theta$  have been added up, resulting in a nearly isotropic angular distribution for all energies. During 1 fyear, a total of 5000 events is expected for the inverse beta decay.

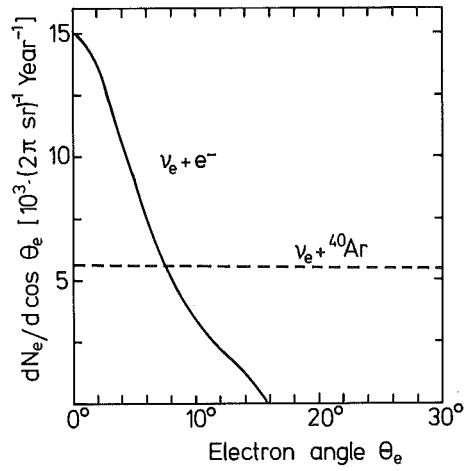


Fig.1: Angular distribution of electrons in LAD with  $E_e > 10$  MeV

In fig.2, the same data are shown for selected electron energies. Dashed lines within the  $\nu_e - e^-$  spectra indicate the nearly isotropic angular distribution of  $\nu_e + {}^{40}\text{Ar}$ , the varying height reflecting the energy spectrum of electrons from this reaction.

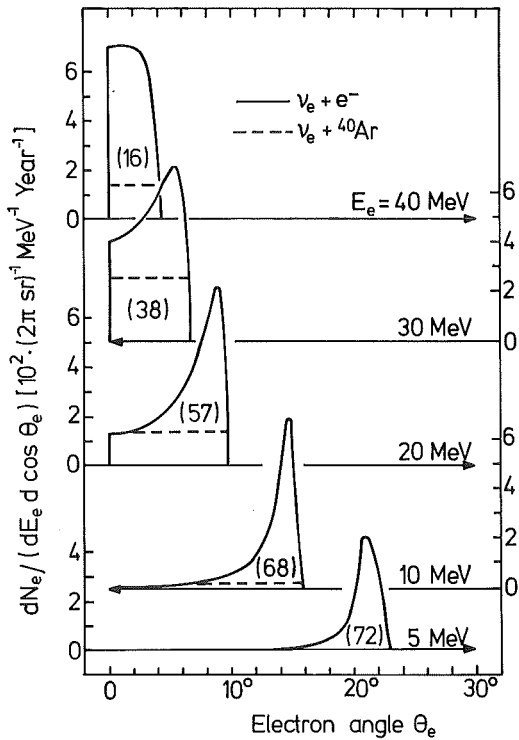


Fig.2: Angular distribution of electrons in LAD for different energies  $E_e$

Due to the narrow angular distribution of electrons from  $\nu_e - e^-$  scattering at a given recoil energy, the double differential data allow for a good separation of both kinds of reactions. This method is limited by counting statistics. The numbers in brackets within distributions in fig.2 denote the total event rate for  $\nu_e - e^-$  with recoil energies of  $E_e \pm 5$  MeV during one full beam year at SNS.

### References

- (1) R.Maschuw, B.Zeitnitz  
Research Proposal for Neutrino physics at SNS  
KfK 1982
- (2) S.Furui  
Inelastic Neutrino Reaction on  $^{40}\text{Ar}$   
University Tübingen, private communication, 1982

### 3.3 Prototype Development of a Neutrino Scintillation Detector

In the neutrino detector system a 50 ton organic scintillator detector simultaneously serves as target and detector for  $\nu$ -induced reactions on carbon and hydrogen nuclei. For the identification of these reactions good energy resolution and timing properties are more important than high granularity. One line followed in the prototype development is therefore the construction of a large liquid scintillator tank with optical segmentation. This is done by totally reflecting sheets forming optical bars with cross section of 15 cm x 15 cm or 20 cm x 20 cm and a length of 350 cm. Spatial resolution of about 10 cm is provided by time difference measurement with photomultipliers at each end of each segment.

Fig.1 shows a scintillation test vessel of 350 cm length. It contains a totally reflecting bar with 17 cm x 17 cm cross section formed by tightly glued thin double sheets of lucite with black paper in between. First tests with different photomultipliers and optical couplings are under way with this test modul filled with mineral oil based scintillator NE 235.

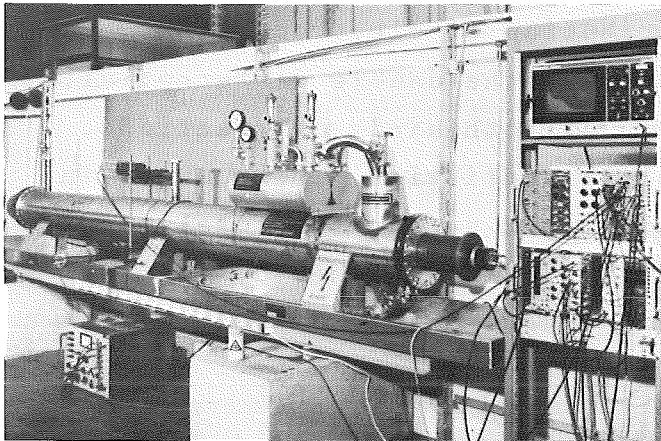


Fig.1: Scintillator test vessel

### 3.4 Prototype Development of a liquid Argon Neutrino Detector \*

For measurement of the purely leptonic neutrino electron elastic scattering in the energy range up to 50 MeV the track and the energy of the recoil electrons must be determined precisely. Good timing properties would help for event identification. A liquid argon ionization chamber with a granularity of smaller than 1 cm would provide these features . To restrict the amount of electronic channels a wide gap solution with electron drift space of 7 cm will be tried to achieve.

A test modul has been built allowing to condensate pure argon gas into two different vessels (see fig.1). One will be

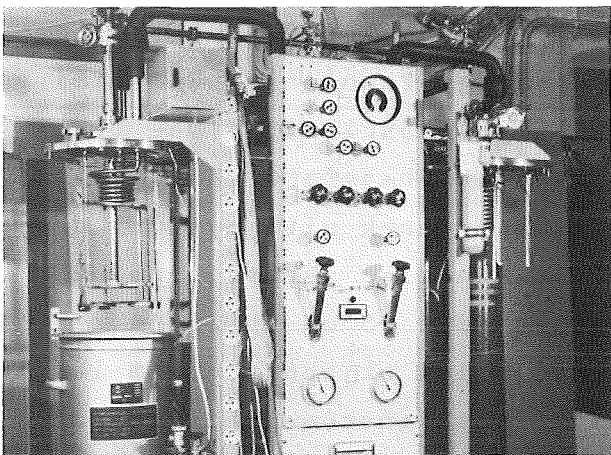


Fig.1: Liquid argon detector test device

used to investigate the properties of the liquid argon and different electrode configurations for variable drift spaces. The other is to investigate the timing properties of liquid argon as a scintillator viewed by a photomultiplier. First tests have just been started.

\* work is performed in collaboration with R.Dittman, J.Engler, B.Forstbauer, H.Keim, KfK, IK 1

4. INTERMEDIATE ENERGY PHYSICS

4.1 MUONIC ATOMS AND QED

4.1.1 The Energy Levels of Muonic Atoms<sup>\*</sup>  
E. Borie, G. A. Rinker<sup>+</sup>

Kernforschungszentrum Karlsruhe, IK II

The theory of muonic atoms is a complicated and highly developed combination of nuclear physics, atomic physics and quantum electrodynamics. In few other places in microscopic physics are such diverse branches so intimately intertwined and yet available for experimental verification. This review discusses in a pedagogical manner all the most important aspects of muonic atom theory, including a discussion of the approximations mode, and show in selected cases how the theory compares with experimental data.

The principal topics covered are: numerical methods, "model independent" interpretation of data on charge distribution, corrections for static nuclear moments, nuclear polarization, electron screening, relativistic recoil correction, radiative correlations (especially vacuum polarization) and a review of experimental tests of QED with muonic atoms.

<sup>+</sup>Los Alamos National Laboratory

<sup>\*</sup>Rev. Mod. Phys. 54(1982) 67-118

#### 4.1.2 Isotope shift measurements of muonic X-rays in $^{134,136,138}\text{Ba}$

W. Kunold, M. Schneider, L.M. Simons, R. Abela<sup>†</sup>, J. Wüst<sup>††</sup>

Kernforschungszentrum Karlsruhe, IK II

From muonic X-ray transition energies information about nuclear charge distribution parameters is obtainable. We have measured the muonic transition energies and evaluated the generalized "Barrett" moments (1) of the charge distribution for the three stable Ba-isotopes with  $A = 134, 136, 138$ . The results were used to evaluate the root mean square radius of each isotope in a model independent way, which can be used to calibrate optical isotope shift measurements.

The experiment was performed at the high intensity muon beam  $\mu\text{E1}$  at the Swiss Institute for Nuclear Research (SIN). In several measurements not only the  $2p \rightarrow 1s$ ,  $3d \rightarrow 2p$ ,  $4f \rightarrow 3d$  transitions, but also the weak, but important,  $2s \rightarrow 2p$  transitions were observed. During the measurement two target pairs ( $^{136}\text{Ba}/^{138}\text{Ba}$  and  $^{134}\text{Ba}/^{138}\text{Ba}$ ) are interchanged automatically to avoid systematic errors. The different spectra are calibrated with several radioactive sources positioned in front of the detectors.

The muonic X-ray transition energies for the three Ba-isotopes were determined in a least squares fit. With these transition energies generalized "Barrett" moments and the root mean square radii were obtained using the program MUON, taking several energy corrections into account. The most important of these were the nuclear polarization shifts from low lying and from high lying nuclear states since these are different for each isotope (2,3). The  $2p_{1/2}$  states were mostly affected with energy shifts of about 410 eV ( $^{138}\text{Ba}$ ), 610 eV ( $^{136}\text{Ba}$ ) and 910 eV ( $^{134}\text{Ba}$ ).

In order to extract information about the nuclear shape the formalism of the model independent "Barrett" moments has been used. Each transition determines

a special moment  $\langle r^k e^{-\alpha} \rangle$  of the charge distribution with  $\alpha=0.1161$  for the Ba-isotopes. Table I gives  $k$  and the equivalent radii  $R_k$  for the three isotopes.

Table I: Evaluated  $\bar{k}$ - and  $R_k$ -values for  $^{138,136,134}\text{Ba}$

Transition	$\bar{k}$	$^{138}\text{Ba}$	$^{136}\text{Ba}$	$^{134}\text{Ba}$
		$R_k$ (fm)	$R_k$ (fm)	$R_k$ (fm)
$2p_{3/2} \rightarrow 1s_{1/2}$	2.1936	6.18980(6)	6.18164(7)	6.17741(10)
$2p_{1/2} \rightarrow 1s_{1/2}$	2.1847	6.18910(9)	6.18110(9)	6.17687(12)
$3d_{1/2} \rightarrow 2p_{3/2}$	4.0571	6.32123(99)	6.32191(186)	6.32986(235)
$3d_{3/2} \rightarrow 2p_{3/2}$	4.0548	6.31653(317)	6.31598(382)	6.32013(747)
$3d_{3/2} \rightarrow 2p_{1/2}$	3.4909	6.28566(97)	6.28270(158)	6.28424(178)
$2s_{1/2} \rightarrow 2p_{1/2}$	1.4885	6.12885(100)	6.11601(100)	6.10943(193)
$2s_{1/2} \rightarrow 2p_{3/2}$	1.6192	6.14325(73)	6.13282(81)	6.12309(142)

For the first time the lack of a model independent method which permits a comparison of the muonic X-ray and optical measurements was overcome using a new description for the root mean square radius. With the results

$$\Delta \langle r^2 \rangle_{138-136} = - 0.0333(22) \text{ fm}^2$$

$$\Delta \langle r^2 \rangle_{138-134} = - 0.0379(28) \text{ fm}^2$$

the isotopic shifts of the root mean square radius  $\delta\langle r^2 \rangle$  could be compared with the frequency shifts of the optical measurements

$$\Delta\nu_{AA'} = M_i \frac{A-A'}{AA'} + F_i \delta\langle r^2 \rangle_{AA'}$$

M: mass effect factor (sum of the normal and the specific mass effect)

F: field effect factor.

Combining our  $\delta\langle r^2 \rangle$ -values with results of two laser spectroscopy groups (4,5) in a regression analysis, M and F could be determined:  $M = -4.1 \pm 14$  MHz and  $F = 3990 \pm 652$  MHz/fm<sup>2</sup>. The data for the differences of the mean square radii are very sensitive to the corrections applied, which are checked at present with corrections used by the LAMPF group (6) working in the same field.

#### References:

- (1) R.C. Barrett; Phys. Lett. 33b(1970)388
- (2) A. Christy, O. Häusser; Nucl. Data Tab. 11(1972)281
- (3) A.M. Kleinfeld, A. Bockisch, K.P. Lieb; Nucl.Phys. A 283(1977)526
- (4) A.C. Müller; Dissertation, Uni Mainz (1981)
- (5) K. Bekk, A. Andl, S. Göring, A. Hauser, G. Nowicki, H. Rebel, G.Schatz;  
Z. Physik A 291(1979)219
- (6) E.B. Shera, H.D. Wohlfahrt, M.V. Hoehn; Phys. Lett. 112B(1982)124

<sup>+</sup>Schweizerisches Institut für Nuklearforschung

<sup>++</sup>Institut für Physik der Universität Basel

#### 4.1.3 Measurement of the polarization of the 2p and 1s states in muonic atoms and the helicity of the muon in pion decay

W. Kunold, R. Metzner, L.M. Simons, R. Abela<sup>+</sup>, G. Backenstoss<sup>+</sup>

Kernforschungszentrum Karlsruhe, IK II

A knowledge of the polarization of excited states of muonic atoms is essential for experiments proposed to measure neutral current effects in muonic atoms (1). Also the study of the polarization during the muonic cascade offers a new way to investigate the atomic capture process, since the polarization is directly related to the initial angular momentum and to its possible alignment (2,3). This opens the possibility of determining the helicity of the  $\mu$  from the parity violating weak  $\pi \rightarrow \mu$ -decay by electromagnetic interactions, avoiding any other weak interaction processes such as  $\mu$ -decay or  $\mu$ -capture. A further aspect is the determination of the polarization of the ground state at the moment the muon reaches this state.

The depolarization mechanism of negative muons in muonic atoms has been studied extensively (4). Assuming a V-A weak interaction the muons produced in pion decay are fully polarized in the rest frame of the pion. The polarization of the muon beams available depends on the momentum band of the decay muons selected and amounts typically to about 80-90%. During the slowing down process the muon beam is not depolarized.

The polarization of the muonic atom states can be calculated by means of a cascade program. During the cascade of the muons from high excited states to the ground state, depolarization takes place due to the spin-orbit coupling. This interaction becomes important for muon states for which the fine structure-splitting  $\Delta E_{FS}$  is larger than the natural width. The polarization is reduced typically by 1/3.

We have determined the polarization of the muonic 2p states by the measurement of the sense and magnitude of the circular polarization of the x-rays emitted in the decay of these states to the ground state (5). In order to fully exploit

the resolving power of solid state detectors, transmission polarimeters were used. The polarimeters consist of a core with a length of 7 cm made from an alloy of iron and cobalt and covered with pure iron having a thickness of 1.5 cm. A magnetizing coil allows one to achieve a saturation field of 22.7 KGauss at 2.0 A. The analyzing power  $\eta$  of the polarimeters was determined by the quadratic Compton effect. A value of  $\eta = (1.9 \pm 0.3) \times 10^{-2}$  at 1.33 MeV was found. The analyzing power at the different muonic energies was calculated by scaling the results by the energy dependence of the polarization sensitive part of the Compton scattering cross section.

The measurements were performed at the  $\mu$ E1-channel at SIN. A momentum combination of  $P_{\pi} = 220$  MeV/c,  $P_{\mu} = 125$  MeV/c was chosen. The beam polarization was taken to the  $(81 \pm 2)\%$ . The angle between the beam direction and the polarization vector was found to be  $(27 \pm 6)^{\circ}$ . Four Ge(Li) coaxial detector with a volume of  $100 \text{ cm}^3$  and high resolution (typically 2.0 keV at 1.33 MeV) were used in order to detect the  $K_{\alpha}$ -muonic x-rays, which passed through the transmission polarimeters placed in front of them. The electronic set-up consisted of the usually employed slow-fast coincidence technique for the measurements of muonic x-rays.

The circular polarization of the muonic  $K_{\alpha}$ -lines of the two allotropic modifications of selenium, of cadmium, palladium and iodine has been measured. All the targets consisted of natural isotope mixtures.

The results are presented in table I. In the cases of cadmium and amorphous-selenium good agreement is found between the measured polarization of the 2p states and calculations. On the other hand there is a strange depolarization of the  $2p_{1/2}$  state in metallic selenium whereas no anomalous depolarization of the  $2p_{3/2}$  state was observed. This effect cannot be explained by nuclear effects. One has to search for effects occurring during the atomic cascade process. The measurements in palladium, where no polarization in the ground state is found, show normal values in the excited states. The ground state depolarization is caused by hyperfine effects in this state.

The results presented can be used to determine the helicity of the muon in  $\pi$ -decay. From a comparison of the values of the polarization of amorphous selenium and cadmium with calculated values (all given in the table) an average value for the  $\mu^{-}$  helicity of  $h_{\mu} = +(0.99 \pm 0.16)$  is found. This value is con-

sistent with the current theory of weak interactions.

	Polarization %			Polarization of $1s_{1/2}$ %	
	$2p_{1/2}$	$2p_{3/2}$	statistical error	derived <sup>b)</sup>	measured ( $\mu$ SR)
Selenium metallic	-6 $\pm$ 9	25 $\pm$ 6	3	16.7 $\pm$ 4	13.8 $\pm$ 2.7
Selenium amorphous	-34 $\pm$ 8	21 $\pm$ 6	3	17.05 $\pm$ 5	17.8 $\pm$ 2.5
Palladium	-29 $\pm$ 9	15 $\pm$ 4	2.6	13 $\pm$ 5	0 $\pm$ 3
Cadmium	-32 $\pm$ 9	18 $\pm$ 5	2.8	16 $\pm$ 5	18 $\pm$ 4 <sup>a)</sup>
Iodine	0.5 $\pm$ 8	9 $\pm$ 8	6	4.5 $\pm$ 6	

Table I: Results of the measurements

a) Ref. 4

b) Derived from the polarization of the  $2p_{1/2}$  and  $2p_{3/2}$  states.

- (1) J. Bernabeu, T.E.O. Ericson and C. Jarlskog, Phys. Lett. 50B(1974)467  
L.M. Simons, Helv. Phys. Acta 48(1975)141  
G. Feinberg and M. Chen, Phys. Rev. D10(1974)190
- (2) V.R. Akylas and P. Vogel, Hyp. Int. 3(1977)77
- (3) G. Ya. Korenman, Sov. J. Phys. 21(1975)298 and Hyp. Int. 7(1979)265
- (4) V.S. Evseev, Depolarization of negative muons and interactions of muonic atoms with the medium, in Muon Physics, Vol. III editors: V. Hughes and C.S. Wu
- (5) R. Abela, G. Backenstoss, W. Kunold, R. Metzner and L.M. Simons, to be published in Nuclear Physics.

<sup>+</sup>Institut für Physik, Universität Basel

## 4.2 HADRONIC ATOMS

### 4.2.1 Physics with antiprotonic atoms\*

L. Adiels<sup>+</sup>, G. Backenstoss<sup>++</sup>, I. Bergström<sup>+</sup>, P. Blüm, K. Fransson<sup>+</sup>,  
D. Gotta, R. Guigas, J. Hauth, H. Koch, Th. Köhler, M. Meyer,  
P. Pavlopoulos<sup>++</sup>, H. Poth, U. Raich, J. Repond<sup>++</sup>, B. Richter,  
M. Suffert<sup>+++</sup>, L. Tauscher<sup>++</sup>, J. Tröster and K. Zioutas<sup>++++</sup>

Kernforschungszentrum Karlsruhe, IK II

The method of using exotic atoms to study atomic, nuclear and elementary particle physics has been a well-established technique for some decades. Much information has been extracted from the X-ray spectra of muonic and hadronic atoms in the past. However, due to poor antiproton beams, little information could be obtained from  $\bar{p}$  atoms up to now. In the near future, intense  $\bar{p}$  beams of high quality will be available from LEAR at CERN. The cooled low-energy  $\bar{p}$  beams will allow a dramatic increase in the stop rate of antiprotons in thin targets.

Antiprotonic atoms can be investigated with high precision and due to the small amount material needed, even rare isotopes can be studied.

The basic observables are the energies, line widths, and intensities of radiative transitions from  $\bar{p}$  atoms and of  $\gamma$ -transitions from nuclear fragments. The spectroscopy of nucleons, light ions and annihilation products emitted after  $\bar{p}$  absorption also contains valuable information. Apart from the mass and the magnetic moment of the antiproton, which can be determined from the energies of  $\bar{p}$  X-ray transitions between states unperturbed by the strong interaction, a precise measurement of the X-ray intensities allows the reconstruction of the  $\bar{p}$  atomic cascade until absorption takes place. The energies, line widths and intensities of X-ray transitions between states where the strong interaction is significant can be related to the  $\bar{p}$ -nucleon scattering amplitude or a  $\bar{N}N$  potential. Since the  $\bar{p}$  bound in an atom is in a well defined state, the magnitude and the range of the annihilation potential can be studied. A comparison of strong interaction effects in isotopes of the same element may permit the  $\bar{p}p$ -to be disentangled from the  $\bar{p}n$  interaction. This information will pave the way for a better understanding and description of the  $\bar{N}N$  interaction at low energies. A satisfactory knowledge of the effective  $\bar{N}N$  interaction will allow one to use the  $\bar{p}$  as a sensitive probe for nuclear physics. Proton and neutron

distributions at the nuclear surface can be explored. Antiproton annihilation can excite the nucleus to extreme states, which can then be studied.

The goal of the experiment is first of all to perform a good statistics survey measurement of strong interaction effects in various antiprotonic atoms in order to establish a phenomenological description of the  $\bar{p}$ -nucleon interaction in nuclear matter. The measurement of relative and absolute X-ray intensities will allow one to establish a comprehensive model for the atomic cascade. The observation of prompt and delayed nuclear  $\gamma$ -ray spectra will allow a determination of the frequency of  $\bar{p}$  absorption on single nucleons and of  $\bar{p}p$  compared to  $\bar{p}n$  annihilation. In the next step particular nuclei will be studied in detail. Also nuclear density distributions will be studied.

The experimental set-up is shown in Fig. 1. An incident  $\bar{p}$  of 300 MeV/c or less will be identified in a beam telescope consisting of a few scintillation counters. In between the scintillators a variable moderator serves for the adjustment of the  $\bar{p}$  range. Thin targets are mounted on a frame which is guided by a ladder fixed in two tubes above and below the beam. With a remote controllable motor drive the various targets can be alternately exposed to the  $\bar{p}$  beam. In the horizontal plane around the target in-beam position five semiconductor detectors are arranged. According to the X-ray energies they have to measure, these are Si(Li), planar Ge, and large-volume coaxial Ge(Li) detectors. The energy and time signal of all fired X-ray detectors will be analysed with CAMAC ADCs and TDCs, which are read out by a fast microprocessor. The event will be stored in a two-dimensional array for each detector in a large memory of the microprocessor, which serves essentially as a fast multi-channel analyser with a big memory capacity. After a given time (typically a stretcher cycle) the contents of the microprocessor memory will be read out by a PDP 11, written on tape, and preanalysed. This data acquisition technique will allow us the digestion of very high  $\bar{p}$  rates ( $< 10^5$ ) without dead-time losses. As instantaneous count rates for all detectors we expect a maximum of 10 kHz.

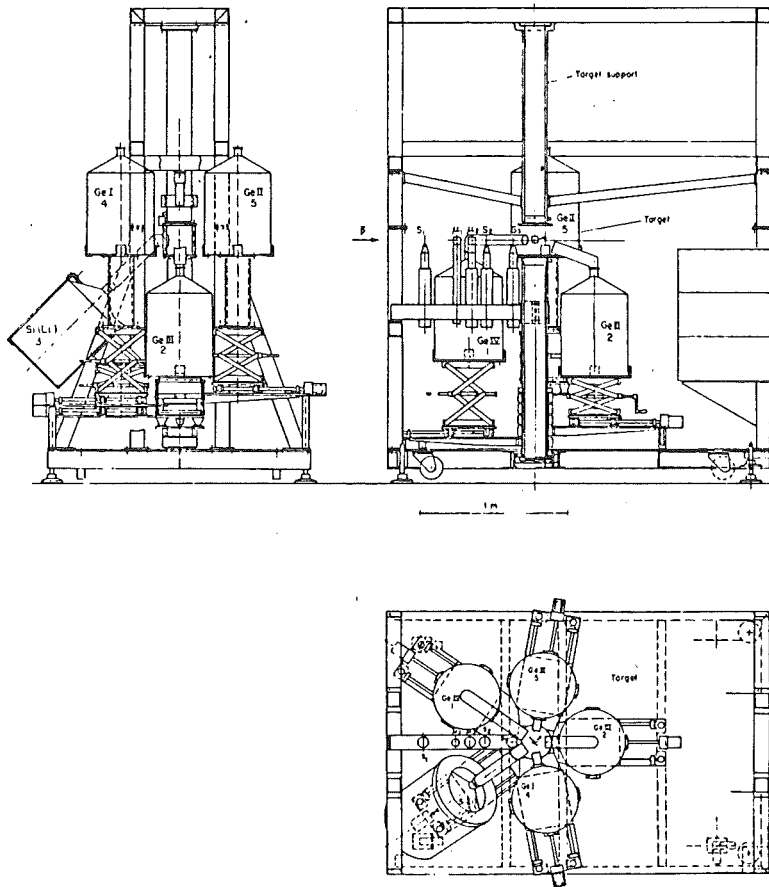


Fig. 1 Experimental set-up of PS176.  $S_1$ ,  $S_2$ ,  $S_3$  scintillation counters.  $\mu_2$ ,  $\mu_2$  variable moderators.

- \* Invited talk given by H. Poth at 3<sup>rd</sup> School of Physics of Exotic Atoms-Physics around LEAR with low energy cooled antiprotons, Erice, 9-16 May 1982
- + Research Institute for Physics, Stockholm, Sweden
- ++ Physikalisches Institut, Universität Basel, Switzerland
- +++ Basses Energies, CRN and University, Strasbourg, France
- ++++ Nuclear Reserach Institut, Thessaloniki, Greece.

#### 4.2.2 Possibilities of X-ray Spectroscopy with A Cyclotron Trap

P. Blüm, E. Borie, D. Gotta, H. Koch, W. Kunold, M. Schneider,  
L.M. Simons

Kernforschungszentrum Karlsruhe, IK II

The "Cyclotron Trap" is designed to form exotic atoms in dilute gases with pressures as low as a fraction of a Torr (1). High stopping densities are achieved by winding up the range curve in the field of a superconducting magnet. Therefore parameters of the electromagnetic (cascade), strong (shifts and broadening) and even weak interaction parity violation can be measured better because the atom-atom interaction and the absorption of the emitted X-rays and/or Auger-electrons are negligible.

The first experiment at SIN is the search for the  $2s \rightarrow 1s$  Auger transition in muonic Ne (208 keV) as a function of pressure. A comparison with the intensity of the K-X-rays yields the  $2s$  population. The detectors will be a pure Ge for the X-rays and the surface barrier detector for the Auger-electrons. At low pressures there will be a chance to see the  $2s \rightarrow 2s + 1\gamma$  M1 transition, which competes in an isolated atom only with the  $2s \rightarrow 1s$  Auger-,  $2s \rightarrow 2p + 1\gamma$  E1- and  $2s \rightarrow 1s + 2\gamma$  transitions. It is possible to get rid of the  $2p \rightarrow 1s$  E1-transitions in a coincidence equipment. The feeding transitions  $2p \rightarrow 2s$  (38.6 keV) and  $3d \rightarrow 2p$  (33.0 keV) are separated with the critical absorber technique using a  $^{57}\text{La}$ -foil (K-edge = 38.9 keV). If the  $2s \rightarrow 1s + 1$  M1-X-rays can be detected in a future experiment there will be a chance to look for a forward-backward asymmetry with respect to the  $2s$  polarization to study parity violating effects of the weak neutral current.

In another experiment the "Trap" will be used to measure the energies and intensities of the  $n \rightarrow 1$  (Lyman-),  $n \rightarrow 2$  (Balmer-) and if possible the  $n \rightarrow 3$  (Paschen) transitions of antiprotonic Hydrogen, deuterium and even tritium (2). For these experiments pressures below 30 Torr are essential to avoid Stark mixing and consequently get sufficient yields to study the strong interaction effects in the low-lying levels of the  $\bar{p}$  cascade. The X-rays of the Lyman- and Balmer series will be detected with a small Si(Li) and a high purity Ge detector. For the Paschen series a windowless Si(Li) will be necessary. A gas scintillation detector (GSD) of large which angle for coincidence measurements is also foreseen.

The complex s-wave scattering length is directly related to the width and shift of the Lyman transitions. On the other hand, spin dependence leads to a splitting (HFS) of the protonium ground state (3). The 2p annihilation width  $\Gamma_p$  is determined from the intensities of the  $n \rightarrow 2$  and the  $2p \rightarrow 1s$  transitions. A coincidence measurement between  $3p \rightarrow 1s$  (GSD) and a  $n \geq 3$  X-rays (windowless Si(Li) selects the transitions, which populate the 3p level and therefore the comparison of the intensities yields the 3p annihilation width  $\Gamma_{3p}$ . The ratio  $\Gamma_{2p}/\Gamma_{3p}$  tests the scaling law for  $\Gamma_{np}$ , i.e. the assumptions about the radial part of the wave function (4). The systematics of the observed intensities as a function of pressure (1-300 Torr) and the comparison of  $\bar{p}p$  and  $\bar{p}d$  will give a lot of (indirect) information about the processes in the upper intermediate part of cascade ( $n \geq 8$ ) as well as the  $\bar{p}n$  interaction at threshold (3,5).

Using the critical absorber technique X-ray energies can be measured very precisely whenever an absorption edge in the neighbourhood of the examined transition exists. Additionally lines close together are separated by absorber materials which have their absorption edges in between. Thus, the higher Lyman- and Balmer transitions and the Paschen-transitions may be resolved as well as a possible HFS of the  $\bar{p}\bar{p}(\bar{p}d)$  ground state.

- (1) P. Blüm, E. Borie, D. Gotta, R. Guigas, H. Koch, W. Kunold, M. Schneider, L.M. Simons: SIN proposal R-81-02.1
- (2) P. Blüm, D. Gotta, R. Guigas, H. Koch, W. Kunold, M. Schneider, L.M. Simons: CERN-proposal PS 175/1980
- (3) V.E. Markusin: ITEP-65, Moscow preprint 1980
- (4) W.B. Kaufmann and H. Pilkuhn: Phys. Rev.C17(1978)215
- (5) E. Borie: TKP 79-20, Universität Karlsruhe  
Contribution to Erice Workshop on Antiproton Physics, May 1982.

4.2.3 Vacuum Polarization and Spin-Orbit Splitting  
in Antiprotonic Atoms

E. Borie, Kernforschungszentrum Karlsruhe, IK II

Precise measurements of the energies of X-ray transitions in antiprotonic atoms at LEAR will require similarly precise calculations of all electromagnetic effects in order to be able to analyse the data for measurements of the antiproton's mass and magnetic moment or in order to be able to extract accurate hadronic shifts and widths. In the case of antiprotonic atoms, the most important QED correction is vacuum polarization. Since the antiproton has a large anomalous magnetic moment, the standard Dirac equation is not the best lowest order equation. Furthermore, relativistic recoil corrections will be more important for antiprotonic atoms than is the case for other exotic atoms. In fact, for the lightest nuclei, it will be necessary to use a two body formalism which treats the antiproton and the nucleus on an equal footing. However for the case of heavy nuclei ( $A \geq 10$ ) it turns out that a modified version of the Dirac equation, including the effect of the anomalous magnetic moment gives sufficiently accurate results. The coupled radial equations can be solved using a modified version of standard programs which were developed for use in the analysis of muonic X-rays <sup>1)</sup>. Vacuum polarization and relativistic recoil corrections are easily calculated numerically. The results can be summarized as follows: The Ühling contribution to the vacuum polarization must be included in the unperturbed problem. Using perturbation theory gives rise to an error of about 15 eV in the binding energy of the  $n = 10$ ,  $l = 9$  state of antiprotonic lead (out of a total binding energy of 1.68 MeV and VP correction of 6.4 keV). The influence of vacuum polarization on the wave functions and on the potential gives rise to a change of about 1% in the fine structure splitting. Effects of this size will be easy to measure at LEAR.

1) G.A. Rinker, Comp. Phys. Comm 16 (1979)221

E. Borie, G.A. Rinker, Rev. Mod.Phys. 54 (1982)67

#### 4.2.4 Pressure Dependence of X-Ray Yields in Protonium\*

E. Borie, Kernforschungszentrum Karlsruhe, IK II

The cascade calculations for the atomic  $\bar{p}p$  system presented in an earlier paper (1) have been extended over a wider range of target pressures and with some minor improvements in the input data and mechanisms for collisional deexcitation. The processes involved. Stark mixing, annihilation, chemical (or Coulomb) deexcitation, Auger and radiative transitions have been described in (1) and references therein. For the present calculation we took  $\Gamma_{1s} = 700$  eV,  $\Delta E_{1s} = 1100$  eV,  $\Gamma_{2p}(\text{ann})/\Gamma_{2p}(\text{rad}) = 10$  or  $75$ , atomic kinetic energy  $1$  eV, stark mixing rate multiplier =  $2$ . At low pressures the X-ray yields are not very sensitive to any parameter except  $\Gamma_{2p}(\text{ann})/\Gamma_{2p}(\text{rad})$ . Some typical results are shown in Figs. 1 and 2. Fig. 1 shows  $K_{\alpha}/K_{\text{tot}}$ , which decreases from about  $0.9$  at very low pressures to less than  $0.05$  in liquid hydrogen. The range of values displayed in these curves indicates the rather weak sensitivity of this result to assumptions about the deexcitation mechanism early in the cascade, velocity of the  $\bar{p}p$  atom, exact value of stark mixing rate, etc. Results calculated using other values of the adjustable parameters are similar. In liquid,  $K_{\alpha}/K_{\text{tot}}$  depends only on the annihilation width of the  $2p$  state. Most of the K X-rays are emitted in the transitions  $4-1$ ,  $5-1$ ,  $6-1$  in this case. The total yield of K X-rays depends strongly on  $\Gamma_{2p}(\text{ann})$  and is never larger than  $10\%$ . The yield of L X-rays approaches  $90\%$  at pressures below about  $20$  Torr but decreases rapidly as the pressure is increased. Of particular interest is the percent of  $\bar{p}p$  atoms annihilating from a  $p$ -state. Results are shown in Fig. 2. If  $\Gamma_{2p}(\text{ann}) = 30$  meV this remains rather large ( $>40\%$ ) even in liquid hydrogen. A smaller total  $p$ -state annihilation probability ( $15-20\%$ ) is most easily obtained by reducing  $\Gamma_{2p}(\text{ann})$  to  $4$  meV, the experimental lower limit (2). The uncertainties in the cascade calculations will be substantially reduced once this quantity has been measured. The appropriateness of using spinaveraged shifts and widths, as well as the possibility of velocity changes during stark collisions (or collisions associated with collisional deexcitation) require further investigation.

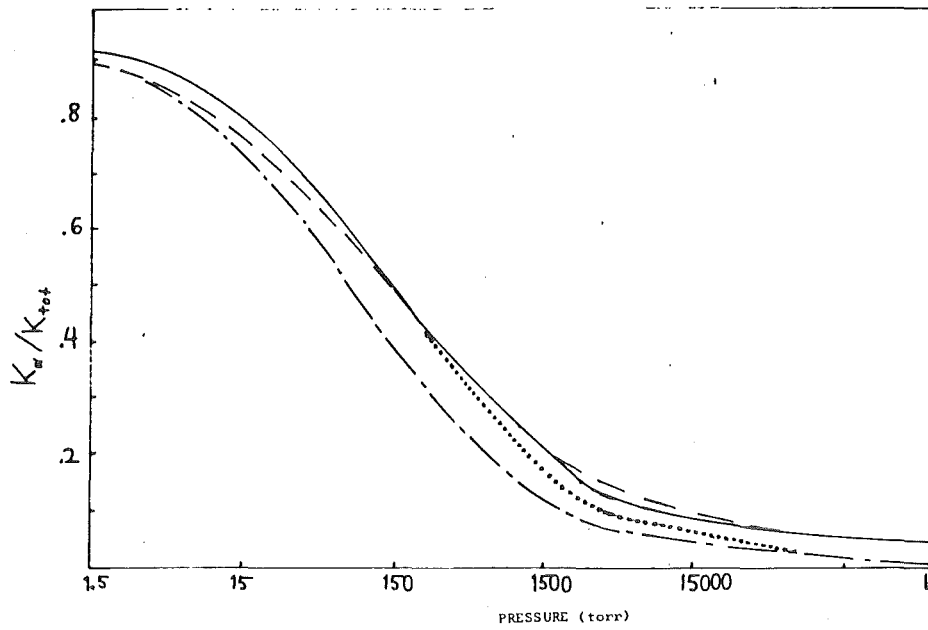


Fig. 1.  $K_\alpha/K_{tot}$  as function of pressure for protonium. Solid curve: Coulomb deexcitation,  $\Gamma_{2p}=4\text{meV}$ ; dashed curve: chemical deexcitation,  $\Gamma_{2p}=4\text{meV}$ ; dot-dash curve: chemical deexcitation,  $\Gamma_{2p}=30\text{meV}$ ; dotted curve: Coulomb deexcitation,  $\Gamma_{2p}=30\text{meV}$ .

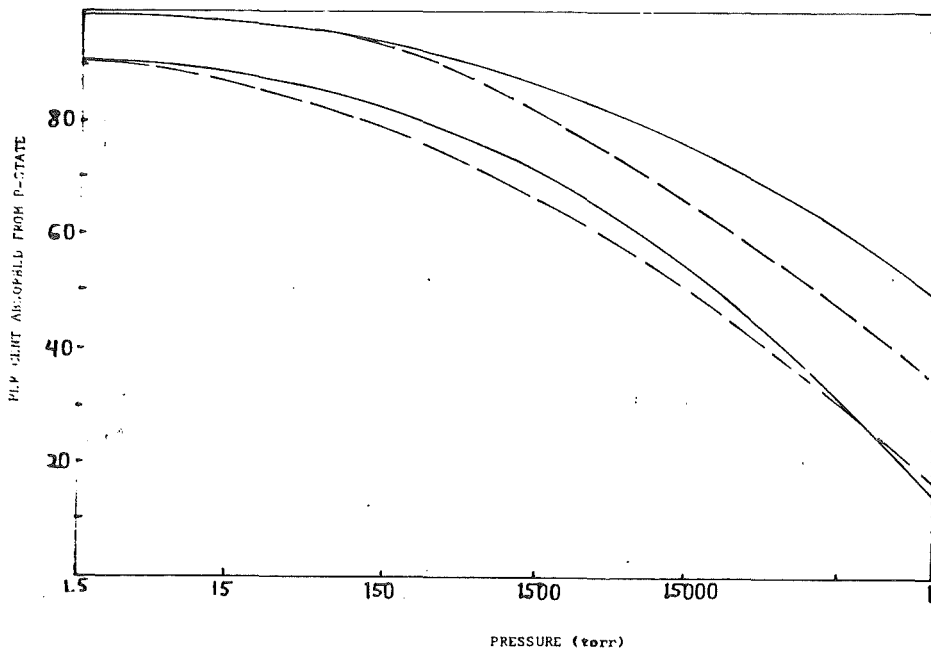


Fig. 2. Percent of  $\bar{p}p$  atoms annihilating from a p-state as a function of pressure. Solid curves: Coulomb deexcitation; dashed curves: chemical deexcitation. The upper curves correspond to  $\Gamma_{2p}=30\text{ meV}$ , the lower ones to  $\Gamma_{2p}=4\text{ meV}$ .

- (1) E. Borie, M. Leon, Phys. Rev. A21 (1980) 1460
- (2) E.L. Auld et al. Phys. Lett. 77B (1978) 454

### 4.3 PION NUCLEUS INTERACTION

#### 4.3.1 Coulomb-Nuclear Interference of $\pi^{\pm}$ $^{12}\text{C}$ scattering at 75 MeV

H. Degitz, U. Klein, W. Kluge, H. Matthäy

Last year measurements of the elastic scattering of 76.5 MeV  $\pi^{\pm}$  on  $^{12}\text{C}$  were performed at SIN for an angular interval between  $7.5^{\circ}$  and  $27.5^{\circ}$  in the laboratory system in order to cover the Coulomb-nuclear interference region, where the nuclear and the Coulomb force are of comparable magnitude. Thus the interference effects are maximum. In the case of isoscalar nuclei, the real part of the nuclear scattering amplitude  $f_N$  can in principle be extracted from the difference of the  $\pi^+$  and  $\pi^-$  scattering:

$$d\sigma^+/d\Omega(t) - d\sigma^-/d\Omega(t) \propto \text{Re } f_c^* f_N(t), \quad \text{if } f_N^- = f_N^+$$

$f_c$  being the Coulomb amplitude,  $f_N$  the nuclear amplitude,  $t$  the momentum transfer. It turns out, however, that the proper treatment of the pure Coulomb part and the pure hadronic part of the total amplitude calls for a realistic description of the Coulomb corrections. Therefore the data are compared with improved calculations of the Coulomb corrections<sup>1)</sup>. Both the magnitude and the sign of the real part as well as the imaginary part of the pure hadronic scattering amplitude can be determined.

The results should contribute to a better understanding of the appropriate Coulomb corrections. The knowledge of  $\text{Re } f_N$  and  $\text{Im } f_N$  is important for checking dispersion relations and the validity of various theoretical models describing pion-nucleus scattering. Furthermore they should serve as an input for dose calculations and the determination of LET-distributions, which are important for pion cancer therapy projects.

The main experimental problem is the large number of decay muons which are present at small angles. Hence our apparatus is particularly suited for their rejection. Incident as well as scattered particles are registered by three multiwire proportional chambers. In order to gain as much information as possible of the scattered particles, they are detected by a matrix of six 3 mm thick Si(Li) detectors (area  $50 \times 30 \text{ mm}^2$ ) to determine their energy losses, by a plastic scintillator to determine their time of flight and by a NaI(Tl) detector of  $15 \times 15 \times 15 \text{ cm}^3$  to determine their full energies.

Incident pions, muons and electrons are distinguished by a time-of-flight measurement relative to the RF signal of the cyclotron.

The data are presently evaluated. Figure 1 shows preliminary cross-sections of  $\pi^\pm$   $^{12}\text{C}$  elastic scattering at  $T_\pi = 75.6$  MeV. Final results will be presented at the end of 1982.

The present investigation is also regarded as a preparation of future measurements of the elastic scattering of  $\pi^\pm$  on protons at low energies and small angles and as a preparation of measurements with the new low energy magnetic spectrometer at SIN.

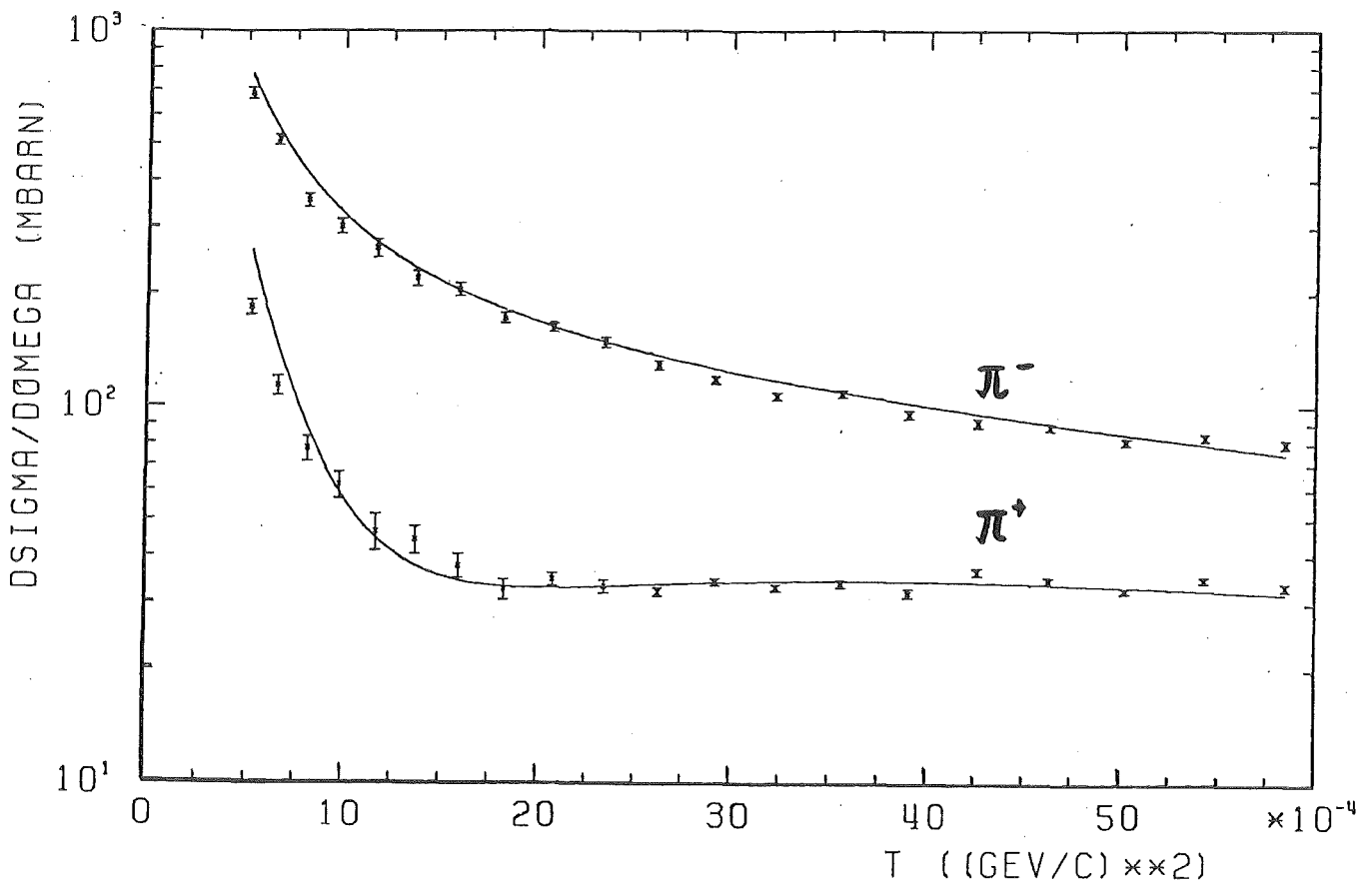


Fig. 1: Angular distribution of elastic scattering of  $\pi^\pm$  on  $^{12}\text{C}$  at 75.6 MeV and forward angles (between  $7.5^\circ$  and  $27.5^\circ$  in the laboratory system). The solid lines are calculations based on Ref. <sup>1)</sup>, taking into account an amplitude for Coulomb correlations.

<sup>1)</sup> J. Fröhlich, H.G. Schlaile, L. Streit, H. Zingl  
Z. Phys. A302 (1981)89

4.3.2 Energy spectra of charged particles emitted following the absorption of negative pions stopped in oxygen-containing organic compounds\*

D. Münchmeyer, H.I. Amols, G. Büche, W. Kluge, H. Matthäy,  
A. Moline<sup>+</sup> and H. Randoll

The flux of charged secondary particles with high linear energy transfer (LET) emitted following the absorption of negative pions on nuclei of tissue like carbon, oxygen, calcium in the star (or stopping) region makes pion beams attractive for the radiotherapy of cancer. LET-distributions of negative pion beams were measured, and also calculated on the basis of experimental energy spectra of secondary particles from  $^{12}\text{C}$  because of the lack of experimental oxygen data<sup>1)</sup>. From the LET distributions the relative biological effectiveness (RBE) and the oxygen enhancement ratio (OER) can be predicted by means of experimentally determined dependences of both RBE and OER on LET. Such information is a basic input for all future therapy planning with negative pions. In order to accomplish the therapy planning oxygen data are urgently needed. Therefore, we have continued our program of the investigation of pionic interactions with biologically relevant nuclei and present in this paper the energy spectra of charged particles (protons, deuterons, tritons,  $^3,^4\text{He}$ ,  $^6,^7\text{Li}$ ) emitted following the absorption of stopped negative pions on two carbon and oxygen-containing organic compounds, which are commercially available as thin foils: cellulose acetate and mylar (with stoichiometric C:O ratios of 2.5 and 1.5, respectively). The spectra are measured from 1.5 MeV up to the kinematical limit. Targets of different thickness are used (about 0.1 and 1.4 mm thick), in order to check the corrections to be made for particle and energy losses due to the finite target thickness. Thick target yields of biological and medical relevance are evaluated. The integrated particle yields for oxygen are determined. In particular the emission of heavier secondary particles like  $^3,^4\text{He}$  is significantly lower. The emission of lithium nuclei from oxygen is not observed. The shapes of the spectra as well as the mean energies of the emitted particles from the organic targets do not change with increasing oxygen content.

It is concluded, that the biological effectiveness of stopped pions is reduced in tissue compared with estimates based on the particle emission following the absorption of stopped pions in pure carbon. The data contribute to our understanding of radiotherapy with negative pions and have consequences for therapy planning codes being developed at present.

<sup>1)</sup>G. Büche and G. Przybilla, Nucl. Instr. Meth. 179 (1981)321

<sup>+</sup>SIN, Villigen (AG), Switzerland

\*Phys. Med. Biol. 27 (1982) 1131

#### 4.3.3 Energy spectra of charged particles emitted following the absorption of stopped negative pions in calcium\*

H. Randoll, H.I. Amols, W. Kluge, H. Matthäy, A. Moline<sup>+</sup> and D. Münchmeyer

The investigation of pion absorption at rest in nuclei is done in order to understand better the mechanism of the absorption process and the subsequent interaction of the emitted particles with the nucleus. In the present paper we show the energy spectra for protons, deuterons, tritons and <sup>3,4</sup>He nuclei between 2 MeV and the maximum possible energies emitted following the absorption of  $\pi^-$  at rest for a target of natural calcium with 0.022 g/cm<sup>2</sup> thickness. <sup>40</sup>Ca is chosen because possible different contributions of various reaction mechanisms to the  $\pi^-$  absorption process might be revealed by a comparison of the charged particle spectra of the thoroughly studied carbon with calcium data. The spectra show a monotonic decrease with energy in the preequilibrium domain and evaporation peaks for protons, deuterons and tritons. The shape of the deuteron and triton spectra are down by a factor of about 5 and 10, respectively, relative to the yields of the protons. The particularly low <sup>3</sup>He yields compared with the triton yields are due to kinematical shifts (different Q-values) and to absorption of  $\pi^-$  by  $\alpha$ -clusters (with a 10% probability<sup>1)</sup>). The proton data are compared with calculations of Chiang and Hüfner<sup>2)</sup>, who assume a ( $\pi^-$ , NN) absorption process which results in primary protons and protons from subsequent nucleon-nucleon interactions within the recoil nucleus. It turns out that the contribution of the primary protons and the protons from only one NN interaction reproduces the experimental data nicely in the intermediate preequilibrium domain.

- 1) F. Hachenberg, preprint Heidelberg 1982
- 2) H.C. Chiang and J. Hüfner, Nucl. Phys. A352 (1981)442

<sup>+</sup>SIN, Villigen (AG), Switzerland

\*Nucl. Phys. A381 (1982)317-329

#### 4.3.4 Kinematically complete measurement of the absorption of stopped pions in ${}^3\text{He}$ \*

D. Gotta, M. Dörr, W. Fetscher, G. Schmidt, H. Ullrich,  
G. Backenstoss<sup>+</sup>, K. Kowald<sup>+</sup>, I. Schwanner<sup>+</sup>, H.-J. Weyer<sup>+</sup>

Pion absorption on  ${}^3\text{He}$  offers the possibility of a kinematically complete experiment without prohibitive effort, i.e. via the coincident measurement of two of the three nucleons in the final state. Physical interest in such an experiment stems mainly from two sources: The possibility a) of studying quasifree absorption on a (T=1) pp-pair, whereas so far only absorption on a T=0 deuteron is known in some detail, and b) to investigate the role of absorption process which involve more than two nucleons in the initial step.

We have measured the reactions  $\pi^{-}{}^3\text{He} \rightarrow \text{np}$  and  $\pi^{-}{}^3\text{He} \rightarrow \text{nd}$  in a kinematically complete experiment with stopped pions. The results show a strong preference for collinear events. About three quarters of all absorption processes occur as quasifree absorption on np- or pp-pairs with a ratio of  $R = 10.1 \pm 1.5$  which is much higher than most theoretical predictions for s-absorption. The remaining quarter shows energy sharing among all three nucleons and is located in the final-state interaction regions. Branching ratios for all observed final states are given.

<sup>+</sup>Institut für Physik der Universität Basel

\*Phys. Lett. 112B (1982)129

4.3.5 Measurement of the total and partial K-X-ray yields for the pnn- and dn-reaction channels of the  $\pi^-$ -absorption in  $^3\text{He}$ .

M. Dörr, D. Gotta, G. Schmidt, L.M. Simons, H. Ullrich,  
G. Backenstoss<sup>+</sup>, W. Kowald<sup>+</sup>, I. Schwanner<sup>+</sup>, H.J. Weyer<sup>+</sup>

Pion absorption in the three-nucleon system  $^3\text{He}$  is of special interest in order to understand the absorption process in more complex nuclei. For reactions with stopped pions s- and p-interactions are possible and it is therefore important for distinguish between these two absorption types experimentally.

For this reason coincidence measurements between K-X-rays and emitted charged particles have been made and the percentage of absorption from the 1 s atomic orbit, the so-called K-X-ray yield has been determined. For the sum of all reaction channels the result was  $Y^k = (27+7)\%$ . This percentage has shown, however, to be different for different reactions channels: Whereas the partial K-X-ray yield for the nd-channel has been determined to be  $Y_d^k = (49+5)\%$  the respective number for the nnp-channel with protons above 20 MeV has been found to  $Y_p^k (T_p \geq 20 \text{ MeV}) = (29+4)\%$ .

<sup>+</sup>Institut für Physik der Universität Basel

4.3.6 Measurement of the ratio  $\frac{nn}{np}$  following the absorption of stopped  $\pi^-$  in  $^{16}_0$  \*

D. Gotta, T. Maier, G. Schmidt, H. Ullrich,  
G. Backenstoss<sup>+</sup>, W. Kowald<sup>+</sup>, H.-J. Weyer<sup>+</sup>

The quasifree absorption of pions by nucleon pairs is thought to be the basis mechanism of pion absorption in nuclei. Its dependence on the isospin of the absorbing pair is reflected in the ratio of correlated nn- and np-pairs following  $\pi^-$ -absorption; this ratio is expected to be of universal character for all nuclei. The numbers given so far in literature are controversial for both experimental and theoretical results.

We have determined this ratio by a simultaneous measurement of nn- and np-coincidences using position sensitive time-of-flight counters. Particle identification was made by anticounters and the known pulse-height versus time-of-flight relation for charged particles. The detection efficiency for neutrons has been determined using the Kurz Code.

In order to avoid contributions from other than quasifree 2N absorption processes, cuts in the recoil momentum and the missing mass have been applied for both reaction channels during data analysis.

Below the applied limits of the two restricted quantities, the resulting ratio was insensitive to these cuts within the statistical errors. The final result is

$$R\left(\frac{np \rightarrow nn}{pp \rightarrow np}\right) = 7,6 \pm 1,4$$

The error includes statistical as well as systematic uncertainties.

<sup>+</sup>Institut für Physik der Universität Basel

\*Part. of the Diplomarbeit T. Maier

4.3.7  $\pi^-$ -absorption in  ${}^7\text{Li}$  \*

M. Dörr, D. Gotta, J. Reich, G. Schmidt, H. Ullrich,  
G. Backenstoss<sup>+</sup>, K. Kowald<sup>+</sup>, H.-J. Weyer<sup>+</sup>

Two-particle emission following the absorption of stopped negative pions in  ${}^7\text{Li}$  has been measured at SIN with counters capable of detecting neutrons, protons, deuterons and tritons. As the counters are position sensitive, the complete momenta of these particles could be determined in the range  $150^\circ$  to  $180^\circ$  relative angle and above the thresholds of 17, 33, 41, and 45 MeV for n, p, d and t, respectively. In addition 6 NaI-counters have been used for the coincident detection of the (p  $\rightarrow$  1s)-X-rays and hence for the determination of events from the 1s pionic orbit.

Table 1 shows the observed coincidence rates for the measured channels as well as the respective percentage of 1s-absorption. The data are also available in the form of spectra for missing mass, recoil momentum, center-of-mass angle and relative angle of the two particles as well as in two dimensional spectra such as  $E_1$  versus  $E_2$ . They can be used to test current ideas about the occurrence of high energy composite particles in the process of pion absorption such as an initial 2N-absorption followed by pick-up and knock out reaction or cluster absorption.

	n	p	d	t
n	83,7 (56 $\pm$ 16%)			
p	4,9 (23 $\pm$ 6%)	0,002 (63 $\pm$ 22%)		
d	6,9 (37 $\pm$ 6%)	0,03 (45 $\pm$ 12%)	0,05 (36 $\pm$ 13%)	
t	3,9 (55 $\pm$ 10%)	0,08 (24 $\pm$ 8%)	0,23 (64 $\pm$ 8%)	0,17 (74 $\pm$ 10%)

Table 1: Observed coincidence rates for different particle combinations, normalized to 100 for the total sum. The neutron detection efficiency has been taken into account. The numbers in brackets give the percentage of 1s-absorption for the respective channel. The errors are only statical.

<sup>+</sup>Institut für Physik der Universität Basel

\*Part of the Diplomarbeit Jürgen Reich

#### 4.3.8 Pion Absorption on ${}^6\text{Li}$

G. Backenstoß<sup>+</sup>, M. Dörr, W. Fetscher<sup>++</sup>, D. Gotta, H. Koch,  
W. Kowald<sup>+</sup>, H. Ullrich, H.J. Weyer<sup>+</sup>

At the  $\pi\text{E}1$ -channel of SIN, we have measured the spectra of particles, which are emitted after absorption of stopped negative pions by  ${}^6\text{Li}$ .

Two particles are detected in coincidence by large, position-sensitive counters and their momenta are determined completely. The two particles may be any combination of n, p, d or t. The counters are able to detect events with any angle from  $150^\circ$  to  $180^\circ$  between the directions of the outgoing particles, the angular resolution being 1,5 degrees.

As shown by earlier measurements (1), most of the events have an angular correlation close to 180 degrees. The thresholds for the kinetic energy are 17, 21, 28, 32 MeV for n, p, d, t respectively. The energies are measured with a resolution of 2 to 3 MeV.

The high statistics of our measurement (about  $10^6$  events) allow for studying easily the dependence of the spectra on more than one parameter at the same time. Also, due to the precise and continuous measurement of the angular correlation, we could calculate spectra of the recoil momentum of the remaining nucleons with satisfactory resolution ( $\sim 17$  MeV/c).

Hence we obtained a survey over the kinematical conditions which are relevant for all the most important reaction mechanisms. These conditions permit one to draw conclusions on the reaction mechanisms themselves, at least to some degree. The essential results are:

The reaction  ${}^6\text{Li} (\pi, nn){}^4\text{He}$  dominates with about 80% and in general it is consistent with a quasi-free 2N-absorption model, as was also found in earlier work (1). Some reactions, however, are inconsistent with a simple 2N-absorption mechanism. These are reactions in which deuterons and tritons or generally more than two nucleons are emitted with high energy (i.e.  $\geq 20$  MeV). They contribute with about 17% to the total absorption events observed.

In all reactions, except the extremely weak  ${}^6\text{Li} (\pi^-, pp)4n$ , we observe a strong  $180^\circ$ -angular correlation, a fact that makes unlikely any true absorption mechanism on more than 2 nucleons, especially the quasi- $\alpha$  model from Kolybasov (2). For a number of reasons we could essentially preclude secondary scattering processes, in which after absorption on two nucleons,

one of the emitted nucleons scatters on nucleons of the residual nucleus. For example, we could give an upper limit for the knock-out of a proton by a "primary" neutron of  $\lesssim 0,5\%$  of all absorption events.

We support a reaction mechanism in which interactions of the "absorbing" two nucleons with the other nucleons of the nucleus take place coherently with the absorption, i.e. the absorption rate is influenced by the interaction.

This would explain e.g. why the observed energy distribution of the neutron in the process  ${}^6\text{Li}(\pi^-, \text{tn})\text{pn}$  is about 20 MeV higher than it would be in a quasi-free 2N-absorption process with secondary emission of the triton.

The interaction seems to depend strongly on the actual nuclear structure: thus we observe details in the spectra of  ${}^6\text{Li}(\pi^-, \text{dn})\text{pnn}$  which are very similar to those of  ${}^4\text{He}(\pi^-, \text{dn})\text{n}$ , which are described by several authors (3). It seems to be an effect of the  $\alpha$ -cluster structure in  ${}^6\text{Li}$ . On the other hand, the process  ${}^6\text{Li}(\pi^-, \text{dn})\text{t}$  shows a recoil momentum consistent with the  $\tau$ -t-cluster model recently in discussion (4).

As a "by-product" we observe structures which are consistent with the assumption of very broad d-n-resonances (or excited states of the triton) in the processes:

$$\begin{aligned}
 {}^6\text{Li}(\pi^-, \text{dn})\text{t}^* & \quad , \quad E_x \sim 12 \text{ MeV} \\
 {}^6\text{Li}(\pi^-, \text{tt}^*) & \quad , \quad E_x \sim 16,5 \text{ MeV} .
 \end{aligned}$$

- (1) R. Bassaleck et al., Phys. Rev. C19 (1979)1893
- (2) V.M. Kolybasov et al., Nucl. Phys. 14 (1972)418
- (3) C. Cernigoi et al., Nucl. Phys. A352 (1981)343
- (4) J.C. Bergstrom, Nucl. Phys. A327 (1979)458

<sup>+</sup>Universität Basel

<sup>++</sup>Now at ETH, Zürich

#### 4.4 NUCLEON-NUCLEON INTERACTION

##### 4.4.1 Measurements of the Differential Cross Section and Spin Parameters of the Reaction $pp \rightarrow \pi d$ between 500 and 600 MeV

A. Berdoz<sup>+</sup>, P. Chatelain<sup>+</sup>, B. Favier<sup>+</sup>, F. Foroughi<sup>+</sup>,  
 J. Hoftiezer<sup>++</sup>, S. Jaccard<sup>+++</sup>, S. Mango<sup>+++</sup>, T. Konter<sup>+++</sup>,  
 G.S. Mutchler<sup>++§</sup>, C. Nussbaum<sup>+</sup>, J. Piffaretti<sup>+</sup>, P. Walden<sup>+++§§</sup>  
 and Ch. Weddigen<sup>++</sup>

The reaction  $pp \rightarrow \pi d$  is one of the most important processes for pion production in the intermediate energy range. It is of basic interest from several points of view. Its understanding is essential for the interpretation of pion interaction between pions and nuclear matter, with respect to absorption and production. As an inelastic channel in  $pp$  scattering it may have considerable feedback to the elastic channel, in which peaked structures in spin correlated cross sections gave rise to speculations on possible existence of dibaryon resonances. These resonances are highly inelastic. Therefore if real, they should show up as resonance structures in the production amplitudes describing the  $pp \rightarrow \pi d$  reaction, in addition to the well known  $N\Delta$  resonant production mechanisms near 600 MeV.

The theoretical understanding of the  $pp \rightarrow \pi d$  reaction suffers from two basic problems: No unique reaction mechanism is predominant in the  $N\Delta$  resonant region. Different exchange terms interfere. In addition it is technically difficult to perform relativistic calculations taking into account sufficiently high angular momenta. The interpretation of experimental observables is very sensitive to such higher order contributions. Agreement between experimental data and theory to a level better than about 10% cannot be expected in the near future.

One way out of this problem is determine the most important production amplitudes directly from experimental data (1) and then to compare their energy behavior with theoretical predictions. Therefore high quality data are needed for different observables.

A first step in this respect was made by the NESIKA collaboration by measuring the unpolarized differential cross section

$$\begin{aligned} \left(\frac{d\sigma}{d\Omega}\right)_0 &= \frac{1}{32\pi} \sum \gamma_{2i} \cos^{2i}\theta && \text{(old notation (2))} \\ &= \frac{1}{4\pi} \sum a_{2i}^{00} P_{2i}(\cos\theta) && \text{(new notation (3))} \end{aligned} \tag{1}$$

The experiment was performed at SIN between 500 and 600 MeV. Preliminary results (4) were interpreted using a Breit-Wigner energy-dependent width approximation. Only initial singlet states were taken into account which are dominant in our energy region (fig 1). It can be shown that, within these approximations including complete data sets at adjacent energy regions, the important  $^1D_2$  amplitude shows only one resonance, which is consistent with the well known  $N\Delta$  resonance state in energy and width, thus excluding an extra  $^1D_2$  dibaryon resonance in this energy region.

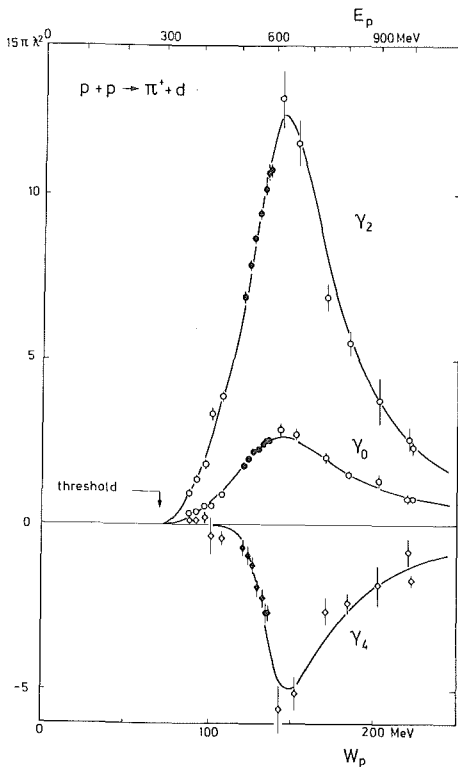


**Fig. 1:** Comparison of the NESIKA results (solid symbols) with data selected from other experiments. The fit to the expansion coefficients of  $(d\sigma/d\Omega)_0$  defined in Eq. 1 was obtained using a Breit-Wigner energy-dependent with approximation with initial singlet state amplitudes only (from ref. 1)).

In the past year these data were corrected for various experimental effects using, in part Monte Carlo simulation. These effects are pion decay, acceptance for decay muons, solid angle effects, multiple scattering, beam extension and divergence and three particle final state contributions. All these effects caused angle dependent corrections between .2 and  $2.3 \pm .3$  percent. Due to these corrections we can exclude a  $\cos^6\theta$  term within statistical precision (i.e.  $|\gamma_6|$  and  $|a_6^{00}| < 5$  and .05 mb respectively).

A second step of the NESIKA activity at SIN concerned the measurement of the analysing power

$$A_{y0} = \frac{1}{4\pi} \sum b_i^{y0} P_i^1(\cos\theta) / \left(\frac{d\sigma}{d\Omega}\right)_0 \quad (2)$$

in the same energy region. The  $b_i^{y0}$  coefficients give access to initial state triplet amplitudes. The large terms  $b_1^{y0}$  and  $b_3^{y0}$  are mainly due to an interference between the amplitudes of the initial states  $^1D_2$  and  $^3F_3$ .

In fig. 2 angular distributions of  $(\frac{d\sigma}{d\Omega})_0$  and  $A_{y0}$  are compared with theoretical predictions of NISKANEN (5) which are not the most recent but still the most complete. They may be representative for discrepancies between

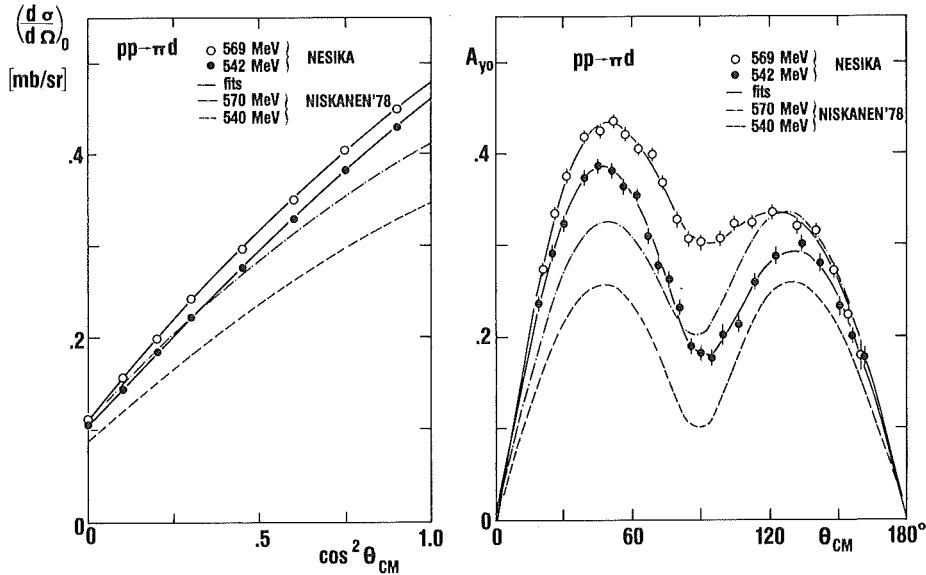


Fig. 2: Typical angular distribution for the unpolarized differential cross section  $(\frac{d\sigma}{d\Omega})_0$  and of the analysing power  $A_{y0}$  and comparison with predictions of NISKANEN (5)

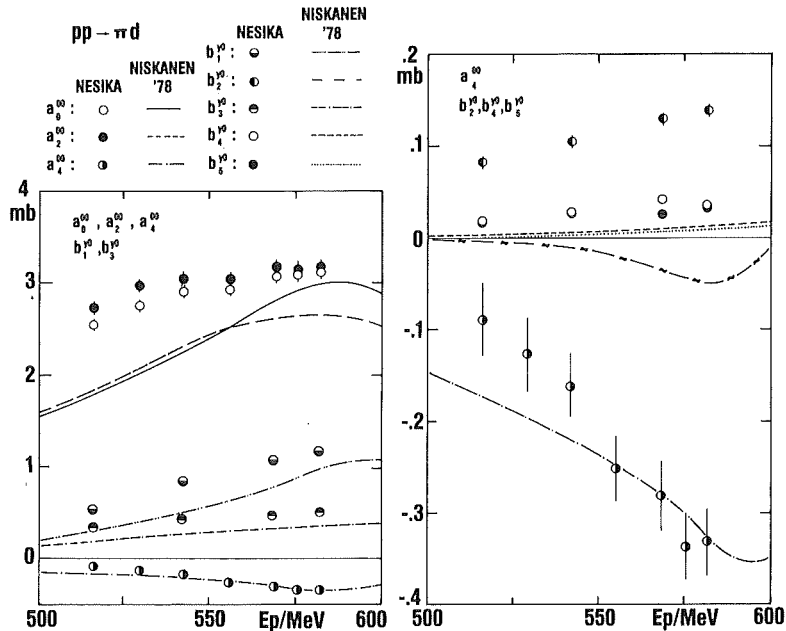


Fig. 3: Energy dependence of the expansion coefficients  $a_{2i}^{00}$  and  $b_j^{y0}$  defined in Eqs. (1) and (2). The results of our NESIKA results are compared with theoretical predictions of NISKANEN (5).

theory and experiment. The energy dependence of the coefficients  $a_{2i}^{00}$  (Eq.1) and  $b_j^{y0}$  (Eq. 2) deduced from our results are plotted in fig. 3 and again compared to an interpolation of the NISKANEN predictions. The highest order significant term for  $A_{y0}$  is  $b_5^{y0}$ , an upper limit for  $|b_6^{y0}|$  being about 10  $\mu$ b. These results will be compared with other experiments and theories in the near future.

A third experiment on the  $p \rightarrow \pi d$  reaction was performed by the NESIKA collaboration at SIN with polarized beam and target measuring angular distributions of the spin correlation coefficient

$$A_{xz} = \frac{1}{4\pi} \sum_i b_i^{yz} P_i^1(\cos\theta) / \left(\frac{d\sigma}{d\Omega}\right)_0$$

at three energies between 500 and 600 MeV. This spin correlation coefficient is the most difficult to measure with conventional coincidence techniques because of solid angle restrictions imposed by the technical structure of usual polarized targets. Therefore a special technique was developed which permits such measurements by detecting only the final state deuteron. From a physical point of view  $A_{xz}$  is of special interest, since it is complementary to  $A_{y0}$  in the sense that  $(A_{xz}(\theta) - iA_{y0}(\pi-\theta))$  is equal to a complex bilinear form of production amplitudes (1). The analysis of the  $A_{xz}$  is in progress.

- (1) Ch. Waddigen, Nucl. Phys. A312(1978)330
- (2) F. Mandl and T. Regge, Phys. Rev. 99(1955)1478
- (3) J.A. Niskanen, Proceedings of the 5th International Symposium on Polarization Phenomena in Nuclear Physics, Santa Fe, edited by G.G. Ohlsen et al. (AIP, New York, 1981) p. 62
- (4) J. Hoftiezer et al., Phys. Lett. 100B(1981)462
- (5) J.A. Niskanen, Phys. Lett. 79B(1978)190

+ Institut de Physique, Université de Neuchâtel, Neuchâtel, Switzerland  
 ++ Kernforschungszentrum Karlsruhe, Institut für Kernphysik und Institut für Experimentelle Kernphysik der Universität, Karlsruhe, West Germany  
 +++ Schweizerisches Institut für Nuklearforschung (SIN), Villigen, Switzerland

§ On leave from Rice University, Houston, TX 771, USA

§§ On leave from TRIUMPF, Vancouver, BC, Canada

4.4.2 The differential cross section for elastic proton-proton-scattering at  $90^\circ$  cm between 500 and 600 MeV \*

M. Chatelain<sup>+</sup>, B. Favier<sup>+</sup>, F. Foroughi<sup>+</sup>, J. Hoftiezer<sup>++</sup>,  
S. Jaccard<sup>+++</sup>, J. Piffaretti<sup>+</sup>, P. Walden<sup>+++§</sup>, C. Weddigen<sup>++</sup>

The proton-proton interaction at medium energies has been of topical interest in the past few years, especially because of observed anomalies in the cross section  $\Delta\sigma_L$  and  $\Delta\sigma_T$  which were interpreted as dibaryon resonances in several models. In addition, precise knowledge of  $\sigma_{el}(\theta)$  can be used as a calibration in measurements of other proton-induced reactions. Here again the absolute normalisation is frequently one of the predominant experimental uncertainties. Therefore the absolute differential cross section for elastic proton-proton scattering has been measured at  $90^\circ$  in the CM system for seven energies between 516 and 582 MeV, taking into account reaction losses in the target and in the scintillation detectors. The experiment has been performed at SIN.

Experimental results for the differential cross section  $\sigma(90^\circ)$  for proton-proton elastic scattering are plotted in figure 1. Our values (full circles) are slightly higher than a phase-shifts prediction by D.V. Bugg (1979, private communication) and differ significantly from the results of some previous experiments.

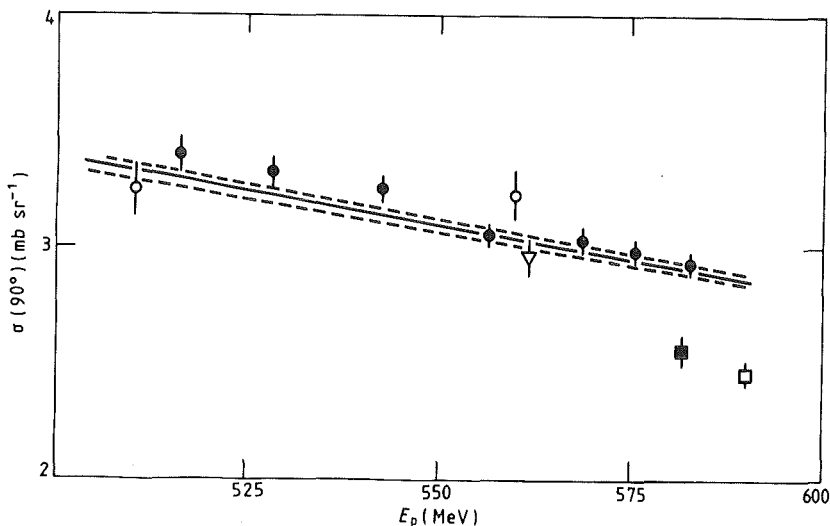


Fig. 1: Comparison of our experimental results (full circles) for the CM differential cross section  $\sigma(90^\circ)$  of elastic pp scattering with a phase-shift prediction by D.V. Bugg (1979, private communication) and with other experiments.

Our precise results will also help to normalise the angular distributions for pp elastic and inelastic scattering above the pion production threshold.

+ Institut de Physique, Université de Neuchâtel, Neuchâtel, Switzerland

++ Kernforschungszentrum Karlsruhe, Institut für Kernphysik und Institut für Experimentelle Kernphysik der Universität Karlsruhe, Karlsruhe, Federal Republic of Germany

+++ SIN, Villigen, Switzerland

§ On leave from TRIUMF, Vancouver, BC, Canada.

\* J. Phys. G8(1982)643

#### 4.4.3 The relative cross section for elastic proton-proton scattering between 500 and 600 MeV \*

A. Berdoz<sup>+</sup>, B. Favier<sup>+</sup>, F. Foroughi<sup>+</sup>, J. Hoftiezer<sup>++</sup>,  
G.S. Mutchler<sup>++§</sup> Ch. Weddigen<sup>++</sup>

Extensive measurements of spin-dependent nucleon-nucleon observables at intermediate energies are in progress at SIN, TRIUMPF and LAMPF. The absolute differential cross section is basic to these measurements. Indeed, all polarisation observables  $X$  are related to a bilinear combination of production amplitudes through the form  $X\sigma(\theta)$ . Therefore, precise  $\sigma(\theta)$  values are needed, due to the inherent error coupling of this formula, in order to constrain the determination of higher partial waves.

Existing elastic proton-proton differential cross-section data in the intermediate energy range are rather sparse and not of high quality. The data suffer from limited angular range, typically less than  $20^\circ$  CM, poor statistics, e.g. early bubble chamber work, or poorly known absolute normalisation, e.g. polarised target work. In the energy range of 500-600 MeV only three papers quote error bars below 10% for a large angular range. To help improve this situation, the relative cross section for elastic proton-proton scattering has been measured to better than 0.5% in  $10^\circ$  steps from  $30^\circ$  to  $90^\circ$  CM for incident beam energies of 529, 556 and 582 MeV. The experiment was performed at SIN by the NESIKA collaboration.

Fig. 1 shows the NESIKA results (full circles) together with earlier results from Boschitz et al. (1) and a phase shift prediction provided by Bugg (2). As can be seen from this figure the absolute normalization differences are within the 1.6 to 1.9% errors of our cross section data (3) at  $90^\circ$  CM. There are, however, significant shape differences. The experimental data have a smoother curvature between  $50^\circ$  and  $90^\circ$  than the phase-shift predictions. These differences will presumably be resolved when the phase-shift data set incorporates our new 0.5% data.

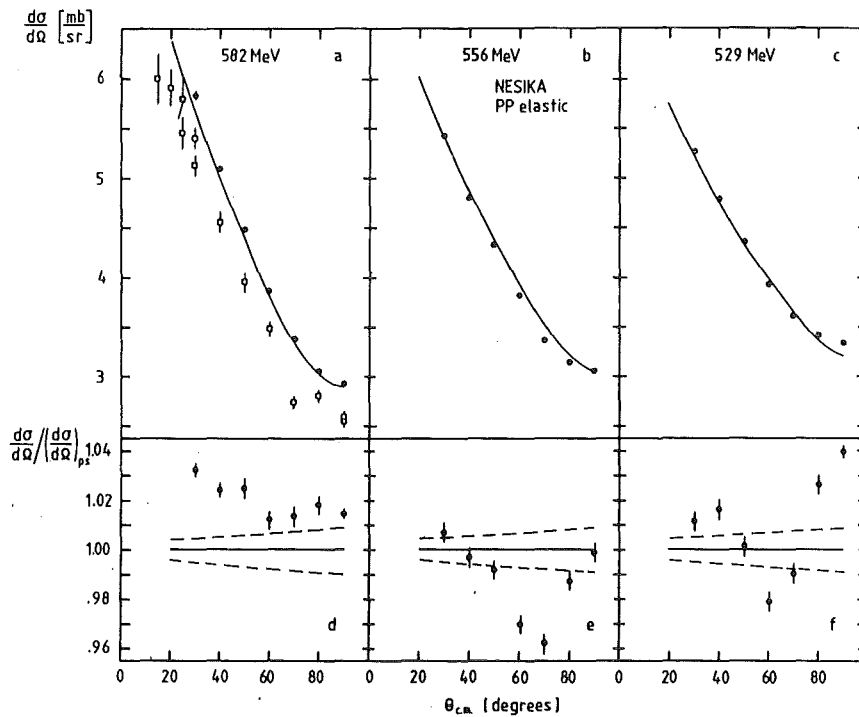


Fig. 1: Comparison of the NESIKA experimental results (full circles) with the phase-shift predictions of Bugg (3) and the data of Boschitz et al. (2) (open squares). Parts (a)-(c) show the variation of cross section with angle. Parts (d)-(f) are the ratio of our data to the predictions of Bugg (3). The broken line presents the error band of the phase-shift predictions. The error bars are the statistical errors from  $d\sigma/d\Omega_{\text{exp}}$  only.

- (1) E.T. Boschitz et al., Phys. Rev. C6(1972)457
- (2) D.V. Bugg, private communication (1979)
- (3) J. Hoftiezer et al., J. Phys. G8(1982)643

+ Institut de Physique, Université de Neuchâtel, CH-2000 Neuchâtel,  
Switzerland

++ Kernforschungszentrum Karlsruhe, Institut für Kernphysik und  
Institut für Experimentelle Kernphysik der Universität Karlsruhe,  
Postfach 3640, D-7500 Karlsruhe 1, Federal Republic of Germany

§ On sabbatical leave from Rice University Houston, TX 771, USA

\* J. Phys. G8 (1982)1363

4.4.4 FURTHER MEASUREMENTS OF  $iT_{11}$  IN  $\pi$ -d<sub>pol</sub> SCATTERING AS  
AN INVESTIGATION OF DIBARYON RESONANCE EFFECTS \*

J. Bolger<sup>+</sup>, E. Boschitz<sup>+</sup>, E.L. Mathie<sup>+</sup>, G.R. Smith<sup>+</sup>  
M. Meyer<sup>++</sup>, F. Vogler<sup>++</sup>, S. Mango<sup>+++</sup>, J.A. Konter<sup>+++</sup>,  
G.S. Mutchler<sup>§</sup>, J. Arvieux<sup>§§</sup>

One of the most interesting questions in intermediate-energy physics today is the existence of dibaryon (B=2) resonances. Invoking quark degrees of freedom, bag-model calculations have predicted states which are believed to be systems of six quarks consisting of colored subclusters. In view of the rather sparse evidence for color the existence of these, possibly narrow, B = 2 states should be investigated. There have been a number of attempts to observe B = 2 resonance effects in cross-section experiments, but no definite results have been obtained. Since B = 2 signals are most likely quite small, one has to employ more sophisticated experiments involving spin observables. Several polarization data sets involving reactions with two baryons have been published in recent years which indicate resonancelike structures. Controversy exists concerning interpretation of these structures as being due to either N- $\Delta$  dynamics or dibaryon resonances.

Previously published data<sup>1</sup> at  $T_\pi = 256$  MeV were found to be in surprisingly good agreement with predictions of dibaryon resonance effects in  $\pi$ -d scattering<sup>2</sup>. From this measurement it was concluded that at least one of the three proposed  $B = 2$  resonances [ $^1D_2(2140)$ ,  $^3F_3(2220)$ , and  $^1G_4(2430)$ ] could be responsible for the oscillatory pattern observed in the angular distribution. The energy dependence of the spin observables is the most important piece of information for extracting the relative importance of the individual resonances and for determining their parameters. Therefore our earlier measurements of  $iT_{11}$  were extended to 219, 275, and 294 MeV. In addition we have repeated measurements for three crucial angles at 256 MeV to reconfirm the striking oscillatory pattern.

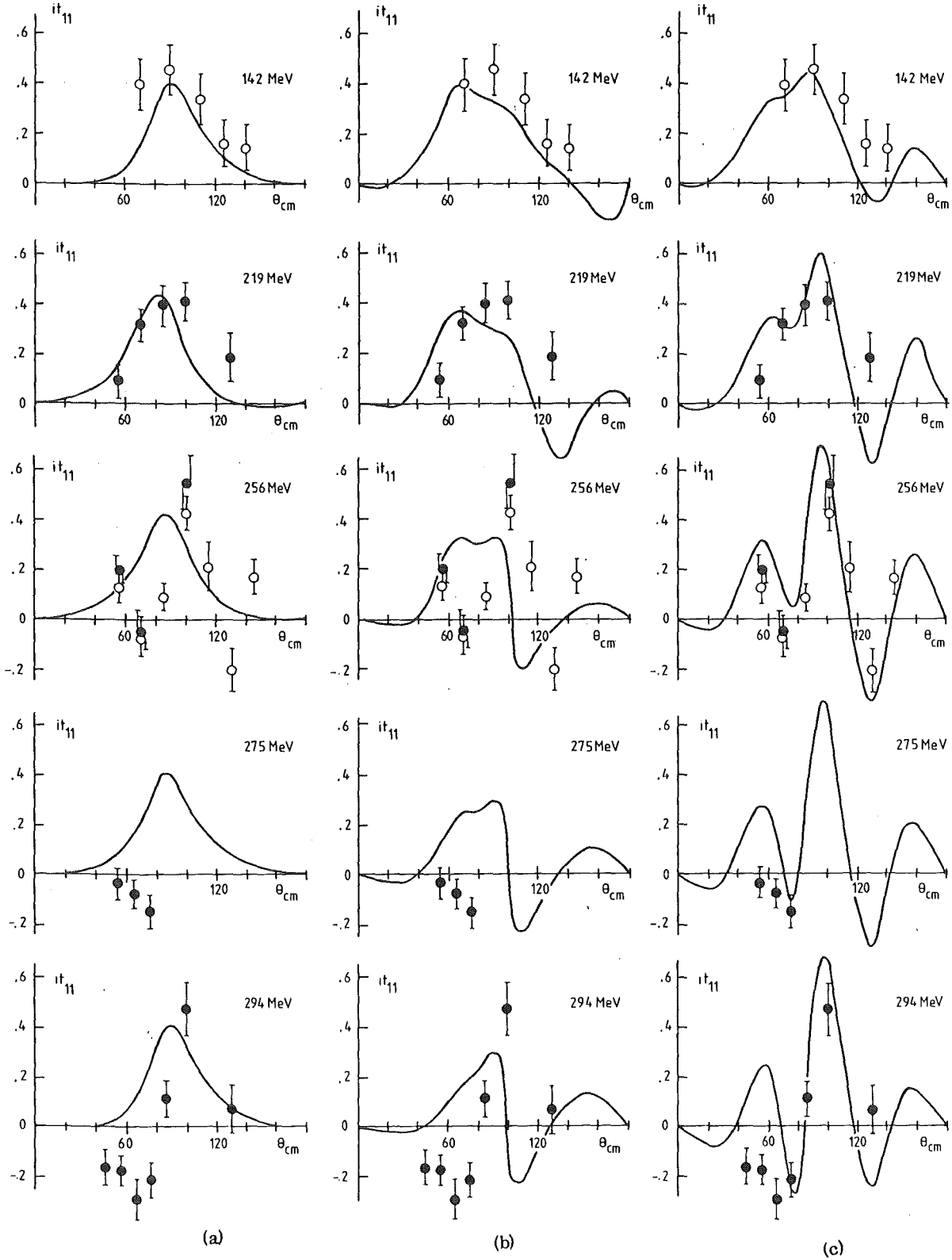
The configuration of this experiment was identical to that described previously<sup>1</sup>; however, a few elements were improved. A completely new polarized target and superconducting magnet were built. A significant improvement was made in the NMR Q-meter circuitry which measured the deuteron polarization in that the solenoidal coil surrounding the target material was replaced by a pancake coil of similar electrical characteristics immersed in the target material. This led to approximately a factor of 2 improvement in the NMR signal strength.

The vector analyzing power, defined as

$$iT_{11} = \frac{\sqrt{3}}{2} \frac{1}{P} \frac{\sigma_{\uparrow} - \sigma_{\downarrow}}{\sigma_{\downarrow} - \sigma_{\uparrow}},$$

where the subscript  $\uparrow$  indicates the direction of  $\vec{k} \times \vec{k}'$  ( $\vec{k}$  is the incident-pion momentum and  $\vec{k}'$  is the scattered-pion momentum), was determined by measuring the differential cross sections  $\sigma_{\uparrow}$  and  $\sigma_{\downarrow}$  of elastic  $\pi$ -d<sub>pol</sub> scattering for the two spin states of a vector-polarized deuteron target of polarization  $P$ . A new four-element scintillator telescope was employed which yielded information on the time of flight, energy loss, and total energy of the coincident recoil particles. This gave much better particle identification between protons and deuterons.

The reproducibility of the data at 256 MeV with respect to the previous experiment is good. The new  $iT_{11}$  values for  $\theta_{c.m.} = 55, 70, \text{ and } 100$  deg are  $(21 \pm 5)\%$ ,  $(-5 \pm 7)\%$ , and  $(53 \pm 11)\%$  compared with the previous experimental values of  $(13 \pm 6)\%$ ,  $(-7 \pm 10)\%$ , and  $(42 \pm 7)\%$ .



In the figure we compare our new data for  $it_{11}$  with the predictions of Grein and Locher<sup>3)</sup>. The curves in fig. 1(a) were calculated including the effect of pion absorption in a Faddeev calculation. In fig. 1(b) the curves show the effect of including only a  ${}^3F_3$  (2220) dibaryon resonance added to the Faddeev amplitudes. In fig. 1(c) the data are compared with calculations in which only the  ${}^1G_4$  (2430) was taken into account, with  $L_\pi = 5+1$ . The general trend of the energy dependence of the data is reproduced semiquantitatively

in the latter curves. However some words of caution are in order. In predicting effects of dibaryon resonances in  $\pi$ -d scattering, the data at forward angles are particularly significant, since the calculations of "background amplitudes" are most reliable for this case. Hence the discrepancies for the smallest angles at higher energies are serious and must be explained.

- 1) J. Bolger, E. Boschitz, G. Pröbstle, G.R. Smith, S. Mango, F. Vogler, R.R. Johnson, J. Arvieux, Phys. Rev. Lett 46, 167 (1981)
- 2) K. Kubodera, M. Locher, A. Thomas, F. Mhyrer, J. Phys. G 6, 171 (1980)
- 3) W. Grein, M.P. Locher, J. Phys. G 7, 1355-1366 (1981)

+ Kernforschungszentrum und Universität Karlsruhe

++ Physikalisches Institut, Universität Erlangen-Nürnberg

+++ Swiss Institute for Nuclear Research

§ Rice University, Houston, Texas 77001

§§ Laboratoire National Saturne, 91190 Gif-sur-Yvette, France

\*Phys. Rev. Lett. 48 (1982)1667

#### 4.4.5 MEASUREMENT OF THE VECTOR ANALYZING POWER $iT_{11}$ FOR THE $\pi d \rightarrow 2p$ REACTION WITH A POLARIZED TARGET \*

G.R. Smith<sup>+</sup>, J. Bolger<sup>+</sup>, E. Boschitz<sup>+</sup>, E.L. Mathie<sup>+</sup>  
G. Pröbstle<sup>+</sup>, M. Meyer<sup>++</sup>, F. Vogler<sup>++</sup>, S. Mango<sup>+++</sup>

The study of the  $\pi d \rightarrow 2p$  reaction and its inverse has been of fundamental interest since the advent of pion beams, in accordance with its importance in the understanding of many basic phenomena in particle and nuclear physics. In the recent past, attention has turned to investigations of dibaryon resonances. No striking effects have been observed in the many years of measurements of incoherent observables, such as differential cross sections. Consequently, experiments have focussed on the measurements of

spin observables, which are in general more sensitive due to the interference of small amplitudes with large ones. Probably the strongest indication for dibaryon resonances in pion induced reactions reported to data has been in the measurement of  $iT_{11}$  for  $\pi d$  elastic scattering. These measurements, reported earlier by this group, show strong oscillations in the angular behaviour of  $iT_{11}$  at  $T_{\pi} = 256$  MeV, which were predicted in calculations including dibaryon and contrary to the smooth behaviour predicted by Faddeev calculations without dibaryon resonances. In order to complement and extend our investigations of  $iT_{11}$  in the  $\pi d$  system, our group has embarked on measurements in the absorption channel as well.

We have measured the vector analyzing power  $iT_{11}$  in the  $\pi d \rightarrow 2p$  reaction, where  $iT_{11}$  is defined

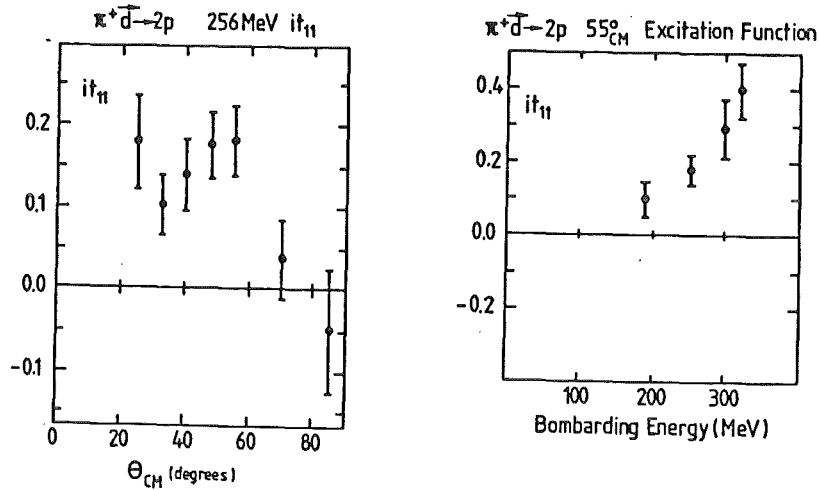
$$iT_{11} = \frac{\sqrt{3}}{2} \frac{1}{P} \frac{\sigma_{\uparrow} - \sigma_{\downarrow}}{\sigma_{\uparrow} + \sigma_{\downarrow}} .$$

In this equation, the postscript  $\uparrow$  indicates the direction of  $K_{\pi} \times K_p$ ,  $K_{\pi}$  is the incident-pion momentum,  $K_p$  is the forward scattered proton momentum, and  $\sigma_{\uparrow}$  and  $\sigma_{\downarrow}$  denote the differential cross sections of the  $\pi d \rightarrow 2p$  reaction for the two spin states of a vector polarized deuteron target of polarization  $P$ .

Our data were collected at the  $\pi M3$  channel of SIN in a kinematically complete experiment. The experimental arrangement has been discussed previously.

The results of the experiment are shown in fig. 1. They consist of an excitation function of  $iT_{11}$  at  $\theta_{cm} = 55^{\circ}$  for incident pion energies of  $T_{\pi} = 180, 256, 295$  and  $320$  MeV, as well as an angular distribution at  $T_{\pi} = 256$  MeV for  $\theta_{cm} = 25^{\circ}, 32.5^{\circ}, 40^{\circ}, 47.5^{\circ}, 55^{\circ}, 70^{\circ}$  and  $85^{\circ}$ . The prominent feature in the excitation function is the rapid increase of  $iT_{11}$  with increasing bombarding energy. No structure in this excitation function is observed near  $T_{\pi} = 256$  MeV, where the strong oscillations in  $iT_{11}$  were observed in  $\pi d$  elastic scattering. Unfortunately, since our measurements were limited by small asymmetries at low energies, and small cross sections at high energies, we were unable to extend the excitation function any further. The angular distribution is relatively featureless, exhibiting a maximum near  $55^{\circ}$ . The apparent minimum in the 256 MeV angular distribution of  $iT_{11}$  near  $\theta_{cm} = 35^{\circ}$  is not deep enough to be statistically significant. Our measurements were limited to angles  $\theta_{cm} \geq 25^{\circ}$  due to the rotation of the incident pion trajectory into the forward detectors by the target magnetic field. Significantly absent

from the angular distribution of  $iT_{11}$  is any indication of strong oscillatory behaviour such as was observed in the measurements of  $iT_{11}$  in  $\pi d$  elastic scattering.



The data were fit with associated Legendre polynomials according to the convention proposed by Niskanen<sup>2)</sup>. The coefficients  $d_k$ , defined by

$$\sigma \cdot iT_{11} = \frac{1}{4\pi} \sum_{k \text{ even}} d_k P_k^1(\cos\theta)$$

where obtained from a least squares fit to the measured asymmetries. The differential cross sections  $\sigma$  were taken from previously published 800 MeV  $pp \rightarrow \pi d$  data. If in such a fit a certain  $d_k$  can be shown to be non-zero, then it follows that partial waves with  $J$  up to at least  $k/2$  are necessarily non-zero. Thus the effective maximum  $J$  can be determined in a model independent way. Although a reasonable fit to these data can already be achieved with only two terms ( $\chi^2=1.3$ ), the best chi-squared ( $\chi^2=1.03$ ) was obtained with three terms:  $d_2 = (0.694 \pm 0.098)$ ,  $d_4 = (0.162 \pm 0.080)$  and  $d_6 = (-0.108 \pm 0.072)$ . The apparent minimum near  $\theta_{cm} = 35^\circ$  can only be reproduced in the fit with the inclusion of a term  $d_8$ , indicating that this minimum would come from  $G$  waves. More data are clearly required, however, before such a term can be meaningfully introduced into the fit.

1) SIN Physics Report No. 3 (1981) 70

2) J.A. Niskanen, Polarization Phenomenon in Nuclear Physics, AIP Conference Proceedings 69 (1980) 77 and private communication (1981)

+ Kernforschungszentrum und Universität Karlsruhe

++ Physikalisches Institut, Universität Erlangen-Nürnberg

+++ Schweizerisches Institut für Nuklearforschung

\*Phys. Rev. C25 (1982)

## 4.5 NUCLEON-ANTINUCLEON INTERACTION

### 4.5.1 Search for Bound Baryonium States and Rare Neutral Annihilations via Photon Spectrometry

B. Richter, P. Blüm, R. Guigas, H. Koch, Th. Köhler,  
M. Meyer, H. Poth, U. Raich  
G. Backenstoß<sup>+</sup>, M. Hasinoff<sup>+</sup>, P. Pavlopoulos<sup>+</sup>, J. Repond<sup>+</sup>,  
L. Tauscher<sup>+</sup>, D. Tröster<sup>+</sup>  
L. Adiels<sup>++</sup>, I. Bergström<sup>++</sup>, K. Fransson<sup>++</sup>, A. Kerek<sup>++</sup>  
M. Suffert<sup>+++</sup>, K. Zioutas<sup>§</sup>

The experiment measuring the inclusive  $\gamma$ -spectrum accompanying  $\bar{p}p$ -annihilation at rest, which took place at the CERN-PS, has been terminated. The single  $\gamma$ -spectra from a high resolution modular (54 modules) NAI(TL)-detector, from a 10" x 12" NAI(TL)-crystal and  $\gamma\gamma$ -coincidences under  $180^\circ$  have been analysed.

The background of the single  $\gamma$ -spectra has been treated using a Monte-Carlo calculation containing 85% of the known annihilation channels. In the second step of background treatment a broad phenomenological function describing multi  $\pi^0$ -annihilations not included in the Monte-Carlo was subtracted. In the third step rare neutral 2 body annihilation channels including  $\pi^0$ -,  $\eta$ - or  $\omega$ -mesons could be identified from the single  $\gamma$ -spectra. Those 2 body annihilation channels result in the  $\gamma$ -spectrum as a rectangular  $\gamma$ -distribution with fixed  $E_{\gamma\min}/E_{\gamma\max}$ . The intensities of the  $\gamma$ -boxes have been fitted at the high energy part of the  $\gamma$ -spectrum, where the sensitivity is larger than at the low energy part. Table 1 summarises the results of the determined rare neutral annihilation channels. In order to describe the  $\gamma$ -spectrum by an optimal fit, it was necessary to assume an additional annihilation channel  $\bar{p}p \rightarrow \pi^0 X$ , where X is a unknown particle with approximately the mass  $M_X \approx 690$  MeV.

$\bar{p}p$ -annihilation channel	optimal fit (in $10^{-2}$ )	other possible fit (in $10^{-2}$ )
$\omega\pi^0$	$(1.98 \pm 0.3)$	$(2.5 \pm 0.5)$
$\omega\eta$	$(0.82 \pm 0.6)$	$(1.4 \pm 1.2)$
$\pi^0\eta, \eta\eta$	$(0.81 \pm 0.2)$	$(1.2 \pm 0.2)$
$\pi^0\pi^0$	$(0.06 \pm 0.05)$	0.048 fixed
$\pi^0\gamma$	$(0.015 \pm 0.004)$	$(0.015 \pm 0.004)$
$\pi^0\eta'$	$(0.3 \pm 0.2)$	--
$\pi^0X$	$(1.2 \pm 0.2)$	0.1 fixed

Table 1: The results of the new rare annihilation channels.

It is worthwhile to mention that these results contain the first measurement of the annihilation channel  $\bar{p}p \rightarrow \pi^0\gamma$  and  $\pi^0\eta'$ . The branching ratios of the channels  $\bar{p}p \rightarrow \omega\pi^0$ ,  $\omega\eta$ ,  $\pi^0\eta$  are unexpectedly higher than those of annihilation channels with similar quark content. A satisfactory explanation for the unknown channel  $\pi^0X$  cannot be given at this time.

After subtraction of these rare annihilation channels in the inclusive  $\gamma$ -spectrum, five  $\gamma$ -lines remain, where four of them can be interpreted as monoenergetic  $\gamma$ -transitions from the reaction  $(\bar{p}p)_{\text{atomic}} \rightarrow (\bar{p}p)_{\text{nuclear}} + \gamma$ . The fifth line is expected and results from secondary  $\pi^-$  from annihilation, which stop in the liquid hydrogen target and make the reaction  $\pi^-_{\text{stop}} p \rightarrow \gamma n$  or  $\pi^0 n$ . These lines occurred in two independent running periods and in two dynamic ranges of the modular NAI(TL)-detector, which increases their significance. Comparing these new results of the measurement  $\bar{p}_{\text{stop}} p \rightarrow \gamma \dots$  with former experiments (/1/) one has to conclude that two lines (180 MeV, 220 MeV) have survived, one former line (420 MeV) did not show up in the recent experiment, but two new lines (102 MeV, 550 MeV) have been consistently seen in the running periods 1979 and 1980. The yields of the confirmed lines in comparison with /1/ are down by the factor of about 3. Table 2 gives an overview over the evaluated  $\gamma$ -lines in the past three experiments.

The  $\gamma$ -spectrum after subtraction of the known (and Monte Carlo generated) annihilation channels and the contribution of multi  $\pi^0$  annihilation is shown in fig.1,

$N/4\text{MeV}$

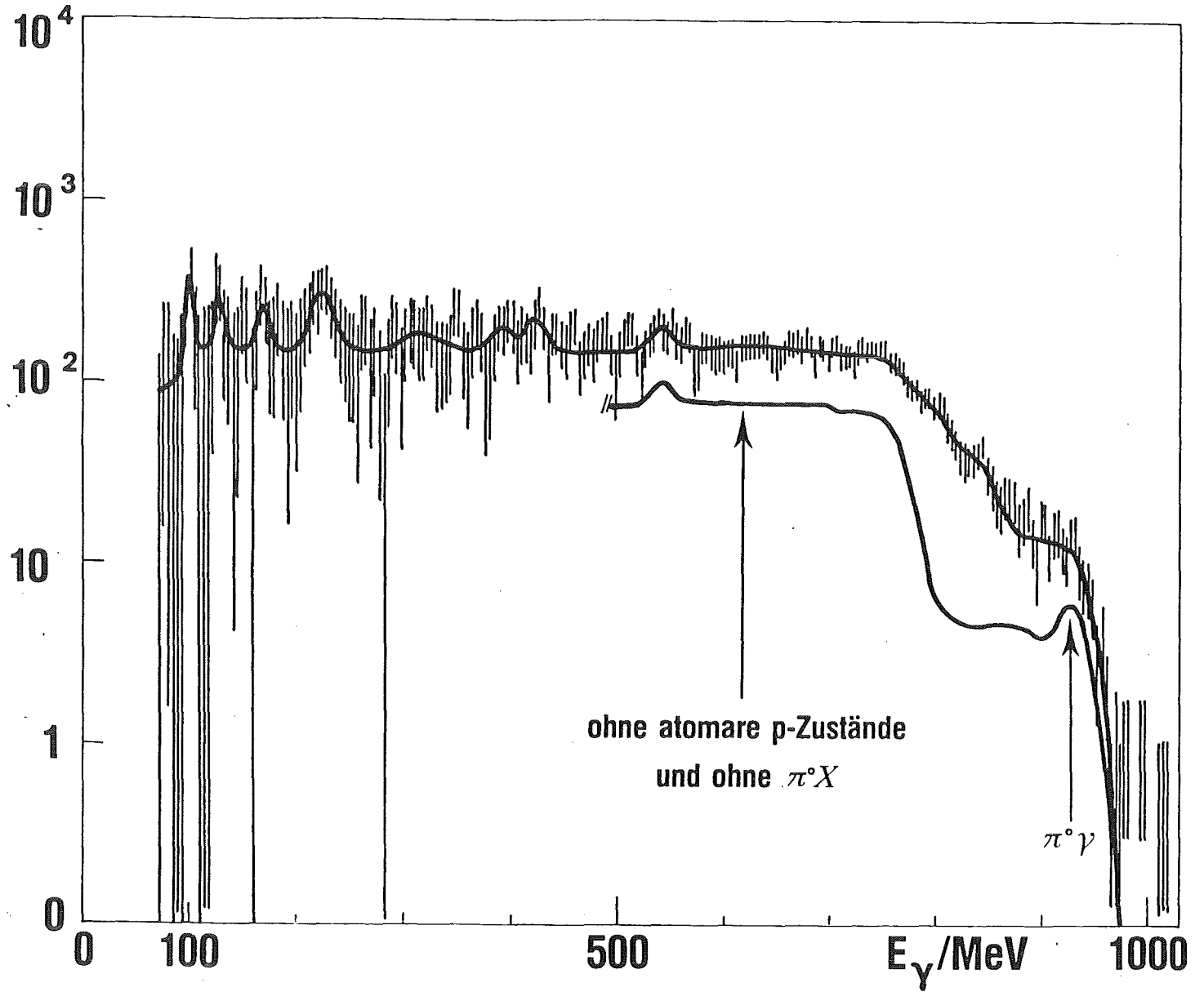


Fig.1: The background subtracted  $\gamma$ -spectrum including rare neutral annihilation channels and monoenergetic  $\gamma$ -lines.

it includes new rare annihilation channels and monoenergetic  $\gamma$ -lines possibly coming from Baryonium formation; the best fit is drawn in.

$E_\gamma$ (MeV)	$M_{\text{Baryonium}}$ (MeV)		Exp. 1979	Exp. 1980	Exp. 1976(/1/)
130 MeV ( $\pi_{\text{stop}}^{p \rightarrow \gamma}$ )	-	E(MeV)	129.5 $\pm$ 1.4	123.8 $\pm$ 2.0	132 $\pm$ 6
		Y(%)	2.24 $\pm$ .77	3.28 $\pm$ .73	5.1 $\pm$ 2.7
		Confid.	2.9 $\sigma$	4.5 $\sigma$	
102 MeV	1771	E(MeV)	102.2 $\pm$ 1.0	102.0 $\pm$ 1.2	-
		Y(%)	2.35 $\pm$ .72	1.50 $\pm$ .41	-
		Confid.	3 $\sigma$	3.6 $\sigma$	-
175 MeV	1693	E(MeV)	170.1 $\pm$ 1.7	174.9 $\pm$ 2.1	183 $\pm$ 7
		Y(%)	1.64 $\pm$ .73	1.47 $\pm$ .47	7.2 $\pm$ 1.7
		Confid.	2.2 $\sigma$	3.1 $\sigma$	
220 MeV	1641	E(MeV)	222.2 $\pm$ 3.8	220.5 $\pm$ 6.3	216 $\pm$ 9
		Y(%)	3.10 $\pm$ 1.19	2.84 $\pm$ 1.05	6.0 $\pm$ 1.9
		Confid.	2.6 $\sigma$	2.7 $\sigma$	
550 MeV	1207	E(MeV)	547.6 $\pm$ 8.5	550.2 $\pm$ 3.4	-
		Y(%)	.92 $\pm$ .38	.86 $\pm$ .22	-
		Confid.	2.4 $\sigma$	3.9 $\sigma$	-

Table 2: The results of the monoenergetic  $\gamma$ -lines from 3 experiments.

+ Universität Basel, Switzerland

++ Research Institute for Physics, Stockholm, Sweden

+++ CNR, Strasbourg, France

§ University of Thessaloniki, Greece

/1/ P. Pavlopoulos et al., Phys. Let. 72B(1978)415.

#### 4.5.2 $N\bar{N}$ Interaction in a Three-Dimensional Relativistic Equation\*

E. Borie, F. Gröss<sup>†</sup>

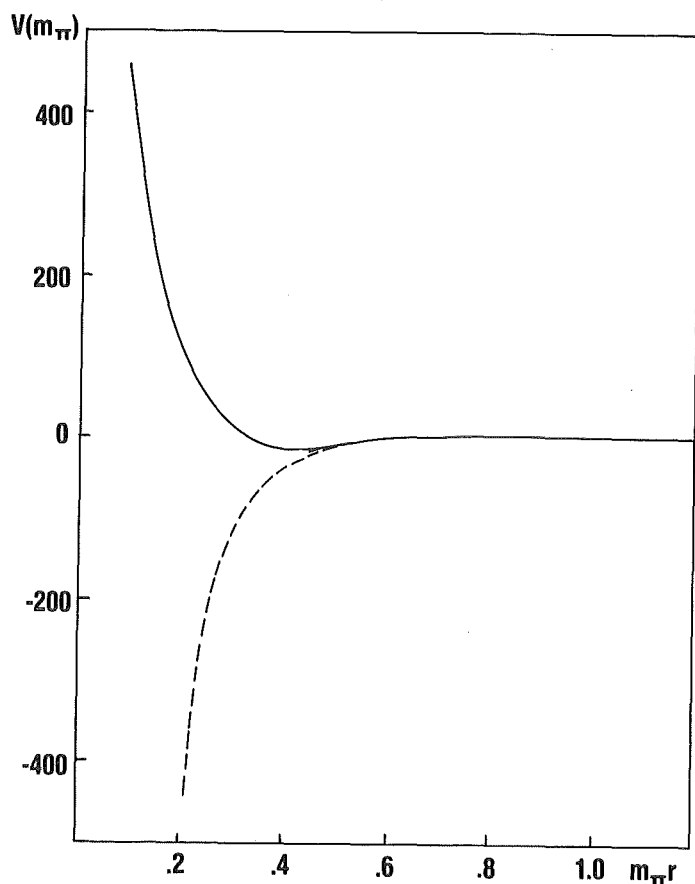
Kernforschungszentrum Karlsruhe, IK II

During the past several years a great amount of work has been performed on the prediction of  $N\bar{N}$  resonances within the framework of a nonrelativistic potential model /1,2/. Such models are based on the one boson exchange (OBE) potentials which have been used to describe NN scattering. The real part of the  $N\bar{N}$  potential is then obtained by a G-parity transformation which reverses the sign of the coupling in the case of  $\pi$ - and  $\omega$ -exchange. Since  $\omega$ -exchange is supposed to be responsible for the short range repulsion in the NN system, one expects strong attraction in the  $N\bar{N}$  system and a number of strongly bound states, at least if the effects of annihilation could be ignored.

The binding energies of many of the quasinuclear states predicted in the literature are large, of the order of several hundred MeV and the strong attraction due to  $\omega$ -exchange is effective at distances of the order 0,5 fm, corresponding to nucleon momenta of the order of 0,4 Mc. The use of a relativistic two body equation should be more appropriate under such circumstances. Furthermore, OBE models of NN scattering based on three dimensional relativistic equations /3,4/ suggest that at least part of the short range repulsion in the NN system is due to quadratic terms in the effective potential which arise when one considers off diagonal terms in the interaction connecting large and small components of the nucleon wave functions. Such terms do not change sign under the G-parity transformation and could give rise to short range repulsion in the  $N\bar{N}$  system.

In the present work we have attempted to check this point quantitatively by examining the effective potential for  $N\bar{N}$  scattering obtained by making a G-parity transformation on the effective potential obtained by Gross using his quasipotential equation /4/. Exchange of  $\pi, \rho, \sigma$  and  $\omega$ -mesons was taken into account. A typical result is shown for the isosinglet  $^{13}P_0$  effective potential. The solid curve shows the effective potential calculated for the quasipotential equation while the dashed curve gives results calculated

without the quadratic terms. (The main effect of these terms is to change the sign of the  $I = 0$  tensor potential at short distances). The effective potentials are qualitatively different for  $\gamma < 0,4 \text{ m}_\pi^{-1} \approx 0,6 \text{ fm}$ . Although this calculation cannot be considered to be a complete description of the  $N\bar{N}$  interaction, since annihilation has been ignored (this work does not even give a complete description of the real part of the potential, since the effect of annihilation has not been taken into account), we find that the contribution from the direct channel to the real part of the potential is sufficiently modified when going from a nonrelativistic framework to a relativistic equation, that the predictive power of nonrelativistic potential models for describing strongly bound  $N\bar{N}$  states has to be regarded as doubtful.



$V_{\text{eff}}$  (units  $m_\pi$ ) for the  $I = 0 \quad {}^3P_0$  channel

solid curve: quadratic terms in relativistic equation included;  
dashed curve: nonrelativistic equation

- /1/ I.S. Shapiro, Phys. Rep. 35C (1978)129
- /2/ W.W. Buck, C.B. Dover, J.M. Richard, Ann. Phys. 121 (1979)47
- /3/ K. Erkelenz, K. Holinde, Z. Naturforsch 28a (1973)353
- /4/ F. Gross, Phys. Rev. D10 (1974)223

<sup>†</sup>Carnegie Mellon University (permanent address: College of William and Mary)

\*Contribution to Erice Workshop, 1982

4.5.3            Measurement of the  $\bar{p}$  annihilation cross-section  
                  of very low energy\*

P. Blüm, H. Poth, and L.M. Simons

A knowledge of the  $\bar{p}$ -nucleon and of the  $\bar{p}$ -nucleus annihilation cross section at very low energy is of great interest for the understanding of the  $\bar{N}N$  interaction. For instance, the low energy limit of  $\beta\sigma_{\text{ann}}$  is an important input for potential calculations. The measurement of partial annihilation channels allows definite bounds to be put on the contribution of partial waves. Below 100 MeV/c  $\bar{p}$ -momentum, annihilation and elastic scattering are the only possible reaction channels. It is of great importance to explore this region with high energy resolution. In order to achieve this, thin targets have to be used and the antiproton momentum has to be determined prior to annihilation. We have investigated the possibility of determining the antiproton momentum from its penetration depth into the target or from the elapsed time from target entry to annihilation. The results are shown in fig. 1 and fig.2, taking into account the energy straggling of the antiproton in the 0.5 mm scintillator or 0.1 mm Be window at the chamber entrance. It can be seen from the plots that it should be possible to measure the annihilation cross section in this way down to 40 MeV/c (1 MeV) with good momentum resolution. requiring only moderate

time or space resolution for the detection of the annihilation. The annihilation rates are estimated for gaseous  $H_2$  at NTP and  $10^6 \bar{p}/s$ . The rate per 10 cm target length is  $R \approx 20 s^{-1}/p_{\bar{p}}$  [GeV/c], while it is constant, if  $\sigma_{ann} \approx \beta^{-1}$  when measured versus time ( $R = 600 s^{-1}$  for 10 ns bin). The latter allows for a very sensitive test of the  $1/v$  law.

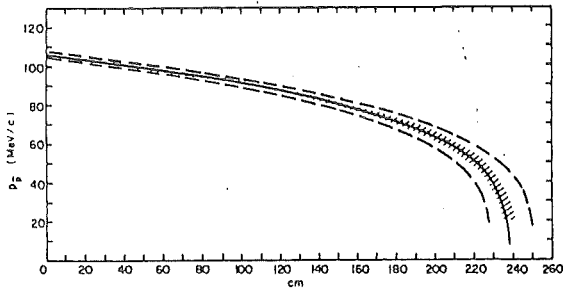


Fig. 1  $\bar{p}$  momentum versus penetration depth  $X$  in gaseous  $H_2$  at NTP. The dashed lines show the initial momentum spread of 1.3% (500  $\mu m$  C), and the hatched area the initial momentum spread of 0.6% (100  $\mu m$  Be).

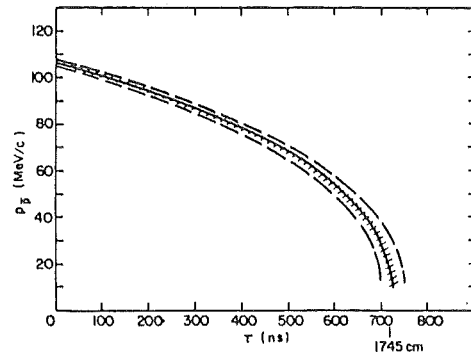


Fig. 2  $\bar{p}$  momentum versus deceleration time  $\tau$  in gaseous hydrogen at 100 Torr

Experimentally the measurements can be realized with very little effort. However, owing to the low annihilation rate in flight, a combination with a stop experiment is opportune. The annihilation cross-section is determined from the number of annihilations per  $\bar{p}$  momentum registered. Normalization is obtained from annihilation at rest. The  $\bar{p}$  momentum is determined from the annihilation time or from the penetration depth deduced from the observation of the annihilation products. If the antiprotons are decelerated in the cyclotron trap (1) the reconstruction of the annihilation vertex would allow an extension of the measurements to still lower energies since the  $\bar{p}$ -momentum can be determined from the radius of  $\bar{p}$ -orbit in the cyclotron trap. For instance the  $\bar{p}$  momentum can be determined to  $\pm 15\%$  at 15 MeV/c (120 keV) in this way.

(1) P. Blüm, D. Gotta, R. Guigas, H. Koch, W. Kunold, M. Schneider  
 and L.M. Simons, CERN/PSCC/80-99

\*Proc. 3<sup>rd</sup> School of Exotic Atoms Physics around LEAR with low energy cooled antiprotons, Erice, 9-16 May 1982.

4.5.4 Low energy proton-antiproton charge-exchange  
and applications

H. Poth, J.M. Richard<sup>†</sup>

The  $p\bar{p} \rightarrow n\bar{n}$  charge-exchange reaction is studied in the low energy region within the framework of potential models. The long range forces are described by the Paris potential, and they are supplemented by an empirical annihilation term adjusted to reproduce the available data on elastic and inelastic integrated cross-sections (1). We investigate the behaviour of  $(d\sigma/d\Omega) (p\bar{p} \rightarrow n\bar{n})$  for energies between the threshold and the pion production threshold. The dip-bump structure already observed near 730 MeV/c (2) shows up also at lower energy. The magnitude of this effect is studied as a function of the strength of the different contributions, namely pion-exchange, rho-exchange and the annihilation term. We conclude that a careful measurement of the charge-exchange differential cross-section provides very rich information on the nucleon-antinucleon force. We also briefly discuss the influence of possible baryonium resonances on the  $p\bar{p} \rightarrow n\bar{n}$  reaction.

The charge-exchange process provides an unique possibility of producing an high flux of antineutrons. We review the physical interest of the reactions induced by antineutrons. In potential model calculations, the charge-exchange reaction has a rather spectacular spin-dependence. In particular, the antineutrons are predicted to be highly polarized if they are produced on a longitudinally polarized hydrogen jet target.

1) C.B. Dover and J.-M. Richard, Phys. Rev. C21 (1980) 1466

2) M. Bogdanski et al., Phys. Lett. 62B (1976) 117.

<sup>†</sup>Division de Physique Théorique, I.P.N., Orsay

5. HIGH ENERGY PHYSICS

G. D'Agostini, W.-D. Apel, S. Banerjee, J. Bodenkamp, D. Chrobaczek, J. Engler, G. Flügge, D.C. Fries, K. Gamedinger, G. Hopp, J. Knapp, M. Mrüger, H. Küster, M. Makowsky, H. Müller, H. Randoll, G. Schmidt, H. Schneider

KfK and Universität Karlsruhe, Federal Republic of Germany

H.-J. Behrend, Ch. Chen, H. Fenner, J.H. Field, V. Schröder, H. Sindt  
Deutsches Elektronen-Synchrotron, Hamburg, Federal Republic of Germany

W. de Boer, G. Buschhorn, G. Grindhammer, P. Grosse-Wiesmann, B. Gunderson, Ch. Kiesling, R. Kotthaus, U. Kruse, H. Lierl, D. Lüers, T. Meyer, H. Oberlack, P. Schacht, M.J. Schachter, A. Snyder, H. Stei  
H. Steiner

MPI für Physik und Astrophysik, München, Federal Republic of Germany

G. Carnesecchi, P. Colas, A. Cordier, M. Davier, D. Fournier, F.J. Grivaz, J. Haissinski, V. Journé, A. Klarsfeld, F. Laplanche, F. LeDiberder, U. Mallik, J.-J. Veillet

Laboratoire de l'Accelérateur Linéaire, Orsay, France

R. George, M. Goldberg, B. Grossetête, O. Hamon, F. Kapusta, F. Kovacs, G. London, L. Poggioli, M. Rivoal

Laboratoire de la Physique Nucléaire et Hautes Energies, Paris, France

R. Aleksan, J. Bouchez, G. Cozzika, Y. Ducros, A. Gaidot, S. Jadach, Y. Lavagne, J. Pamela, J.P. Pansart, F. Pierre

Centre d'Etudes Nucléaires, Saclay, France

The research activities of the physics group of the IK I, who is a member of the CELLO Collaboration, rest at present entirely on the operation and utilisation of the CELLO detector at the  $e^+e^-$  storage ring PETRA (DESY).

After one and a half year of successful data taking the detector was moved out of the beam in July 1981. Since then the work of the Karlsruhe Group consisted a) in hardware activities to upgrade the Liquid Argon calorimeter of the CELLO detector and b) in analysis work using essentially the KfK computer installation. The upgraded CELLO detector moved back into the beam in August 1982.

The analysis work at the KfK has concentrated on special problems, such

as tests of QCD predictions, on effects due to the weak neutral current and on the observation of single isolated high energy electrons and photons.

#### 5.1 HARDWARE DEVELOPMENT: THE LIQUID ARGON CALORIMETER

After the CELLO detector was moved out of the interaction zone at PETRA (July 1981) we began the planned general development and upgrading work of the hardware components in particular of the liquid argon calorimeter.

The upgrading of the quality of the Liquid Argon Calorimeter consisted in increasing the number of read channels by 50%. This way the former 'ghost channel wiring' could be removed (i.e. the fact that for part of the read channels one read amplifier was connected to two different metal strips).

The ghost wiring had introduced a considerable complexity in the analysis of the signals.

3900 new electronic channels consisting of amplifiers, preamplifiers and corresponding multiplexers have been manufactured, tested and installed. In addition the already existing electronic channels were partly improved by rewiring and other modifications.

For the new wiring of lead strips the 24 m<sup>3</sup> liquid argon calorimeter had to be warmed up, the vacuum sealed tank had to be opened and the lead stacks had to be taken out (and shipped to the MPI in München).

During this time we overhauled the cryo-installation for the liquid argon. A second cryo-generator and a large supply tank for liquid nitrogen were installed. The second cryo-generator is foreseen to serve as a stand-by generator for the case that the running generator breaks down or needs to be serviced.

No problems arose in reinstalling the lead stacks in the tank and refilling the calorimeter with liquid argon. By July 1982 the calorimeter was again ready for operation.

## 5.2 HADRONIC FINAL STATES AND TEST OF QCD

### 5.2.1 Analysis of the energy weighted angular correlations in hadronic $e^+e^-$ annihilations at 22 and 34 GeV.

In the process of  $e^+e^-$  annihilation into a quark-antiquark pair one expects a measurable increase of colour-radiative effects with increasing center of mass energies. We have identified and measured these perturbative QCD effects by evaluating the energy weighted angular correlation between final state hadrons in  $e^+e^-$  annihilation (1,2).

The energy correlation function  $F(\theta)$  is given by the semi-inclusive differential cross section for two hadrons in  $e^+e^-$  annihilation:

$$(1) \quad F(\theta) = \frac{1}{\sigma_{\text{tot}}} \sum \int \int z_a z_b dz_a dz_b \frac{d^3\sigma(e^+e^- \rightarrow a + b + X)}{dz_a dz_b d\theta}$$

where  $\theta$  is the angle between the two hadrons  $a$  and  $b$  of the final state,  $z_a$  and  $z_b$  are the relative energies of  $a$  and  $b$  with respect to the center of mass energy  $E_{\text{CM}}$ ,

$\sigma_{\text{tot}}$  is the total hadronic annihilation cross section.

The sum is to be taken over all hadrons in the final state.

Experimentally the correlation function is computed as,

$$(2) \quad f(\theta) = \frac{1}{N} \sum_a \sum_b z_a z_b \frac{1}{\Delta\theta} \int_{\theta-\Delta\theta/2}^{\theta+\Delta\theta/2} \delta(\theta_{ab} - \theta') d\theta'$$

where  $N$  is the total number of hadronic events,

$\Delta\theta$  is the experimental bin width in  $\theta$ ,

$z_a$  and  $z_b$  are the energies of  $a$  and  $b$  relative to  $E_{\text{visible}}$ , the total observed energy.

The uncorrected experimental distribution of  $F(\theta)$  for charged hadrons at a center-of-mass energy of 34 GeV is shown in Fig. 1.

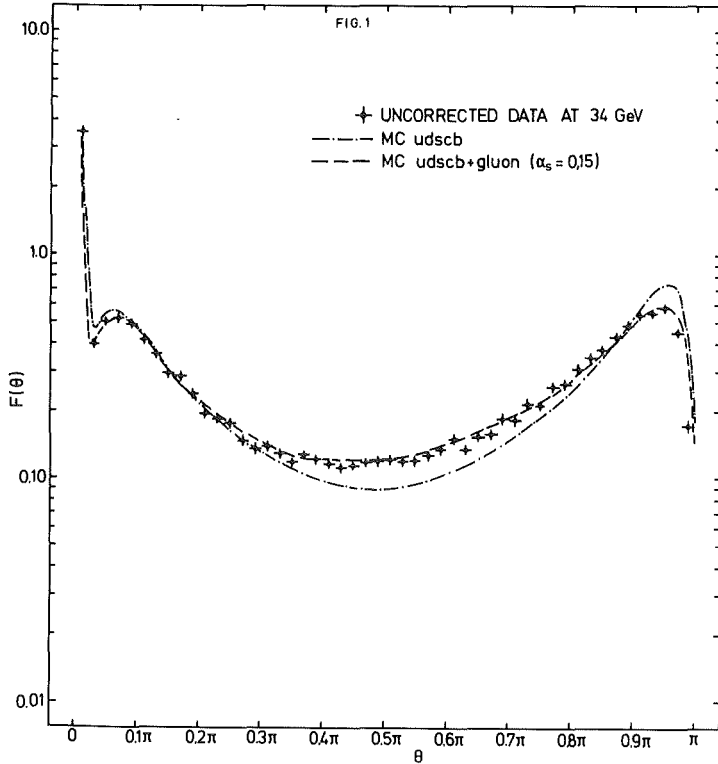


Fig. 1  
 Uncorrected  $F(\theta)$  at  
 34 GeV.  
 Dashed-dotted line:  
 Monte Carlo simulated  
 data  $q\bar{q}$ ,  
 dashed line: Monte Carlo  
 simulated data  $q\bar{q} + q\bar{q}g$

The observed distribution shows a small asymmetry with respect to  $\theta = \pi/2$ .

A comparison with Monte Carlo simulated events of the type:

$$e^+ e^- \rightarrow q\bar{q} + q\bar{q}g + \text{fragmentation}$$

yields a remarkable agreement with the data in most angular regions, whereas simulated data corresponding to only  $q\bar{q}$  production are in clear disagreement with the experiment. In the Monte Carlo procedure (9-12),  $q\bar{q}$  and  $q\bar{q}g$  states ( $q = u, d, s, c, b$ ) are generated, which fragment into primordial hadrons and emerge as 'stable' final state particles through various decay channels.

We have compared the measured correlation function with theoretical calculations (1-8), and deduced values for the strong coupling constant  $\alpha_s$  in first order QCD, and for the QCD scale parameter  $\Lambda$  in the Leading Log Approximation.

In the central region around  $\theta \approx \pi/2$ , the dominant process is the emission of a single hard gluon, the partonic final state consisting of a superposition of  $q\bar{q}$  and  $q\bar{q}g$  has been calculated using perturbative QCD of order  $\alpha_s$ . For the comparison with the data a phenomenological fragmentation term has been added.

The (partonic) first order QCD calculation due to Basham et al. (BBEL) (2) yields

$$(3) \quad F(\theta)_{\text{QCD}} = \frac{\alpha_s}{\pi} g(\theta)$$

where  $g(\theta)$  is independent of the energy. For any reasonable  $\alpha_s$  the perturbative QCD result lies clearly below the data (Fig. 2). Fragmentation effects in the qq production can be taken into account according to a simple model (2) by adding a term

$$(4) \quad F(\theta)_{\text{FRAG}} = c * \langle p_t \rangle / \{ E_{\text{CM}} * (\sin^2 \theta) \}$$

where  $\langle p_t \rangle$  is the average transverse momentum in the fragmentation process and  $c$  is defined by the derivative of the multiplicity  $d\langle n \rangle / d\{\log(E_{\text{CM}})\}$ .

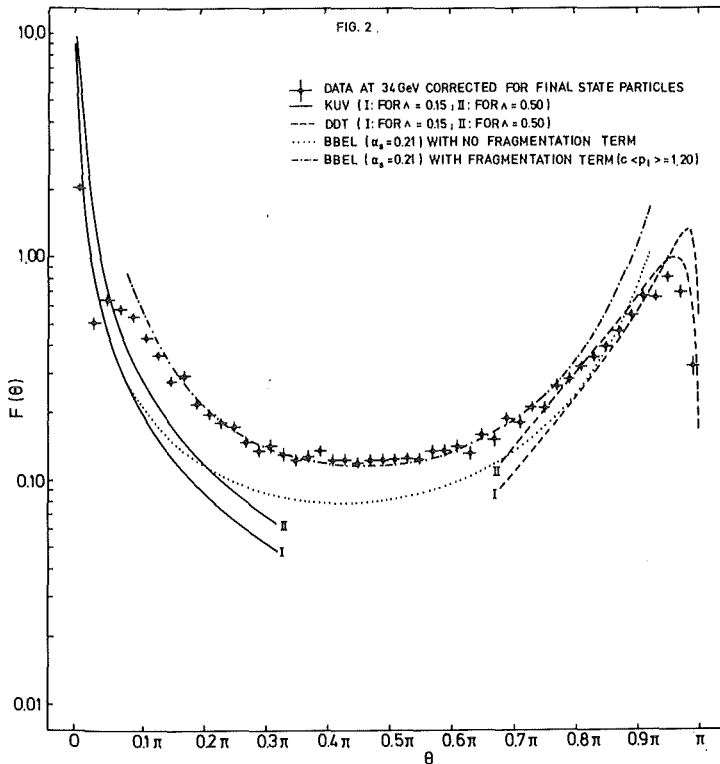


Fig. 2

$F(\theta)$  corrected to the level of final state particles at 34 GeV. Full line: QCD prediction of KUV; dashed line: QCD prediction of DDT; dashed-dotted: QCD prediction of BBEL with fragmentation term; dotted line: QCD prediction of BBEL without fragmentation term.

It has been suggested (2) to use the asymmetry distribution:

$$(5) \quad AS(\theta) = F(\pi - \theta) - F(\theta)$$

for the determination of  $\alpha_s$ , since, in first order QCD,  $AS(\theta)$  isolates the contribution from single gluon emission. In addition, Eq. (4), which is even under the interchange  $\theta \leftrightarrow \pi - \theta$ , suggests that the contribution from fragmentation effects will be greatly reduced.

The experimental asymmetry distributions (5) together with the theoretical results (2) are plotted in Fig. 3a and 3b for the two energies. By fitting the theoretical asymmetry function to the data in the range  $\theta_{\min} = 0.16\pi < \theta < 0.50\pi$ , we obtain the following values for  $\alpha_s$ :

$E_{\text{CM}}$	$\alpha_s$	$\chi^2/\text{DOF}$
22 GeV	$0.14 \pm 0.02$ (stat)	8.1/5
34 GeV	$0.15 \pm 0.02$ (stat)	6.1/5

Although  $\alpha_s$  can be determined by this method with a low statistical error, we are led to conclude that this determination suffers from substantially larger systematic uncertainties.

For the large acollinearity region ( $\theta$  close to  $\pi$ ), where only hadron pairs in opposite jets contribute, the data are expected to be dominated by multiple color radiative effects in the parton cascade. In this region we compared experimental data directly with absolute predictions made on the basis of pure QCD calculations, which generally depend on only one free parameter: the QCD scale  $\Lambda$ . These theoretical approaches based on leading approximations assume, that the computed parton distribution for  $F(\theta)$  will not be modified in a significant way by the hadronization process (1,2-8).

The primordial hadrons emerging are assumed to carry essentially the momenta of the related last parton in the cascade.

The experimental  $F(\theta)$  distribution is broadened due to the transverse momentum of the final hadrons introduced by the decay of the primordial hadrons. We tried to remove this effect by correcting the data to the level of primordial hadrons (using Monte Carlo techniques).

Figs. 4 show  $F'(\theta) = F(\theta)/\sin \theta$  near  $\theta = \pi$  ( $F'$  was chosen in order to remove a kinematic zero). We plotted  $F'(\theta)$  for final and primordial hadrons for two energies each.

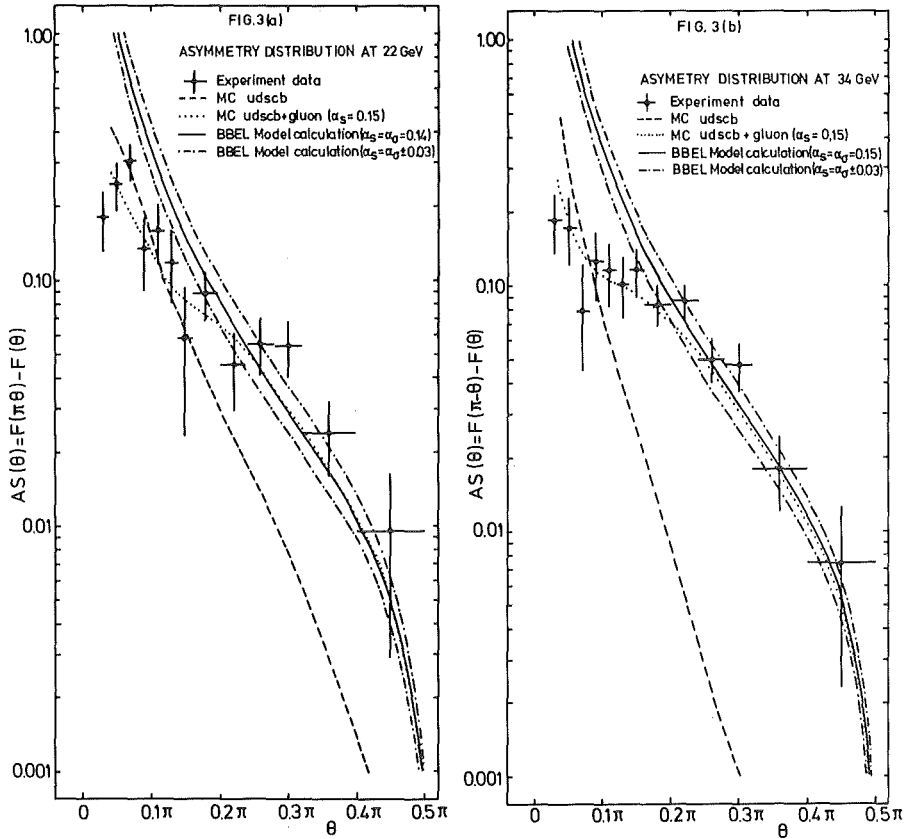


Fig. 3a Asymmetry distribution  $AS(\theta)$  at 22 GeV corrected to the level of final state particles. Full line: QCD predictions of BBEL, dashed line: Monte Carlo ( $q\bar{q}$ ) results, dotted line: Monte Carlo ( $q\bar{q}g$ ) results.

3b Asymmetry distribution  $AS(\theta)$  at 34 GeV corrected to the level of final state particles. Full line: QCD predictions of BBEL, dashed line: Monte Carlo ( $q\bar{q}$ ) results, dotted line: Monte Carlo ( $q\bar{q}g$ ) results.

The data show a reasonable agreement with the QCD predictions.

Generally it is found the the QCD calculations agree better with the primordial hadron distribution. The primordial distributions favor in all cases lower values of  $\Lambda$ . Whereas  $F(\theta)$  for final particles agree best for  $\Lambda$  values between 360 and 700 MeV,  $F(\theta)$  for primordial hadrons favors  $\Lambda$ 's between 100 and 150 MeV.

Recent pure QCD calculations by Rakow and Webber (10) going beyond 'Leading-Log-Approximation' exhibit a remarkable agreement with the data.

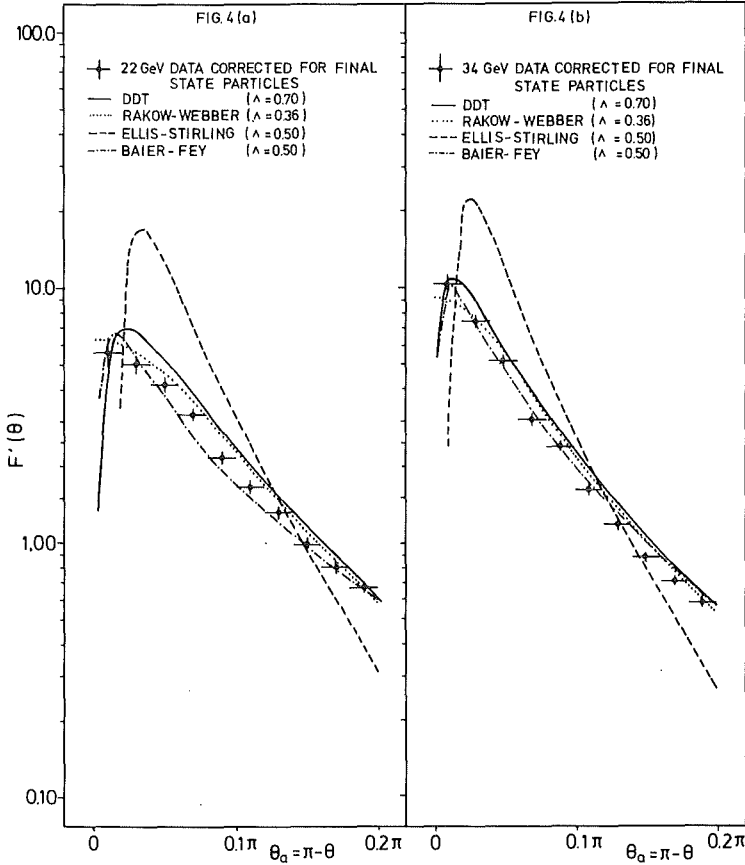
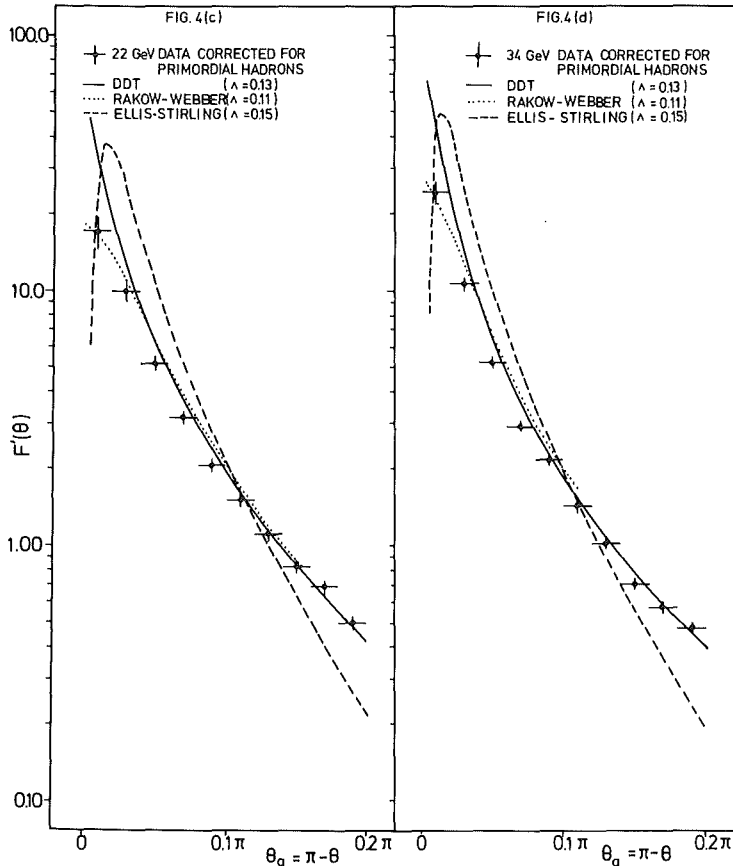


Fig. 4

a.  $F'(\theta)$  distribution at 22 GeV, corrected to the level of final state particles, compared with several QCD predictions: Full line: DDT Formula (5) ( $\Lambda = 0.70$  GeV); dashed line: Ellis and Stirling (6) ( $\Lambda = 0.50$  GeV); dotted line: Rakow and Webber (8) ( $\Lambda = 0.36$  GeV); dashed-dotted line: Baier and Fey (7) ( $\Lambda = 0.50$  GeV).

b.  $F'(\theta)$  distribution at 34 GeV, corrected to the level of final state particles, compared with several QCD predictions: Full line: DDT Formula (5) ( $\Lambda = 0.70$  GeV); dashed line: Ellis and Stirling (6) ( $\Lambda = 0.50$  GeV); dotted line: Rakow and Webber (8) ( $\Lambda = 0.36$  GeV); dashed-dotted line: Baier and Fey (7) ( $\Lambda = 0.50$  GeV).



c.  $F'(\theta)$  distribution at 22 GeV, corrected to the level of primordial hadrons, compared with several QCD predictions: DDT Formula (5) ( $\Lambda = 0.13$  GeV); dashed line: Ellis and Stirling (6) ( $\Lambda = 0.15$  GeV); dotted line: Rakow and Webber (8) ( $\Lambda = 0.11$  GeV).

d.  $F'(\theta)$  distribution at 34 GeV, corrected to the level of primordial hadrons, compared with several QCD predictions: Full line: DDT Formula (5) ( $\Lambda = 0.13$  GeV); dashed line: Ellis and Stirling (6) ( $\Lambda = 0.15$  GeV); dotted line: Rakow and Webber (8) ( $\Lambda = 0.11$  GeV).

References

- (1) Yu.L. Dokshitser, D.I. D'yakonov, S.I. Troyan, Phys.Lett. 78B (1978) 290
- (2) C.L. Basham, L.S. Brown, S.D. Ellis, S.T. Love, Phys.Rev.Lett. 41 (1978) 1585 (Formula 6,7); Phys.Rev. D19 (1979) 2018
- (3) Yu.L. Dokshitser, D.I. D'yakonov, S.I. Troyan, Fizika Elementarnykh Chastits (Leningrad 1979); Phys. Reports 58 (1980) 269 (Formula 208-210)
- (4) K. Konishi, A. Ukawa, G. Veneziano, Phys.Lett. 80B (1979) 259 (Formula 15); Nucl.Phys. B157 (1979) 45
- (5) G. Parisi, R. Petronzio, Nucl.Phys. B154 (1979) 427
- (6) S.D. Ellis, W.J. Stirling, Phys.Rev. D23 (1981) 214 (Formula 5.3a)  
S.D. Ellis, N. Fleishon, W.J. Stirling, Phys.Rev. D24 (1981) 1386
- (7) R. Baier, K. Fey, Nucl.Phys. B179 (1981) 49 (Formula 20)
- (8) P.E.L. Rakow, B.R. Webber, Nucl.Phys. B187 (1981) 254 (Formula 52)
- (9) R.D. Field, R.P. Feynman, Nucl.Phys. B136 (1978) 1
- (10) P. Hoyer, P. Osland, H.G. Sander, T.F. Walsh, P.M. Zerwas, Nucl.Phys. B161 (1979) 349
- (11) A. Ali, J.G. Körner, G. Kramer, J. Willrodt, Z.Physik C1 (1979) 202;  
Nucl.Phys. B168 (1980) 409
- (12) B. Anderson, G. Gustafson, C. Peterson, Z.Physik C1 (1979) 105  
B. Anderson, G. Gustafson, Z.Physik C3 (1980) 223  
T. Sjöstrand, LUND TP 80-3 (1980)

5.2.2 Search for Narrow Quarkonium States and Pair Production of New Heavy Quarks at C.M. Energies from 33.0 to 36.7 GeV \*

The total  $e^+e^-$  annihilation cross section into hadrons had been measured at c.m. energies between 33.0 and 36.72 GeV in steps of 20 MeV. The ave-

\* submitted to Phys.Lett. B

rage ratio  $R = \sigma(e^+e^- \rightarrow \text{hadrons})/\sigma_{\mu\mu} = 3.85 \pm 0.12$  (stat.)  $\pm 0.31$  (syst.) is consistent with the quark-parton model expectation for coloured u, d, s, c, and b quarks. For a narrow  $J^P = 1^-$  quarkonium state of a hypothetical t quark of charge  $2/3 e$ , we find an upper limit  $\Gamma_{ee} \cdot \Gamma_{\text{had}}/\Gamma_{\text{tot}} < 2.2$  keV at 95% c.l.. The observed number of aplanar final states excludes a contribution to R of  $4/3$  from a new quark with a mass between 6 and 16.5 GeV, and a contribution of  $1/3$  for quark masses between 9 and 16.5 GeV.

### 5.2.3 Analysis of the Energy Weighted Angular Correlations in Hadronic $e^+e^-$ Annihilations at 22 and 34 GeV \*

Measurements of energy weighted angular correlations in electron positron annihilations at c.m. energies of 22 GeV and 34 GeV are presented. The data are compared with perturbative QCD predictions. The theoretical predictions which refer to the partons describe the data reasonably well, depending on the approximations chosen. The effective strong coupling constant  $\alpha_s$  has been evaluated using a method where the effect of fragmentation is minimal. At large acollinearity angles QCD calculations going beyond the Leading Double Log approximation appear to be quite successful. The agreement is improved when the smearing effect of heavy resonance decays is taken out of the data.

### 5.2.4 Topology of Hadronic $e^+e^-$ Annihilation Events at 22 and 34 GeV CM Energy \*\*

The topology of hadronic  $e^+e^-$  annihilation events has been analysed using the sphericity tensor and a cluster method. Comparison with quark models including gluon bremsstrahlung yields good agreement with the data. The strong coupling constant is determined in 1st order QCD to be  $\alpha_s = 0.19 \pm 0.04$  (stat.)  $\pm 0.04$  (syst.) at 22 GeV and  $\alpha_s = 0.16 \pm 0.02 \pm 0.03$  at 34 GeV. The differential cross section with respect to the energy fraction carried by the most energetic parton agrees with the prediction of QCD, but cannot be reproduced by a scalar gluon model. These results are stable against va-

\* submitted to Z. Physik C

\*\* Phys.Lett. B110 (1982) 329

riations of the transverse momentum distribution of the fragmentation function within the quoted errors.

### 5.2.5 An Analysis of the Charged and Neutral Energy Flow in $e^+e^-$ Hadronic Annihilation at 34 GeV, and a Determination of the QCD Effective Coupling Constant \*

Using both charged and neutral components, 2600 multihadronic  $e^+e^-$  annihilation events, recorded at 34 GeV by the CELLO detector at PETRA, have been analysed in a calorimetric approach.

The fraction of energy carried by gamma rays is measured to be  $f_\gamma = 26.0 \pm 0.4$  (stat.)  $\pm 4.0$  (syst.) %. The neutral energy flow is seen to follow closely the overall energy flow. From the corrected oblateness distribution, a first order determination of  $\alpha_s = .16 \pm .01$  (stat.)  $\pm .03$  (syst.).

### 5.2.6 Scalar Lepton Search with the CELLO Detector at PETRA \*\*

We report on the search for "supersymmetric" scalar leptons conducted with the CELLO detector, at the PETRA  $e^+e^-$  storage ring. 11.1  $\text{pb}^{-1}$  of high energy data were analysed ( $33 \text{ GeV} < \sqrt{s} < 36.72 \text{ GeV}$ ). At a 95 X C.L., the existence of a scalar  $e$  is ruled out for masses between 2 GeV and 16.8 GeV; correspondingly, a scalar  $\mu$  is excluded between 3.3 GeV and 16 GeV, and a scalar  $\tau$  between 6 GeV and 15.3 GeV, as well as between the  $\tau$  mass and 3.8 GeV.

## 5.3 QED PROCESSES AND ELECTRO-WEAK INTERFERENCE

### 5.3.1 Coupling Strengths of Weak Neutral Currents from Leptonic Final States at PETRA

At the highest PETRA energies  $e^+e^-$  interactions start to be sensitive to weak neutral current effects and become an important test for the standard model of electromagnetic and weak interactions (1). Studies of these

\* Phys.Lett. B113 (1982) 427

\*\* Phys.Lett. B114 (1982) 287

effects have concentrated mainly on purely leptonic reactions because of clean experimental signatures and unambiguous theoretical predictions. Charge asymmetries in the angular distribution of  $\mu^+\mu^-$  and  $\tau^+\tau^-$  final states generated via interference of the electromagnetic current with the weak neutral axial vector current have been observed (2). In  $e^+e^- \rightarrow e^+e^-$  the differential cross section is quite sensitive to the weak vector current.

We report on results on the weak vector and axial vector coupling constants, determination of  $\sin^2\theta_w$  within the standard model, and upper limits for the deviation from the standard model current structure at high energies, based on new data for  $e^+e^- \rightarrow e^+e^-$  at  $\sqrt{s} = 34.2$  GeV and already published data for  $e^+e^- \rightarrow \mu^+\mu^-$  and  $e^+e^- \rightarrow \tau^+\tau^-$  from the CELLO detector.

The data used in this analysis correspond to a total integrated luminosity of  $\sim 11 \text{ pb}^{-1}$  taken with the CELLO detector in the center of mass energy region between 33 GeV and 36.7 GeV.

The differential cross sections for  $e^+e^- \rightarrow e^+e^-$  at  $\sqrt{s} = 34.2$  GeV and, for comparison, at  $\sqrt{s} = 22$  GeV, are shown in Fig. 1. The data sample contains  $16.5 \cdot 10^3$  events for  $\sqrt{s} = 34.2$  GeV and  $11.5 \cdot 10^3$  events for  $\sqrt{s} = 22$  GeV. In order to stress the features relevant to this analysis, the data are represented normalized to the first order QED expectation:

$$\delta(\cos \theta) = \frac{d\sigma/d\Omega}{d\sigma/d\Omega}_{\text{QED}}$$

At both energies the data are consistent with QED.

For  $\mu^+\mu^-$  and  $\tau^+\tau^-$  final states at  $\sqrt{s} = 34.2$  GeV the measured forward-backward weighted asymmetries are shown in Fig. 2. For details of the data analysis see Ref. (2).

The asymmetrie is defined as

$$A(\cos \theta) = \frac{d\sigma(\cos \theta) - d\sigma(-\cos \theta)}{d\sigma(\cos \theta) + d\sigma(-\cos \theta)}$$

Since the data have been corrected for radiative effects no asymmetry ( $A(\cos \theta) = 0$ ) is expected for pure QED.

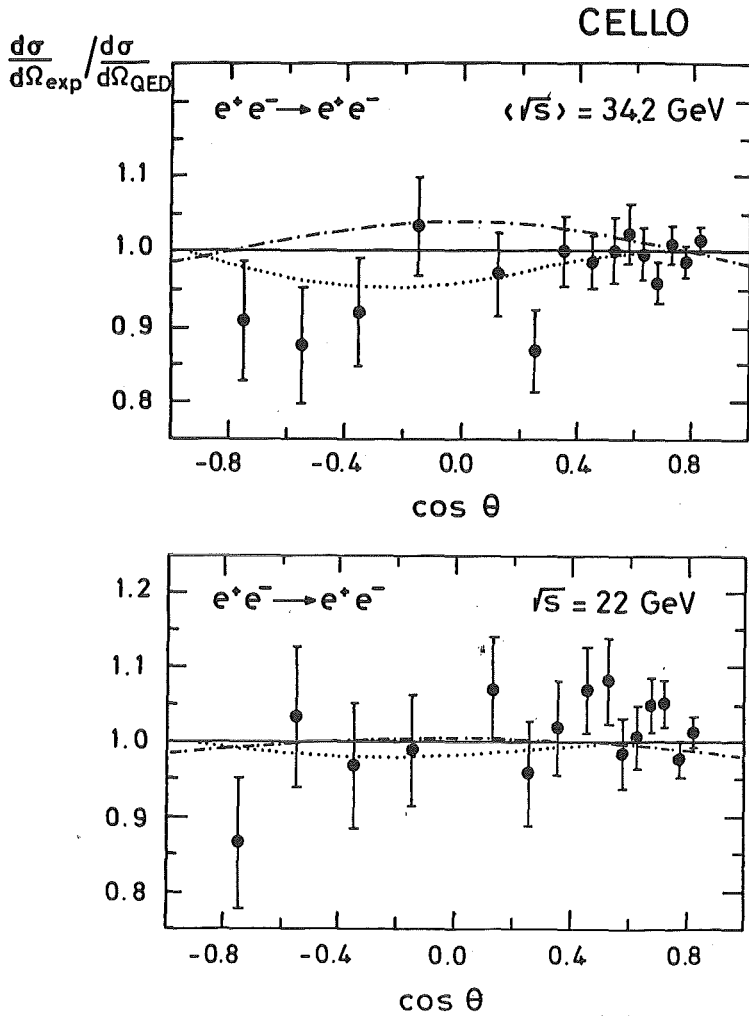


Fig. 1

The differential cross section  $d\sigma/d\Omega$  for Bhabha scattering at  $\langle \sqrt{s} \rangle = 34.2 \text{ GeV}$  and  $\sqrt{s} = 22 \text{ GeV}$  normalized to the QED cross section. The full line is the QED prediction. The dotted line represents the best fit for  $a^2$  and  $v^2$ . The dotted-dashed line shows the prediction for neutrino electron scattering ( $v^2 = 1.08$ ,  $a^2 = 0.0$ ).

Assuming  $\mu, \tau$  universality the asymmetries can be combined to yield  $\langle A \rangle = -8.7 \pm 4.0$  in good agreement with the expectation of  $-9.1\%$  from the standard model. The total cross sections for both reactions agree well with the QED expectation, but are less sensitive to an electroweak contribution compared to differential cross sections.

For the model-independent determination of the vector and axial vector coupling constants  $v^2$  and  $a^2$ , weak-electromagnetic interference and purely weak terms are considered.

Assuming lepton universality of the weak interaction all the above described data are used in a simultaneous fit for  $v^2$  and  $a^2$ . The mass of the vector boson  $M_Z^0$  was set to infinity which gives the weakest constraints. Including the normalisation uncertainty in the fit the following results are obtained:

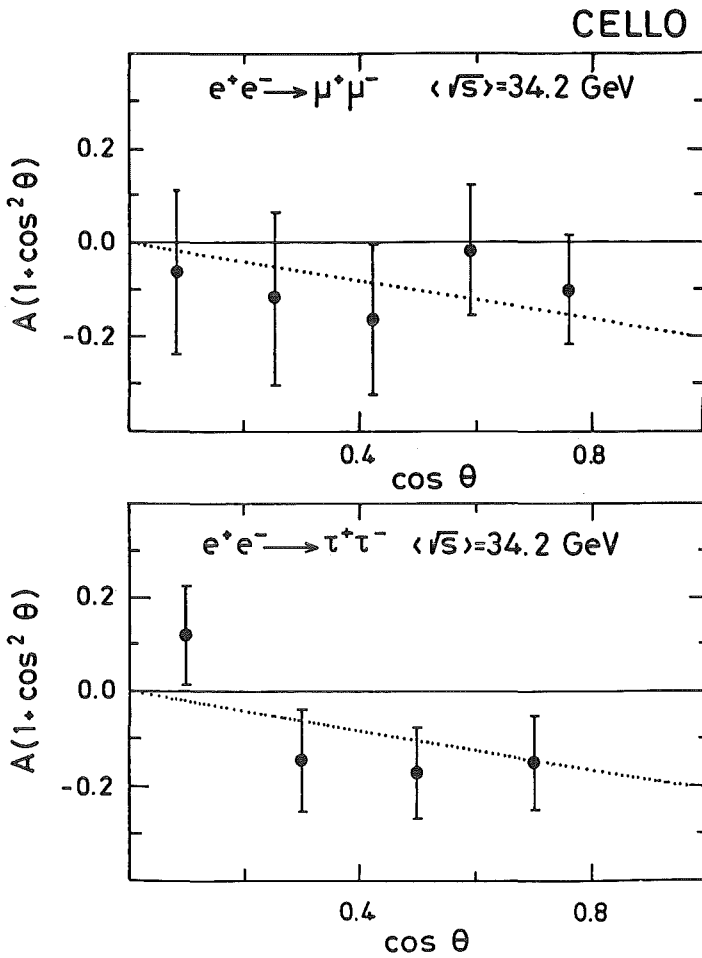


Fig. 2

The weighted asymmetry  $(1+\cos^2\theta) A(\cos\theta)$  for lepton pair production at  $\langle \sqrt{s} \rangle = 34.2 \text{ GeV}$ . The full line is the QED prediction. The dotted line represents the best fit for  $a^2$  and  $v^2$ .

$$a^2 = 1.22 \pm .47$$

$$v^2 = -.12 \pm .33$$

The expectation from the standard model is

$$a^2 = 1$$

$$v^2 = (4\sin^2\theta_w - 1)^2 = .008 \text{ for } \sin^2\theta_w = .228$$

Our results are in agreement with this prediction and the value measured for  $\sin^2\theta_w$  at low  $q^2$  (3). They are compared with determinations by other experiments in Table 1 (4).

The 95% C.L. contours of the fit result in the  $v^2 - a^2$  plane are shown in Fig. 3 together with the 2 allowed regions from neutrino electron scattering (3). The axial vector dominated solution from the neutrino data is fa-

Experiment	$a^2$	$v^2$	$\sin^2\theta_w$	C 95% C.L.	used reactions
CELLO	$1.22 \pm .47$	$-.12 \pm .33$	$.21 \begin{smallmatrix} + .14 \\ - .09 \end{smallmatrix}$	$<.031$	ee, $\mu\mu$ , $\tau\tau$
JADE	$1.56 \pm .44$	$.20 \pm .32$	$.25 \pm .15$	$<.039$	ee, $\mu\mu$
HAC	$0.16 \pm .88$	-	$.25 \pm .16$	-	ee, $\mu\mu$
MARK II	$0.96 \pm .64$	$<.61$	-	-	ee, $\mu\mu$
MARK J	$1.12 \pm .36$	$.04 \pm .44$	$.24 \pm .11$	$<.027$	ee, $\mu\mu$ , $\tau\tau$
PLUTO	$-.76 \pm .96$	$-.08 \pm .66$	$.23 \pm .17$	$<.06$	ee, $\mu\mu$ , $\tau\tau$
TASSO	$1.40 \pm .36$	$-.16 \pm .24$	$.27 \begin{smallmatrix} + .06 \\ - .07 \end{smallmatrix}$	$<.020$	ee, $\mu\mu$

Electroweak Coupling Parameters from Leptonic Reactions in  $e^+e^-$  Annihilation [2], [9].

Table 1  
Electroweak Coupling Parameters from Leptonic Reactions in  $e^+e^-$  Annihilations (2), (4).

vored by our result over the vector dominated by more than 2 standard deviations.

For Bhabha scattering  $v^2$  and  $a^2$  are correlated, the data prefer an  $a^2$  contribution but mainly constrain  $v^2$  to small values. The muon and tau pair asymmetry measurement gives the main constraint to  $a^2$  and is responsible for the non-zero weak effect.

Within the framework of the standard model the axial vector coupling is a constant. Only  $v^2$  and the mass of the neutral intermediate vector boson  $M_Z^0$  are dependent on  $\sin^2\theta_w$ .

$$v^2 = (4 \sin^2\theta_w - 1)^2$$

$$M_Z^0 = 37.2 \text{ GeV} / \sin \theta_w \cos \theta_w$$

Fitting all leptonic data with this single parameter we obtain

$$\sin^2\theta_w = .21 \begin{smallmatrix} + .14 \\ - .09 \end{smallmatrix}$$

This determination of the Weinberg angle is compared with results from other experiments in Table. 1.

As mentioned above the  $e^+e^-$  induced neutral current reactions are sensitive to contributions to vector currents not accounted for in the standard model and not observable in neutrino electron scattering or e D parity vio-

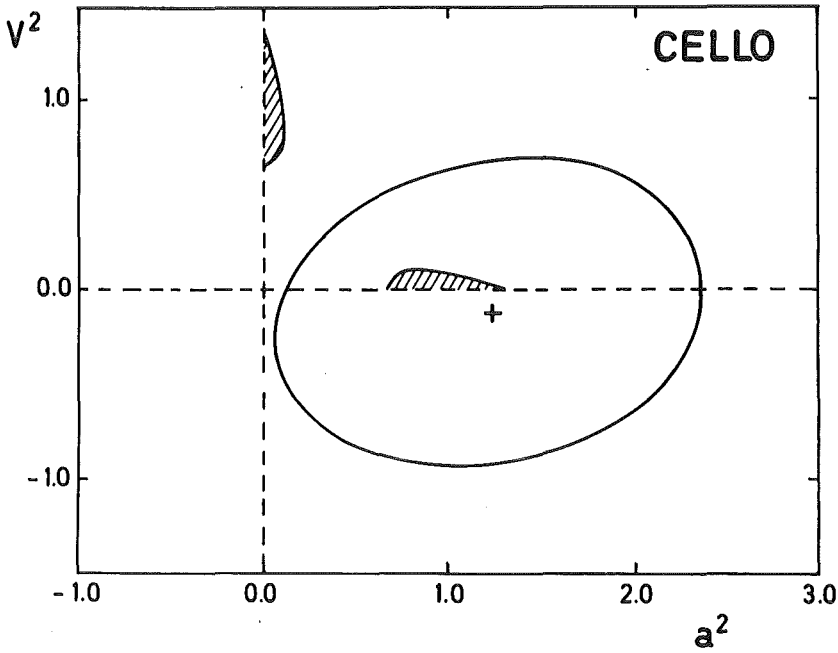


Fig. 3

Fig. 3  
The 95% confidence level contours for the electroweak coupling constants  $a^2$  and  $v^2$ . The two dashed areas show the 95% confidence level contours obtained by neutrino electron experiments.

lation experiments (5). In terms of  $v^2$  and  $a^2$  this possible contribution may be characterized by the parameter C

$$L_{\text{eff}}^{\text{NC}} = \frac{4G_F}{\sqrt{2}} \left[ (j^{(3)} - \sin^2\theta_w j_{\text{em}})^2 + C j_{\text{em}}^2 \right]$$

and

$$a^2 = 1$$

$$v^2 = (4 \sin^2\theta_w - 1)^2 + 16 C$$

In the standard model C should be zero. Assuming  $\sin^2\theta_w = .228$  our data are consistent with  $C = 0$ . Fitting for the parameter C with  $\sin^2\theta_w = .228$  we obtain the 95% C.L. upper limit

$$C < .031$$

Table 1 shows for comparison values of C obtained by other experiments. s

A mass of the intermediate vector boson considerably smaller than the standard model prediction should show up as a propagator effect which is ne-

glected in the above fit for  $v^2$  and  $a^2$ . Assuming  $v^2$  and  $a^2$  to the measured values of the neutrino electron scattering (10), our data set a lower limit at the 95% C.L. for the  $Z^0$  mass:

$$M_Z^0 > 57 \text{ GeV} \quad 95\% \text{ C.L.}$$

### References

- (1) G. Glashow, Nucl.Phys. 22 (1961) 579  
S. Weinberg, Phys.Rev.Lett. 19 (1967) 1264  
A. Salam in: Elementary Particle Theory, ed. H. Sventholm, Stockholm 1968
- (2) JADE Collaboration, W. Bartel et al., Phys.Lett. 108B (1982) 140  
TASSO Collaboration, R. Brandelik et al., Phys.Lett. 110B (1982) 73  
CELLO Collaboration, H.-J. Behrend et al., DESY 82-019, DESY 82-020  
MARK J Collaboration, B. Adeva et al., MIT-LNS 124 (1982)
- (3) G. Barbiellini, 1981 Int. Symposium on Lepton and Photon Interactions at High Energies, Bonn 1981, p. 623  
J.E. Kim et al., Reviews of Modern Physics 52 (1981) 211
- (4) MARK J Collaboration, D.P. Barber et al., Phys.Lett. 95B (1980) 149  
JADE Collaboration, W. Bartel et al., Phys.Lett. 99B (1981) 281  
TASSO Collaboration, R. Brandelik et al., DESY 82-0-32  
R. Hollebeek, 1981 Int. Symposium on Lepton and Photon Interactions at High Energies, Bonn 1981, p. 1

#### 5.3.2 Measurement of $e^+e^- \rightarrow \tau^+\tau^-$ at High Energy and Properties of the $\tau$ Lepton \*

The  $e^+e^- \rightarrow \tau^+\tau^-$  process has been measured using the CELLO detector at a mean total center of mass energy of 34.2 GeV using essentially all the decay channels of the  $\tau$  lepton. The measured cross section yields  $R = 1.03 \pm 0.05$  (stat.)  $\pm 0.07$  (syst.). Topological branching fractions are given for  $\tau \rightarrow 1$ ,

\* Phys.Lett. B114 (1982) 282

3 or 5 charged tracks. The angular distribution shows a clear  $1 + \cos^2\theta$  dependence with a forward-backward asymmetry of  $-.103 \pm .052$  corresponding to an axial-vector coupling  $a_\tau$  of the  $\tau$  to the weak neutral current given by  $a_\tau = -1.12 \pm .57$ .

### 5.3.3 Measurement of the Reaction $e^+e^- \rightarrow \mu^+\mu^-$ for $14 \leq \sqrt{s} \leq 36.1$ GeV \*

The reaction ( $e^+e^- \rightarrow \mu^+\mu^-$ ) has been measured between  $\sqrt{s} = 14.0$  GeV and  $\sqrt{s} = 35.4$  GeV. The total cross section result is in good agreement with the QED prediction and the following  $\Lambda_- = 101$  GeV.

The angular distribution at high energy ( $\langle\sqrt{s}\rangle = 34.2$  GeV) shows a fitted charge asymmetry of  $-.064 \pm .064$  in agreement with the W-S model prediction of  $-0.092$ , corresponding to an axial coupling parameter  $a^2 = 4 g_a^2 = 0.69 \pm 0.69$ .

## 5.4 ELECTRONS AND PHOTONS IN FINAL STATES OF $e^+e^-$ ANNIHILATION

### 5.4.1 Observation of Topologically Isolated Energetic Electrons in $e^+e^-$ Interactions

In  $e^+e^-$  interactions at 34 GeV center of mass energy, in an integrated luminosity of  $7.4 \text{ pb}^{-1}$ , 18 events are observed where an electron (positron) appears with an energy above 4 GeV, at large angle with respect to the beam direction, and well separated from other charged and neutrals produced in the reaction. Their characteristics are found to be in agreement with what is expected from deep inelastic e photon scattering and inelastic Compton scattering, with some multihadron annihilation contribution.

In order to search for isolated electrons we used the following criteria: let us consider the particles, charged and neutrals, going in the same hemisphere as the candidate. We call  $P_\parallel^\pm$  the sum of the momenta of the charged particles projected on the candidate track direction, and  $P_\parallel^0$  the corresponding quantity for the neutral ones. A track is called isolated if  $P_\parallel^\pm < 1 \text{ GeV}/c$  and  $P_\parallel^0 < 2 \text{ GeV}/c$ . These cuts were chosen to remove most of the events

coming from multihadronic production through one photon exchange. The neutral particle cut is softer because the calorimetric measurement is less precise than the central detector measurement and to avoid rejecting electrons accompanied by a soft bremsstrahlung photon.

Electrons were identified requiring that the calorimetric energy  $E$  must agree with the momentum  $P$  measured in the central detector and the longitudinal development of the shower must be consistent with the expected development of an electromagnetic shower.

The detected cross section is  $2.4 \pm 0.6$  (stat.)  $\pm 0.2$  (syst.) pb.

Several mechanisms can be invoked to interpret these data.

A first mechanism which has been considered is the reaction:

$$(1) \quad e^+ e^- \rightarrow e^+ e^- + X \quad (C = +)$$

where  $X$  is a hadronic system. When one of the emerging electrons is at large  $\theta$ , this process is called deep inelastic electron-photon scattering (DIS), the photon being a quasi-real one emitted by the electron scattered at small angle. The corresponding Feynman graph is shown in Fig. 1a.

The contribution of reaction (1) has been computed by generating events according to structure functions, which takes into account contributions from vector dominance (Fig. 1b), the quark parton model (Fig. 1c), and QCD corrections to the quark-parton model (Fig. 1d). The value of the QCD scale parameter used in the structure function was 0.1 GeV.

The predicted number of events is 9.3. In the kinematic region involved this result does not depend significantly on the QCD correction.

A second possible process is inelastic compton scattering (IC):

$$(2) \quad e^+ e^- \rightarrow e^+ e^- + X \quad (C = -)$$

This is a radiative Bhabha process where a real photon is replaced by a massive one which converts to a hadronic system  $X$  (Fig. 1e). A simulation

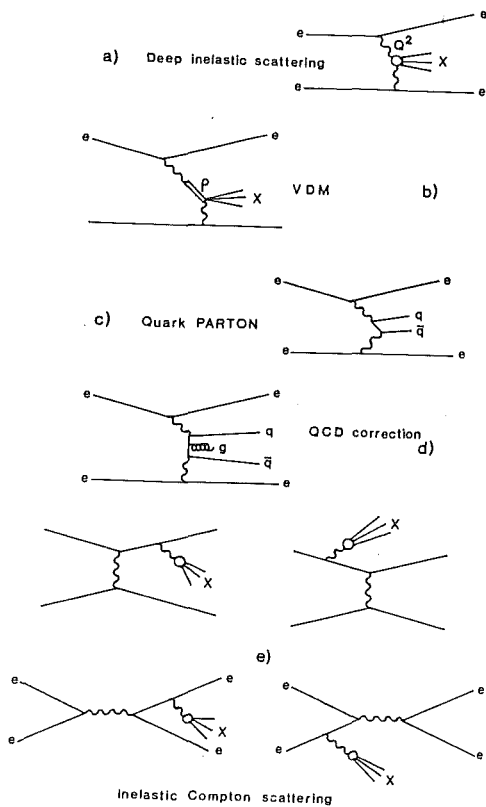


Fig. 1  
Inelastic Compton scattering

procedure similar to the one used for reaction (1) has been applied to reaction (2) and predicts 4.6 events.

Finally we have considered annihilation into hadrons:



which can contribute to the observed events through several mechanisms: hadron misidentification, very asymmetric photon conversion, Dalitz decay, or prompt electron emission via charm or beauty decay. The sum of all these mechanisms has been estimated by means of the detector simulation. Radiative corrections, c and b quark production and decay, and gluon emission are taken into account. The expected number of events is  $4.5 \pm 4.5$ , the error being a systematic one which reflects uncertainty in the modelling.

A summary of a comparison between the experimental data and the predictions for reaction (1) to (3) is shown in Figs. 2 and 3a) to 3f), together with the simulation of the sum of the non-annihilation processes (reactions (1) and (2)).

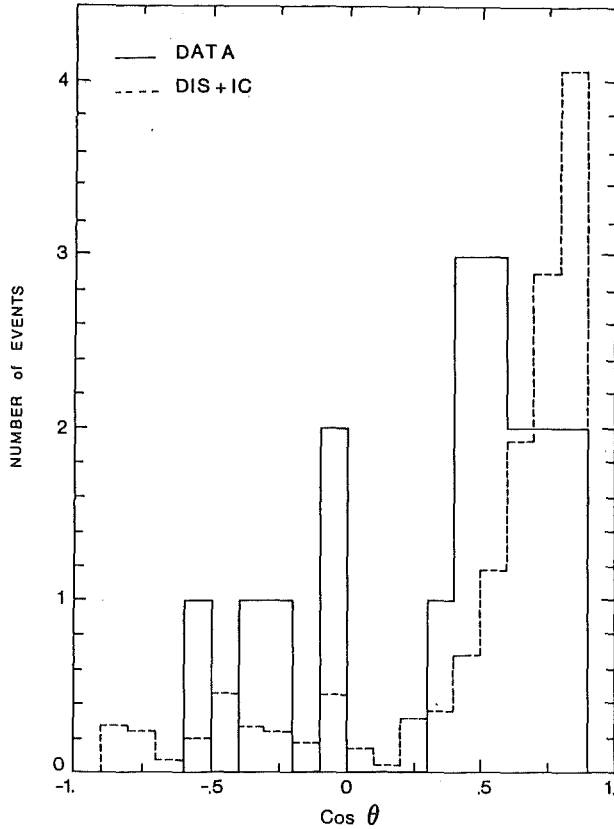
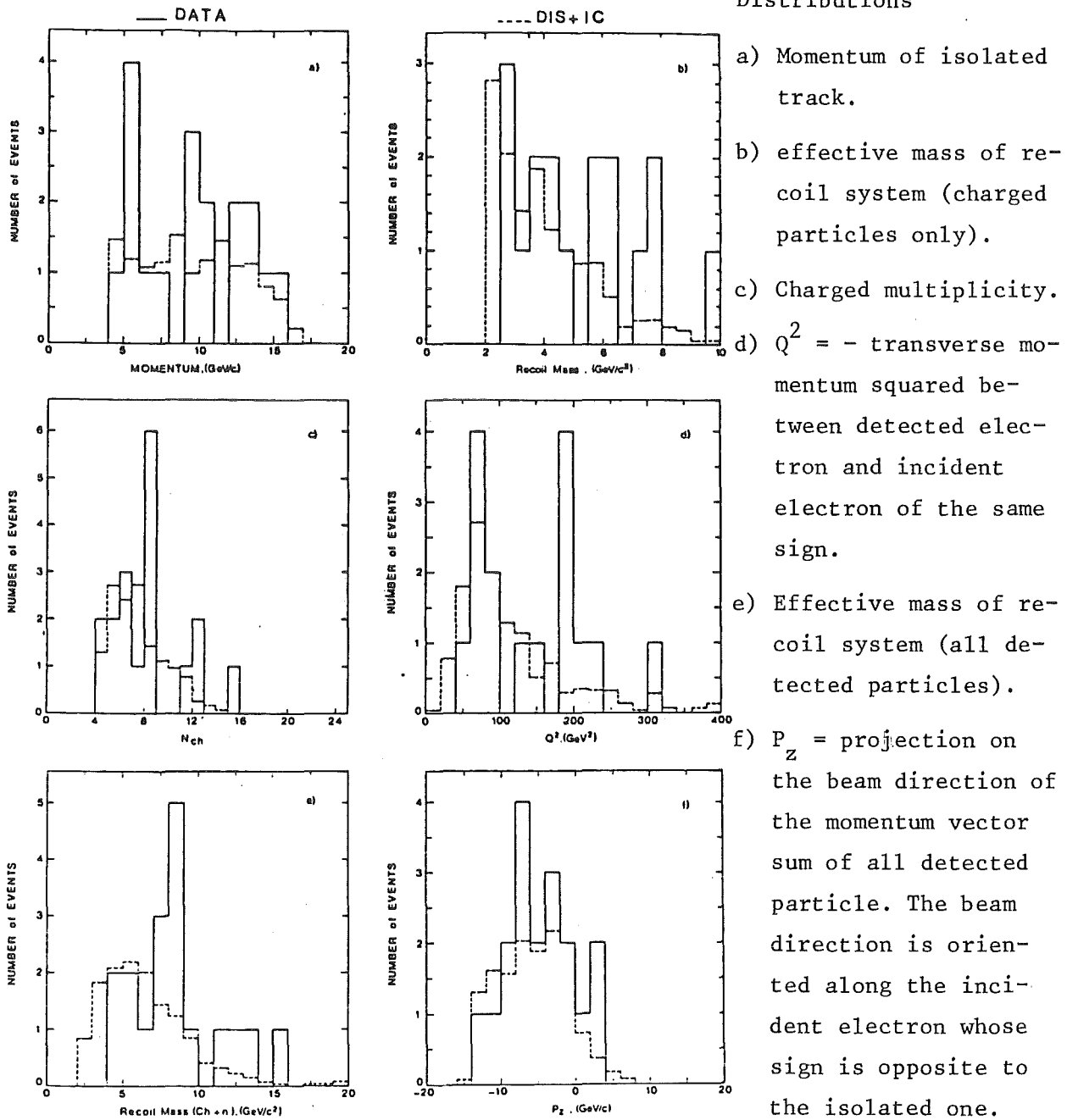


Fig. 2  
Cos  $\theta$  distribution,  
where  $\theta$  is the angle be-  
tween the outgoing de-  
tected electron and the  
incoming electron of the  
same sign.

From the angular distribution (Fig. 2) and the longitudinal momentum ( $P_z$ ) distributions (Fig. 3f) - which are expected to be symmetric for reaction (3)) - we see that the bulk of the observed events comes from a non-annihilation process. This confirms more strongly and independently of the cross section comparison the dominance of reactions (1) and (2).

Relative enhancement of reaction (1) can be achieved by selecting events for which  $\cos \theta > 0$ . and  $P_z < 0$ . 11 events are observed, at an average  $Q^2$  of  $118 \text{ GeV}^2$ , to be compared to expected numbers of 8.1, 2.5 and  $1.1 \pm 1.1$  for reactions (1), (2), and (3) respectively. In particular, by subtracting the expected contributions of reactions (2) and (3) from the real data, we get  $7.4 \pm 3.9$  events to be compared to the prediction, 8.1. This first investigation of the photon structure function at large  $Q^2$  is consistent with the  $\text{Log}(Q^2)$  dependence predicted by the theories (3). It is interesting to note that the QCD structure function term  $\text{Log}(Q^2/\Lambda^2)$  varies by a factor  $\sim 1.4$  from our small angle data (2) to our large angle data.

Fig. 3  
Distributions



- a) Momentum of isolated track.
- b) effective mass of recoil system (charged particles only).
- c) Charged multiplicity.
- d)  $Q^2 = -$  transverse momentum squared between detected electron and incident electron of the same sign.
- e) Effective mass of recoil system (all detected particles).
- f)  $P_z =$  projection on the beam direction of the momentum vector sum of all detected particle. The beam direction is oriented along the incident electron whose sign is opposite to the isolated one.

More detailed comparison between models and data would require additional statistics.

#### 5.4.2 Experimental test of QED predictions in $e^+e^-$ annihilation into hadrons

Most of the physics results in  $e^+e^-$  annihilation into hadrons rely on the correct application of radiative corrections. These have been calculated

from Quantum Electrodynamics (QED) by several authors. The leading order process in the fine structure constant  $\alpha$  leads to the final state

$$(1) \quad e^+ e^- \rightarrow q \bar{q} \gamma$$

We have performed an experimental test of the QED predictions for (1). For this purpose we have studied hadronic annihilation events with geometrically isolated photons. We have investigated whether these events originate from (1) and whether the photon distributions agree with the QED predictions.

Data samples of 2444 (1717) hadronic annihilation events have been taken at 34 GeV (22 GeV) cm energy with the CELLO detector at the  $e^+ e^-$  storage ring PETRA. Hadrons and photons have been analysed in the angular region  $|\cos \theta| \leq 0.86$  covered by the inner detector and the barrel LAr shower counter. Charged particles are measured with a momentum resolution of  $\sigma p/p = 2\% \times p$  (GeV). The energy of geometrically isolated electromagnetic showers can be determined with a precision of  $\sigma E/E = 13\%/\sqrt{E(\text{GeV})}$ . We searched for candidates of reaction (1) requiring an isolated photon to be emitted into the barrel shower detector ( $|\cos \theta| < 0.86$ ) with the following criteria:

- neutral showers emitted at less than  $5^\circ$  with respect to the candidate shower are absorbed into the neutral cluster
- electromagnetic energy of the neutral cluster  $E_\gamma$  larger than 2 GeV.
- If  $\vec{p}_i$  are the momenta of all particles (charged and neutral) occurring within an opening angle of  $60^\circ$  around the direction of the momentum of the neutral cluster  $\vec{p}_\gamma$ , the following cut is applied:

$$\sum_i \frac{\vec{p}_i \cdot \vec{p}_\gamma}{|\vec{p}_\gamma|} \leq 0.5 \text{ GeV}$$

After this selection we are left with 41 (37) candidate events for reaction (1) at 34 (22) GeV. This corresponds to  $(1.7 \pm 0.3)\%$  ( $2.2 \pm 0.3\%$ ) of all hadronic events at  $\sqrt{s} = 34$  (22) GeV.

Background for reaction (1) is expected from  $\pi^0$  and  $\eta$  production in the hadronic system. Our Monte Carlo simulation which fragments the quark-anti-quark pair according to the prescription of Feynman and Field shows, that

this contamination is low (25%) at  $\sqrt{s} = 34$  GeV whereas nearly half of the  $\sqrt{s} = 22$  GeV data (43%) are due to this background source, mainly  $\pi^0$ . We perform a background subtraction.

The differential cross section of radiative events with respect to the scaled shower energy  $z = 2E_\gamma/\sqrt{s}$  is shown in Figs. 1a and 1b.

The experimental results are compared to MC generated events of type (1). The initial state bremsstrahlung is generated following the QED calculation performed by Behrends and Kleiss (1). We observe good agreement at both energies within the statistical errors.

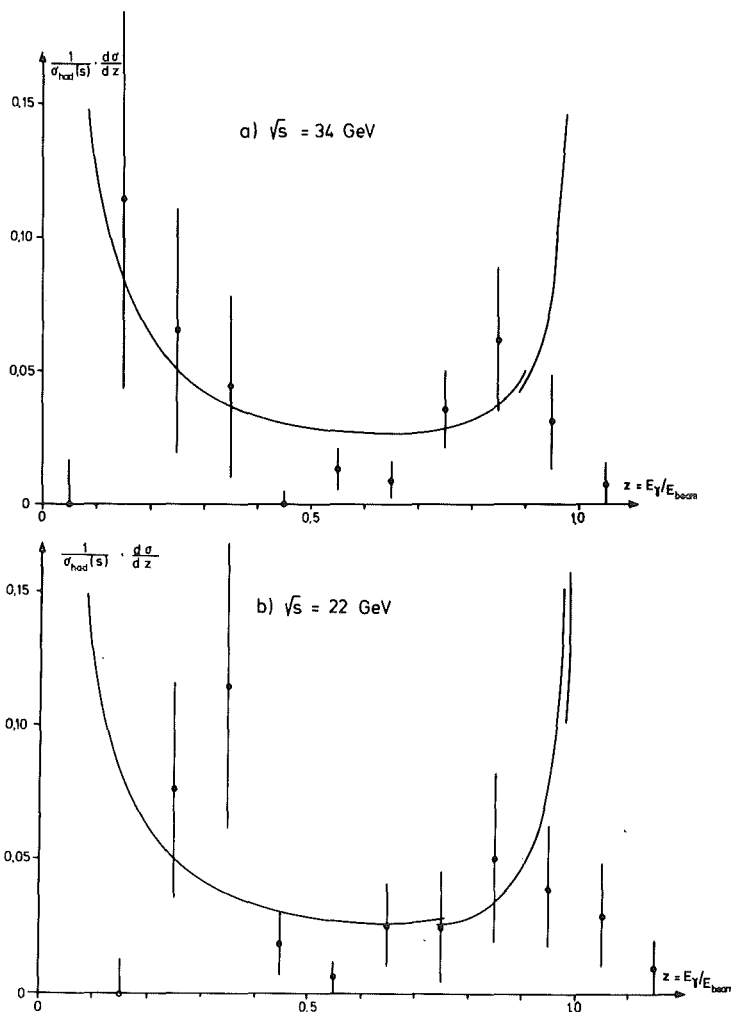


Fig. 1

Differential cross section of radiative events with respect to the scaled shower energy  $z = 2 E_\gamma/\sqrt{s}$  normalised to the total number of hadronic events

(a) at  $\sqrt{s} = 34$  GeV cm energy

(b) at  $\sqrt{s} = 22$  GeV cm energy

Since low background is expected at  $\sqrt{s} = 34$  GeV data should allow for further tests of the production process (1). The hadronic system should show all features of the non radiative two-jet events in its own rest frame. To study this the hadronic system of the isolated photon events at  $\sqrt{s} = 34$  GeV were boosted back by the observed momentum of the isolated shower. Two-jet variables were calculated and corrected for detector effects. Figs. 2 and 3 show average thrust and sphericity of the resulting hadronic systems as a function of the total hadronic energy  $E_{\text{had}} = \sqrt{s^T} = 4 E_B (E_B - E_\gamma)$ . Within the large statistical errors, data are in good agreement with measurements obtained in non radiative two-jet events.

We conclude that the predominant source of hadronic events including geometrically isolated neutral showers is initial state bremsstrahlung. The differential cross section with respect to the photon energy agrees well with QED predictions.

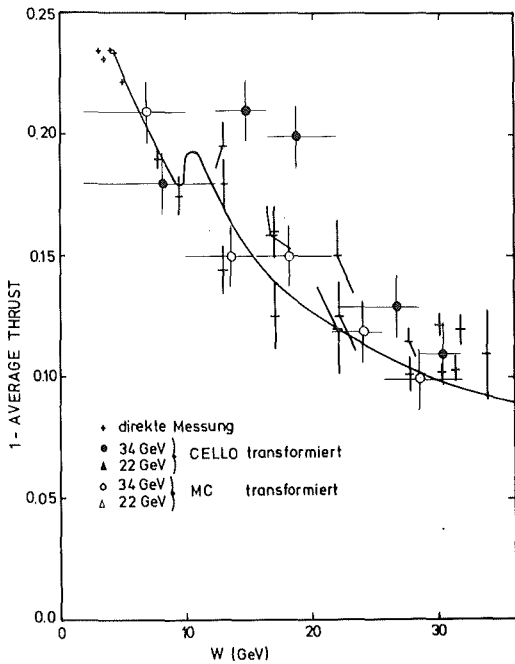


Fig. 2

$\langle 1-T \rangle$  versus center of mass energy

- transformed events measured at the CELLO detector at  $\sqrt{s} = 34$  GeV
- transformed MC events at  $\sqrt{s} = 34$  GeV
- + directly measured results from other experiments.

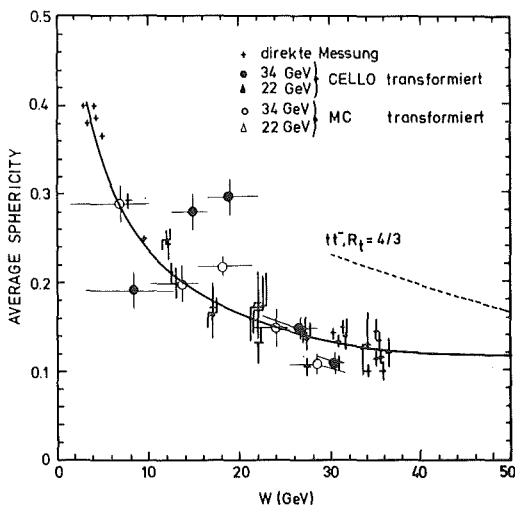


Fig. 3

$\langle S \rangle$  versus center of mass energy

- transformed events measured at the CELLO detector at  $\sqrt{s} = 34$  GeV
- transformed MC events at  $\sqrt{s} = 34$  GeV
- + directly measured results from other experiments.

Reference

- (1) F.A. Behrends and R. Kleiss, Nucl.Phys. B178 (1981) 141

5.4.3 Determination of the radiative width of the  $\eta'$  and  $A_2$  from two photon exchange production \*

From the two photon exchange processes  $e^+e^- \rightarrow e^+e^-\eta'$  (1958)  $\rightarrow e^+e^-\pi^0\gamma$  and  $e^+e^- \rightarrow e^+e^-A_2$  (1310)  $\rightarrow e^+e^-\pi^+\pi^-\pi^0$  observed using the CELLO detector at PETRA the radiative widths of the  $\eta'$  and  $A_2$  have been determined with the results:

$$\Gamma_{\gamma\gamma}(\eta') = 5.4 \pm 1.0(\text{stat.}) \pm 0.7 (\text{syst.}) \text{ keV}$$

$$\Gamma_{\gamma\gamma}(A_2) = 0.59 \pm 0.15 (\text{stat.}) \begin{matrix} + 0.31 \\ - 0.08 \end{matrix} (\text{syst.}) \text{ keV}$$

5.4.4 Measurement of inclusive  $\gamma$  and  $\pi^0$  spectra and a comparison of the neutral and charged components in hadronic  $e^-$  events in  $e^+e^-$  annihilation at 34 GeV \*\*

The photonic part of multihadronic  $e^+e^-$  annihilation events has been analysed at c.m. energy of 34 GeV. The photonic energy fraction per event is determined to be  $f_\gamma = 0.251 \pm 0.003 (\text{stat.}) \pm 0.04 (\text{syst.})$ . The neutral and charged components of the events are analysed separately revealing close similarity in thrust axis directions and momentum distributions in agreement with the hypothesis that most photons result from  $\pi^0$  decay.  $\pi^0$ 's are reconstructed separately and used to determine the inclusive cross section. Comparing these cross sections with lower energy data from SPEAR we find some indication for scaling violation.

\* Phys.Lett. B114 (1982) 378

\*\* submitted to Zeitschrift f. Physik C

## 6. INSTRUMENTATION

### 6.1 Status of the Magnetic Spectrograph "Little John"

H.J. Gils, J. Buschmann, M. Heinz, J. Krisch<sup>+</sup>, H. Rebel,  
and S. Zagrowski

Kernforschungszentrum Karlsruhe, IAK II

The magnetic spectrograph "Little John" at the Karlsruhe Cyclotron Laboratory has been designed for low background nuclear reaction studies at small reaction angles (down to  $0^\circ$ ) induced by light complex ions ( $^2\text{H}$ ,  $^4\text{He}$ ,  $^6\text{Li}$ ,  $^{12}\text{C}$ ,  $^{14}\text{N}$ ,  $^{16}\text{O}$ ,  $^{20}\text{Ne}$ ) (1). The magnets of the spectrograph (two quadrupoles, one  $60^\circ$  deflecting dipole, one sextupole) have been constructed and mounted on a rotatable support in the experimental area of the cyclotron in July 1981. After loading the support with the magnets an undesired tumbling of the central axis was observed. It was reduced to a negligible amount by reinforcing the mounting of the axis considerably. A view of the spectrograph looking from the focal plane detector towards the target chamber is shown in Fig. 1.

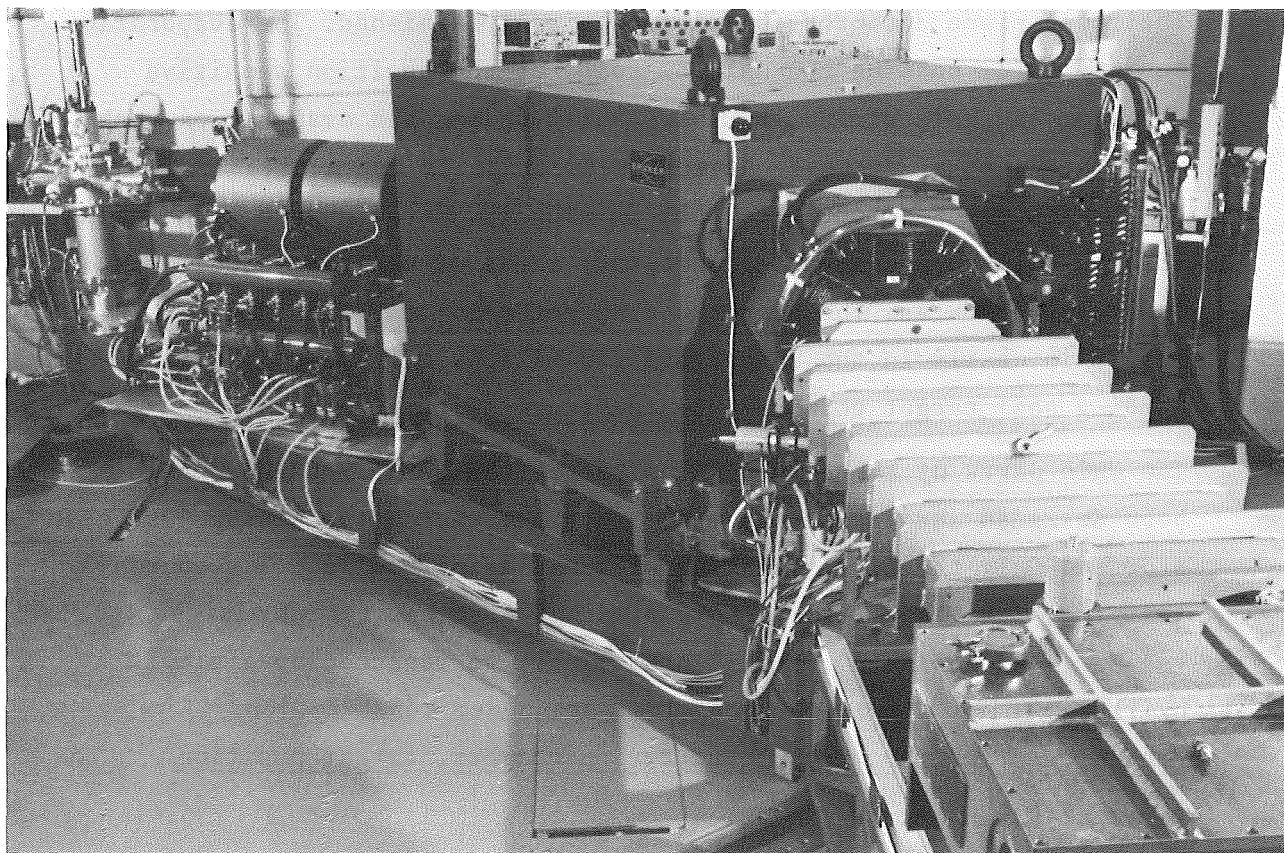


Fig. 1 View of the magnetic spectrograph "Little John" looking from the focal plane detector towards the target chamber.

Presently, the status of the different components of the spectrograph is as follows

- Magnets and power supplies

The magnets have been adjusted with an accuracy of about 0.1 mm. The power supplies are connected and have been tested together with the magnets.

- Vacuum system

Except of the final sliding seal target chamber (2) (which is preliminary replaced by a simple fixed angle chamber) the vacuum system is completely mounted and has been operated (3). Measurements of the total leakage rate yielded  $2 \times 10^{-3}$  mbar l/sec. The localization of the remaining small leaks will be performed soon. Since in the beam guiding system the pressure is usually one order of magnitude higher and also containing pumping oil contaminants a cryotrap (4) was installed at the entrance of the scattering chamber consisting of a 150 l/min diffusion pump and a cooled pipe.

- Focal plane and acceptance detectors

The focal plane detector (5) is mechanically finished. The evaporation equipment for coating the cathode foils of the position sensitive detectors by gold stripes has been built up and the evaporation technique has been elaborated. Several sets of foils are available. The gas supply and control system is also in operation and forthcoming efforts will be focussed on laboratory tests of position sensitivity and other features. The acceptance detector (6) including its gas supply is nearly in the same stage and will be tested soon.

- Sliding seal target chamber and acceptance slits

The main parts of the sliding seal target chamber (2) have been designed and constructed (Fig. 2). The vacuum tests have just been started. Only the final mounting of the sliding seal and its connection to the rotatable support is missing. Also the target sluice yet has been designed. It will preliminary be replaced by a simple existing sluice. The acceptance slits are under construction.

- Control systems for vacuum, scattering chamber, target position and acceptance slits

The control systems for driving the vacuum components, detector holder inside the target chamber, the target holder and the acceptance slits are under construction and partly already tested (3,4). In particular, the installations connecting the com-

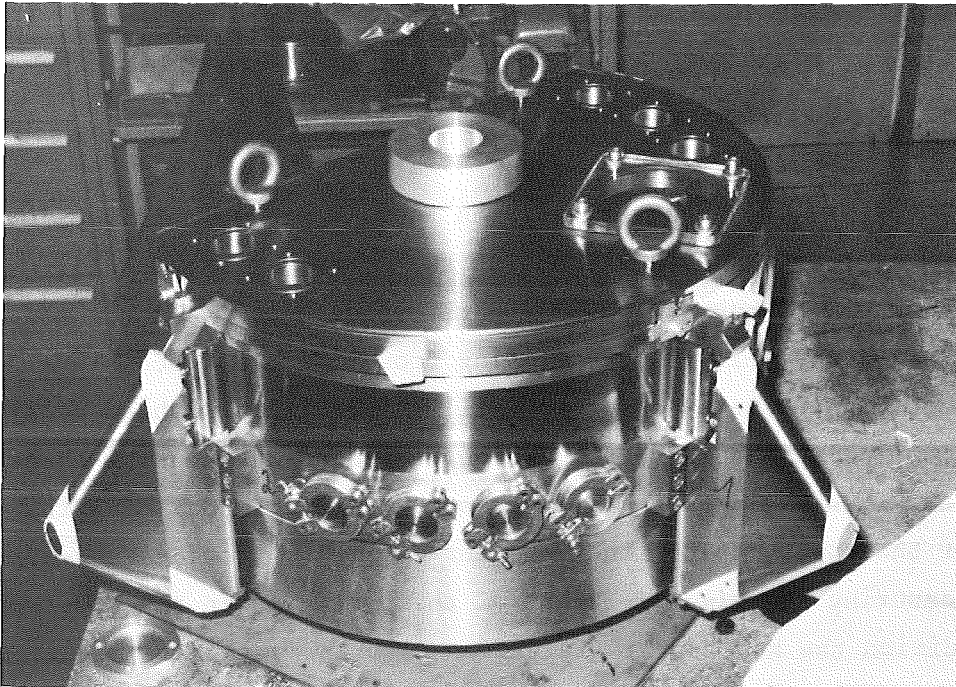


Fig. 2 The sliding seal target chamber during vacuum tests in the workshop

ponents and the different operation switch boards in- and outside of the experimental hall are nearly finished.

The further time schedule for bringing the spectrograph into operation is marked by a first beam time planned in autumn 1982 in order to perform rough measurements of the main features like dispersion and momentum resolution by use of a position sensitive surface barrier detector instead of the focal plane detector. Extensive measurements of its ion optical properties (needing the acceptance slits and the focal plane detector) will follow. First nuclear physics experiments are planned for spring 1983.

- (1) H.J. Gils, KfK Report 2972 (1980)
- (2) J. Buschmann, H.J. Gils, J. Krisch, H. Rebel, S. Zagromski, and K. Feißt, unpublished report, 1981
- (3) J. Buschmann, F. Deutsch, H.J. Gils, H. Rebel, K.J. Rist, W. Seith, R. Weber, S. Zagromski, and K. Altai, unpublished report, 1981
- (4) G. Ludwig, J. Buschmann, unpublished report, 1982
- (5) S. Zagromski, unpublished report, 1980
- (6) M. Heinz, unpublished report, 1982

<sup>+</sup>Kernforschungszentrum Karlsruhe, IT-M

## 6.2 An Acceptance Detector for the Magnetic Spectrograph "Little John"

M. Heinz, H.J. Gils, and H. Rebel

Kernforschungszentrum Karlsruhe, IAK II

The magnetic spectrograph "Little John" should predominantly allow low background nuclear reaction studies at small reaction angles (1). One important origin of background in a particle detector (also in a spectrograph) in general is slit scattering from the acceptance slits. In order to avoid this the spectrograph will be equipped with an active acceptance slit (acceptance detector) which is placed between the target chamber and the first magnet of the spectrograph. Besides defining the acceptance of the spectrograph the detector will also provide the start signal for measuring the time-of-flight of the particles in the spectrograph. In addition the horizontal (furtheron also the vertical) position of a particle transversing the detector will be measured. Thereby the angle of the particle trajectory with respect to the optical axis can be determined. This is important for achieving a high angular resolution in spite of a high angular acceptance. Also the calculation and correction of ion optical aberrations of the spectrograph is much easier when knowing the trajectory angle. A position sensitive parallel plate avalanche counter (PPAC) has been shown (2) to be most appropriate for these purposes. Its main features are:

- it is a gas detector, which works in the proportional region,
- due to a low gas pressure and small thickness the energy loss and the energy and angle straggling of the particles which pass the detector are small,
- it has good time and position resolution.

Fig. 1 shows the acceptance detector schematically. The window foils separate the gas filled volume (Isobutan) of the detector from the vacuum system of the spectrograph. The anode and the cathode are gold coated foils of polypropylen ( $60 \mu\text{g}/\text{cm}^2$ ). The gold coating on the anode is homogeneously distributed, whereas on the cathode there are gold stripes, connected by a delay line providing position information.

The acceptance of the detector is defined by the homogeneous gold area of the anode. This is also the acceptance of the spectrograph. Particles could pass the area beyond the gold layer but inside the foil frame.

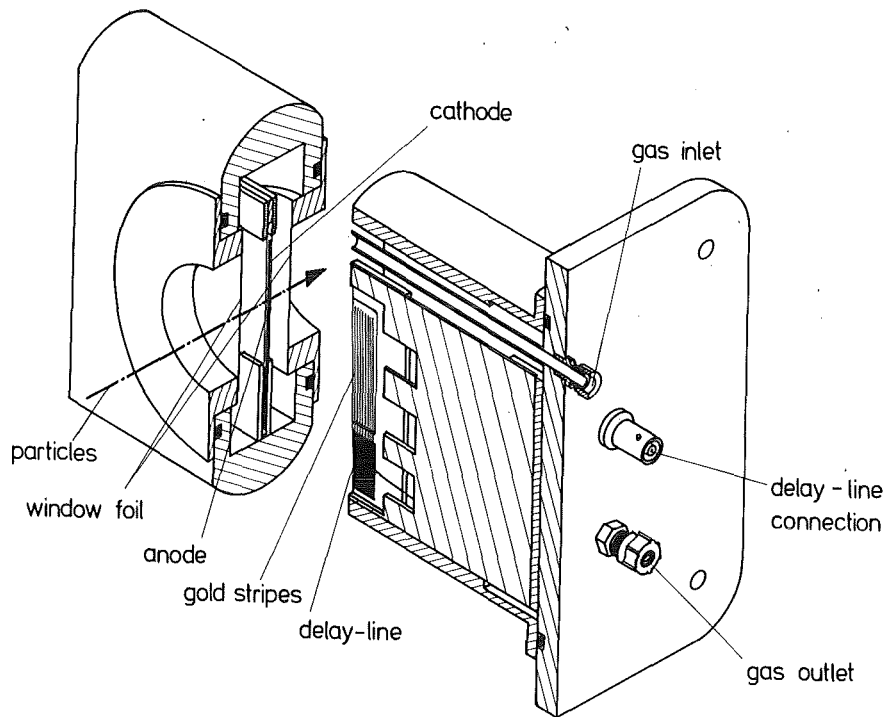


Fig. 1 The set-up of the acceptance detector

This part of the foil is electronically insensitive and particles which passed this area are not accepted even if they reach the focal plane detector (3). When a charged particle passes the active area of the detector there is a time difference between the pulses from the anode and the cathode. This gives the horizontal position of the particle. The signal from the anode is also the start signal for the time-of-flight measurement.

The mechanical construction of the detector is finished and the electrical components are ready. Presently, tests of the detector have been started.

- (1) H.J. Gils, KfK Report 2972 (1980)
- (2) H. Lettau, H.G. Bohlen, M.R. Clorer, G. Ingold, H. Ossenbrink, and W. von Oertzen, Nucl. Instr. and Meth. 184 (1981) 461.
- (3) S. Zagromski, unpublished results, 1980.

### 6.3 Computer Control of the Vacuum System of the Magnetic Spectrograph "Little John"

D. Manger, T.J. Thouw, and J. Buschmann  
Kernforschungszentrum Karlsruhe, IAK II

The computer control concept of the vacuum system (1) is based on the aim of protecting the vacuum equipment and environment from damage caused by technical defects/malfunctions and/or operator mistakes.

Each change of state of the vacuum system (e.g. by manual action) will be reported to the computer control program in the form of an "interrupt" request by the "CAMAC" interface modules (2). It is the responsibility of the control program to identify the CAMAC interrupts and to perform the appropriate reaction.

The control program, whose basic structure is shown in Fig. 1, is written in Fortran IV (3) on a Data General Nova-2 mini computer under the real time, disk oriented operating system "RDOS". Only the CAMAC interrupt driver used is written in assembler (4).

The control program is built around two essential abilities of the Nova-2/RDOS computer system: Multitasking and overlay program structuring. Overlay technique, although quite slow, is used extensively to economize core memory (36 K bytes of effective user space) as in most cases the vacuum process is not time critical (time critical events are handled by core resident tasks), whereas multitasking mode ensures that events can be processed in parallel.

At program start, the main task takes charge and "swaps" in the dialog program which does the initialization of the experimental parameters etc. The swapped program is invoked from disk to core whereas the core image of the invoking program is temporarily saved on disk. Upon completion, the dialog program stores all essential data on a disk file and returns control to the control program which then retrieves this data. This method enables all - crucial - "user core space" to be used by the actual control tasks.

After the initialization phase, the main task loads an overlay routine which checks the state of the vacuum system and - if needed - does the necessary reactions to bring up the vacuum system to a defined safe state.

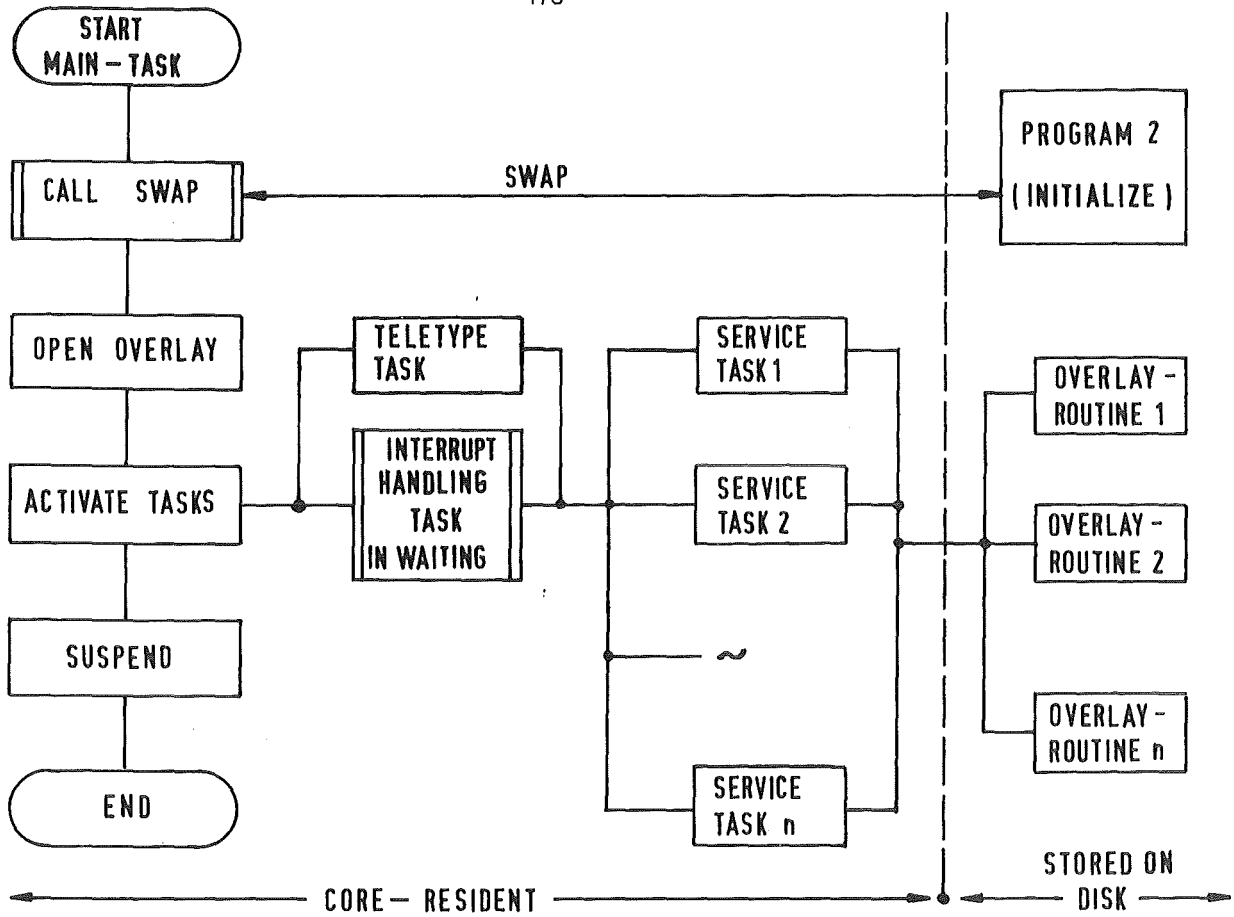


Fig. 1 Structure of the control program

The next step is to define the other tasks which then suspend themselves, which means that these tasks are not ready to proceed, but are still alive until they are needed. Only the interrupt decoding task and a task which accepts predefined commands from the teletype are ready to proceed.

The interrupt decoding task waits for and identifies interrupts whenever a CAMAC request is generated by a CAMAC module. Immediately after that, this task activates the appropriate "service task" according to the interrupt code. On his part, the service task (which is core resident) loads an overlay routine which does the actual "event" processing. After activating a service task, the interrupt decoding task immediately returns to the "waiting state" until the next interrupt occurs. In this way, a new interrupt can be accepted while the old one is still being processed. Task priorities, overlay and task flags determine which task runs first, the use of overlay space and whether a task is still busy or not.

All other tasks not belonging to the vacuum system such as the stepping motor control, magnetic field monitoring, on line data processing etc. can be built in this control program in the same manner as the vacuum control tasks.

This structure renders program flexibility and the possibility for program growth and unforeseen future demands.

- (1) J. Buschmann, H. Rebel,  
unpublished report, 1980
- (2) CAMAC, ein modulares Informationssystem in der Datenverarbeitung  
EUR 4100 d (1969)
- (3) Data General Corporation: Fortran IV User's Manual (1978)
- (4) G. Leinweber,  
unpublished Report, 1981

#### 6.4 Splitting Interface Connecting an ADC-System to two Independent On-Line Computers

S. Zagromski, G. Pätzold, and F. Deutsch  
Kernforschungszentrum Karlsruhe, IAK II

In multiparameter experiments performed at the cyclotron, e.g., with solid state or gas detector telescopes or in future with the magnetic spectrograph, the signals from the detection system are digitized by an ADC system and then stored event by event on magnetic tape. The whole acquisition system is controlled by a NOVA 2 computer. Due to the limited central memory of the computer an on-line data evaluation like particle identification was not realized up to now. However, for operating the magnetic spectrograph correctly, a supervision of sorted and evaluated data is necessary and will be also very useful for conventional detector experiments. A simple and rather unexpensive way to realize an on-line data processing was offered by the availability of another NOVA 2 computer very similar to the first one which is used for the control of the magnets and vacuum system of the spectrograph. This second computer can be used for data evaluation in parallel. For that purpose an interface was designed and brought into operation which connects the ADC-system to both computers.

A block diagram, showing the splitting interface integrated into the ADC and computer system is shown in Fig. 1. Data coming from the ADC's via

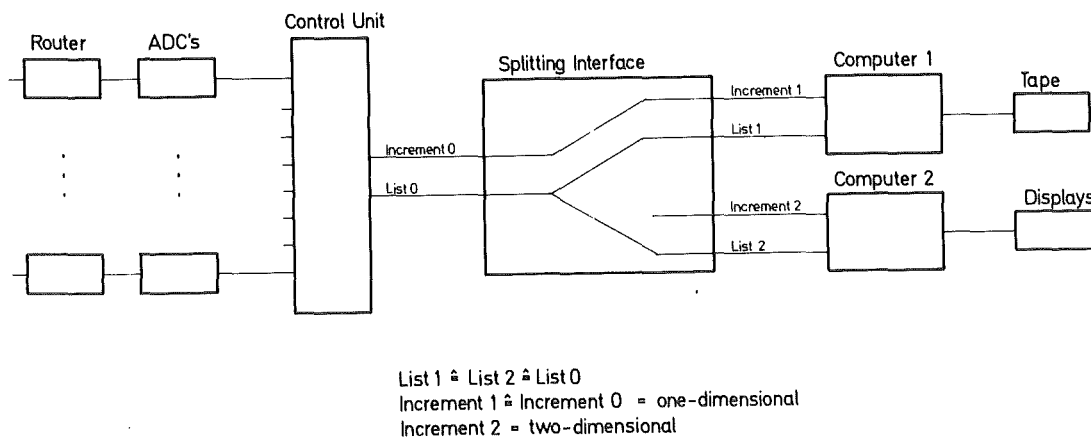


Fig. 1 Block diagram of interconnected splitting interface

the control-unit are transmitted serially to the computers. Transmission in the list and increment channel are independent with its own "data ready" and "data accepted" signals.

List-mode data contain a router as well as an ADC-assignment and are stored event by event. Increment data are generated by hardware in the control-unit and transmitted as addresses in such a way, that spectra for each parameter are placed one after the other in the external memory.

The splitting interface allows parallel data supply to both computers as shown in the block diagram. In addition, it generates two-parameter-spectra by hardware, up to four of them, from the list-mode data, which can be fed into the increment input of one of the two computers (without further evaluation). These two-parameter spectra can be displayed.

The list-mode input of one or both of the two computers is always supplied with data when it is free for data acceptance. In the computers the data are buffered by software. If one of the buffers is full, the flux to the other computer is not disturbed during the switching time of the first computer. Each of the two list outputs is accompanied with a separate dead-time signal. Even if one computer accidentally stops, the operation of the second computer and the data flux to it is not disturbed.

## 6.5 Recent Improvements of the Experimental Set-up for Neutron Capture Cross Section Measurements

G. Rupp

Kernforschungszentrum Karlsruhe, IAK II

The experimental set-up for neutron capture cross section measurements has been improved recently in two points:

(i) The automatic sample changer was redesigned to achieve better reliability and to facilitate sample adjustments. To this end the mechanical switches for the definition of the sample position were replaced by electromagnetic switches with a reproducible accuracy of  $\pm 0.01$  mm. In addition, the range of adjustment of the switches is no longer limited to a narrow region but extends over the total active length of 700 mm. The old drive of the sample changer has also been replaced by linear drive nuts which greatly reduced the vibrations during movements.

(ii) The extremely fragile construction of the sample frame (which is mounted on the sample changer) gives rise to small but non-negligible differences in the distance between the various samples and the neutron target. Additional distance differences occur due to the different sample thicknesses. In order to normalize the measured count rates of all samples to a common solid angle, regular distance measurements are carried out during the experiments. On our set-up distance measurements by mechanical means (caliber etc.) are limited to an accuracy of  $\pm 0.2$  mm. Therefore, an eddy current device has been installed which allows for contact-free distance measurements with an uncertainty of less than 0.01 mm.

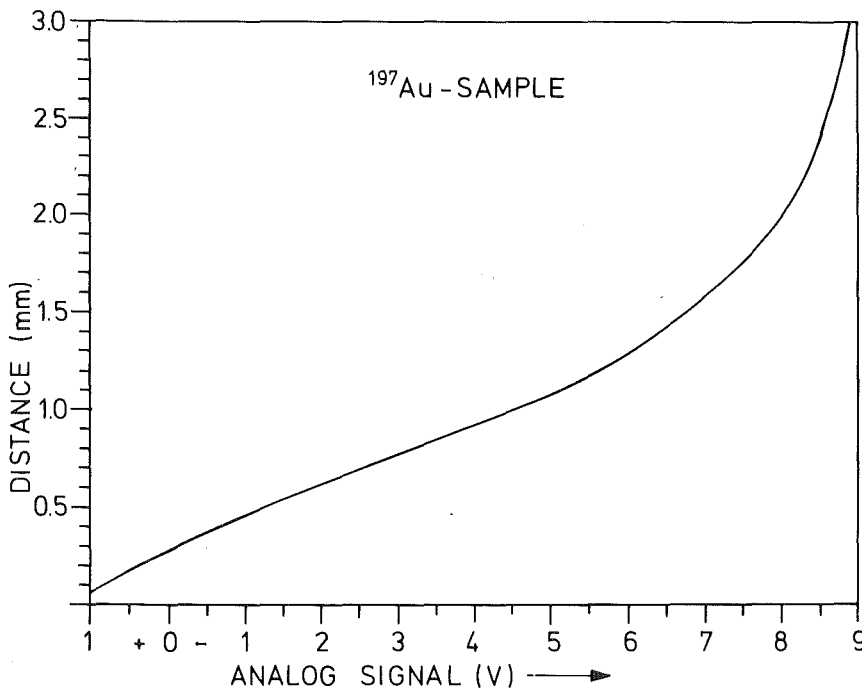


Fig. 1  
Calibration curve for a  $^{197}\text{Au}$  sample taken for the eddy current device for contact free distance measurements. Uncertainties correspond to the thickness of the line.

6.7 A New Cryostat for  $^3\text{He}$ - $^4\text{He}$  Dilution Refrigerators

R. Gumbsheimer, W. Heringa, H. Hucker, R. Maschuw, and H. Skacel  
Kernforschungszentrum Karlsruhe, IK I

We designed a new cryostat in which  $^3\text{He}$ - $^4\text{He}$  dilution units with minimum temperatures below 10 mK can be mounted. The cryostat shows some novel features, which have up to now not been employed for  $^3\text{He}$ - $^4\text{He}$  refrigerators.

1. The precooling of the dilution unit from room temperature to 4 K will be done by forced flow of liquid nitrogen and subsequently liquid helium. For this purpose a permanently installed tube is connected to all parts of the dilution unit. Its inlet is in the 4K bath, where it can be closed by a needle valve. Its outlet is connected to a pump outside the cryostat. The tube is dimensioned in such a way that the effective cool-down time is less than 1 hour. On the other hand, its influence on the performance of the dilution unit at its lowest temperatures is negligible. The advantage of this method compared to the common way of cooling with contact gas is that no contact gas has to be removed. Although the precooling with contact gas is fast enough, its removal takes many hours. Moreover, the cryostat needs only one vacuum system when no contact gas is employed.
2. The cooling of the  $^3\text{He}$  during normal circulation, from 4 K in the helium bath to 0.7 K at the still, will be done by helium at 2.2 K and at atmospheric pressure. For this purpose the 4K bath possesses a small tail in which the helium is cooled to 2.2 K. This helium is in open contact with the 4K bath. It is cooled by a small box hanging in the liquid on a tube which is connected to a pump. Helium is expanded into this box through a needle valve which can be adjusted from outside. This method is employed frequently to cool superconducting magnets below 4.2 K but has not been used in dilution refrigerators so far. Its advantage over the usually separated 1K bath is that the connection to the 4K bath can not block: the 2.2K bath is never empty. A very fine needle valve is needed to regulate the flow of superfluid helium into the box. Prototypes of this valve have already been built and tested successfully.
3. The same type of needle valve will be tested as a flow restriction in the  $^3\text{He}$  condensation line. This enables to adjust the flow restriction even during circulation. It allows, e.g., for a quicker starting up of the circulation by reducing the restriction temporarily to a very low value.

The cryostat, which is designed for maximum flow rates of at least 2 mmol, is under construction now in the workshop of our institute.

6.8 Production and Properties of Pressed Samples of  $TiH_2$  Powder to be Used as Polarized Proton Targets

R. Aures, R. Gumbsheimer, W. Heeringa, R. Maschuw,  
H. Skacel, and F.K. Schmidt  
Kernforschungszentrum Karlsruhe, IK I

Two samples of pressed  $TiH_2$  powder were prepared which will be used to produce polarized protons with the brute force method. The starting material was titanium turnings taken from a rod of 99.6 % purity. These were hydrogenated in our hydrogen oven. The H/Ti ratio obtained was  $1.96 \pm 0.02$  determined by mass and by volume measurements. The powder which remains after the hydrogenation has to be pressed as tight as possible in order to obtain a sample that can be cooled to very low temperatures in a reasonable time. For this purpose a pressing tool was built, which can withstand a pressure of  $2 \times 10^5$  N/cm<sup>2</sup> on a surface of 5 cm<sup>2</sup>. The powder was pressed in copper cylinders with 25 mm inner diameter and 1 mm wall thickness. In this way two samples with a length of about 35 mm were made.

The density of the pressed powder was determined by mass-volume measurements and also by means of the absorption of gamma rays from a <sup>137</sup>Cs source. The result is  $\rho = 3.78 \pm 0.04$  g/cm<sup>3</sup>. This agrees well with the density of  $TiH_2$  found in the literature, where the values scatter also around  $\rho = 3.78$  g/cm<sup>3</sup>. Thus the pressure employed was sufficient to press the powder to its highest possible density. The proton density of these samples is  $8.95 \times 10^{22}$  protons/cm<sup>3</sup>, which is the highest value, that is technically achievable.

(1) W. M. Mueller, J.P. Blackledge, and G.G. Libowitz,  
Metal Hydrides, Academic Press, New York, 1968, p. 367.

6.9 The Heat Conduction of Pressed  $TiH_2$  Powder Between 10 and 40 mK

R. Aures, R. Gumbsheimer, W. Heeringa, R. Maschuw, H. Skacel,  
and F.K. Schmidt  
Kernforschungszentrum Karlsruhe, IK I

A sample of  $TiH_2$  powder (see 6.8) has been pressed into a copper cylinder with a 6 mm diameter copper rod at the position of its cylinder axis.

This sample was used for heat conduction measurements of the pressed powder. For this purpose the central rod was heated with a small coil, while the temperatures of the rod and the outer cylinder wall were measured simultaneously. This measurement was done by determining the gamma-anisotropy of  $^{60}\text{Co}$  imbedded in cobalt single-crystals. The results are listed in Table 1 together with the resulting values of the heat conductivity  $\kappa$ .

Table I The measured temperatures  $T_i$  of the central rod and  $T_o$  of the outer cylinder wall of the  $\text{TiH}_2$  sample at various heat loads. The last column contains the values of the heat conductivity  $\kappa$  that were obtained.

$Q(\mu\text{W})$	$T_i$ (mK)	$T_o$ (mK)	$\kappa$ (W/cm K)
0	$11.0 \pm 0.4$	$10.0 \pm 0.4$	
0.1	$13.9 \pm 0.5$	$12.5 \pm 0.5$	$4.2 \pm 2.2 \times 10^{-6}$
0.2	$16.5 \pm 0.8$	$14.8 \pm 0.7$	$7.2 \pm 4.5$
0.3	$18.6 \pm 0.9$	$16.3 \pm 0.8$	$8.0 \pm 4.0$
0.5	$24.7 \pm 1.6$	$19.5 \pm 1.0$	$5.9 \pm 2.3$
0.8	$29.0 \pm 2.5$	$21.2 \pm 1.4$	$6.3 \pm 2.3$
1.6	$38.6 \pm 5.0$	$28.6 \pm 2.7$	$9.8 \pm 5.6$

The values of  $\kappa$  are also displayed in Fig. 1. The straight line through the points represents the best fit assuming a linear temperature dependence of  $\kappa$ ,  $\kappa = aT$ . We found for the proportionality constant the value  $a = 0.29 \pm 0.06 \times 10^{-3} \text{ W/cm K}^2$ .

The two upper curves are extrapolations of the heat conductivity of titanium metal measured at higher temperatures for different purities of the metal (1). The purity of our starting material is 99.6 % and lies between these two. So the heat conductivity of our pressed  $\text{TiH}_2$  powder is about one order of magnitude below that of the bulk metal.

Calculations have shown that this conductivity is sufficient for the sample to be used as a brute force polarized proton target.

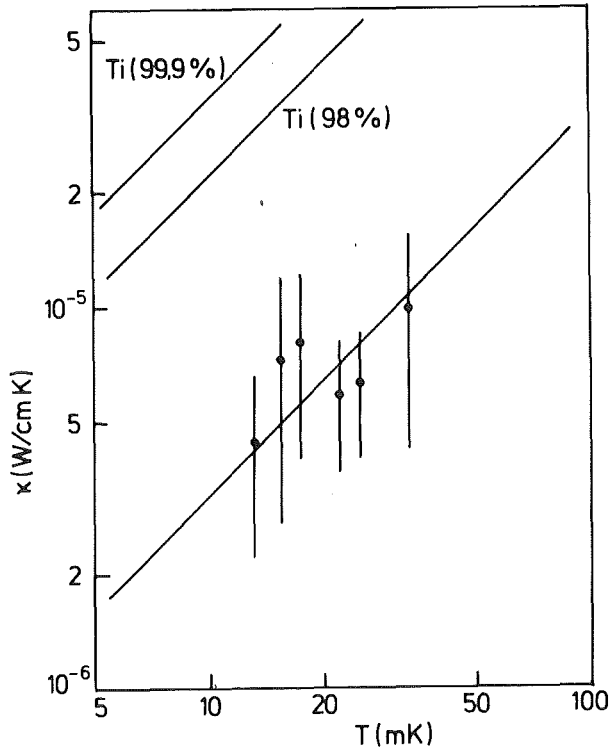


Fig. 1  
The experimental values of the heat conductivity of pressed  $\text{TiH}_2$  powder. See text for further explanations

- (1) G.E. Childs, L.J. Ericks and R.L. Powell, Thermal Conductivity of Solids at Room Temperature and Below, NBS Monograph 131, 1973, p. 46.

6.10 Polarization and Demagnetization of the Protons in a Pressed Sample of  $\text{TiH}_2$  Powder

R. Aures, R. Gumbsheimer, W. Heeringa, R. Maschuw,  
H. Skacel, and F.K. Schmidt  
Kernforschungszentrum Karlsruhe, IK I

A sample of pressed  $\text{TiH}_2$  powder (see 6.8 and 6.9) was used for our first experiments to obtain polarized protons. It was cooled by a dilution refrigerator to a temperature between 10 and 20 mK while in a field of 4.5 T produced by a superconducting magnet. The cooldown time was about one day compared to 1 h without magnetic field. This is assumed to be due to the polarization heat of the protons. Subsequently, we performed a slow demagnetization of the sample in order to check whether polarization was really achieved. The demagnetization should cause a further decrease in temperature if the protons were polarized. The result obtained was a minimum temperature of 2.8 mK after demagnetization in two hours from a starting temperature of 16 mK. This confirms qualitatively that the protons were

polarized. The demagnetization was not adiabatic because the sample could not be thermally decoupled from the dilution unit. Meanwhile a thermal switch has been mounted and tested. So more quantitative experiments can be done in the near future.

### 6.11 Properties of a He-MWPC as a Neutron Polarimeter

G. Giorginis, S. Kiontke, R. Maschuw, R. Schulz, and J. Wochele  
Kernforschungszentrum Karlsruhe, IK I

A high pressure He-MWPC is being developed as a polarimeter for a collimated neutron beam with a white energy spectrum. The  $n$ - $^4\text{He}$ -scattering process is determined by track recognition of the He-recoil particle. The measurement of angle  $(\theta_{\text{He}}, \phi_{\text{He}})$ , track length and energy loss completely determines the kinematics of the  $n$ - $^4\text{He}$  scattering process.

A test chamber has been operated satisfactory using a gas mixture of  $\text{He}/\text{CO}_2 = 10/1$ . Tracks of alpha-particles from a  $^{241}\text{Am}$  source were identified from six crossed anode wire planes consisting of 32 wires each and using a digital single wire readout system. To save the amount of electronic channels, needed for a large scale chamber of about 100 wire planes a new anode wire configuration has been tested successfully. Instead of 32 or more single wires the anode plane consists of only one wire, wound as a meander with 5mm wire spacing. Charge sensitive readout at both ends of the resistive wire allows position measurement by charge division. Simultaneously energy loss is measured by the sum of the charges.

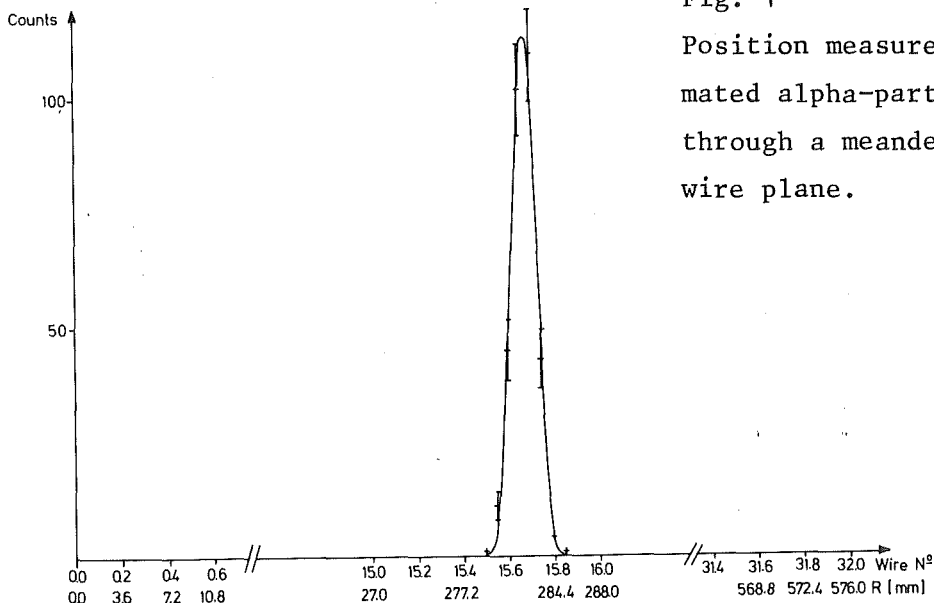


Fig. 1  
Position measurement of collimated alpha-particles passing through a meander wound anode wire plane.

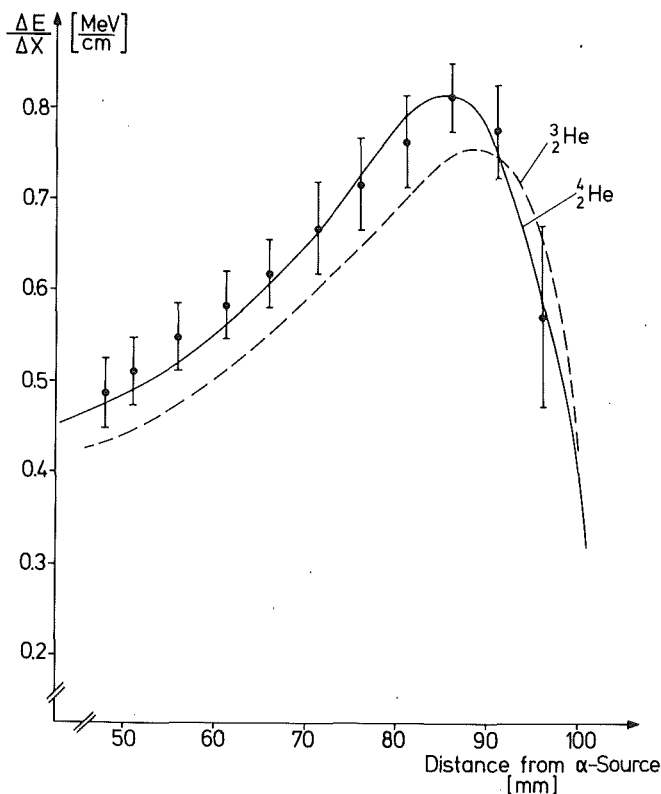


Fig. 2  
Energy loss of 5.5 MeV alpha-particles measured with the meander anode wire plane at different distances from the  ${}^{241}\text{Am}$  source. Curves are calculated from stopping power tables of  ${}^4\text{He}$ - and  ${}^3\text{He}$ -particles, respectively, assuming the same maximum range

The spatial resolution along the anode wire with a total length of 5.8 m is  $\sigma = 1.0$  cm and is shown in Fig. 1. This is totally sufficient to define the wire number, hit by the charged particle. To remove a left-right ambiguity in the case of a two wire prong a double meander wire plane can be used where two meander planes are shifted by half the wire distance.

Fig. 2 shows the energy loss of alpha-particles from a  ${}^{241}\text{Am}$  source along the Bragg curve measured with the meander anode wire plane at different distances from the source. The solid line is calculated from stopping power tables (1) for a 8 %  $\text{CO}_2$  admixture to He-gas of 1 bar. The dotted line shows the calculated energy loss that  ${}^3\text{He}$ -particles would have, assuming the same maximum range as for the alpha-particles.

Thus the determination of track length and energy loss along the track unambiguously allows for particle identification. This is important for the detection of neutrons with energies above 20 MeV to get rid of the inelasticities, i.e.,  $n + {}^4\text{He} \rightarrow n + n + {}^3\text{He}$ ;  $n + d + d$ ,  $n + p + t$  etc., Measurements with polarized neutrons from  ${}^4\text{Be}(\alpha, \gamma){}^{12}\text{C}$  and  ${}^3\text{H}(d, n){}^4\text{He}$  are prepared at the Van de Graaff-accelerator. The test chamber will then contain 6 single wire- and 12 meander wire planes with the corresponding electronics.

(1) L.C. Northcliffe, R.F. Schilling, Nuclear Data Tables A7, 223-463 (1970).

6.12 A Liquid Deuterium Target for Neutron Production

H. Krupp, H. Hucker, and H.O. Klages

Kernforschungszentrum Karlsruhe, IK I

A cryogenic target for the production of fast polarized neutrons has been built. The polarized deuterium source at the Karlsruhe cyclotron and the deuterium target are used in connection to employ polarization transfer in the  $D(\vec{d}, \vec{n})$  reaction. This reaction yields high polarization for the two-body reaction peak as well as for the break-up neutrons. Very few gamma rays are produced in the target.

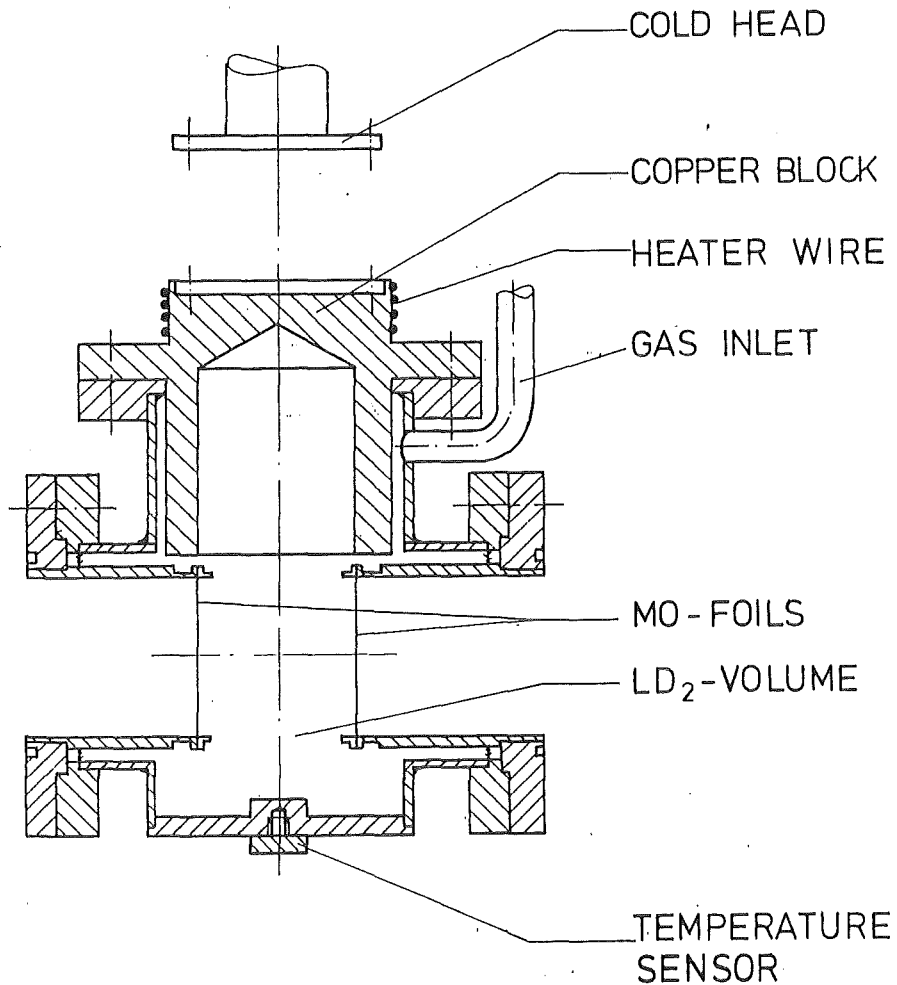


Fig. 1 Schematic view to the liquid deuterium target assembly.

The main components of the cryogenic target system are:

1. target body
2. cold head (expansion unit)
3. helium compressor and gas transfer lines
4. temperature controller with sensor elements and heater wire
5. 40 l deuterium storage tank
6. pressure gauge

The target consists of a stainless steel cylinder. On both sides indium-sealed tubes are mounted which carry window foils. The tubes can be exchanged easily to obtain targets with different thickness. In the first experiments a 1 cm thick target with 12  $\mu\text{m}$  molybdenum windows was used, corresponding to an energy loss of about 4 MeV for the 52 MeV deuterons.

A copper block mounted at a flange on top of the target provides good thermal contact between the cold head of the refrigerator and the deuterium. The refrigerators cooling power at 20 K is 2 W, normally.

Constant target temperature is achieved by means of a controller. This unit measures the temperature with a calibrated Si diode. A heater wire is used for additional load if the measured temperature is lower than the pre-set. The temperature is determined independently by measuring the vapour pressure of the deuterium in the storage vessel.

In the working range of the system the temperature can be held stable within 0.1 K for many days.

#### 6.13 A Multiwire Proportional Chamber as Monitor for Collimated Fast Neutron Beams

A. Bischoff, P. Doll, and H.O. Klages  
Kernforschungszentrum Karlsruhe, IK I

A multiwire proportional chamber has been constructed as monitor for fast neutron beams. The detector is designed to measure the spatial and time distribution of the polarized neutron beam from the collimator POLKA (see 1.2.1).

Figure 1 shows the sideview of the monitor. Charged particles emerging

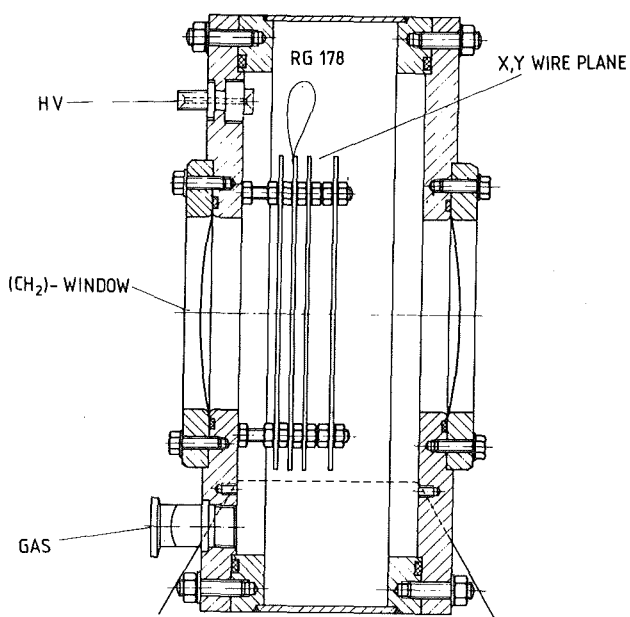


Fig. 1  
Side view of the monitor chamber

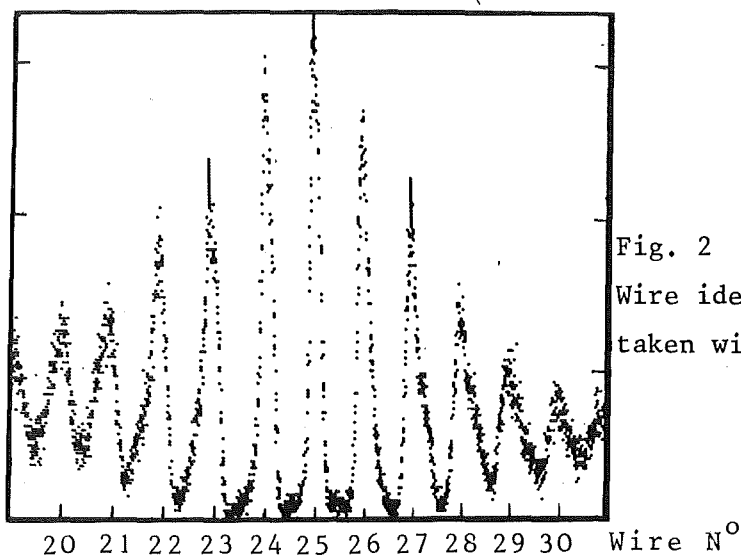


Fig. 2  
Wire identification spectrum taken with an Am-Pu alpha source

from the CH<sub>2</sub>-converter enter the gas volume of the detector. Between two cathode planes made out of aluminized Hostaphan (2 μm) an anode wire plane is centered. The distance between the cathode and anode was chosen to be 4.8 mm. The wire spacing is 2 mm, 50 wires cover the full width of the monitor. The anode wires are made out of tungsten and have a diameter of 20 μm. The negative high-voltage is supplied through a 3 MΩ resistance to each cathode plane. The anode wires are connected on one side with 50 Ω, RG 178 cables, providing a delay line with little damping and very small cross-talk for fast anode signals.

When a signal propagates into both sides of the delay-line the time difference at both ends is used for the identification of the wire.

The monitor has been tested with an argon-methane gas mixture and an Am/Pu alpha-source ( $E_{\alpha} \sim 5-6$  MeV) and an Am-Be neutron-source ( $E_n \sim 5-10$  MeV). Under normal gas pressure and a cathode voltage of -2300 volts, fast anode signals of about -10 mV were observed on 50  $\Omega$  load with alpha-particles. Figure 2 shows the wire-spectrum obtained with an uncollimated alpha-source placed 25 mm in front of the anode plane.

For detection of 10-50 MeV neutrons the monitor will be operated with "magic" gas<sup>+</sup> and high gain preamplifiers (VT 110<sup>++</sup>). The arrangement of cathodes and wire planes will be optimized in test experiments using the fast neutron beam.

#### 6.14 Efficiency of Large Volume Neutron Detectors

P. Schwarz, B. Haesner, and H.O. Klages  
Kernforschungszentrum Karlsruhe, IK I

Measurements and Monte-Carlo calculations of the efficiency of large volume neutron detectors have been reported in the preceding annual report (1). Final results and conclusions will be presented here.

Two different detectors were built and tested. The first one (BD I) has a cylindrical scintillation volume of 130 l filled with NE 213. The scintillation light is collected by five photomultiplier tubes. The second detector (BD II) has a larger volume of 350 l viewed by six photomultiplier tubes and was filled with NE 224.

Various electronic set-ups were tested with calibrated monoenergetic neutron beams at the PTB in Braunschweig and with the "white" neutron beam of the Karlsruhe cyclotron. These tests revealed that for each event the coincidence of two or more multipliers has to be required to reduce the background. With a higher number of multipliers measured in coincidence the efficiency of the detector decreases. This disadvantage, however, is more than compensated by the better calorimetric property of the detector. Fig. 1 shows the efficiency of BD I for different coincidence conditions. The data points are the results of the measurements, while the dashed bands represent the calculations with the Monte-Carlo code BDCALC.

<sup>+</sup> Argon, Isobutan, Methylal, Freon

<sup>++</sup> Fast Timing Amplifier, ESN, Darmstadt

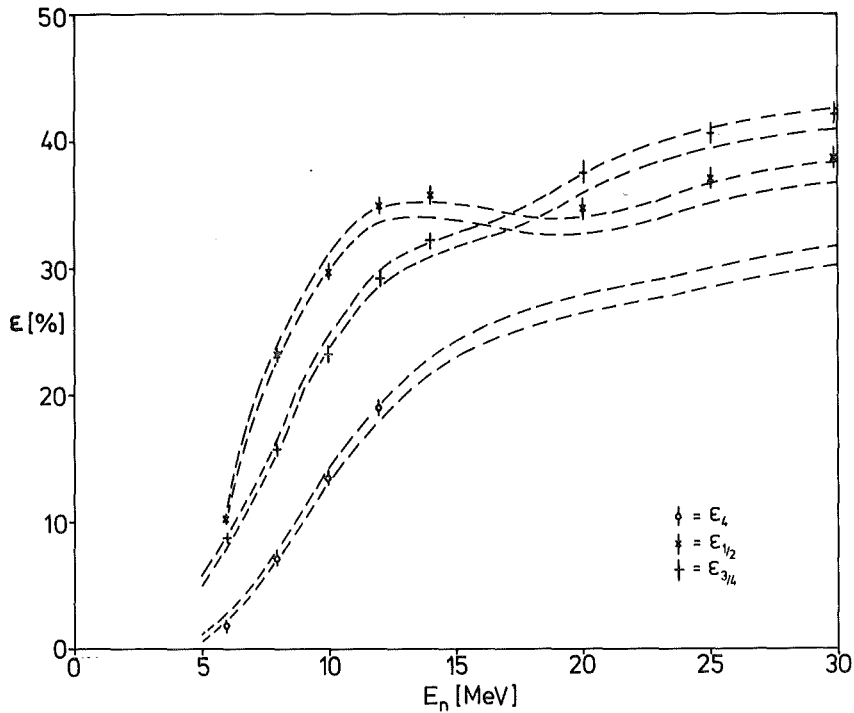


Fig. 1 Efficiency curve of BD I for different twofold coincidences ( $\epsilon_{1/2}$  and  $\epsilon_{3/4}$ ) and for the fourfold coincidence ( $\epsilon_4$ ).

$\epsilon_4$  indicates the efficiency for a fourfold coincidence.  $\epsilon_{1/2}$  and  $\epsilon_{3/4}$  are the efficiencies for a twofold coincidence of the front pair and the second pair of multipliers, respectively. The crossover of the efficiency curves at 17 MeV is due to the fact that the neutron mean free path grows with increasing energy.

For the measurement of neutrons with higher energies up to 50 MeV the second detector type BD II with a larger scintillation volume was designed.

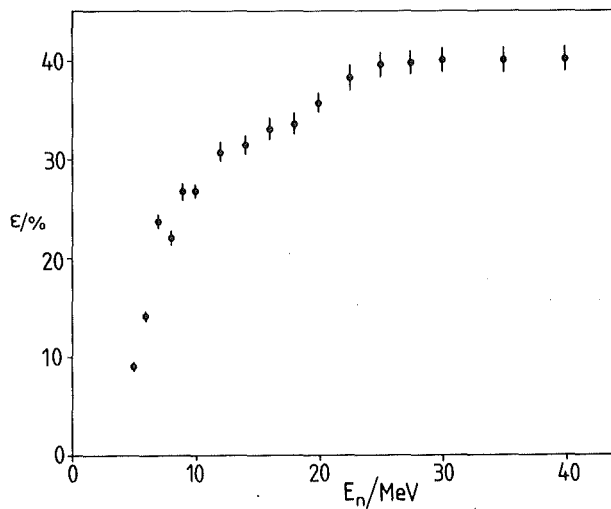


Fig. 2 Efficiency of BD II as a function of the neutron energy measured with a fourfold coincidence condition.

Fig. 2 shows the efficiency of BD II measured with the Karlsruhe "white" neutron beam.

In the energy range from 25 to 40 MeV the efficiency of BD II is nearly constant and about 30 % higher than that of BD I (Fig. 1) for a fourfold coincidence. Due to the larger light attenuation length of NE224 in BD II, this detector is even suitable for energies lower than 10 MeV, although it is optimized for the higher neutron energies.

The results of the measurements and Monte-Carlo calculations have shown, that these neutron detectors can be used as absolute flux monitors for collimated neutron beams with a relative accuracy of 3 %. In particular the second detector type has the important advantage that its efficiency is nearly constant over a wide dynamical range.

(1) KfK Report 3280 (1982)

6.15 A System of Computer Codes to Analyze Multidimensional Data from Polarized Neutron Scattering Experiments  
J. Hansmeyer, H.O. Klages, P. Schwarz, and J. Wilczynski  
Kernforschungszentrum Karlsruhe, IK I

A new program system was developed for the analysis of raw data from fast neutron scattering experiments. The procedure of analyzing the data and the performance of the codes will be described briefly.

An event in a typical neutron scattering experiment at POLKA is defined by the following parameters:

1. Time of flight from neutron producing target to scatterer
2. Energy of the recoil particle
3. Time of flight from scatterer to detector
4. Pulse height of the detector signal
5. Pulse shape discrimination between neutrons and gammas
6. Routing signal to identify the detector and the status of the polarization of the deuteron source.

These data are stored on tape as a list of events by a ND 4420 multi-parameter data acquisition system (Nuclear Data). The first step of the analysis is the reduction of these data files to two dimensions which dis-

play par. 2 vs. par. 3. The other parameters are used during this process to sort the data according to incident energy bins chosen, the detectors and the two spin states, as well as to separate neutrons from gamma events via cuts in the par. 4 vs. par. 5 matrices.

For this purpose a program SORTLIST was developed which allows the user to sort data using gating conditions in several parameters including two dimensional windows. To keep track of the data the program creates projections on one or two parameters. These spectra and matrices are used to control the data reduction procedure.

To display the spectra and matrices and to perform the final analysis, i.e., the integration within two-dimensional projections, the interactive computer code SPM has been developed.

Because of the great number of matrices (about 300) which have to be analyzed carefully in the final step of the procedures, computer graphics is used extensively. Menu techniques allow us to invoke about 20 different functions realized in SPM without difficulties and with a minimum of input. These functions include: Plotting on a graphic display; interactive integration; arithmetic operations with the spectra and matrices; several utility functions. The program system is completed by several additional codes for testing, translating data into different structures and plotting.

The system allows the analysis of experimental scattering data in an efficient way, saving CPU time and operator effort.

#### 6.16 Generalization and Improvement of the Peak Analyzing Program "WQJOE" for Charged Particle Spectra

J. Oehlschläger and H.J. Gils

Kernforschungszentrum Karlsruhe, IAK II

In nuclear reaction studies with charged particles the analysis of the energy spectra of the ejectiles is one of the most important steps in data processing and analysis. Since the characteristic features of the spectra like peak form, energy resolution and linearity, background and scale depend on the experimental arrangement (detection system, target material, data acquisition) there is no general solution to this count rate depend on the experimental arrangement (detection system, target material, data acquisition) there is no general solution to this

problem of data analysis but the particular experimental conditions have to be considered.

The past generations of peak analyzing programs (1,2) which aimed to fit the changing requirements of the nuclear reaction group was found to be no longer adequate for the present and future requirements in particular when experimental results from the magnetic spectrograph "Little John" will be available (3). Therefore, a new program system for peak analysis has been developed the main aims of which are:

- analysis of only the interesting regions of the spectrum
- separating analysis of up to five overlapping peaks
- implementation of different approaches for background subtraction
- improvement of peak analysis for low counts per channel

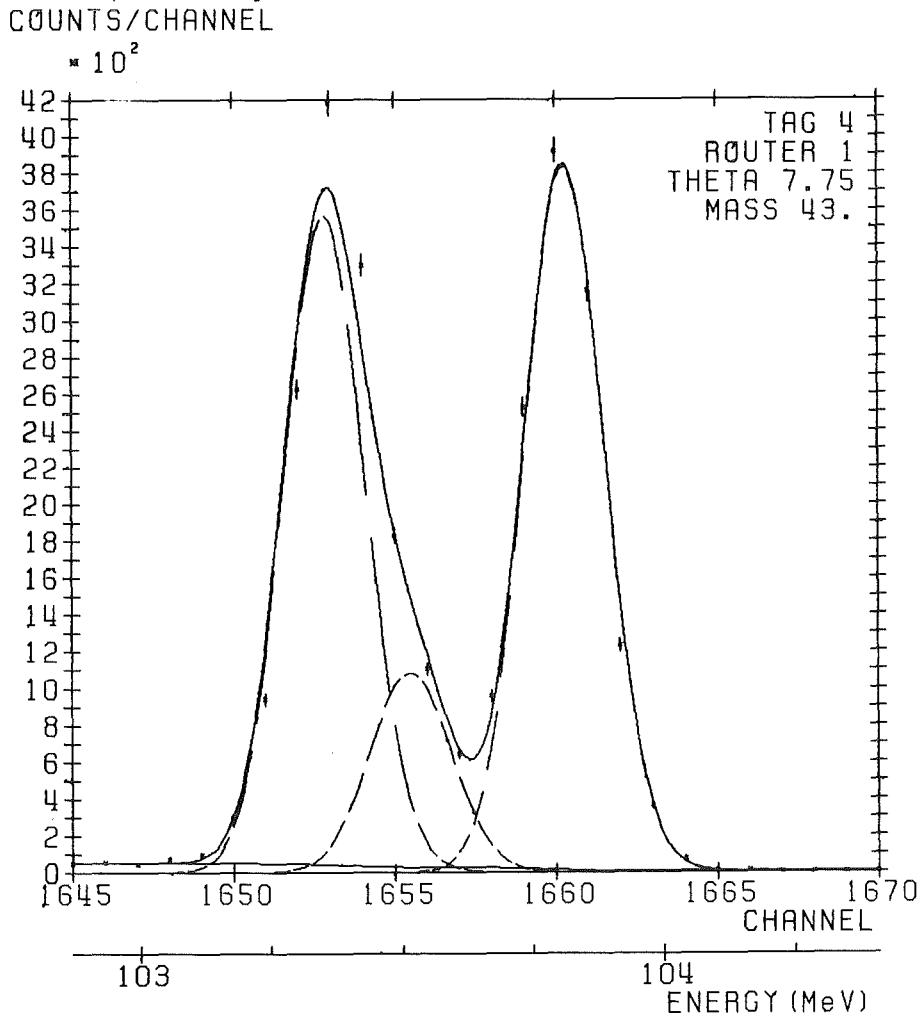


Fig. 1 Peak analysis of an energy spectrum of alpha particles scattered by a <sup>43</sup>Ca target. The solid curve is the fit result, the dashed curves represent the contributions of the single peaks to the spectrum.

- improvement of program handling and reduction of input in particular for analysis of many similar spectra

From the earlier programs (1,2) the new system uses only the parametrization of the peak form (4) and the method for separating two overlapping peaks (5) which has been extended to five peaks.

Further features of the program are:

- analysis of up to ten peaks per spectrum
- separation of target and contaminant (e.g.  $^{12}\text{C}$ ,  $^{16}\text{O}$ ) peaks
- finding and handling of groups of adjacent or overlapping peaks as well as of separated peaks
- determination of the energy calibration with polynomials up to degree 2
- plot of the analyzed spectrum region on printer or VERSATEC-plotter

The program has been tested by the analysis of about 600 spectra from alpha particle and  $^6\text{Li}$  scattering covering most of the typical features of energy spectra measured by the nuclear reaction group at the cyclotron. An example of the analysis of a spectrum of alpha particles scattered by  $^{43}\text{Ca}$  is shown in Fig. 1. The separation of target and contaminant peaks is clearly indicated. Also the step formed background is well approached. Some further refinements and special versions of the program are in hand.

- (1) G. Hoffmann, G.W. Schweimer, J. Specht, private communication, 1970
- (2) H.J. Gils and W. Nowatzke, unpublished reports, 1974, 1976, 1977
- (3) H.J. Gils, J. Buschmann, J. Krisch, H. Rebel, S. Zagromski, K. Feißt, unpublished report, 1981
- (4) J. Specht and G.W. Schweimer, unpublished report, 1970
- (5) J. Specht, H. Rebel, G. Schatz, G.W. Schweimer, G. Hauser, and R. Löhken, KfK Report 967 1969

#### 6.17 Status Report on HISKA and First Injection of Fully Stripped Nitrogen Ions into the Cyclotron

V. Bechtold, H.P. Ehret, L. Friedrich, J. Kaltenbaek,  
H. Schweickert, L. Wiss, and P. Ziegler  
Kernforschungszentrum Karlsruhe, IAK II

When the new building for all external ion sources of the cyclotron was finished, the assembly of HISKA (1) started at the end of the last year. The main features of the Karlsruhe ECR source HISKA (Hheavy Ion Source Karlsruhe)

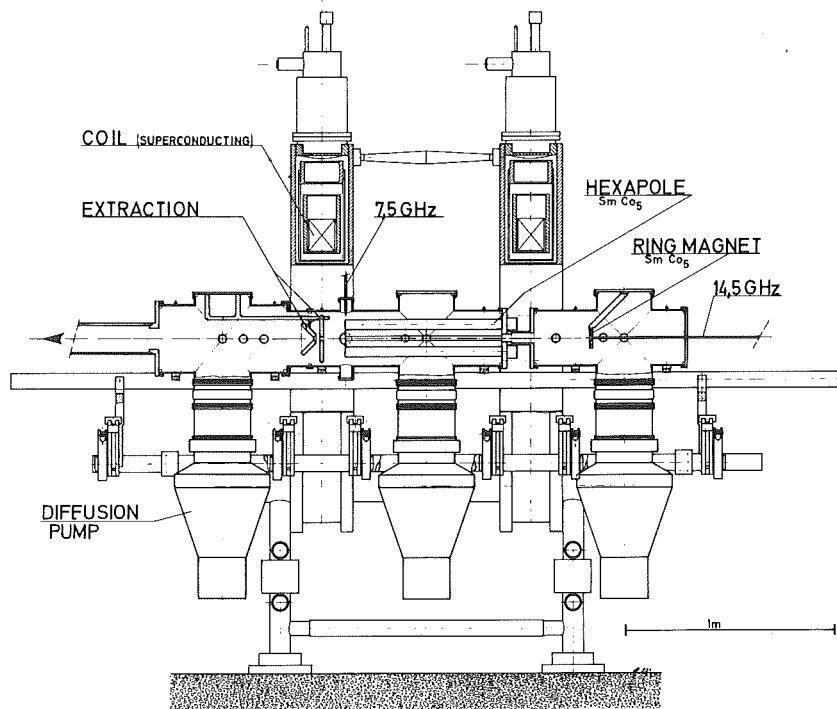


Fig. 1 HISKA, present state of design. The first stage is operated at 14.5 GHz and at a magnetic field of 5.2 KG. This field is produced by a small permanent ring magnet made of Samarium Cobalt. This is a compact Mini source. In the second stage the 7.5 GHz microwaves are fed into a magnetic field configuration generated by two superconducting coils and a permanent hexapole (SMCo<sub>5</sub>) inserted into the vacuum. The source is pumped with special diffusion pumps with negligible oil backstreaming.

are: low power consumption, great flexibility, good vacuum conditions and easy access for diagnostics.

Figure 1 shows a schematic drawing of the two stage device HISKA. In the first stage a cold plasma is created at 14.5 GHz. In the second stage ionization to high charge states takes place. The necessary high electron energy and density is achieved by microwave heating at 7.5 GHz in a magnetic bottle which is generated by two superconducting ring coils (Fig. 2) and a permanent hexapole magnet (Fig. 3).

In early summer '82 in initial test of HISKA was very successful. 200 nA N<sup>6+</sup> could be produced. The charge state distribution (Fig. 4). was measured with a Wienfilter. The test run demonstrated a rather good stability and reproducibility of the source.

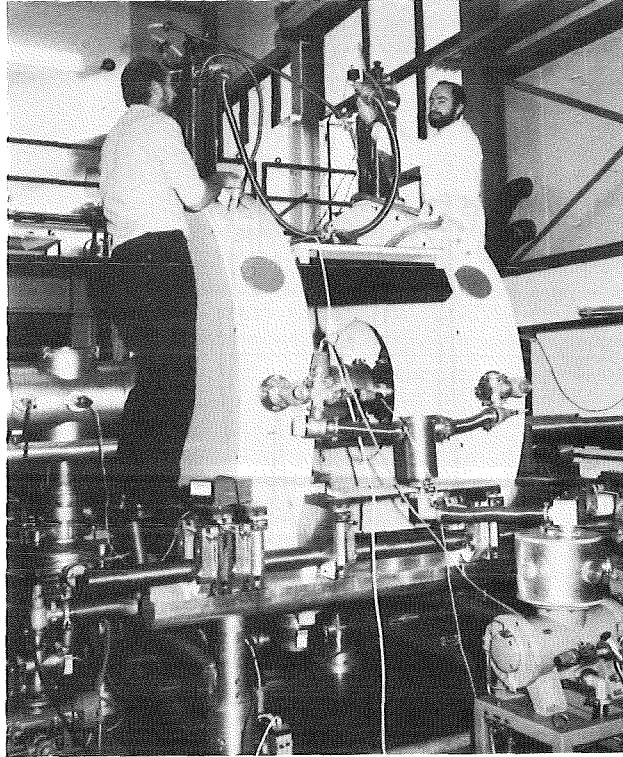


Fig. 2 The superconducting ring coil on the test bench in the laboratory.

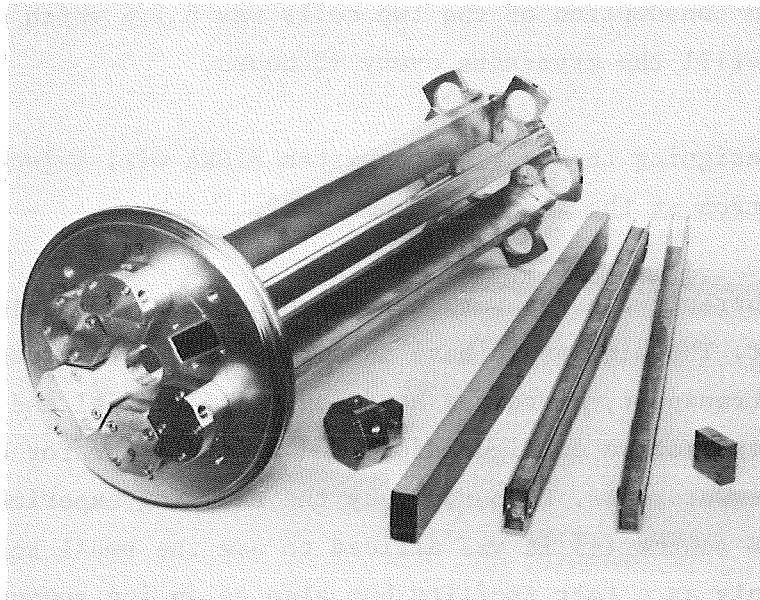


Fig. 3 The permanent hexapole mounted on a stainless steel flange. The six bars consist of  $\text{SmCo}_5$ -pieces pasted in U-profiles which are inserted into rectangular stainless steel tubes. The whole device which can be inserted into vacuum, is 70 cm in length, with 8 cm inner diameter and has a field strength of 4.2 KG on the surface of the poles.

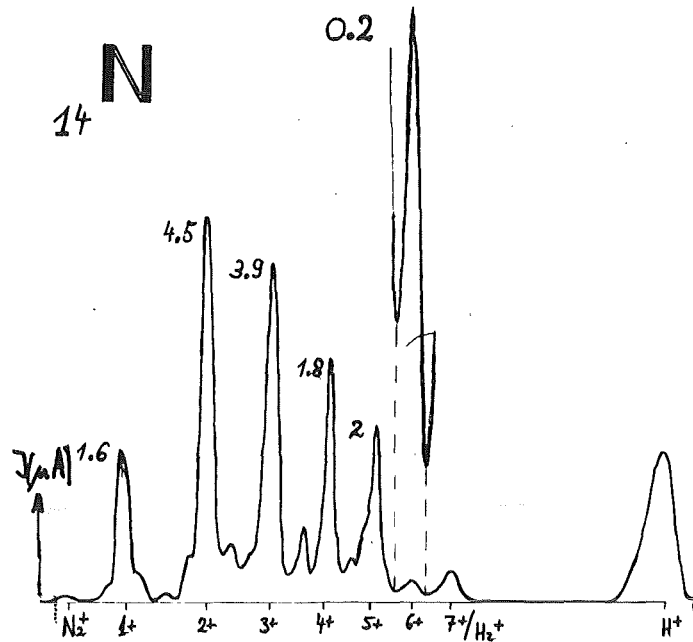


Fig. 4 Charge state distribution for nitrogen ions of HISKA. Because they have the same  $e/m$ -value the fully stripped nitrogen ions cannot be discriminated from the  $H_2^+$ -ions. However, from results in Grenoble the relation  $N^{6+}/N^{7+}=10$  is known so that about 20 nA  $N^{7+}$ -ions can be deduced.

The helium consumption of the two coils was 5 l/h which made it necessary to refill the cryostats every 12 hours.

After redesigning the extraction system HISKA will inject its first beam into the cyclotron at the end of October 1982.

p-HISKA: Concurrent with the work described above a 1:3 scale version of HISKA was built. The aim was to have an arrangement for testing plasma injection and transport, microwave handling, differential and lateral pumping, various extraction configurations and a Wienfilter for charge state distribution measurements. Encouraged by the exciting experimental results of the  $\mu$ -MAFIOS source (1) it was decided to use the small scale version of HISKA not only as a test facility but also as an ion source for the Karlsruhe cyclotron. At the end of August 1981 we injected with p-HISKA into the cyclotron. About 250 pA fully stripped nitrogen ions at an energy of 364 MeV could be measured on target. The emittance of p-HISKA was determined to be between (200-500) mm rad at 10 keV injection energy.

Because p-HISKA is a test arrangement we investigated whether an ECR source is also able to deliver metal ions. We started with Lithium.

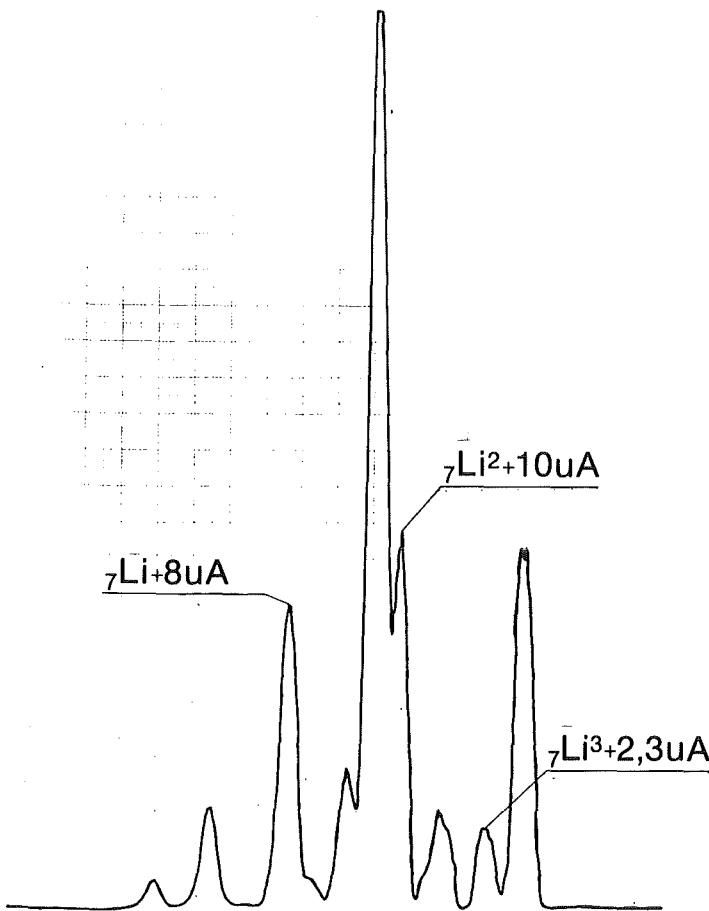


Fig. 5  
Charge state distribution  
for lithium ions. In order  
to separate the fully stripped  
lithium ions from  $\text{H}_2^+$  the  
isotope  ${}^7\text{Li}$  was chosen.  
 $2,3 \mu\text{A } {}^7\text{Li}^{3+}$ -ions could be  
produced.

For this purpose the first stage of p-HISKA was replaced by an Li-oven (2). Lithium is evaporated and diffuses into the second stage where it is ionized. The charge state distribution for  ${}^7\text{Li}$ -ions is shown in Fig. 5.  $2,3 \mu\text{A } {}^7\text{Li}^{3+}$ -ions could be produced.

- (1) A. Geller, B. Jacquot, R. Panthenet, Rev. Phys. Appl. 15 (1980) 995
- (2) F. Schulz and H. Schweickert, KfK Report 3068

#### 6.1 8 A SETUP FOR THE ON-LINE MEASUREMENT OF THE POLARIZATION OF THE KARLSRUHE DEUTERON BEAM

M. Oexner, P. Doll, H. Hucker, H. O. Klages

Kernforschungszentrum Karlsruhe, IK 1

A polarimeter was constructed to serve as a monitor for the polarization of the 52 MeV deuteron beam at the Karlsruhe cyclotron delivered by the Lamb-Shift source.

The accurate knowledge of the beam polarization is important to verify that at each stage a well-known polarization is transferred to the neutrons, which are produced in POLKA by  $D(\vec{d}, \vec{n})$  reactions. In addition such a polarimeter serves as a sensitive position monitor for the deuteron beam before entering POLKA. The polarization is determined from the measured asymmetry of the elastic scattering of deuterons from  $^{12}\text{C}$  at  $\pm 47^\circ$  (lab.). At this angle the analyzing power of the carbon is  $0.318 \pm 0.035$  (1). Both carbon- ( $100 \mu\text{g}/\text{cm}^2$ ) and polyethylene foils ( $1.2 \text{ mg}/\text{cm}^2$ ) have been investigated to find an optimum for energy resolution and count-rate.

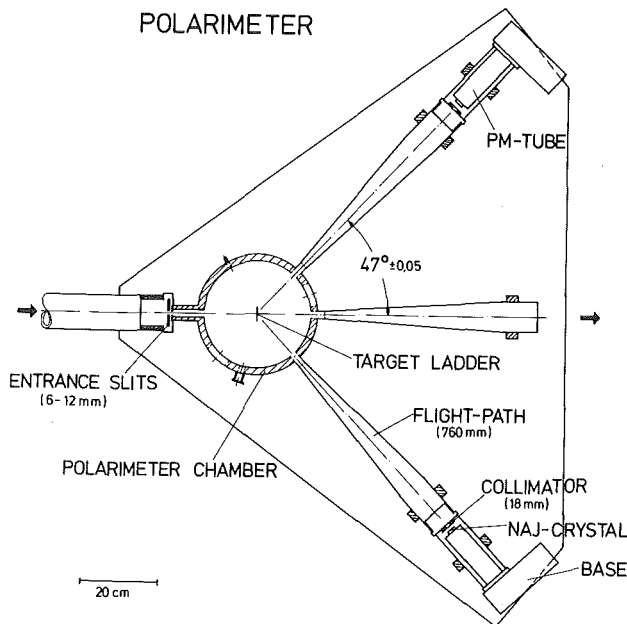


Fig.1: Topview of the polarimeter

Adjustable graphite entrance slits allow control of the position of the beam entering the polarimeter chamber. A target ladder provides several positions, e.g. 2 target foils, a ZnS viewer, and an aperture ( $\phi = 8 \text{ mm}$ ). The scattered deuterons are detected in two 7 mm thick NaI(Tl) crystals, which stop 52 MeV deuterons but only about 40 MeV protons. Energy and timing signals are recorded on magnetic tape. The TOF-information offers a good possibility for particle identification. The polarimeter has already proven its reliability in monitoring several neutron scattering experiments. Off-line data analysis was performed to obtain accurate polarization values.

Fig.2 shows the measured polarization of the deuteron beam for an entire experimental time of 10 days. The solid line represents the average beam polarization with an accuracy of 0.1%. The second part of the figure shows the spin-averaged ratio of left-to-right count rates, which is sensitive to any variation in the beam position and is used to adjust the ion optics frequently.

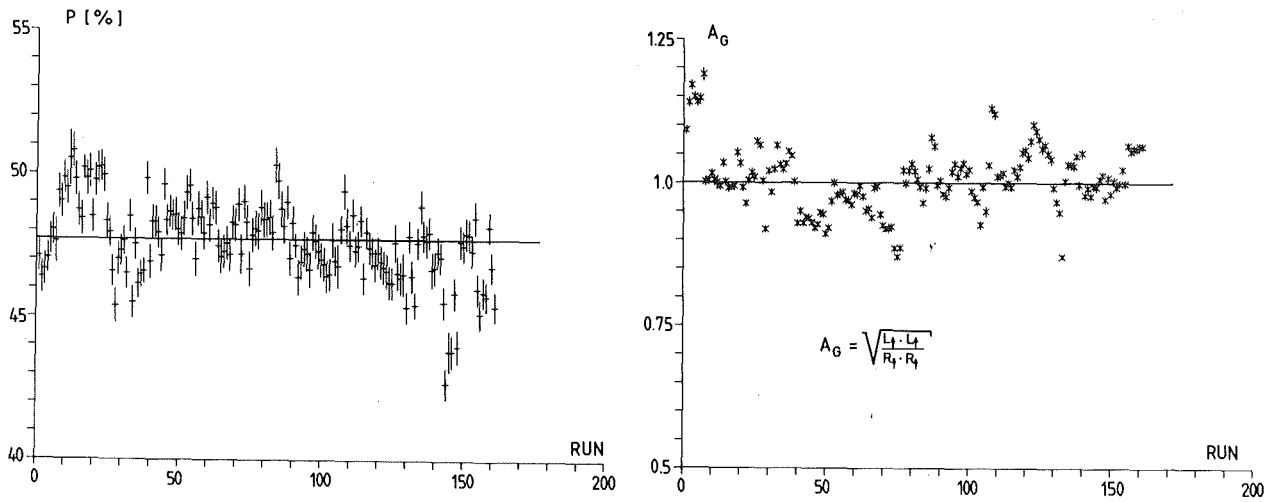


Fig.2: Long-time behaviour of the deuteron beam polarization and the geometrical asymmetry; statistical errors are indicated for each measuring period

The development of computer codes for on-line data acquisition and evaluation using CAMAC and a LSI 11/23 microcomputer is in progress.

- (1) E.Seibt and C.Weddigen, Nucl.Inst. and Meth. 100 (1972) 253 and KfK report 1357 (1971)

We thank B.Schührer and H.Wirth from MPI Heidelberg for preparing the Carbon foils.

6. 19            Status of preparation and planned experiments  
with a cyclotron trap

P. Blüm, E. Borie, D. Gotta, H. Koch, W. Kunold,  
M. Schneider, L.M. Simons

Kernforschungszentrum Karlsruhe, IK II

A high stopping density is the most important experimental prerequisite for an experiment with exotic atoms. The development of the cyclotron trap serves to attain this goal for muonic and antiprotonic atoms. Especially the planned observation of Lyman X-rays (1) of antiprotonic gaseous hydrogen (deuterium) at pressures around 7.6 Torr shows the necessity of a focussing device. If an antiproton beam with a momentum spread of 100 keV/c at 100 MeV/c (conditions planned for LEAR at a later stage of development) is stopped in hydrogen gas, a range width of 110 m (range  $\approx$  200 m) will be typical, with correspondingly larger widths at lower pressures. This practically prevents the use of high resolution semiconductor detectors necessary to measure strong interaction shifts and widths of Lyman transitions.

Particles which are injected into the trap will spiral to the center of the trap due to the focussing properties of its magnetic field of cyclotron type and due to the energy loss experienced by charged particles.

A Monte Carlo simulation of the deceleration process including multiple scattering has been performed and served to optimize the construction of the

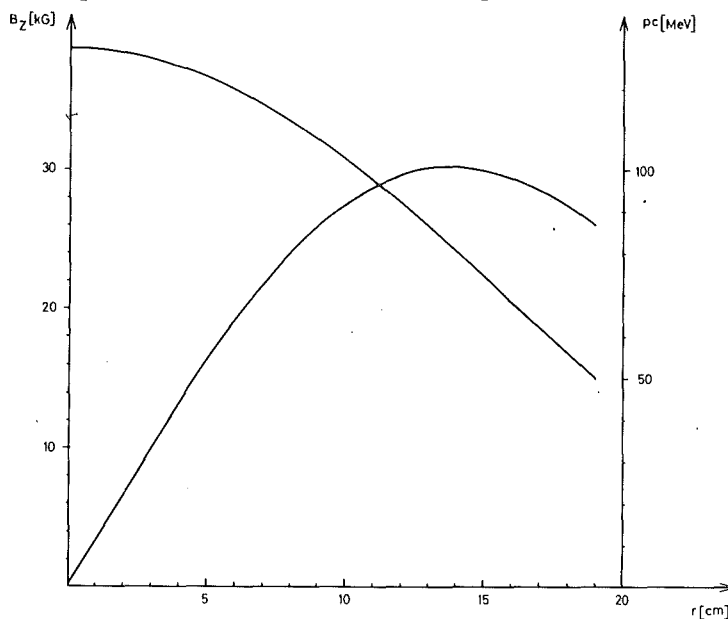


Fig. 1: Magnetic field  $B_z$  in the cyclotron trap and accepted antiprotonic momentum  $p_c$  for equilibrium orbits

trap not only for antiprotons but also for muons. The field configuration finally chosen is illustrated in fig. 1. It can be realized with a mechanical set-up shown in fig. 2.

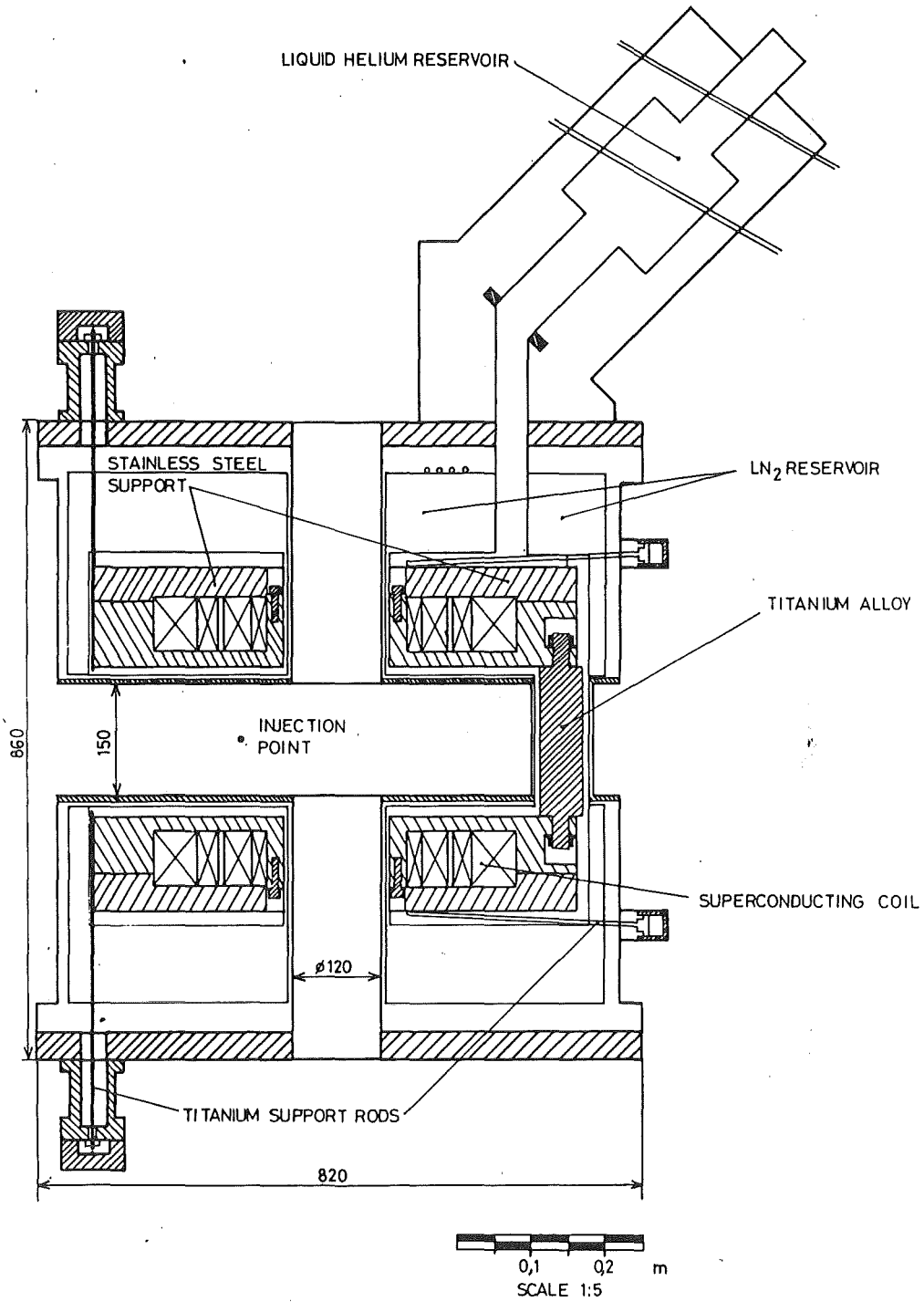


Fig. 2: Mechanical set-up of the cyclotron trap

The construction guarantees maximum access to the stop volume. Therefore a clear bore hole of 12 cm diameter and a clear gap of 15 cm width is foreseen. The split coil magnet consists of 8 coil sections kept apart by three support bars with a minimum radial distance from the center of 25 cm (attraction force: 36 tons).

The magnet itself is being built by the firm Cryogenic Consultants in London and will be delivered to SIN in autumn 1982. There the field characteristics will be examined and first decelerating tests will be performed with alpha sources. First experiments with muons will take place at SIN between November 1982 and March 1983.

The measurements with muons (2) will study the cascade process in muonic neon and especially the decay behaviour of the 2s-state in order to decide about the feasibility of a later parity violation experiment involving the  $2s \rightarrow 1s M1$  transition. It is the aim to find a pressure such that the 2s level remains metastable and the stopping density is high. Therefore a coincidence measurement will be performed between the  $2 \rightarrow 1$  transition and the  $3p \rightarrow 2s$  transition. The latter transition will be filtered out of the  $3d \rightarrow 2p$  transitions with a differential absorber technique.

Similar techniques will presumably be used with antiprotonic atoms in a later stage of the CERN experiments when a similar set up will be used.

Pulse shape studies of planar detectors have been performed and lead to a method to increase the peak to background ratio for X-rays below 20 keV. These laboratory measurements influenced the choice of detectors to be used. Moreover a gas scintillation detector is being developed at Karlsruhe in close collaboration with the detector group at SIN. This detector will serve to detect antiprotons Lyman X-rays in  $H_2(D_2)$  with high solid angle in order to perform a coincidence measurement.

(1) LEAR proposal PS 175

(2) SIN proposal R81-02.1

6. 20 A new low level counting system

L.M. Simons, J. Wüest<sup>+</sup> Kernforschungszentrum Karlsruhe, IK II

For a measurement of the  $\mu^- - e^+$ -conversion rate in muonic iodine a very efficient Low Level Counting System (LLCS) for  $\beta^-$  with energies between 100 and 700 keV was developed (1).

The LLCS used up to now was limited by its efficiency and the background activity of the detector itself. These problems could be solved by using several surface barrier detectors in coincidence and placing them in a magnetic guiding field (fig. 1).

A coincidence measurement using two detectors reduces the background coming from one detector. By placing them horizontally, cosmic background is considerably reduced. The magnetic field increases the efficiency and keeps away the activity from the surrounding material used for cooling the detectors and for the vacuum chamber. The solenoid field replaces the passive shielding used in conventional LLCS's (2).

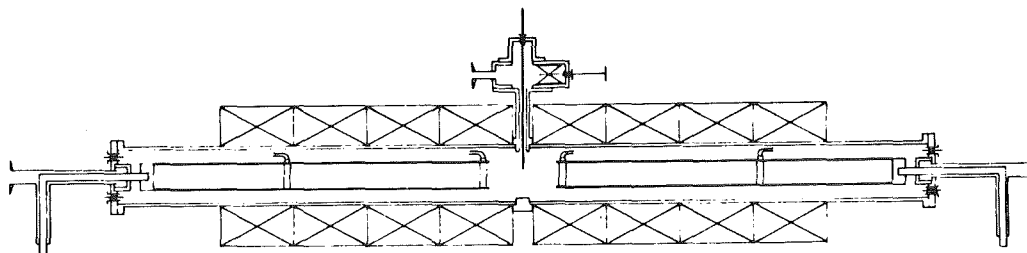


Fig. 1: Cross-view of the Low Level Counting System.

D1 - D4: surface barrier detectors, V: Vacuum connection,  
CF: cooling finger, S: sample holder

The thin detector in front was chosen as thin as possible to reduce possible gamma-background and to minimize the losses in efficiency by cutting off the low energy part of the beta-spectrum. Unfortunately the noise of surface barrier detectors increases rapidly with decreasing thickness. On the other hand the energy loss of minimum ionising electrons is only  $0.4 \text{ keV}/\mu\text{m}(\text{Si})$ . We chose a  $50 \mu\text{m}$  thick detector and improved the noisewidth from 25 keV to 8 keV FWHM. Electrons with energies up to 100 keV are stopped

in the front detector, resulting in a loss of only about 10% of the spectrum. There is also cut at the upper end of the spectrum because of the chosen discriminator level in the thin detector.

Another reduction factor of 45% is given by the magnetic mirror effect because the two coil systems are kept apart by 3 cm in order to allow fast sample exchange.

For a pointlike source with beta-energy of 700 keV the efficiency was calculated to be 45%. Because of finite diameter and thickness of the source the measured efficiency is about 30%. Considering the  $\Delta E$  and  $E$  spectrum in a two-dimensional way, a background rate of 3 counts/h was reached. Compared to the old LLCS this results in an increase of the FOM =  $S^2/B$  ( $S$  = signal rate,  $B$  = background) by a factor of 8.

Both energy-loss of a particle in the front detector and its time of flight between the two detectors are functions of its energy and the crossing angle. Thus a further reduction in background can be expected if one combines all information ( $\Delta E, E$  and  $T$ ) of one event.

- (1) R. Abela, G. Backenstoss, W. Kowald, H.G. and M. Seiler, L.M. Simons, J. Wüest, Phys. Lett. 95B(1980)318
- (2) F.J. Walter, R.R. Boshart, Nucl. Instr. Meth. 42(1966)1

+ Institut für Physik, Universität Basel

6. 21            PATRAC: A fast computer code for the simulation of slowing down particles in inhomogeneous magnetic fields

W. Kunold      Kernforschungszentrum Karlsruhe, IK II

During the last two years a device - "Cyclotron Trap" - was developed by our group to achieve high stopping densities of different particles (muons, pions, antiprotons) in gases even at pressures lower than 1 Torr (1).

This is achieved by winding up the paths of the slowed down charged particles in a magnetic field (fig. 1). The field has to be cyclotron-like, because of its focusing properties, which compensate transversal straggling.

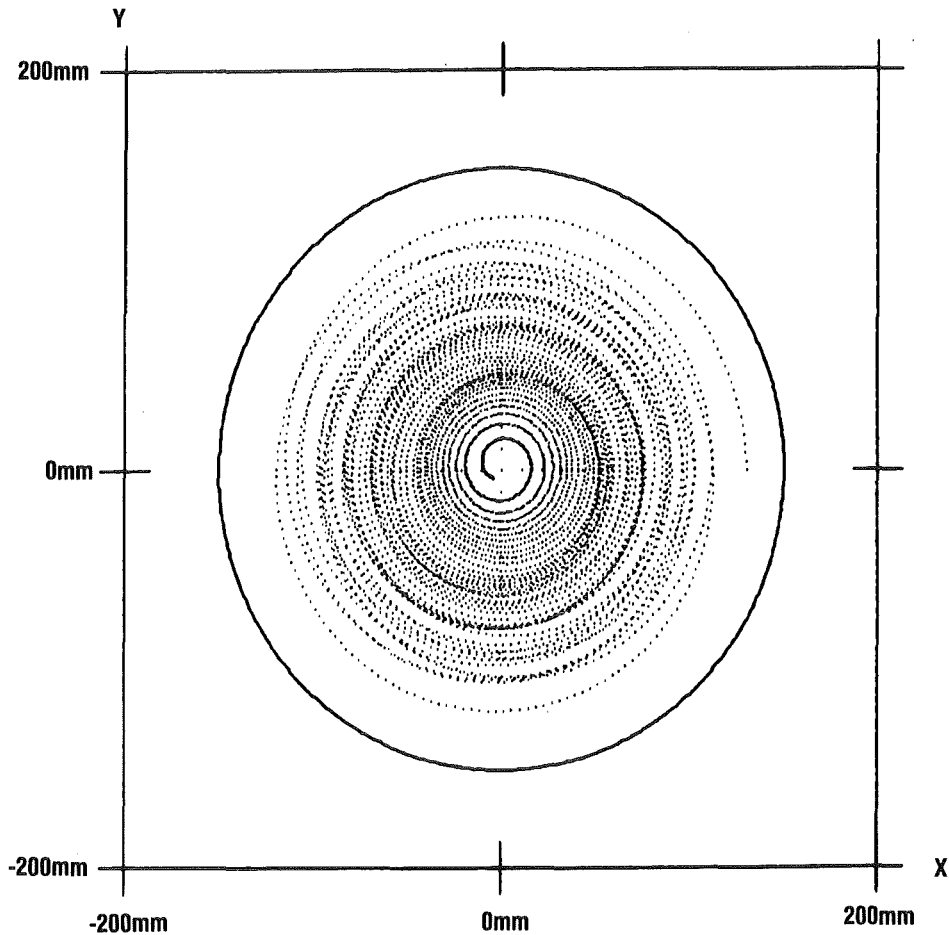


Fig. 1: Trace of a slowing down and finally stopped muon decelerated in neon gas at 760 Torr pressure

To simulate the dynamics of the particles in the "Trap" on a computer, it became necessary to develop the new code PATRAC, because other codes are not sufficient to solve all the problems, for example calculating stopping distributions (fig. 2). The code has to be fast, and it is also necessary to calculate the traces of charged decay products (muons, pions, electrons, Augerelectrons), flying in any direction, even far outside the mirror plane. For example, the SIN-code FIXPO (2), dedicated to cyclotron problems is neither fast nor can it calculate particle traces far outside the mirror plane.

The equations of motion in cylindrical coordinates are solved with a simple power series in the time interval  $dt$ :

$$X(t + dt) = X(t) + a_1 dt + a_2 dt^2 + a_3 dt^3 \dots$$

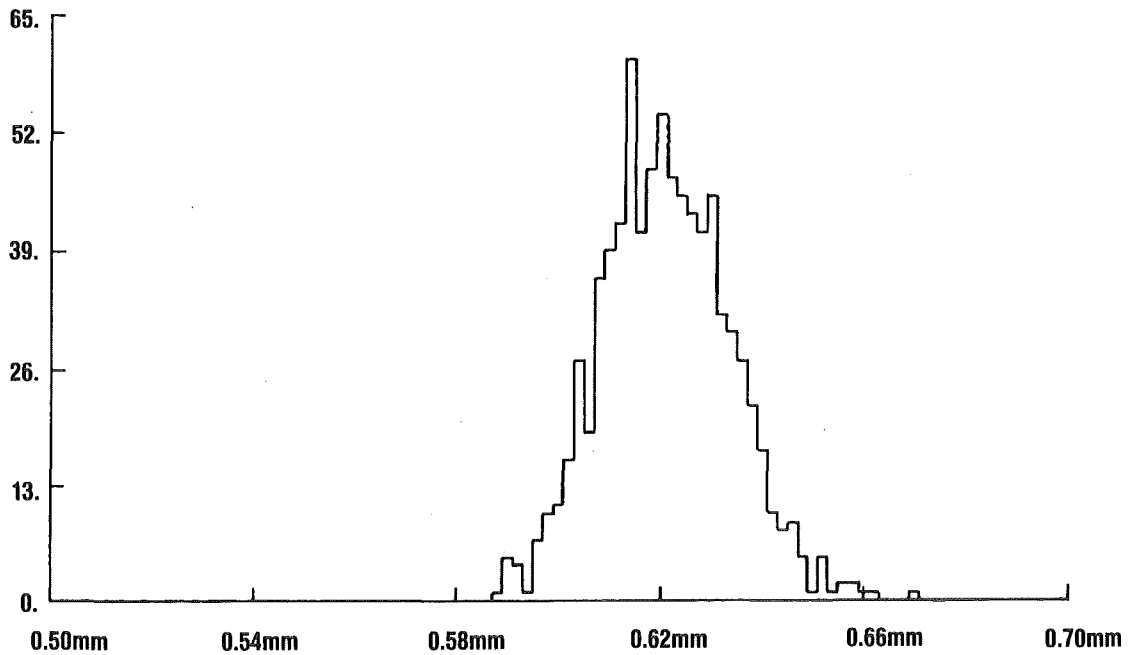


Fig. 2: Radial stopping distribution of a monoenergetic muon beam, started at the point  $r = 13$  cm,  $\phi = 0$ . Only energy straggling is taken into account. The stopping energy is assumed more or less arbitrarily to be less than 20 keV.

X can stand for any variable in the cylindrical coordinate system. Using this ansatz in the equations of motion, one obtains the coefficients  $a_i$ . This method converges for  $cdt \leq 1$ , that means  $dt \leq 3.333\dots$  nsec. For the purpose of the "Trap" it is useful to take  $dt \leq 100$  psec.

The relativistic mass of the particle is kept constant during the time interval  $t$  to  $t + dt$ , and is then recalculated for the actual velocity of the particle.

The values of the magnetic field are read in by the subroutine FIELD as a field map normalised to unity in the center, which then can be scaled by a chosen factor to reproduce the needed field strengths. The actual field values and their derivations are obtained by double parabolic interpolation (one for  $r$ , one for  $z$ ) with the help of the given values from the field map in the surrounding.

The magnetic field can be expanded locally in a Taylor series up to second order, if there are fast fluctuations in the shape of the field or if  $dt$  is rather large.

The energy loss of the particles in the different media is calculated in the subroutine ELOSS. Energy straggling and angular straggling can be taken into account with the help of Monte-Carlo-calculations in the subroutine ESTRAGG and ANGSTRAGG, respectively. For the calculation of energy loss, energy straggling and angular straggling, newest results are or will be used (3).

The arrangement of the moderators and the slowing down chamber is given in the subroutines GEOM and CHAMBER, respectively.

Because unstable particles do not stop decaying when they are in the "Trap", particle decay will be taken into account soon. This is unimportant for antiprotons.

Up to now, first stopping distributions under different assumptions have been calculated, but because of lack of statistics (no real production runs) no detailed analysis has been made. Extensive particle injection studies have been made, since the final design of the entrance moderator system depends on these.

- (1) SIN-Proposal R-81-02.1, CERN-proposal PS-175
- (2) FIXPO, G. Rudolf, W. Joho, SIN
- (3) J.F. Ziegler et al., Stopping Power and Range in All Elements, Vol. 3,4; Pergamon Press, 1977.

6. 22      Fast  $\mu$ P-controlled data acquisition system emulates  
5 (or more) multi channel analysers

Th. Köhler, U. Raich, J. Hauth, M. Meyer

Kernforschungszentrum Karlsruhe, IK II

One of the first experiments at LEAR (Low Energy Antiproton Ring) at CERN will examine antiprotonic atoms. After an antiproton is captured by the target nucleus it cascades down the Bohr levels and emits X-rays. By comparing the experimental values of the transition energies of the X-ray spectrum with those calculated assuming pure electromagnetic interactions, one can obtain information about the strong interaction between the antiproton and the nucleus from the observed shifts and widths of the lines.

It may also to be possible to learn something about annihilation. The experiment will measure the energies of the X-ray lines using semiconductor detectors. One of the main problems will be the suppression of background events due to high energy X-rays which are Compton scattered in the detectors and due to charged particles. This can be solved using the timing characteristics of the X-rays. Therefore one has to measure the energy and the timing of the X-rays. Using 5 semiconductor detectors and taking into account the antiproton rates expected at LEAR and the solid angle covered by the detectors one expects an event rate of about  $10^4$ /s. Usually multichannel analysers are used in such experiments. There the resolution of the 2 dimensional time-energy spectra is rather poor because of the limited amount of memory available. Since 5 of these analysers including tape stations would be necessary for such an experiment the cost would be rather high. This leads us to look for a better solution. It is also not possible to let e.g. a PDP-11 do the complete job of readout, tape writing and displays because it is too slow and because the address space accessible is too small for the 2 dimensional spectra. Hence we decided to use a M6800  $\mu$ P in a VME crate (new Motorola bus system) with an address space of 24 Mbyte for the readout while the PDP-11 does the tape writing etc. in parallel. Since the M6800 does only the readout no operating system is necessary on this machine. Only a very small (and therefore very fast) program is needed to build up spectra in the local VME memory. These spectra can be transferred to the PDP-11 host machine.

As explained above we use 2 computers: a VME system for the fast data acquisition and a PDP-11 for further data handling. The VME system was chosen because of its very large address space, its rigid mechanics and the future possibility to buy standard VME modules for system expansion. The interface of the VME bus to CAMAC is accomplished by CAMPORT, a micro-programmed CAMAC unit designed by M. Meyer. CAMPORT together with an A2 crate controller acts as an auxiliary crate controller, thus allowing the M6800 in the VME crate to access to CAMAC. Using this interface the M6800 can perform any desired CAMAC function. On the other hand CAMPORT looks like a normal CAMAC station viewed from the PDP-11. The CAMAC functions accessible by the PDP include the possibility to read or write VME memory (128kbytes maximum) in DMA mode. The complete bus request protocol is handled by CAMPORT. When CAMPORT was designed only the KDM design board was available on the market.

This board is an Exorciser bus compatible development system having an address capability of only 128 kbytes and other severe limitations compared to the new VME bus. (e.g. only 2 interrupt levels etc.) This is why we need a bus adapter which does some level conversion (the databus in the Exorciser is active low, the VME databus is active high) and which does the decoding of the high order address lines A 17 - A 23. Figures 1 and 2 show the dataflow in our experiment.

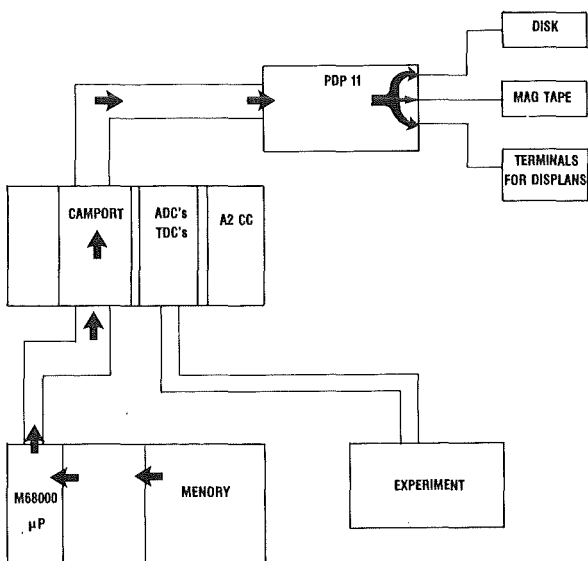


Fig. 1: Data flow during DMA

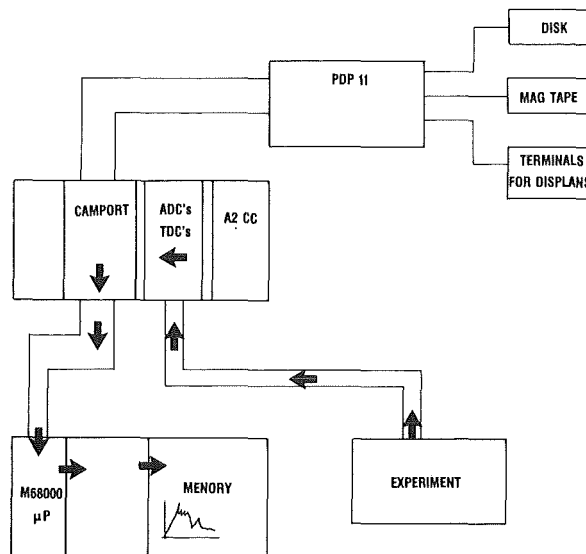


Fig. 2: Data flow during readout

During the 20 minutes of a normal LEAR cycle the data are collected by CAMAC units which are read by the M6800 through CAMPORT and the bus adapter. The M6800 builds up spectra in its local memory (figure 2). During the 1 minute LEAR pause the content of the VME memory is transferred to the PDP-11 memory and from there directly to disk. Since CAMPORT can access only 128 kbytes of the VME memory a 64 kbytes communication area is defined in the VME memory. All data to be transferred to the PDP-11 are first copied into this area. This implies no transfer speed limitation because the PDP-11 cannot keep more than 48 kbytes of data in its memory anyway. Hence after a transfer of a 48 kbyte data block these data have to be copied to disk before more can be accepted. During disk writing there is enough time for the M6800 to copy the new data into the communication area (figure 2). During the next LEAR cycle the VME machine continues data taking while the PDP-11 writes the transferred data to tape, produces the displays, makes fits etc.

6. 23 Progress of Low Energy Pion Spectrometer project

H. Matthäy, W. Kluge and H.A. Thiessen<sup>+</sup>

Kernforschungszentrum Karlsruhe, IK II

The ion optical design of the magnetic  $QQQ(DD)_s$  spectrometer for low energy pions LEPS<sup>\*</sup>) has been completed. The design parameters of the split pole have been fixed and are given in table 1. Since then, the main effort has been put into optimizing the quadrupole triplet, which is used to reimage the beam spot on the scattering target by a detector positioned in front of the split pole. This imaging is necessary, as the spectrometer is planned to be operated in the 'absolute' mode with a dispersed pion beam of high intensity.

Consequently the basic ion optical requirements to be met by the triplet are as follows.

1. Point to point imaging [ $(X/\theta) = 0$ ] between the target and the intermediate detector in the x-z plane (i.e. the plane that coincides with the median plane of the split pole). This allows the first order determination of the primary momentum of the incoming pions by measuring the x coordinate at the position of the intermediate focus.
2. Parallel to point imaging [ $(y/y) = 0$ ] in the y-z plane. This results in a first order measurement of the reaction angle by measuring the y coordinate at the position of the intermediate focus in the x-z plane. Besides this, attention had to be paid to some other mechanical and magnettechnical constraints.
3. In order to minimise losses from pion decay the triplet should be short but enough space (ca. 0.5 m) should be provided at both sides for the installation of the scattering chamber and the detector system at the intermediate focus position.
4. In order to guarantee an angular acceptance of  $\Delta\theta = \pm 100$  mrad in the x-z plane the aperture radius was chosen to be 8 cm.
5. The stray field should not affect significantly the incoming beam at backward angles.
6. The field at the pole tips should not exceed 0.75 T, in order to keep the saturation effects of the pole bases as small as possible.

<sup>\*</sup>Low Energy Pion Spectrometer to be installed at SIN <sup>+</sup>LAMPF, Los Alamos

The calculations were done for a symmetric triplet (+ - + in the x-z plane) imposing the additional condition  $(\theta/x) = 0$  (simultaneous point to point and waist to waist imaging)

The result is a triplet with the parameters given in table 2.

The three quadrupoles are mounted in a common return yoke assembly. The pole profile was chosen to be hyperbolic, the hyperbola being approximated by straight sections. The cut off was adjusted carefully by TRIM-calculations to provide a good quadrupole field up to the nominal aperture limit with coils close to the pole tips in order to minimise the strayfield.

bending radius of central ray:	0.5 m	
maximum field $B_0$ max:	1.35 T	<u>TABLE 1</u>
maximum momentum:	240 MeV/c	
momentum bite:	+ 20%, - 15%	
solid angle:	20 msr	
angular acceptance radial:	$\pm 100$ mrad	} (nominal)
axial:	$\pm 50$ mrad	
gapwidth in dipoles:	0.1 m	
in split :	0.55 m	

Object distance: 0.5 m  
Dipol D1

deflection angle:  $\phi_1 = 60^\circ$   
entrance face angle:  $\alpha_1 = 20^\circ$   
exit face angle:  $\beta_1 = 21.3^\circ$   
curvature at entrance:  $R_1 = -1.00$  m  
curvature at exit:  $R_2 = 1.43$  m

Split

deflection angle  $\phi_2 = 9.2^\circ$   
field  $B_s \approx 0.2 B_0$

Dipole D2

deflection angle:  $\phi_2 = 60^\circ$   
entrance face angle:  $\alpha_2 = 41.3^\circ$   
exit face angle:  $\beta_2 = -15^\circ$   
(no curvature)

Image distance: 0.8 m

focal plane angle:  $\psi \approx 43^\circ$   
length (central ray): 2.75 m

Distance between target and pole of $Q_1$ :	55.8 cm	<u>TABLE 2</u>
Distance between pole of $Q_3$ and intermediate focus position:	55.8 cm	
pole length of $Q_1$ and $Q_3$ :	17.3 cm	
pole length of $Q_2$ :	24.8 cm	
Distance between poles of adjacent quadrupoles:	13.2 cm	
Field at the pole tip for max. centre momentum $p = 200$ MeV/c	$\left\{ \begin{array}{l} Q_1, Q_3: 0.75 \text{ T} \\ Q_2: -0.75 \text{ T} \end{array} \right.$	

6. 24 Design and test of a vertical drift chamber (VDC)

J. Jaki, H. Matthäy, H. Degitz, A. Höhne, K. Kärcher,  
W. Kluge, U. Klein

The new Karlsruhe magnetic spectrometer LEPS<sup>\*)</sup> to be used for the scattering of low energy pions at SIN has a focal plane tilt angle of approximately  $43^\circ$  with respect to the central trajectory. This favours the use of a vertical drift chamber (VDC) as a focal plane detector measuring simultaneously with high precision both the coordinate and the angle of the intersection of each trajectory's projection on the bending plane with the detector plane (1).

Hence, a prototype of this detector has been built and tested. The principle of operation of the VDC can be seen from fig. 1 which shows a cross-sectional view of the chamber perpendicular to the direction of the sense wires. It differs from standard MWPC's mainly by the additional shielding wires positioned between any two sense wires. The diameter of the shielding wires has to be chosen so that they cause only a small gas amplification and provide an effective shielding against positive induced signals from adjacent sense wires.

Depending on the gap width (i.e. the distance between the sense wires and a H.V.-plane), the distance between adjacent sense wires, and the angle of incidence each track intersects a certain number of sensitive drift cells. The simultaneous measurement of the drift times in all these cells allows a precise reconstruction of the track within the chamber. An additional specific advantage of using this type of drift chamber as a focal plane detector for LEPS is that it avoids all problems resulting from right-left ambiguity.

The present prototype has a sensitive area of  $292 \times 164 \text{ mm}^2$ . Its read out plane consists of sense wires (20  $\mu\text{m}$  thick, 4 mm apart) alternating with the shielding wires (45  $\mu\text{m}$  thick, 4 mm apart). The high voltage planes are made of 20  $\mu\text{m}$  aluminium foils. The gap width is 10 mm. The chamber was filled with a gas mixture of 50% argon and 50% isobutane. A high voltage of -7.9 kV was applied.

The chamber has been tested with electrons of a  $^{90}\text{Sr}$  source and with pions and protons of a momentum of 300 MeV/c at SIN at various angles of inclination  $\alpha$  between  $0^\circ$  and  $60^\circ$ . Preliminary results for  $\alpha = 60^\circ$  are shown in figs. 2-4.

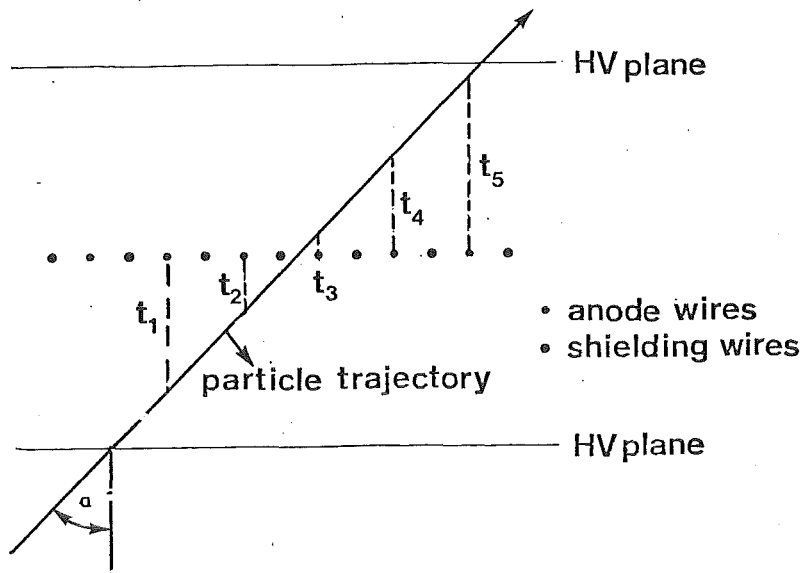


Fig. 1: Principle of operation of the vertical drift chamber

Fig. 2 shows the dispersion of the quantity  $[t_1 - t_2 - (t_4 - t_3)]$  which by definition (see fig. 1) should be zero. The F.W.H.M. of this distribution turns out to be 8 ns. This includes the variance of four drift time measurements. Hence the absolute accuracy corresponding to one cell equals 4 ns (F.W.H.M.) which is equivalent to an inherent spatial resolution of at least  $\pm 100 \mu\text{m}$ . A more detailed evaluation of the spatial resolution finally achievable is presently underway and has to include all measured drift times which are e.g. five or six for an inclination angle of  $45^\circ$ .

Fig. 3 shows the experimentally measured angular resolution of the VDC. The angle was measured relative to the particle trajectory determined independently with an uncertainty of less than  $\pm 1 \text{ mrad}$  by two MWPC's placed 1,25 m before and behind the VDC. The angular resolution obtained for the VDC is  $\pm 8 \text{ mrad}$  ( $\hat{=} \pm 0.5^\circ$ ).

In fig. 4 the drift time is plotted against the length of the drift path. The latter is determined to be the shortest distance between a sense wire and a straight line obtained by a least square fit from all drift times measured simultaneously. A perfect linear relation is found except for a region with 0.5 mm radius surrounding the wire where the electric field is highly inhomogeneous.

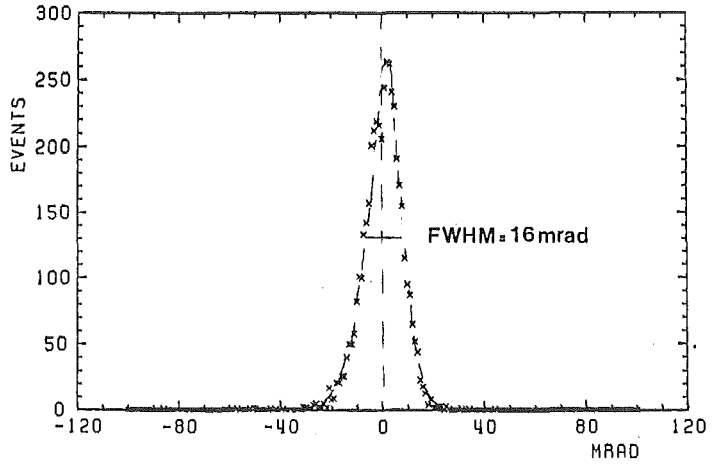
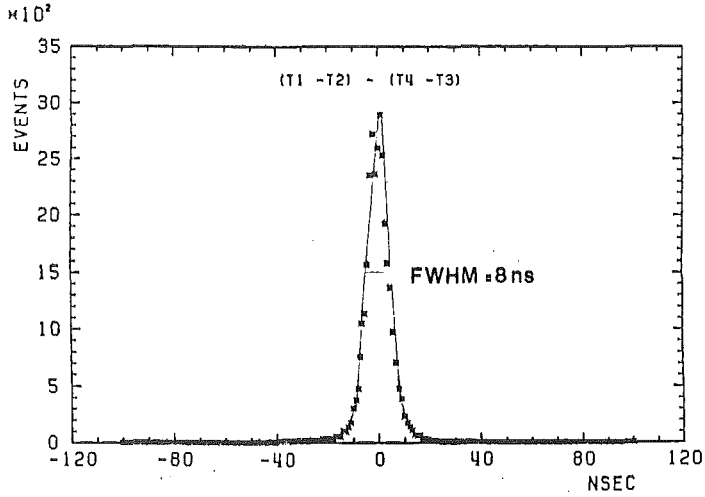


Fig. 2: Dispersion of the quantity  $[t_1 - t_2 - (t_4 - t_3)]$

Fig. 3: Angular resolution of the vertical drift chamber

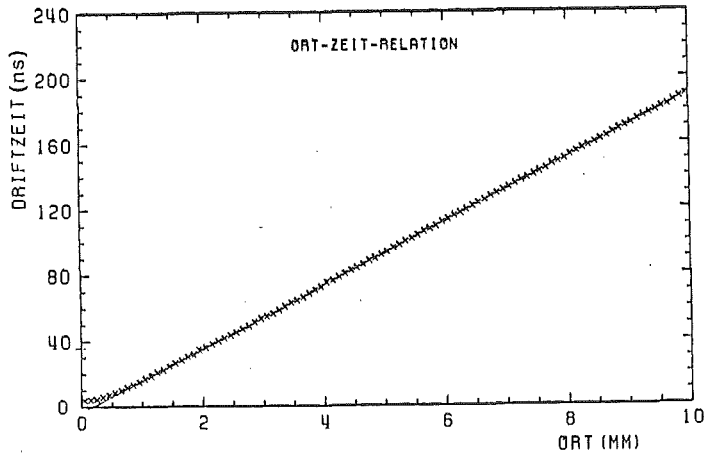


Fig. 4: Relation between drift time and drift path.

\* Low Energy Pion Spectrometer

(1) W. Bertozzi et al., Nucl. Instr. Meth. 141 (1977)457

6. 25      The Electron Cooling Device for LEAR \*

L. Hütten, H. Poth, A. Wolf, H. Haseroth<sup>+</sup> and Ch. Hill<sup>+</sup>

Kernforschungszentrum Karlsruhe, IK II

Experiments (1,2,3) in which low energy protons were cooled by a "cold" electron beam have proved that this is a very powerful technique to improve low energy beams and to increase their phase space density by several orders of magnitude in about a second. The encouraging results obtained in the electron cooling experiment in ICE and their theoretical understanding (2,4) provide an incentive for the application of this technique for the cooling of antiproton beams stored in LEAR. Electron cooling in LEAR allows one to obtain high quality antiproton pencil beams with a momentum spread of  $10^{-4}$  or better and permits the operation of a thin ringinternal target at low energy. It would also allow the deceleration of the antiprotons to extremely low energies beyond the lower LEAR operation energy (5 MeV). This would improve the stop-density of antiprotons in thin targets by several orders of magnitude and give access to the study of rare and eventually even radioactive isotopes. The combination of electron cooling and internal target operation provides the most efficient use of antiprotons and allows for high resolution spectroscopy which is virtually impossible to reach with external beams and targets at low energy.

The electron cooling apparatus for LEAR is shown in fig. 1. It is an improved version of the ICE experimental set-up (2). Electrons emerging from the hot cathode ( $1350^{\circ}\text{K}$ ), which is at negative high potential, are accelerated by five ring shaped electrodes of increasing potential to their nominal energy. The electron beam is prevented from blowing up by the solenoidal magnetic field and retains its size of 5 cm diameter.

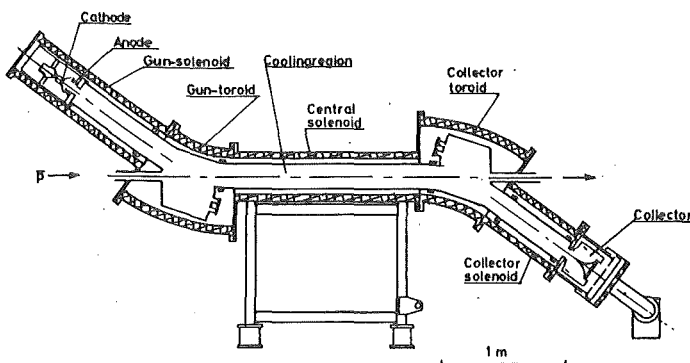


Fig. 1: LEAR Electron cooler

The electrons follow the magnetic field lines through the adjacent toroidal section, where they are bent into the  $\bar{p}$ -beam, through the central solenoid and the collector toroid to the collector solenoid. At the end of this section the electrons are decelerated to a few KeV and captured in the collector. Initially the cooler will be operated in the range between 3 and 40 KV ( $\beta = 0.1 \div 0.36$ ) with an electron current between a few mA and 5A (at 40 KV). The cooling region of 1.5 m length is about 2% of the LEAR circumference. The cooler has to operate under ultra-high vacuum conditions. Special attention is paid to the generation of a very cold e-beam which requires a highly stable high voltage and a very homogenous magnetic field.

From the experience gained in ICE we expect to achieve e-fold emittance cooling times of 2 to 5 s (at 300 MeV/c  $\bar{p}$ -momentum). As equilibrium emittances we expect values of at least  $\sqrt{\pi}$  mm mrad. The momentum spread  $\Delta p/p$  should be cooled down to about  $10^{-4}$ . The cooling times increase at lower energies as  $\beta^{-2}$  for a constant perveance gun which is easy to operate during deceleration. With this performance hydrogen targets of up to  $2 \cdot 10^{-10}$  g/cm<sup>2</sup> could be used at 300 MeV/c in internal target operation mode.

Presently the required improvements of the vacuum system are underway. The main magnetic field system is assembled and the field measurements are completed. The rest of the year will be dedicated to vacuum studies, setting-up of the power supplies and the development of the control hard- and software. In the next year, effort will be concentrated on the achievement of the required vacuum conditions for LEAR and the investigation of the electron beam properties. The installation of the cooler in the long straight section 3 of LEAR is foreseen around 1985.

- (1) G.I. Budker et al., Part Accel. 7, 197 (1976) and Sov. Phys. Usp. 21, 277 (1978)
- (2) M. Bell et al., Nucl. Instr. Methods 190, 237 (1981)
- (3) R. Forster et al., IEEE Trans. Nucl. Sci., NS 28, 2386 (1981)
- (4) KfK Report 3280 (1981), 3.5.13, 3.5.16, 3.5.17

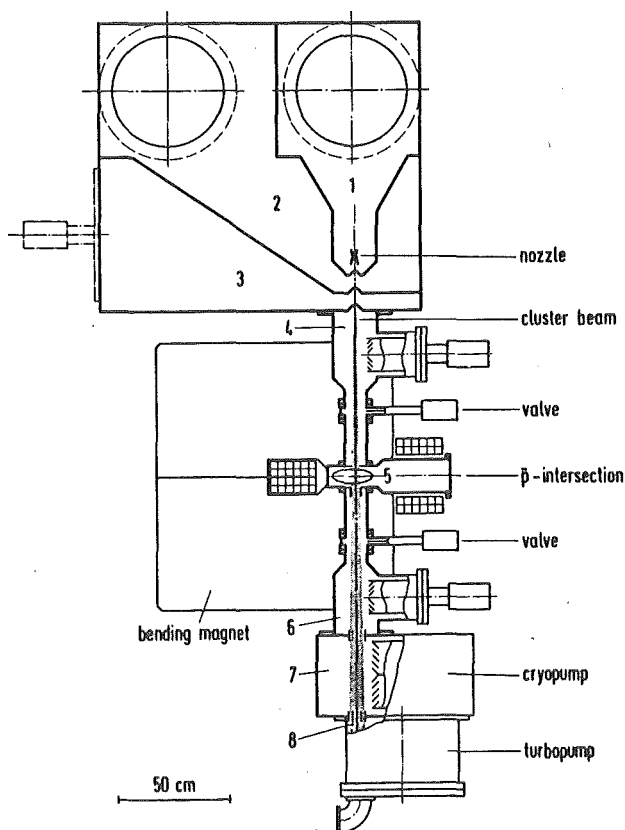
<sup>+</sup>CERN, Geneva

\*Proceedings of the 3<sup>rd</sup> Int. School of Physics of Exotic Atoms-Physics around LEAR with low energy cooled Antiprotons, Erice, 9-16 May 1982

6. 26 Internal cluster beam target for antineutron production in LEAR\*

J. Gspann<sup>+</sup> and H. Poth Kernforschungszentrum Karlsruhe, IK II

An internal hydrogen cluster beam target dedicated to antineutron production is proposed for installation in one of the bending magnets of LEAR. Running in the wedge-shaped gap in the center of the magnet, the cluster beam will intersect the antiproton beam vertically (fig. 1). The design target thickness is  $2 \times 10^{-10}$  g/cm<sup>2</sup>, with lower values being readily available. The antineutron production rate is expected to be larger than  $5.5 \times 10^4$   $\bar{n}$ /s at 600 MeV/c and optimum target thickness (fig 2). In fig. 3 the number of antineutrons produced per second into a Laboratory forward angle of 14 m strd and 1.7 m strd is shown. The cluster beam source will be located on top of the magnet together with its main pumping stages while the main sink stages will be placed below the magnet (fig. 1). Turbomolecular pumps will be used for pumping the higher gas loads at the source as well as for removing the main part of the beam flux. For the intermediate pumping stages, refrigerator cryopumps are proposed. Later installation of the facility in a long straight section of LEAR would be possible.



Pressure stage specifications

Pressure stage	$\frac{S_{eff}}{10^3 \text{ l/s}}$	$\frac{L}{\text{l/s}}$	$\frac{p}{\text{mbar}}$	$\frac{J}{\text{mbar l/s}}$
1	5	17.9	$10^{-2}$	50
2	5	26.5	$3.6 \times 10^{-5}$	0.18
3	5	34.2	$2 \times 10^{-7}$	$9.5 \times 10^{-4}$
4	1	553	$4.4 \times 10^{-9}$	$6.8 \times 10^{-6}$
5	2		$6.8 \times 10^{-8}$	$1.37 \times 10^{-4}$
6	1	800	$1.7 \times 10^{-7}$	$3 \times 10^{-4}$
7	25	1000	$3 \times 10^{-7}$	$7.9 \times 10^{-3}$
8	33	400	$2 \times 10^{-5}$	0.65

$S_{eff}$  = effective pumping speed  
 L = conductance to next stage facing LEAR  
 p = stage pressure  
 J = mass flow into stage

Fig. 1: Schematic view of an internal cluster beam target for  $\bar{n}$  production.

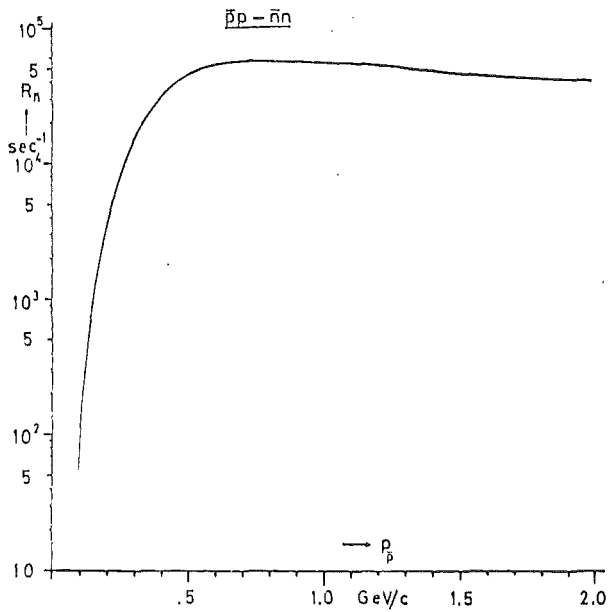


Fig. 2: Total  $\bar{n}$  production rate versus antiproton momentum (for a antiproton consumption rate of  $10^6 \text{ s}^{-1}$  on target).

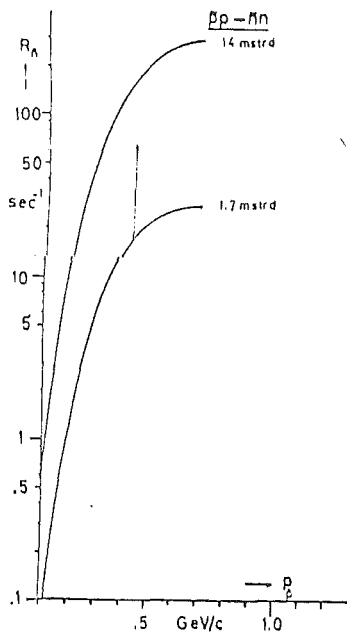


Fig. 3: Number of anti-neutrons produced into a forward angle of 14 mstrd and 1.7 mstrd assuming isotropical CM production ( $\bar{p}$  consumption rate  $10^6 \text{ s}^{-1}$ ). Arrow indicates increase of  $\bar{n}$  rate if the measured nonisotropical CM production at 430 MeV/c is used.

6. 27 Antiproton mass measurement using stored beams cooled by electrons\*

H. Poth Kernforschungszentrum Karlsruhe, IK II

A precise knowledge of the antiproton-proton mass difference is of basic interest for a test of the validity of fundamental invariance principles. With the availability of cooled low energy  $\bar{p}$  beams from LEAR high-precision measurements can be anticipated. Here a method is proposed to measure the mass of the antiproton relative to that of the  $H^-$  ion.

Antiprotons and  $H^-$  ions are kept circulating simultaneously in a storage ring at low energy and are cooled by an electron beam to nearly equal velocity. As outlined in the following the  $\bar{p}$ - $p$  mass difference can be determined by measuring the revolution frequency of the coasting beams. The revolution frequency spectrum of a coasting beam is given by

$$\frac{f-f_0}{f_0} = \eta \frac{p-p_0}{p_0}, \quad \eta = \frac{1}{\gamma_t^2} - \frac{1}{\gamma^2} : \text{ off-momentum function}$$

$$m_{\gamma_t} c^2 : \text{ transition energy of the storage ring}$$

$$\gamma = (1-\beta^2)^{-1/2}$$

Particles with momentum  $p_0 = m\beta_0\gamma c^2$  circulate on the nominal orbit (with a circumference  $2\pi R$ ) with a revolution frequency  $f_0 = c\beta_0/2\pi R$ . A beam momentum distribution characterized by its r.m.s. width  $\Delta p$  leads to a distribution of the same shape in the frequency domain with a width  $\Delta f$ . For coasting  $\bar{p}$  and  $H^-$  beams of equal velocities the momenta differ by the relative mass difference  $\mu = \delta m/m \approx 10^{-3}$  ( $\delta m = m_{H^-} - m_{\bar{p}}$ ,  $m = m_{H^-}/2 + m_{\bar{p}}/2$ ). If there is a slight velocity difference  $\delta\beta = \beta_{H^-} - \beta_{\bar{p}}$  the measurement of the revolution-frequency spectrum of the two coasting beams will result in the observation of two separated peaks with a spectral width proportional to the velocity (momentum) spread of each beam. The centres of the peaks will be separated by

$$\frac{\delta f}{f_0} = \eta \cdot \left( \mu + \frac{\delta\beta}{\beta_0} \right)$$

In order to determine the  $\bar{p}H^-$  mass difference with high precision it is necessary that  $\delta\beta/\beta_0 \ll \mu$ . This can be achieved by cooling both beams with

a monochromatic electron beam. Antiprotons and  $H^-$ -ions are cooled to the same velocity if provision is made for the electron velocity not to depend on the radial position or if both beams intersect the electron beam at the same position. The limitation of the ultimate precision that can be obtained comes mainly from the realization of these conditions, the beam emittances and momentum spread achievable with electron cooling and the relative magnetic field homogeneity of the storage ring. The frequency spectrum can be measured with a resonant Schottky pick-up system tuned to a high harmonic of the revolution frequency. The frequency analysis of both beams can be made simultaneously. It should also be possible to measure directly the beat frequency  $\mu f_0$  between the two revolution frequencies. The stored beam currents can be very low for this measurements.

An estimate for the accuracy which could be obtained with LEAR and its foreseen electron cooling system shows that  $\mu$  could be measured to a precision of  $\Delta\mu = \pm 2 \cdot 10^{-7}$  without special effort. The method outlined is non-destructive almost no antiprotons are lost. Such a precision would lower the limit for a possible  $\bar{p}$ -p mass difference to 200 eV. This is 250 times more precise than the measured  $\bar{p}$  mass and more than one order of magnitude better than  $m_p$ .

\* Nucl. Instr. and Methods, Vol. 200 (1982)

6. 28      Production of antideuterons in antiproton rings\*

D. Möhl<sup>+</sup>, K. Kilian<sup>+</sup>, H. Pilkuhn<sup>++</sup> and H. Poth

Kernforschungszentrum Karlsruhe, IK II

In the near future, intense  $\bar{p}$  beams will be available from LEAR at CERN. For various purposes it may be desirable to produce also heavier antinuclei. A first step in this direction is the production of antideuterons. The production of low-energy antideuterons in the reaction  $\bar{p}\bar{p} \rightarrow \bar{d}\pi^-$  by colliding antiproton beams of equal momenta has already been suggested (1). Here, however, we propose a scheme in which  $\bar{d}$  synthesized in this reaction are successively accumulated and stored. The cross-section for  $\bar{p}\bar{p} \rightarrow \bar{d}\pi^-$  should be identical with that of  $pp \rightarrow d\pi^+$ . It has a maximum of about 3.2 mb at  $\sqrt{s} = 2.16$  GeV. The total  $pp$  cross-section is 38 mb at this energy. The only other inelastic reactions are  $pp \rightarrow pn\pi^+$  ( $\approx 10$ mb) and  $pp \rightarrow pp\pi^0$  (3mb).

The essential trick for producing and storing  $\bar{d}$  is to choose the momenta  $p_1$  and  $p_2$  of the colliding antiprotons such that the  $\bar{d}$  momentum  $p_d$  is equal to the larger  $\bar{p}$  momentum ( $p_1$ ). Then the  $\bar{d}$  emerging under  $0^\circ$  from the colliding region are stored in the larger ring. One needs two rings as indicated in fig. 1.

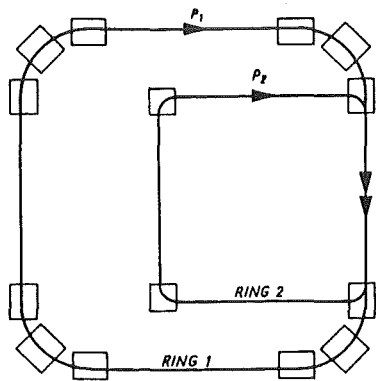


Fig. 1:  
Schematic view of the double ring collider for  $\bar{d}$  production. The  $\bar{p}$  in rings 1 and 2 overlap in a common straight section. Here  $\bar{d}$  are produced and stored in ring 1.

For a given  $p_1$ ,  $p_2$  must be taken as shown in fig. 2. As the ring accepts practically only forward produced  $\bar{d}$ , parallel motion is an order of magnitude better than antiparallel motion, because of the Lorentz transformation from the c.m. to the Lab. system.

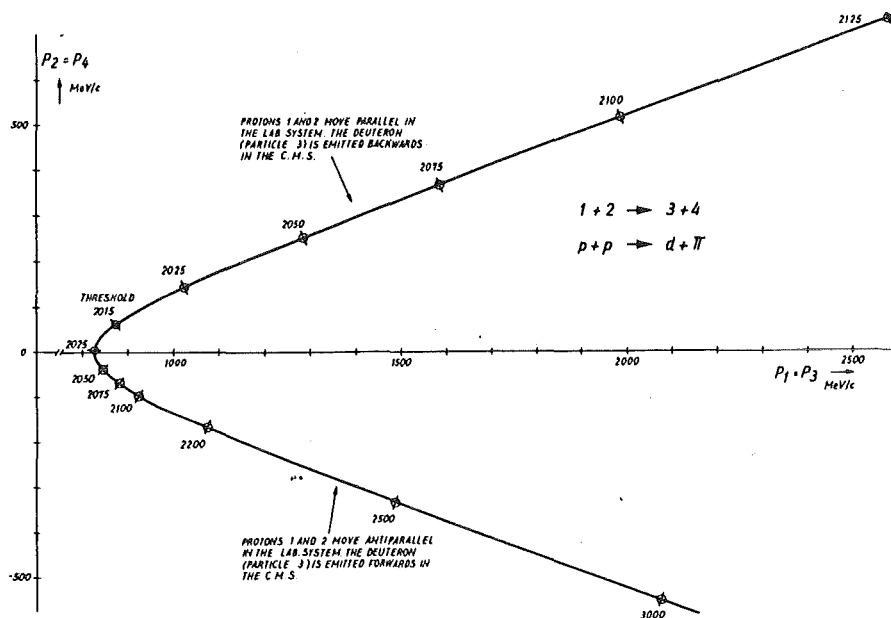


Fig. 2: Combinations of (anti)proton momenta  $p_1$  and  $p_2$  which produce, in collinear collisions, (anti)deuterons with the momentum  $p_1$ . Considered is the two-body reaction  $pp \rightarrow d\pi$ . Positive (negative)  $p_2$  correspond to parallel (antiparallel)  $pp$  collisions. The parameter on the curve is the invariant mass  $\sqrt{s}$  in MeV.

We have evaluated the  $\bar{d}$  yield per  $\bar{p}\bar{p}$  pair for several combinations of  $p_1$  and  $p_2$  and found a maximum value of about  $10^{-3}$ . If a luminosity of  $1.5 \cdot 10^{31} \text{ cm}^{-2} \text{ s}^{-1}$  could be reached, corresponding to a  $\bar{p}$  consumption rate of  $10^6 \text{ s}^{-1}$  ( $= \bar{p}$  accumulation rate), 500  $\bar{d}/\text{s}$  could be stored and accumulated at  $p_{\bar{d}} = 2 \text{ GeV}/c$  in the larger ring. With a practicable luminosity of  $1.6 \cdot 10^{28} \text{ cm}^{-2} \text{ s}^{-1}$  given by the phase space density limit of the stored beams only 1000  $\bar{p}/\text{s}$  would be consumed to produce and accumulate 0.5  $\bar{d}/\text{s}$ . Since the antideuterons can be continuously cooled and accumulated over a long time in the storage ring a high quality  $\bar{d}$  beam is obtained at the end of the accumulation cycle. It can be then accelerated or decelerated without losses to the desired experimental energy and efficient use of the  $\bar{d}$  can be made for instance by having them interact with an internal target.

(1) H. Pilkuhn and H. Poth, CERN  $\bar{p}$  LEAR Note 86.

+ CERN, Geneva

++ Institut für Theoretische Kernphysik, Universität Karlsruhe

\* Nucl. Instr. and Methods Vol. 200 (1982)

6. 29 Test of a large position-sensitive scintillation counter with cosmic ray muons

S. Ljungfelt, K. Sambale, G. Schmidt, H. Ullrich

A position sensitive time-of flight counter with  $2\text{m}^2$  active area ( $0.3 \text{ m}^3$  active volume) for the detection of neutrons, protons and deuterons in the 10 - 100 MeV range has been constructed. It consists of 30 plastic scintillator bars  $2 \text{ m} \times 10 \text{ cm} \times 5 \text{ cm}$  and 5 anticounter  $2 \text{ m} \times 25 \text{ cm} \times 0,4 \text{ cm}$ . All bars and anticounters carry a X<sup>-</sup>P 2230 Phototube on each side, the signal of which is recorded by a TDC and a ADC. The position sensitivity along the 2 m is achieved via the time difference of the light signal on both ends of the bars. It has been tested by measuring the angular distribution of cosmic-ray muons. The data points (see fig. 1) can be fitted by

$$I(\alpha) = 0,84 \times 10^{-2} (\cos\alpha)^{2,15} \frac{1}{\text{s} \cdot \text{sr} \cdot \text{cm}^2}$$

The shape of this distribution as well as the absolute value of the measured intensity are in excellent agreement with the data of Alkhofer et al. (1).

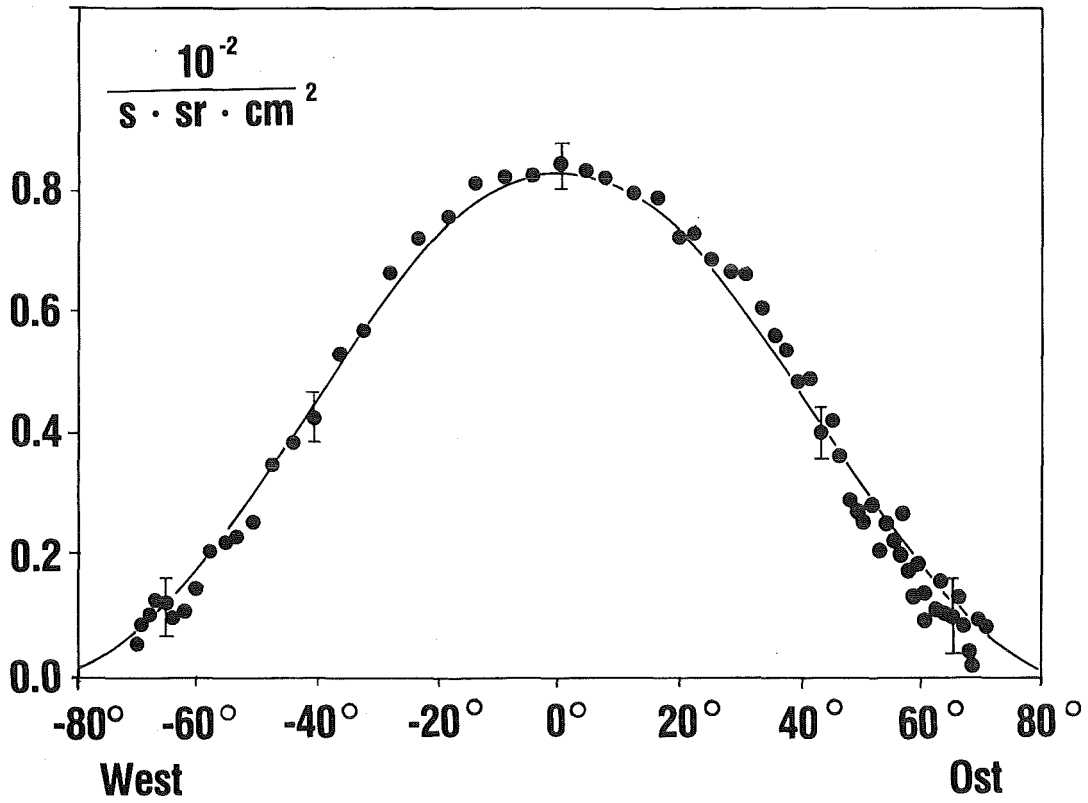


Fig. 1: Directional Distribution of muons for channel number zero. The crosses indicate the data points. The solid line corresponds to the distribution  $I(\alpha) = 0.084 \cos^{2.15} \alpha$  ( $\text{s}^{-1} \text{sr}^{-1} \text{cm}^{-2}$ ). The statistical errors for  $\alpha = 0^\circ \pm 40^\circ$  and  $\pm 60^\circ$  are indicated.

(1) O.C. Alkhofer, Fortschritte der Physik 15 (1967)113

## 7. APPLICATIONS

### 7.1 Elemental Mapping with the Karlsruhe Nuclear Microprobe\*

D. Heck

Kernforschungszentrum Karlsruhe, IAK II

Charged particle reactions have been used successfully in the Karlsruhe nuclear microprobe for the analysis of light elements. Heavier elements with  $Z \geq 13$  are identified by means of particle induced X-rays in concentrations down to the ppm range. The primary ion beams are generated in a 3.5 MV Van de Graaff accelerator. By collimation and focussing with a magnetic quadrupole doublet the beam diameter is reduced to  $\sim 3 \mu\text{m}$  with currents of  $\sim 600 \text{ pA}$ .

Mapping of the elemental concentrations is performed by sweeping the ion beam in one or both dimensions across the sample surface, thus an area up to  $1 \times 1 \text{ mm}^2$  may be covered at once. The electric beam deflection is controlled digitally and the number of analysis points may be chosen in binary steps up to 256 in each direction. Some examples of nuclear microprobe measurements are presented.

\*Nucl. Instr. and Meth. 197 (1982) 91

### 7.2 Trace Element Analysis of Single Cells of Organic Matter

D. Heck and E. Rokita<sup>+</sup>

Kernforschungszentrum Karlsruhe, IAK II

Trace element analyses of single cells of organic matter have been performed with proton induced X-ray emission (PIXE). A 3 MeV proton beam generated by the 3.5 MV Van de Graaff accelerator is collimated and focussed down to a diameter of  $\sim 2.5 \mu\text{m}$  at currents up to 1 nA, and is swept periodically across the target surface in a meandric pattern. The X-rays are detected in a Si(Li) diode of  $80 \text{ mm}^2$ , mounted at 26 mm distance in  $135^\circ$  position relative to the incident beam. The mass of the irradiated sample volume is simultaneously determined by counting the protons which have undergone Rutherford scattering (RBS) backward into a Silicon surface barrier detector ( $450 \text{ mm}^2$ ,  $300 \mu\text{m}$  depletion depth, distance 40 mm

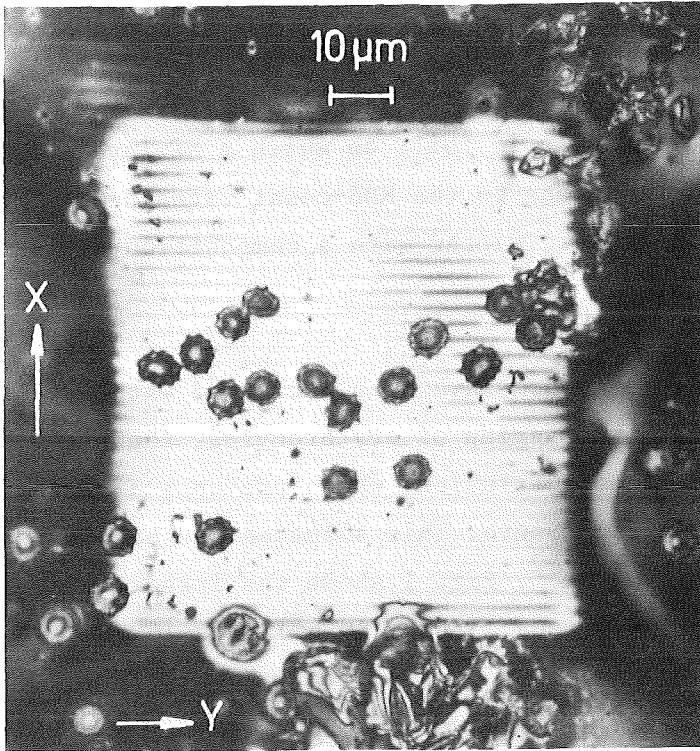


Fig. 1  
Scanned area of the  
blood sample.

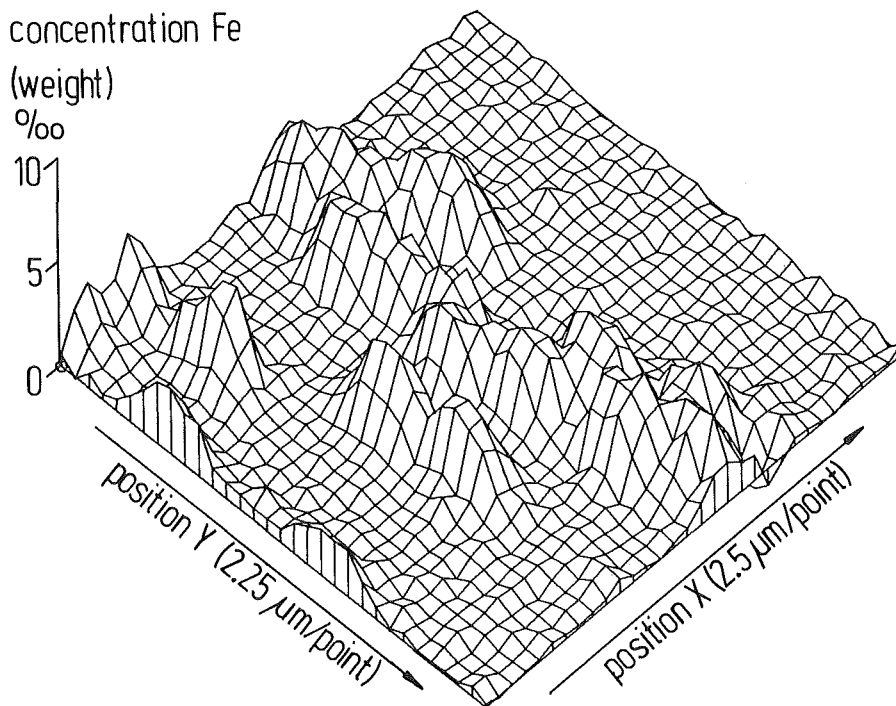


Fig. 2 Perspective plot of the Fe-concentration of the  
blood sample of Fig. 1.

in  $135^\circ$ ). It is adopted, that the elemental composition of the dominant matrix materials is homogeneous, and that the influence of the trace elements on the RBS-count rate is negligible. Calibration of the mass determination and X-ray emission is performed with a reference standard consisting of a thin high purity plastic foil, on which a Ni-layer of  $600 \text{ \AA}$  has been evaporated. Corrections to the RBS-count rates have to be applied when changing over to organic matter with a composition different from the plastic foil material.

First tests of the analysis method have been performed with erythrocytes (red blood cells). To avoid an overlap of erythrocytes, the blood has been thinned with physiological NaCl-solution, which prevents a rupture of the cellular walls by osmotic pressure. This solution has been dried on Formvar backing foils of  $30 \mu\text{g cm}^{-2}$ . Fig. 1 shows the irradiated portion of such a sample (scanning area  $73 \mu\text{m} \times 80 \mu\text{m}$ ) with 16 erythrocytes of  $7 \mu\text{m}$  diameter.

The division of the local Fe  $K_\alpha$  X-ray intensity by the local RBS count rate results in the local Fe concentration, which has to be normalized and corrected for the self absorption of X-rays by the local thickness of the sample. This concentration distribution is plotted perspectively in Fig. 2 in dependence on the position coordinates. The increased Fe concentration at the positions of the erythrocytes is clearly visible. The absolute amounts of Fe are  $0.04 \text{ pg}$  per point in the middle of the erythrocytes and about  $0.0007 \text{ pg}$  per position at the blank backing foil.

<sup>+</sup>Jagellonian University of Cracow, Poland

### 7.3 K-Edge Jump of the Photon Mass Attenuation Coefficient for Uranium and Plutonium

H. Eberle, I. Michel-Piper, and H. Ottmar  
Kernforschungszentrum Karlsruhe, IAK II

Photon absorptiometry with a continuous X-ray beam at the K absorption edge has been recently developed to a prove technique for accurate measurements of heavy element concentrations in solutions (1,2). With this technique the element concentration  $\rho$  is determined from the ratio of photon transmissions,  $T_L/T_H$ , on the low and high energy side of the K absorption edge.

$$\rho \text{ [g/cm}^2\text{]} = \frac{\ln T_L/T_H}{\Delta\mu},$$

where  $\Delta\mu$  [cm<sup>2</sup>/g] is the difference of the photon mass attenuation coefficient across the K edge of the element to be measured.

Values of the  $\Delta\mu$  for U and Pu have been determined from the transmission of a continuous X-ray beam through well-characterized nitrate solutions of both elements. Since the energy dependence of the mass attenuation coefficient follows a power law,  $\mu(E) \sim E^{-m}$ , with  $m$  being approximately constant within limited energy ranges, a linear relationship on a log log scale holds for the values of  $\ln T(E)$  vs.  $E$ :

$$\log \ln T(E) \sim m \log E.$$

The photon transmissions  $T(E)$  measured within about  $\pm 8$  keV of the K absorption edge have been fitted to this relationship. The values  $\Delta\mu$  and the slopes  $m$  in the vicinity of the K absorption edge measured for U and Pu on the reference solutions are listed in Table 1. The measured  $\Delta\mu$  values are compared with values from 3 different compilations of theoretically calculated photon cross sections.

Table I  $\Delta\mu$  values and energy dependence of  $\mu$  in the vicinity of the K absorption edge for U and Pu

Element	K-Edge Jump $\Delta\mu$ [cm <sup>2</sup> /g]				Slope $m$ ( $E_K \pm 8$ keV)	
	Experiment		Theory		Below Edge	Above Edge
	This work	(3)	(4)	(5)		
U	3.548 $\pm$ 0.020	3.605	3.501	3.651	2.26 $\pm$ 0.07	2.60 $\pm$ 0.11
Pu	3.291 $\pm$ 0.014	3.223	3.193	3.397	2.17 $\pm$ 0.14	2.46 $\pm$ 0.11

- (1) H. Eberle, P. Matussek, I. Michel-Piper and H. Ottmar, Report ESARDA 11 (1980) 372, edited by L. Stanchi, Joint Research Centre Ispra, Italy.
- (2) H. Eberle, P. Matussek, I. Michel-Piper, and H. Ottmar, Report ESARDA 13 (1981) 109, edited by L. Stanchi, Joint Research Centre, Ispra, Italy.
- (3) W.M.J. Veigele, Photon Cross Sections from 0.1 keV to 1 MeV for Elements Z=1 to Z=94, Atomic Data Tables 5 (1973) 51-111.
- (4) E. Storm, H. Israel, Photon Cross Sections from 1 keV to 100 MeV for elements Z=1 to Z=100, Nuclear Data Tables 7 (1970) 6.

measurement result is found to be well below 1 %.

Other parameters that affect the accuracy of the  $^{235}\text{U}$  enrichment assay such as sample material composition, thickness and shape of the container wall, minimum sample size, and collimator-detector geometry have been carefully investigated. The results will be presented as a part of the User's Manual delivered with the  $^{235}\text{U}$  calibration standards that are presently fabricated at CBNM Geel.

Fig. 1 shows as an example the minimum sample dimensions for different uranium compound required for 99.9 % of the gamma-ray intensity measured from a really infinite thick sample, when a cylindrical collimator of 4 cm diameter and 2 cm depth is used.

(1) H. Eberle and P. Matussek, KfK Report 2504 (1977) 78

#### 7.5 Isotope Production at the Karlsruhe Isochronous Cyclotron

K.H. Assmus, N. Kernert, W. Maier, J.W. Peters, F. Schulz,  
and H. Schweickert

Kernforschungszentrum Karlsruhe, IAK II

Since the decision in 1980 to install an additional cyclotron (CP24H<sup>-</sup> from TCC), which will be mainly used for isotope production, we have started to develop large scale (200  $\mu\text{A}$  of protons on an external target) production facilities for medical isotopes. The first isotopes, to be produced in amounts of Curies, will be  $^{201}\text{Tl}$  and the  $^{81}\text{Rb}/^{81\text{m}}\text{Kr}$  generator system. If the development to separate  $^{123}\text{I}$  from  $^{124}\text{I}$  via a molecular laser excitation process succeeds, the production of  $^{123}\text{J}$  will also get a high priority with this machine.

#### $^{201}\text{Tl}$

During the last few years  $^{201}\text{Tl}$  has become a very important radioisotope for use in myocardial diagnostics. Until now it has not been produced in West Germany, so that it has had to be imported from German Users with all the attendant risks and costs of transportation.

A production method for  $^{201}\text{Tl}$  has been developed at the Karlsruhe Isochronous Cyclotron in cooperation with HOECHST, which is handling the chemical processing.

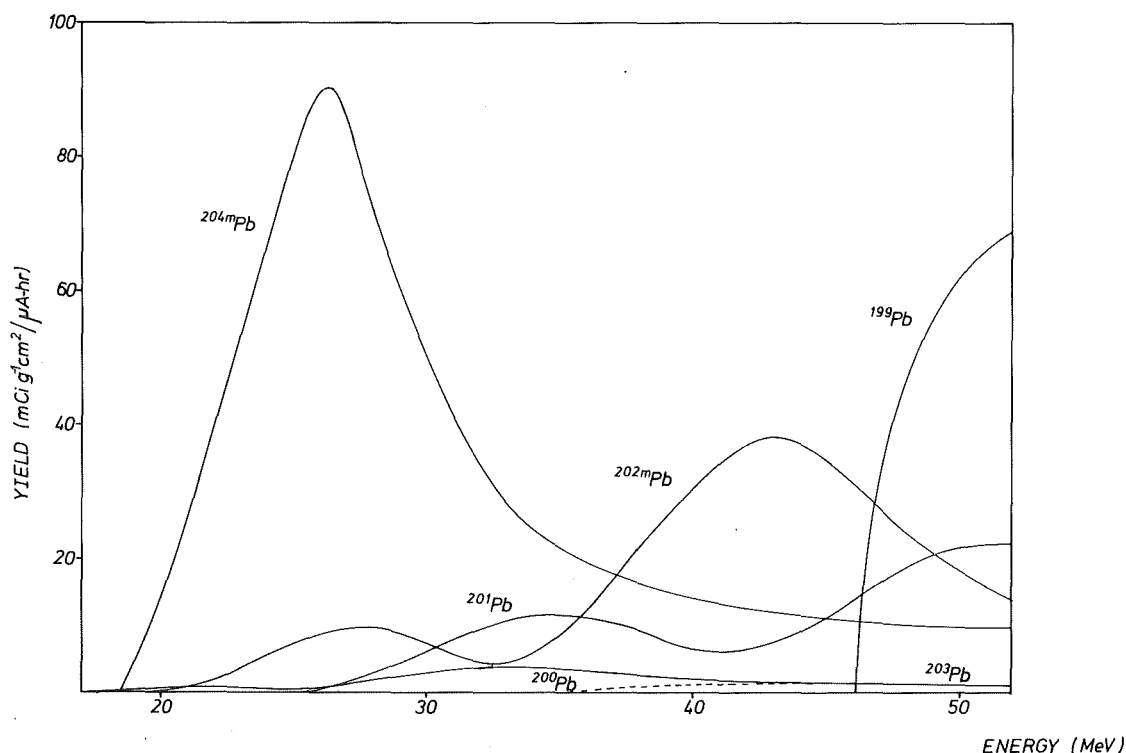


Fig. 1 Excitation function of the  $^{nat}\text{Tl}(d,xn)\text{Pb}$  reaction.

$^{201}\text{Tl}$  can be produced via its precursor  $^{201}\text{Pb}$  using a thallium target with either a proton or deuteron beam. Since the maximum available proton energy (26 MeV) is not sufficient to produce acceptable yields (2,3) excitation functions for deuterons were taken. Fig. 1 shows the excitation functions of the various Pb isotopes.

The energy range used for the production of  $^{201}\text{Pb}$  was optimized to give a high yield while at the same time minimizing the  $^{200}\text{Tl}$  and  $^{202}\text{Tl}$  contamination of  $^{201}\text{Tl}$ . Since January 1981 irradiated targets have been routinely delivered to HOECHST for development of the chemical separation.

#### $^{81}\text{Rb}/^{81m}\text{Kr}$ Generator

The first  $^{81}\text{Rb}/^{81m}\text{Kr}$  generators were delivered to the St. Vincentius Krankenhaus Karlsruhe for medical use in September 1980. Following this trial production run the target set-up was extensively modified and the beam guiding system improved. Production resumed from June 1981 till the end of July 1982, with a total of 146 generators having been delivered to 8 different hospitals. At present 8 generators are produced weekly, but the facility for the production of 6 generators simultaneously is to be installed at the beginning of 1983.

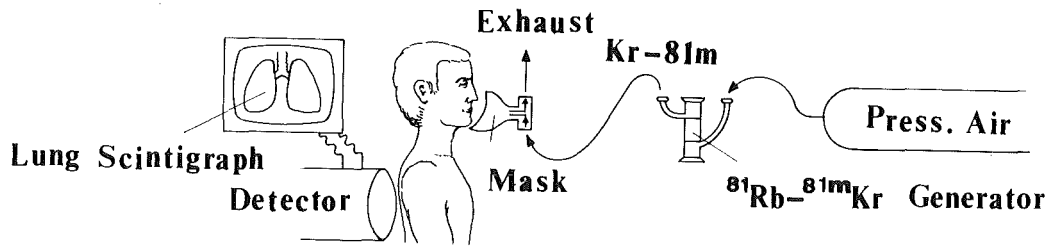


Fig. 2 Schematic diagram of elution process.

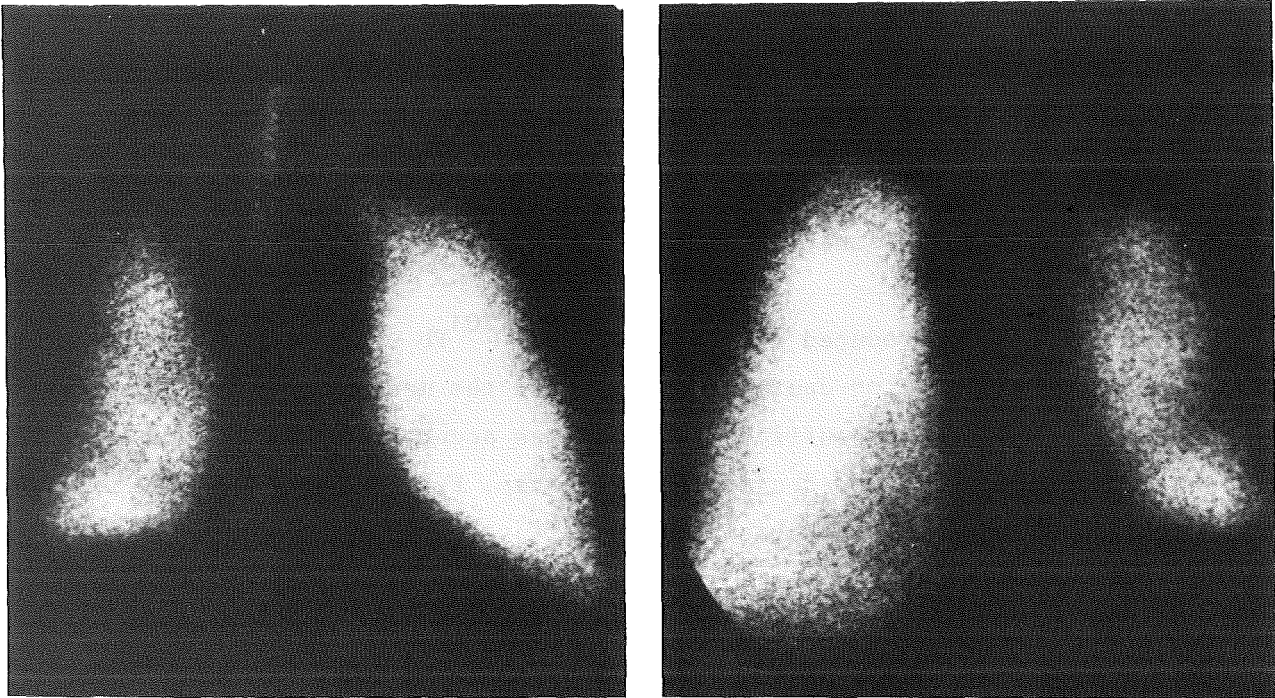


Fig. 3 Lung ventilation scintigraphs with  $^{81m}\text{Kr}$

To optimize the elution of  $^{81m}\text{Kr}$  from a generator during routine medical use close cooperation with the hospitals using the generators was necessary. The  $^{81m}\text{Kr}$  is eluted by a small flow of pressured air through the generator and then mixed with the patient's breathing air. Thus the distribution of  $^{81m}\text{Kr}$  in the patient's lung is the same as the normal ventilation. The gamma decay of 13 s  $^{81m}\text{Kr}$  is simultaneously observed by the use of a commercial Anger gamma camera. The elution process is schematically illustrated in Fig. 2.

Using this technique high quality scintigraphs are achieved. An example is shown in Fig. 3 of a patient with reduced ventilation of the right lung.

### I-123

During the period of report the production of iodine-123 via the (p,2n) reaction (1) has been used routinely to prepare 650 batches with a total of 25 Ci for application at 12 hospitals. Again the production has been performed with a high reliability as 99 % of the scheduled deliveries were in time.

- (1) K.H. Assmus, K. Jäger, R. Schütz, F. Schulz, and H. Schweickert  
Routine Production of Iodine-123 at the Karlsruhe Isochronous  
Cyclotron, 8th International Conf. on Cyclotrons and Their Applications,  
Bloomington, Ind., USA; Sept. 18-21, 1978.
- (2) M.C. Lagunas-Solar et al., Int. J. of Appl. Rad. and Isotopes,  
2a (1978)159.
- (3) S.M. Qaim et al., Int. J. of Appl. Rad. and Isotopes 30, (1979) 85.

### 7.6 The Production of Pure $^{81}\text{Rb}$ and its Use to Measure Blood Flow

R. Berberich<sup>+</sup>, B. Feurer, A. Hanser, and E. Oberhausen<sup>+</sup>  
Kernforschungszentrum Karlsruhe, IAK II

The isotope  $^{81}\text{Rb}$  is of medical interest because it enables one to determine the blood flow of highly perfused organs (kidneys, myocardium, liver) in a special manner (1). Intravenously injected  $^{81}\text{Rb}$  is taken up, by the cells of such organs and the disturbance of the radioactive equilibrium with the very short-lived daughter  $^{81m}\text{Kr}$  (13 sec.), being washed out

by the blood stream, can be used as a measure of the blood flow. Because the precise locus-dependent determination of the  $^{81}\text{Rb}/^{81\text{m}}\text{Kr}$ -ratio in the tissue is a difficult task, no disturbing radiation from any other isotope should be present. Unfortunately, contaminants, especially  $^{82\text{m}}\text{Rb}$  having a half-life similar to that of  $^{81}\text{Rb}$  and emitting a strong and penetrating gamma-radiation, were also produced in the usual production processes for  $^{81}\text{Rb}$ . As an electromagnetic isotope separator with a surface-volume ionization ion source (2,3) is a good tool to purify  $^{81}\text{Rb}$  without great losses, we are developing on this base a production procedure for pure  $^{81}\text{Rb}$ . At present we produce the  $^{81}\text{Rb}$  by irradiating enriched  $^{82}\text{Kr}$  with 26 MeV protons in a small target specially designed for a speedy and simple transfer to the succeeding electromagnetic isotope separation, which is characterized by an efficiency of  $\sim 85\%$  and by direct implantation of the  $^{81}\text{Rb}$  into a small quantity of sodium chloride (4). Dissolving the sodium chloride containing the  $^{81}\text{Rb}$  in pyrogene-free saline and filtering through a millipore filter yields the ready injection solution. A sample of the purified  $^{81}\text{Rb}$ , carefully studied with gamma-spectroscopic means, showed no contaminants (activities relatively to  $^{81}\text{Rb}$ , 3 hours after EOB:  $^{79}\text{Rb} < 10^{-4}$ ;  $^{82\text{m}}\text{Rb} < 10^{-4}$ ;  $^{83}\text{Rb} < 10^{-7}$ ;  $^{84}\text{Rb} < 10^{-7}$ ;  $^{81\text{m}}\text{Se} < 10^{-3}$  etc.)

Preliminary experiments with animals using a high performance gamma camera (Anger camera) in connection with a data evaluation system were encouraging but showed that the usual collimator has to be replaced by one specially designed for the high gamma-ray energies of  $^{81}\text{Rb}$  ( $\sim 500$  keV), and that the signals arising from scattered radiation have to be eliminated as well as possible. For this, these signals have to be recorded separately, setting the energy window between the full energy peaks of  $^{81}\text{Rb}$  and  $^{81\text{m}}\text{Kr}$ . First experiments with normal persons and some patients, including the improvements mentioned, resulted in qualitatively good scintigrams of the myocardium. The variation of the  $^{81\text{m}}\text{Kr}/^{81}\text{Rb}$ -ratio enabled better recognition of areas less perfused.

- (1) T. Jones and E.M.E. Matthews, *Nature* 230 (1971) 119
- (2) G.J. Beyer, E. Herrmann, A. Piotrowski, V.J. Raiko and N. Tyrroff, *Nucl. Instr. Meth.* 96 (1971) 439.
- (3) P.G. Johnson, A. Bolson and C.M. Henderson, *Nucl. Instr. Meth.* 106 (1973) 83.
- (4) A. Hanser and B. Feurer, *Int. Journ. Appl. Rad. Isot.* 32 (1981) 775

<sup>+</sup> Abt. f. Nuklearmedizin d. Radiologischen Univ.-Klinik Homburg (Saar)

## 7.7 Energy Deposition Spectra of $\pi^-$ Calculated from Pion Nucleus Interaction Data \*

G. Büche

Kernforschungszentrum Karlsruhe , IK II

Distributions of absorbed dose in linear energy transfer (LET) and in lineal energy ( $y$ ) are calculated for beams of negatively charged pions in a water phantom. The calculation is based on a comprehensive set of experimental data. The production of  $\delta$ -ray electrons by fast particles is taken into account semiempirically. The results are compared with experimentally obtained spectra of ionization yields. The equivalence of data derived from pion nucleus interaction and taken from microdosimetry is clearly revealed. The distribution of absorbed dose is given in a sequence of contributions from the various secondary particles, i.e., the so-called 'star' particles emitted following a nuclear capture process or the recoil nuclei from pion scatterings. This unique feature of calculated spectra will be useful for a characterization of the beam quality in view of the existing dependence of biological effects on track structure properties.

\*Radiat Environ Biophys. 20 (1982) 255

## 7.8 Beam optical measurements at the SIN PIOTRON \*

U. Wiedner

Kernforschungszentrum Karlsruhe, IK II

Investigations of the magnetoptical properties of the new superconducting pion irradiation facility of the Swiss Institute of Nuclear Research are reported in this paper. The so called PIOTRON has been used for cancer therapy with negative pions since 1980. Sixty identical beams can be directed at the tumor by two sets of 60 superconducting coils. The following parameters which are essential for any therapy planning have been measured by using scintillation counters and multiwire proportional chambers: Muon and electron contamination, beam sizes and phase space distributions for all 60 beams. The experimental set-up was mounted precisely

on a device which can be rotated within the patient chamber. For a single beam these parameters have also been measured as a function of pion momentum, momentum band and for various pion production targets.

Particular attention has been paid to a calibration of the therapy control system used routinely for patient irradiations relative to the counting rates measured with our independent detecting devices. It turns out that the therapy control systems work reliably. Furthermore the results show that the phase space distributions and beam sizes differ little for the 60 beams. Mechanical misalignments of the coils have not been observed. The measurements confirm the excellent operation of the PIOTRON, which is in full agreement with original specifications.

\* KfK Report 3356 (1982)

8. LIST OF PUBLICATIONS  
PUBLICATIONS AND REPORTS

Almeida, J.

The Capture Cross Sections of the Neon Isotopes and the s-Process  
Neutron Balance  
KfK Report 3347 (1982).

Amols, H.I., Büche, G., Kluge, W., Matthäy, H., Moline, A., Münchmeyer, D.  
Multiple Scattering Distributions for Therapeutic Pion Beams  
Physics in Medicine and Biology 26 (1981) 277.

Andl, A.

Laserspektroskopische Untersuchung der optischen Isotopieverschiebung  
und Hyperfeinstruktur bei stabilen und radioaktiven Kalzium-Nukliden  
KfK Report 2191 (1981).

Beck, R.

On Calculating Matrix Elements of Slater-Determinant Wave  
Functions in the Cluster Model  
KfK Report 3261 (1981)

Beer, H., Käppeler, F., Wisshak, K., Ward, R.A.

$^{176}\text{Lu}$ : Cosmic Clock or Stellar Thermometer?  
Astrophys. J Suppl. 46 (1981) 295

Beer, H., Käppeler, F., Wisshak, K.

Fast Neutron Capture on  $^{180}\text{Hf}$  and  $^{184}\text{W}$  and the Solar Hafnium  
and Tungsten Abundance  
Astronomy and Astrophysics 105 (1982) 270.

Besset, D., Do, H.Q., Favier, B., Greeniaus, L.G., Heer, E., Hess, R.,  
Lechanoine-Leluc, C., Rapin, D., Werren, D.W., Daum, M., Mango, S.,  
Steiner, E., Vecsey, G., Weddigen, Ch.

An Experimental Ensemble Used for the Study of Proton-Proton  
Scattering at SIN  
Nucl. Instr. and Meth. 184 (1981) 365

Bolger, J., Boschitz, E., Mathie, E.L., Smith, G.R., Meyer, M., Vogler, F.,  
Mango, S., Konter, J.A., Mutschler, G.S., Arvieux, J.

Further Measurements of  $iT_{11}$  in  $\pi$ - $d_{\text{pol}}$  Scattering as an  
Investigation of Dibaryon Resonance Effects  
Phys. Rev. Lett. 48 (1982) 1667

Bolger, J., Boschitz, E., Pröbstle, G., Smith, G.R., Mango, S.,  
Vogler, F., Johnson, R.R., Arvieux, J.

Evidence for a Dibaryon Signal in the Measurement of elastic  $\pi^+$ - $d_{\text{pol}}$   
Scattering  
Phys. Rev. Lett. 46 (1981) 167

Borie, E., Rinker, G.A.

The Energy Levels of Muonic Atoms  
Rev. Mod. Phys. 54 (1982) 67

Borie, E.

Hadronic Vacuum Polarization Correction in Muonic Atoms  
Z. Phys. A302(1981) 187

Borie, E.

Use of Furry-Sommerfeld Wave Functions in Pair Production  
of Medium and High Energies  
Z. Phys. A302 (1981) 219

CELLO-Collaboration

Topology of Hadronic  $e^+e^-$  Annihilation Events at 22 and 34 GeV cm  
Energy.  
Phys. Lett. 110B (1982) 329

CELLO-Collaboration

An Analysis of the Charged and Neutral Energy Flow in  $e^+e^-$  Hadronic  
Annihilation at 34 GeV and a Determination of the QCD Effective Coupling  
Constant  
Phys. Lett. 113B(1982) 427

Chatelain, P., Favier, B., Foroughi, F., Hoftziezer, J., Jaccard, S.,  
Piffaretti, J., Walden, P., Weddigen, Ch.

The Differential Cross Section for Elastic Proton-Proton Scattering  
at 90° cm Between 500 and 600 MeV  
Journ. of Phys. G - Nucl. Phys. 8 (1982) 643

Cierjacks, S., Swinhoe, M.T., Buth, L., Howe, S.D., Raupp, F.,  
Schmitt, H., Lehmann, L.

The Absolute Detection Efficiency of an NE 213 Liquid Scintillator  
for Neutrons in the Energy Range 50-450 MeV  
Nucl. Instr. and Meth. 192 (1982) 407

Cook, J., Gils, H.J., Rebel, H., Majka, Z., Klewe-Nebenius, H.  
Optical Model Studies of  ${}^6\text{Li}$  Elastic Scattering at 156 MeV  
KfK Report 3233 (1981)

Corcalciuc, V., Gils, H.J., Rebel, H., Buschmann, J., Pesl, R.  
Dumitrescu, R., Zagrömski, S., Feibt, K.

104 MeV Alpha Particle Scattering from  ${}^{90,92}\text{Zr}$   
KfK Report 3105 (1982)  
Z. Phys. A305 (1982) 351

Corcalciuc, V., Rebel, H., Pesl, R., Gils, H.J.

Isoscalar Octupole Transition Rates in  ${}^{50}\text{Ti}$ ,  ${}^{52}\text{Cr}$  and  ${}^{208}\text{Pb}$  from  
Model-Independent Analyses of 104 MeV Alpha-Particle Scattering  
KfK Report 3377 (1982)

Engler, J.

Atomic and Nuclear Properties of Materials  
KfK Report 3286 (1982)

Eyrich, W., Hassold, H., Hofmann, A., Mühlendorfer, B., Scheib, U.,  
Rebel, H.

Search for EO Strength in the Giant Resonance Region of  $^{12}\text{C}$   
Phys. Rev. C24 (1981) 2720

Flügge, G.

The CELLO Detector and LAr Colarimeters at PETRA  
KfK Report 3286 (1982)

Flügge, G.

Experimental Evidence of Quarks and Gluons  
In: Quarks and Nuclear Forces  
Fries, D., Zeitnitz, B. (Hrsg.)  
Springer Tracts in Modern Physics, Vol. 100 (1982) 1

Friedman, E., Gils, H.J., Rebel, H.

Comparison Between Radial Sensitivity of Different Strongly  
Interacting Probes  
Phys. Rev. C25 (1982) 1551.

Fries, D.C., Zeitnitz, B. (Hrsg.)

Quarks and Nuclear Forces  
Springer Tracts in Modern Physics, Vol. 100 (1982)

Gabathuler, K., Domingo, J.J., Gram, P., Hirt, W., Jones, G.,  
Schwaller, P., Zichy, J., Bolger, J., Ingram, Q., Albanese, J.P.,  
Arvieux, J.

Elastic Pion-Deuteron Scattering Near the 3-3 Resonance  
Nucl. Phys. A350 (1980) 253

Gotta, D., Doerr, M., Fetscher, W., Schmidt, G., Ullrich, H.,  
Backenstoß, G., Kowald, W., Schwanner, I., Weyer, H.J.

Kinematically Complete Measurement of the Absorption of Stopped Pions  
in  $^3\text{He}$   
Phys. Lett. 112 B (1982) 129

Gotta, D.

Untersuchung der Reaktion  $\pi^- \ ^3\text{He} \rightarrow \text{pnn}$  mit gestoppten Pionen in einem  
kinematisch vollständigen Experiment  
KfK Report 3226 (1981)

Gspann, J., Poth, H.

Internal Cluster Beam Target for Antineutron Production in LEAR  
KfK Report 3198 (1981)

Guigas, R.

Untersuchung des antiprotonischen Röntgenspektrums der Lithiumisotope  
 $^6\text{Li}$  and  $^7\text{Li}$   
KfK Report 3208 (1981)

Hage, W., Wisshak, K., Käppeler, F.,

Neutron Fission Cross Section Measurement of Americium -241 in the  
Energy Range from 10 to 1030 keV  
Nucl. Sci. Eng. 78 (1981) 248

Hanser, A., Feurer, B.

Pure  $^{81}\text{Rb}$  for Medical Use Obtained by Electromagnetic Isotope Separation  
Internat. Journ. of Appl. Radiation and Isotopes 32 (1981) 775

Heck, D.

Elemental Mapping with the Karlsruhe Nuclear Microprobe  
Nucl. Instr. and Meth. 197 (1982) 91.

Hoftiezer, J., Weddigen, Ch., Favier, B., Jaccard, S., Walden, P.,  
Chatelain, P., Fofoughi, F., Nussbaum, C., Piffaretti, J.

Energy Dependence of the  $pp \rightarrow \pi^+ d$  Differential Cross Section Between  
500 and 600 MeV  
Phys. Lett. 100B (1981) 462

Käppeler, F., Beer, H., Wisshak, K., Clayton, D.D., Macklin, R.L.,  
Ward, R.A.

s-Process Studies in the Light of New Experimental Cross Sections:  
Distribution of Neutron Fluences and r-Process Residuals  
KfK Report 3210 (1981) - The Astrophys. Journ. 257 (1982) 821

Majka, Z., Gils, H.J., Rebel, H.

Cluster Folding Model for  $^{12}\text{C}(^6\text{Li}, ^6\text{Li})$  Scattering at 156 MeV  
Phys. Rev. C25 (1982) 2996

Maschuw, R., Zeitnitz, B.

Neutrino Physics at the Pulsed Spallation Neutron Source SNS  
KfK Report 3362 (1982)

Müller, K.R.

Ein theoretischer und praktischer Beitrag zum Triotron, einem  
neuartigen UHF-Hochleistungsverstärker mit hohem Wirkungsgrad.  
KfK Report 3364 (1982)

Miller, R., Naqvi, A.A., Käppeler, F., Bao, Z.Y.,

Numerical Results of a  $(2E, 2\nu)$ -Measurement for Fast Neutron Induced  
Fission of  $^{235}\text{U}$  and  $^{237}\text{Np}$   
KfK Report 3220 (1981)

Neumann, B., Rebel, H., Gils, H.J., Planeta, R., Buschmann, J.,  
Klewe-Nebenius, H., Zagromski, S., Shyam, R., Machner, H.,

Inclusive Break-Up Reactions of  $^6\text{Li}$  at an Incident Energy of  
26 MeV/nucleon  
KfK Report 3277 (1982) - Nucl. Phys. A382 (1982) 296

Pesl, R.

Untersuchungen von Kernmaterieverteilungen und isoskalaren Übergangsdichten von  $^{48}\text{Ca}$ ,  $^{50}\text{Ti}$  und  $^{52}\text{Cr}$  durch Streuung von 104 MeV Alpha-Teilchen  
KfK Report 3242 (1982)

Pröbstle, G.

Messung der Vektoranalysierstärke  $iT_{11}$  in der elastischen Pion-Deuteron Streuung im Gebiet der (3,3) Resonanz.  
KfK Report 3235 (1981)

Reffo, G., Fabbri, F., Wisshak, K., Käppeler, F.,

Fast Neutron Capture Cross Sections and Related Gamma-Ray Spectra of Niobium-93, Rhodium-103, and Tantalum-181  
Nucl. Sci. Eng. 80 (1982) 630

Schatz, G.

Die Entstehung der schweren Elemente im stellaren s-Prozeß - Grundlagenforschung im Kernforschungszentrum Karlsruhe  
KfK-Nachrichten 13 (1981) 192

Smith, G.R., Bolger, J., Boschitz, E., Mathie, E.L., Pröbstle, G., Meyer, M., Vogler, F., Mango, S.

Measurement of the Vector Analyzing Power  $iT_{11}$  for the  $\pi d \rightarrow 2p$  Reaction with a Polarized Target  
Phys. Rev. C25 (1982) 70

Simonius, M., Hemeck, R., Jacquemart, Ch., Lang, J., Häberli, W., Weddigen, Ch.

Effects of Transverse Polarization Components in Parity Tests with Longitudinally Polarized Nucleons  
Nucl. Instr. and Meth. 177 (1980) 471

Thompson, R.C., Hanser, A., Bekk, K., Meisel, G., Froelich, D.

High Resolution Measurements of Isotope Shifts in Lead  
Z. Phys. A305 (1982) 89

Thompson, R.C.

An Instrumental Effect on Spectral Line Profiles  
Journal of Quantitative Spectroscopy and Radiative Transfer  
27 (1982) 417

Walter, G., Beer, H.,

Population Probabilities of Excited States in Radioactive Nuclei for s-Process Studies  
KfK Report 3327 (1982)

Wiedner, U.

Strahlenoptische Messungen am Piotron des SIN  
KfK Report 3356 (1982)

Ward, R.A., Beer, H.,

On the Origin of the Solar-system Abundances of  $^{113}\text{In}$ ,  $^{114}\text{Sn}$ , and  $^{115}\text{Sn}$   
Astron. Astrophys. 103 (1981) 189

Ziock, H.J., Ellis, R.J., Ziock, K.O.H., Bolger, J., Boschitz, E.  
Arvieux, J., Corfu, R., Piffaretti, j.

Quasifree Scattering of Positive Pions on Carbon  
Phys. Rev. C24 (1981) 2674

### CONFERENCE CONTRIBUTIONS

#### 9th Int. Conf. on High Energy Physics and Nuclear Structure Versailles, (France) July 6-10, 1981

Backenstoß, G., Kowald, W., Schwanner, I., Tauscher, L.,  
Weyer, H.J., Dörr, M., Gotta, D., Ljungfelt, S., Schmidt, G.  
Ullrich, H.

Measurement of the K X-Ray Yield for Pionic  $^3\text{He}$

Backenstoß, G., Hasinoff, M., Pavlopoulos, P., Repord, J.,  
Tauscher, L., Tröster, D., Blüm, P., Guigas, R., Koch, H.,  
Meyer, M., Raich, U., Richter, B., Adiels, L., Bergström, I.,  
Fransson, K., Kerek, A., Suffert, M., Ziontas, K.

Study of Rare  $\bar{p}p$  Application Channels

Blüm, P., Guigas, R., Koch, H., Meyer, M., Poth, H., Richter, B.,  
Backenstoß, G., Izychi, M., Pawlopoulos, P., Tauscher, L.,  
Fransson, K., Nilsson, A., Suffert, M., Ziontas, K.

Measurement of Antiprotonic X-Rays from the Isotopes  $^6\text{Li}$  and  $^7\text{Li}$

Boschitz, E., Hoftiezer, J., Mathie, E.L., Smith, G.R., Meyer, M.

Cross Sections for  $\pi^+d \rightarrow 2p$  with 170-285 MeV Pions

Bolger, J., Boschitz, E., Pröbstle, G., Smith, G.R., Mango, S.,  
Vogler, F., Johnson, R.R., Arvieux, J.

Evidence for a Dibaryon Signal in the Measurement of Elastic  
 $\pi^-d_{\text{pol}}$  Scattering

Friedman, E., Gils, H.J.

Combined Analysis of Pionic Atoms and Alpha Particle Scattering

Gils, H.J., Friedman, E., Rebel, H., Pesl, R.

Nuclear Sizes of  $^{40,42,44,48}\text{Ca}$ ,  $^{50}\text{Ti}$ ,  $^{52}\text{Cr}$  from  
Elastic Scattering of 104 MeV Alpha-Particles

Koch, H., Blüm, P., Guigas, R., Köhler, T., Meyer, M., Poth, H.,  
Raich, U., Richter, B., Backenstoß, G., Hasinoff, M., Pavlopoulos, P.,  
Repond, J., Tauscher, L., Tröster, D., Adiels, L., Bergström, I., Fransson, K.,  
Kerek, A., Suffert, M., Ziontas, K.

Search for Baryonium via Neutral Transitions

Poth, H., Richard, J.M.

Low Energy Proton-Antiproton Charge-Exchange and Applications

Smith, G.R., Bolger, J., Boschitz, E., Mathie, E.L., Pröbstele, G.

The Reaction  $\pi^+ d(\text{pol}) \rightarrow 2p$  with a Polarized Deuteron Target

Internat. Conf. on High Energy Physics, Lisboa, Portugal,  
July 9-15, 1981

Apel, W.D., Augenstein, K.H., Bertolucci, E., Donskov, S.V.,  
Inyakin, A.V., Kachanov, V.A., Abdel Khalek, F., Krasnokutsky, R.N.,  
Krüger, M., Leder, G., Lednev, A.A., Manelli, I., Mikhailov, Yu.V.,  
Müller, H., Pierazzini, G.M., Prokushkin, Yu.D., Quaglia, M.,  
Schneider, H., Scribano, A., Sergiampietrie, F., Shuvalov, R.S.,  
Sigurdsson, G., Voncelli, M.L.

Analysis of the Reaction  $\pi^- p \rightarrow \pi^0 n$  at 40 GeV/c Beam Momentum  
Nucl. Phys. B 193 (1981) 269

Fourth International Symposium on Neutron-Capture Gamma-Ray  
Spectroscopy and Related Topics, Grenoble (France) September 7-11,  
1981

Beer, H., Käppeler, F.,  
Population of Isomeric States by keV Neutron Capture:  
Clues to Stellar s-Process Nucleosynthesis

U.S. German Workshop on Radioactive Ion Beams and Small Cross  
Section Measurements, Columbus, Ohio, August 31 - Sept. 4, 1981

Schatz, G.

Laser Techniques for the Detection of Small Numbers of Atoms  
(Invited Talk)

9th Int. Conf. on Cyclotrons and Their Applications,  
Caen, France, September 7-10, 1981

Bollmann, E., Fehsenfeld, F., Kleinrahm, A.

Irradiation Technique of Machine Parts for Wear Measurements  
in Mechanical Engineering. Poster.

Schatz, G.

Industrial and Environmental Applications of Cyclotrons.

Schweickert, H.

SULEICKA: A Proposal for a Superconducting Light Ion Cyclotron  
at Karlsruhe

Microprocessor College, Trieste, Italy, September, 9-26, 1981

Raich, U.

MPL Cookbook. A Guide to MPL

2nd Int. Conf. on Microanalysis Using Charged Particle Accelerators,  
Namur, Belgium, September 8-10, 1981

Heck, D.

Elemental Mapping with the Karlsruhe Nuclear Microprobe

European Symposium on Few Body Problems, Ferrara (Italy)  
14.-19. September 1981

Klages, H.O.

Total Cross Sections for Neutron Induced Reactions on  $^3\text{He}$

IAEA Consultants Meeting on Uranium and Plutonium Isotope Resonance  
Parameters, Vienna, September 28 - October 2, 1981

K. Wisshak, F. Käppeler, and F.H. Föhner

Review of the  $^{240}\text{Pu}$  and  $^{242}\text{Pu}$  Unresolved Resonance Region

INDC (NDS)- 129/9J p. 165 International Atomic Energy Agency Vienna 1982

Workshop on Direct Reactions in Nuclear Physics, Bad Honnef,  
October 5-9, 1981

Gils, H.J.

$^6\text{Li}$  Break-Up Reactions at 26 MeV/Nucleon

Linear Accelerator Conf., Santa Fe, N.M., October 19-23, 1981

Citron, A.

The Linear Accelerator for the Proposed German Spallation Source

4th Int. Workshop on ECR Ion Sources and Related Topics,  
Grenoble, France, January 13-16, 1982

Bechtold, V., Friedrich, L., Schweickert, H.

ECR-Ion Source Development at the Karlsruhe Cyclotron, Status of  
p-HISKA and HISKA

Bechtold, V., Friedrich, L., Haushahn, G., Möllenbeck, J.  
Schulz, F., Schweickert, H.

Injection of ECR Ions at the Karlsruhe Isochronous Cyclotron

20th Int. Winter Meeting on Nuclear Physics, Bormio, Italy,  
January 25-30, 1982

Rebel, H., Shyam, R., Neumann, B., Gils, H.J., Machner, H.

Studies of Inclusive Charged Particle Spectra from 156 MeV  $^6\text{Li}$  Induced  
Reactions in Terms of Spectator Break-Up of the Projectile

Expertentreffen für Kernphysik, Schleching, March 4-13, 1982

Käppeler, F.

Der Neutronenfluß im s-Prozeß

Klages, H.O.

Analysierstärke der n-p Streuung im Energiebereich bis 50 MeV

NEANDC/NEACRP Specialists' Meeting on Fast Neutron Capture Cross Sections, Argonne, Ill., April 20-23, 1982

Wisshak, K., Käppeler, F., Reffo, G., Fabbri, F.

Fast Neutron Capture in Actinide Isotopes: Recent Results from Karlsruhe.

Wisshak, K., Käppeler, F., Reffo, G., Fabbri, F.

Neutron Capture Widths of s-Wave Resonances in  $^{56}\text{Fe}$ ,  $^{58,60}\text{Ni}$  and  $^{27}\text{Al}$

Conf. on Lasers in Nucl. Phys., Oak Ridge, Tenn., April 21-23, 1982

Rebel, H., Schätz, G.

Laser Induced Fluorescence Spectroscopy in Atomic Beams of Radioactive Nuclides  
(Invited Talk)

Frühjahrstagung DPG, Kernphysik, Karlsruhe, March 22 - 26, 1982

Abela, R., Wüst, J., Effenberger, B., Kunold, W., Schneider, M., Simons, L.M.

Isotopieverschiebung in myonischem  $^{134,136,138}\text{Ba}$

Abela, R., Wüst, J., Effenberger, B., Kunold, W., Schneider, M., Simons, L.M., Österle, W.

Messung des g-Faktors gebundener negativer Myonen im Grundzustand myonischer Atome

Almeida, J., Beer, H., Erbe, D., Käppeler, F., Leugers, B., Rupp, G., Walter, G., Wisshak, K., Bao, Z.Y.

Die Messung von Neutroneneinfangquerschnitten und ihre Bedeutung für die Nukleosynthese im s-Prozeß

Amols, H.I., Büche, G., Degitz, H., Hofmann, K., Klein, U., Kluge, W., Matthäy, H., Markus, R., Mechttersheimer, G., Münchmeyer, D., Przybilla, G., Randall, H., Schmidt, D., Wiedner, U., Moline, A.

Physikalische Grundlagenuntersuchungen zum Projekt Strahlentherapie mit negativen Pionen am SIN

Aures, R., Heeringa, W., Kiontke, S., Maschuw, R., Giorginis, G., Schmidt, F.K., Schulz, R., Wochele, J.

Apparative Entwicklungen für Experimente mit polarisierten Kernen

Aures, R., Heeringa, W., Maschuw, R., Schmidt, F.K.

Ein polarisiertes Protonentarget.

Bauer, Th.S., Domingo, J.J., Ingram, Q., Kyle, G., Bacher, R., Smith, G.R.,  
Stamminger, R.

Doppelter Ladungsaustausch von Pionen an  $^{16,18}\text{O}$

Bechtold, V., Friedrich, L., Schulz, F., Schweickert, H.

Aktuelle und zukünftige Experimentiermöglichkeiten mit leichten  
Ionen am Karlsruher Isochronenzyklotron

Bechtold, V., Doll, P., Friedrich, L., Hucker, H., Husson, L.,  
Klages, H.O., Krupp, H., Oexner, M., Schmalz, G.

POLKA - Strahlen schneller polarisierter Neutronen am Karlsruher  
Zyklotron

Beck, R., Dickmann, F.

Untersuchung der Cluster-Struktur in  $^6\text{Li}$

Blüm, P., Simons, L.M.

Die Bahndynamik negativ geladener Teilchen in einer Zyklotronfalle

Bolger, J., Boschitz, E., Mathie, E.L., Smith, G.R., Meyer, M.,  
Vogler, F., Mango, S., Konter, T., Mutchler, G.S.

Messung der Vektoranalysierstärke der elastischen Pionenstreuung  
an Deuteronen im Gebiet der Dibaryon-Resonanzen

Buschmann, J., Bbzychczyk, J., Freindl, L., Gils, H.J.,  
Grotowski, K., Klewe-Nebenius, H., Majka, Z., Micek, S., Neumann, B.,  
Panaciewicz, A., Planeta, R., Rebel, H., Zagromski, S.

Investigation of Z Spectra from  $^{40}\text{Ca} + ^6\text{Li}$  Reaction at 156 MeV

Corcalciuc, V., Pesl, R., Rebel, H., Gils, H.J.

Suche nach Unterschieden in den Neutron- und Proton-Komponenten bei  
den  $0^+ - 3_1$  Oktupolübergängen von  $^{208}\text{Pb}$ ,  $^{50}\text{Ti}$  und  $^{52}\text{Cr}$

Dörr, M., Fetscher, W., Gotta, D., Maier, T., Reich, J., Schmidt, G.,  
Ullrich, H., Backenstoss, G., Kowald, W., Schwanner I., Weyer, H.J.

Messung der Reaktion  $^6\text{Li}(\pi^-, dt)n$  mit gestoppten Pionen

Dörr, M., Fetscher, W., Gotta, D., Maier, T., Reich, J., Schmidt, G.,  
Ullrich, H., Backenstoss, G., Kowald, W., Schwanner, I., Weyer, H.J.

Untersuchung der s-Absorption in  $^3\text{He}$  mit gestoppten Pionen

Dörr, M., Fetscher, W., Gotta, D., Maier, T., Simmons, L.M., Schmidt, G.,  
Ullrich, H., Backenstöss, G., Kowald, W., Schwanner, I., Weyer, H.J.

Bestimmung des nn/np-Verhältnisses bei der Absorption gestopper Pionen  
in  $^{16}\text{O}$ .

Dörr, M., Fetscher, W., Gotta, D., Maier, T., Reich, J., Schmidt, G.,  
Ullrich, H., Backenstoss, G., Kowald, W., Schwanner, I., Weyer, H.J.

Emission von Teilchenpaaren nach  $\pi^-$ -Absorption in Li.

Doll, P., Haesner, B., Hansmeyer, J., Hiebert, J., Klages, H.O.,  
Krupp, H., Oexner, M., Plischke, P., Schwarz, P., Wilczynski, J.

Erste Experimente zum Wenig-Nukleonen-Problem am Karlsruher  
polarisierten Neutronenstrahl

Doll, P., Haesner, B., Kecskemeti, J., Klages, H.O., Schwarz, P.,  
Wilczynski, J., Zeitnitz, B.

Messung des differentiellen Wirkungsquerschnitts der elastischen  
(n,d)-Streuung im Energiebereich von 2 bis 30 MeV.

Doll, B., Haesner, B., Kecskemeti, J., Klages, H.O., Schwarz, P.,  
Wilczynski, J., Zeitnitz, B.

Messung des differentiellen Wirkungsquerschnittes der elastischen  
 $n$ - $^3\text{He}$ -Streuung im Energiebereich von 5 bis 30 MeV

Eyrich, W., Hassold, H., Hofmann, A., Mühdorfer, B., Scheib, U.,  
Rebel, H.

Suche nach E0-Stärke im Riesenresonanzgebiet von  $^{12}\text{C}$

Eyrich, W., Fuchs, K., Hofmann, A., Ortner, H., Rebel, H.,  
Scheib, U., Stamminger, R., Steuer, D., Steuer, H.

Der Neutronenzerfall des Gebietes der isoskalaren Riesenresonanzen  
in schweren Kernen

Gils, H.J., Rebel, H., Buschmann, J., Zagromski, S.,  
Klewe-Nebenius, H., Oehlschläger, J.

Elastische Streuung von 104 MeV Alpha-Teilchen an  $^{42,43,44}\text{Ca}$  und  $^{50}\text{Ti}$ ,  
 $^{51}\text{V}$ ,  $^{52}\text{Cr}$  zur Untersuchung von Gerade-Ungerade Effekten der  
Kernmaterieverteilungen

Gils, H.J., Buschmann, J., Zagromski, S., Rebel, H., Krisch, J.,  
Heinz, M.

Ein einfacher Magnetspektrograph für das Isochron-Zyklotron Karlsruhe

Haesner, B., Klages, H.O., Schwarz, P.

Eigenschaften großvolumiger Szintillationsdetektoren

Haesner, B., Heeringa, W., Hucker, H., Klages, H.O., Maier, Ch.

Eigenschaften eines verbesserten flüssig- $^3\text{H}$ -Szintillationsdetektors  
für schnelle Neutronen

Kilian, K., Möhl, D., Pilkuhn, H., Poth, H.

Produktion von Antideuteronen in Antiproton-Speicherringen

Maier, T.

Austrittskorrektur bei der Berechnung der Neutronen-Nachweiswahrscheinlichkeit mit Hilfe des Kurz-Codes

Meyer, M., Olszewski, R., Vogler, F., Boschitz, R., Mathie, E.L.,  
Smith, G.R., Dehnhard, D.

Messung von ( $\pi, \pi'$  gamma) Winkelkorrelationen an  $^{12}\text{C}(2^+)$ .

Neumann B., Rebel, H., Gils, H.J., Planeta, R., Buschmann, J.,  
Klewe-Nebenius, H., Zagromski, S., Shyam, R., Machner, H.

Analyse von  $^6\text{Li}$ -Aufbruchreaktionen bei 26 MeV/Nukleon

Thompson, R.C., Anselment, M., Bekk, K., Göring, S., Hanser, A.,  
Rebel, H., Schatz, G.

Laserspektroskopie stabiler und instabiler Bleisotope

#### Frühjahrstagung DPG, Teilchenphysik, March 25-27, 1982

Blüm, P., Guigas, R., Koch, H., Köhler, T., Meyer, M., Raich, U.,  
Richter, B., Backenstoss, G., Hasinoff, M., Pavlopoulos, P.,  
Repond, J., Tauscher, L., Tröster, D., Adiels, L., Bergström, I.,  
Ernasson, K., Kerek, A., Suffert, M.

Photonennachweis mit hoher Energieauflösung im Bereich von 40-1000 MeV

#### CELLO-Collaboration

Apel, W.D.

Erzeugung von Quark und Gluon Jets

Randoll, H.

Hadronische Jets in der  $e^+e^-$ -Annihilation

Banerjee, S.

A Study of Energy Correlation in Hadronic  $e^+e^-$ -Annihilations.

Knapp, J., Makowsky, M.

Untersuchung von hadronischen Ereignissen mit harten, isolierten  
Photonen in der  $e^+e^-$ -Annihilation

Küster, H.

Tau-Paar-Erzeugung in  $e^+e^-$ -Vernichtung

Fries, D.C.

Was ist ein Proton?

Unser derzeitiges physikalisches Bild vom Nukleon

Poth, H., Hasenroth, H., Hill, Ch., Wolf, A.

Elektronenkühlung von Antiprotonen im LEAR

Wolf, A., Poth, A.

Simulation des Elektronenkühlprozesses gespeicherter Strahlen

Reunion Commune de la Societe Francaise de Physique et de la  
Societe Suisse de Physique, Lyon, France, April 21-23, 1982

Chatelain, P., Favier, B., Foroughi, F., Piffaretti, J., Nussbaum, C.,  
Hoftiezer, J., Weddigen, Ch., Jaccard, S.

Sections Efficaces et Pouvoir d'Analyse de la Reaction de  
Production  $p^+p^- \rightarrow \pi^+ + d$  entre 516 et 582 MeV

4th Annual Symp. on Safeguards and Nuclear Material Management:  
Petten, The Netherlands, April 27-29, 1982

Ottmar, H., Matussek, P.

Possibilities and Limitations in the Harmonization and  
Standardization of Radiometric Measurements for Nuclear  
Material Accountancy.

Workshop on Radiobiology and Tumor Therapy with Heavy Particles  
Brugg, CH, April 27-30, 1982

Kluge, W. Matthäy, H.

Physical Input to the SIN Pion Therapy Project

Workshop on Physics with Low Energy Antiprotons at LEAR, Erice, May 1982

H. Poth

Physics with Antiprotonic Atoms

H. Poth

A Possibility to determine the  $\bar{p}H^-$  Mass Difference with Stored and Cooled  
 $\bar{p}$  and  $H^-$  Beams in LEAR

L. Hütten, H. Poth, A. Wolf, H. Hasenroth, Ch. Hill

The Electron Cooling Device for LEAR

P. Blüm, H. Poth, L.M. Simons

Measurements of the  $\bar{p}$ -Annihilation Cross-Section at Very Low Energy

K. Kilian, B. Möhl, J. Gspann, H. Poth

Internal Targets for LEAR

D. Gotta

X-Ray Spectroscopy of  $\bar{p}$ -Hydrogen in the Cyclotron Trap

P. Blüm, L.M. Simons

The Extraction of Low Energetic Antiprotons of the Cyclotron Trap

L. M. Simons

The Cyclotron Trap: Status of Preparation and Planned Experiments

H. Koch, K. Kilian, D. Möhl, H. Pilkuhn, H. Poth  
Antideuterons at LEAR

E. Borie

Pressure Dependence of X-Ray Yield in Protonium

E. Borie, F. Gross

$\bar{N}N$  Interaction in a Three Dimensional Relativistic Equation

E. Borie

Vacuum Polarization and Spin-orbit Splitting in Antiprotonic Atoms

E. Borie, P. Blüm, D. Gotta, H. Koch, H. Poth, L.M. Simons,  
M. Suffert

Further possibilities for measurements on the  $\bar{p}p$  System using  
the cyclotron trap

Symposium on Production and Physics of Highly Charged Ions,  
Stockholm, Sweden, June 1-5, 1982

Bechtold, V., Friedrich, L., Schweickert, H.  
The ECR-Source for the Karlsruhe Cyclotron

19th European Cyclotron Progress Meeting, Grenoble, France,  
June 10-11, 1982

Bechtold, V., Friedrich, L., Schweickert, H.  
Status Report on the Karlsruhe ECR-Ion-Source HISKA

LECTURES

Bechtold, V.  
Status of the Karlsruhe Cyclotron Facility  
TRIUMF, Vancouver, Canada, May 28, 1982

Beer, H.  
Die s-Prozeß Nukleosynthese der uu-Isotope  $^{176}\text{Lu}$  und  $^{180}\text{Ta}$   
Max-Planck-Institut für Chemie, Mainz, February 10, 1982

Borie, E.  
QED in gebundenen Systemen  
Universität Bochum, March 3, 1982

Borie, E.  
Präzisionstests der QED  
Universität Dortmund, May 18, 1982

Flügge, G.

Test des GWS Modells in der Elementarteilchenphysik  
Gemeinsames Seminar Karlsruhe/Tübingen, 6.5.1982

Flügge, G.

Untersuchungen zur Quantenchromodynamik in  $e^+e^-$  Vernichtung  
Kolloquium Bonn, November 1981

Flügge, G.

Talk and Panel Discussion in the General Meeting on LEP: Experimental Areas  
at PETRA

Villars, Schweiz, June 1-7, 1982

Flügge, G.

The CELLO Detector and LAr Calorimeters at PETRA  
Tristan Workshop, Tokyo, Japan, November 1981

Flügge, G.

New Experimental Techniques

Invited talk at the Int. Conference on High Energy, Physics, Lisbon, July 81

Fries, D.C.

Evidenz für Quarks

Gemeinsames Seminar Karlsruhe/Tübingen, Oktober 1981

Fries, D.C.

Ergebnisse der DPG Frühjahrstagung auf dem Gebiet der Teilchenphysik  
ÖPG Tagung, Silberberg, Österreich, September 28, 1982

Gils, H.J.

Ein Vergleich der radialen Empfindlichkeit verschiedener stark wechselwirkender Proben auf die Neutronenverteilung in Atomkernen  
Universität Erlangen, February 15, 1982

Gils, H.J.

Kernradien und Übergangsdichten aus "modellunabhängigen" Analysen der elastischen und unelastischen Alpha-Teilchen Streuung  
Universität München, May 25, 1982

Käppeler, F.

The present Status of Experimental Techniques for Neutron Capture Cross Section Measurements

Comitato Nazionale per l'Energia Nucleare, Bologna, Italien, October 15, 1981

Käppeler, F.

Elementsynthese durch Neutroneneinfang und das Alter der Milchstraße  
Max-Planck-Institut für Radioastronomie, Bonn, December 4, 1981

Klages, H.O.

Experimente am Karlsruher Neutronenflugzeitspektrometer  
Universität Stuttgart, July 17, 1981

Klages H.O.

Experiments with the polarized Neutron-beam at the Karlsruhe Cyclotron  
ETH Zürich, January 12, 1982

Klages, H.O.

Erste Experimente am polarisierten Neutronenstrahl des Karlsruher Zyklotrons  
Universität Tübingen, February 5, 1982

Klages, H.O.

Few body experiments at POLKA  
Universität Basel, April 22, 1982

Klages, H.O.

Experimentelle Untersuchungen am polarisierten Neutronenstrahl  
Universität Hamburg, June 21, 1982

Kluge, W.

Physikalische Grundlagen der Strahlentherapie mit negativen Pionen  
Physikalisch-Technische Bundesanstalt, Braunschweig, June 10, 1982

Küster, H.

$\tau$ -Paarerzeugung in  $e^+e^-$  Vernichtung  
DESY Seminar, January 1982

Meisel, G.

Präzisions-Laserspektroskopie an Atomen: Anwendungen auf Probleme der Atom-  
und der Kernphysik  
Universität Hamburg, May 4, 1982

Müller, H.

Results from CELLO  
Nordic Meeting, Oslo, Norwegen, January 10, 1982

Rebel, H.

High Resolution Laser Spectroscopy of Radioactive Atoms  
Michigan State University, East Lansing, Mich., USA, April 19, 1982

Schatz, G.

Das Alter der schweren Elemente  
Universität Tübingen, November 25, 1982

Schatz, G.

Medical and Engineering Application of the Karlsruhe Isochronous Cyclotron  
University of Petroleum and Minerals, Dhahran, Saudi-Arabien, January 28,  
1982

Schatz, G.

Nuclear Charge Radii of Unstable Nuclei from Laser Spectroscopy  
University of Petroleum and Minerals, Dhahran, Saudi-Arabien, January 27,  
1982

Ullrich, H.

Pionenabsorption am  $^3\text{He}$   
Universität Mainz, December 1981

Zeitnitz, B.

Neutrino physics at the Pulsed Neutron Spallation Source SNS  
Rutherford Lab., Chilton, England, March 12, 1982

Zeitnitz, B.

Neutrino physics at the Pulsed Neutron Spallation Source SNS  
Université de Montreal, Canada, August 19, 1982

Zeitnitz, B.

Nuclear Physics Experiments at the Neutron Spallation Source SNQ  
Euratom, Geel, Belgium, July 7, 1981

Zeitnitz, B.

Kernphysik an der Spallationsneutronenquelle SNQ  
Universität Tübingen, July 8, 1981

Zeitnitz, B.

Kernphysik an der Spallationsneutronenquelle SNQ  
Universität Erlangen, September 1981

Zeitnitz, B.

Neutrino physics at the pulsed spallation source SNQ  
Max-Planck-Institut für Kernphysik, Heidelberg, November 1981

Zeitnitz, B.

Neutrino physics at the pulsed spallation source SNQ  
Universität Frankfurt, January 14, 1982

Zeitnitz, B.

Neutrino physics at the pulsed spallation source SNQ  
KFA Jülich, January 11, 1982

9. PERSONNEL

Institut für Kernphysik

Head of the Teilinstitut I (IK 1): Prof. Dr. Bernhard Zeitnitz

Scientific and Technical staff:

D'Agostini, Giulio, Dr.	Keim, H.
Apel, W.-D., Dr.	Kiontke, S., DP
Aures, R., DP	Klages, H.-O., Dr.
Banerjee, S., Dr.	Knapp, J.
Bischoff, A.	Krüger, M., DP
Bodenkamp, J., Dr.	Krupp, H.
Brady, F.P., Prof.Dr.	Küster, H.
Cernohorsky, I.	Maier, Ch.
Chrobaczek, D., DP	Makowsky, M.
Deutsch, G.	Maschuw, R., Dr.
Dittmann, R.	Mischok, M.
Doll, P., Dr.	Müller, H., Dr.
Engler, J., Dr.	Oexner, M.
Finckh, E., Prof.Dr.	Plischke, P., Dr.
Flügge, G., Prof.Dr.	Randoll, H., DP
Forstbauer, B.	Remane, E.
Fries, D.C., Dr.	Schmalz, G., DI
Fues, W., Dr.	Schmidt, F.K., Dr.
Gamerding, K.	Schmidt, G., DP
Giorginis, G., Dr.	Schneider, H., Dr.
Gumbsheimer, R., Ing.grad.	Schulz, R.
Haesner, B., Dr.	Schwarz, P., Dr.
Hagert, H.	Skacel, H.
Hansmeyer, J.	Spohrer, G.
Heeringa, W., Dr.	Ullrich, G.
Hiebert, J., Prof.Dr.	Wilczynski, J., DP
Hofmann, K., DP	Wochele, J.
Hopp, G., DP	Zeitnitz, B., Prof.Dr,
Hucker, H.	Ziegler, P.
Husson, L., Ing.	
Kecskemeti, J., Dr. (bis 31.7.1981)	

Head of the Teilinstitut II (IK II): Prof. Dr. Anselm Citron

Scientific and technical staff:

Blüm, P., Dr.	Reich, J.
Bolger, J., Dr.	Richter, B., DP
Borie, E., Dr.	Sambole, K.
Boschitz, E., Prof.Dr.	Schmidt, G., Dr.
Büche, G., Dr.	Schneider, M., DP
Citron, A., Prof.Dr.	Simons, L.M., Dr.
Degitz, G., DP	Smith, G., Dr.
Dröge, M.	Ullrich, H., Prof.Dr.
Effenberger, B.	Vogel, R.
Engelhardt, D., Prof.Dr.	Weddigen, Ch., Dr.
Feißt, W.	Wiedner, U., DP
Gotta, D., Dr.	Wolf, A., DP
Guigas, R., Dr.	
Hauth, J.	
Höhne, A.	
Hoftiezer, J., Dr.	
Jaki, J.	
Kärcher, K.	
Klein, U., DP	
Kluge, W., Prof.Dr.	
Koch, H., Prof. Dr.	
Köhler, T., DP	
Kunold, W., DP	
Ljungfelt, S., DP	
Maier, Th.	
Mankin, U.	
Markus, R.	
Mathie, E., Dr.	
Matthäy, H., Dr.	
Meissner, K.	
Meyer, M., DI	
Oesterle, W.	
Poth, H., Dr.	
Pröbstle, G., Dr.	

Institut für Angewandte Kernphysik II

Head of the Institute: Prof. Dr. Gerhard Schatz

Scientific and technical staff:

Almeida, J., Dipl.-Phys.	Kruppa, H., Dr.
Anselment, M. Dipl.-Phys.	Kunigkeit, G., Mrs., Ing.
Bao, Z.Y., Mrs., Dipl.-Phys.	Maaß, E., Mrs.
Beck, R., Dr.	Manger, D.
Beer, H., Dr.	Matussek, P., Dipl.-Phys.
Bekk, K., Dr.	Meisel, G., Dr.
Buschmann, J., Dr.	Mengoni, A., Dr.
Dickmann, F., Dr.	Michel-Piper, I., Mrs., Ing.
Dohrmann, H., Ing.	Micek, St., Dr.
Eberle, H., Ing.	Ottmar, H., Dr.
Erbe, D.	Pesl, R., Dipl.-Phys.
Feurer, B.	Planeta, R., Dr.
Friederich, H.M., Mrs.	Rebel, H.G., Prof. Dr.
Gils, H.J., Dr.	Rupp, G.
Göring, S., Dipl.-Phys.	Schmidt, K.A., Dipl.-Phys.
Hanser, A., Dr.	Schmitt, St.
Heck, D., Dr.	Thompson, R., Dr.
Heinz, M.	Walter, G., Dipl.-Phys.
Käppeler, F., Dr.	Wisshak, K., Dr.
	Zagromski, S., Ing.

Head of the Cyclotron Laboratory: Dr. Hermann Schweickert

Scientific and technical staff:

Acharya, H., Mrs.	Kauther, P.
Assmus, K.H.	Kernert, N., Dipl.-Phys.
Bauer, G.	Kessel, M.
Bechtold, V., Dr.	Kirste, E., Mrs.
Bialy, J., Dipl.-Phys.	Kleinrahm, A., Dr.
Biber, J.	Kögel, B.
Blank, R.	Maier, W.
Bollmann, E., Dipl.-Phys.	Mangold, D.
Dressen, R.	Mayl, R.
Ehret, H.P.	Möllenbeck, J., Ing.
Erbe, D.	Peters, J.-W., Dipl.-Phys.
Erdel, E.	Pfeifer, R.
Ernst, R.	Rämer, Ch., Miss, Ing.
Fehsenfeld, P., Dr.	Roth, H.
Fischböck, T.	Schimpf, P.
Franz, J.	Schüssler, B.
Friedrich, L., Dr.	Schulz, F., Ing.
Gegenheimer, B.	Seidel, H.
Günther, O.	Seitz, J.
Haßpacher, G.	Seufert, H.
Haushahn, G., Dipl.-Phys.	Sheikh, S.
Heidenreich, K.	Stöbener, E., Ing.
Heinzmann, H., Dipl.-Inf.	Thouw, T., Dr.
Herlan, A.	Uchatius, R., Mrs.
Herrmann, P.	Uhlemann, S., Mrs.
Hirth, W.	Wiss, L.
Holler, H.	Ziegler, P.
Kaltenbaek, J.	Zimmermann, H.
Kappel, W.-R., Ing.	